UNIVERSITY OF OKLAHOMA

GRADUATE COLLEGE

INVESTIGATING BASIC CHARACTERISTICS OF TURBULENCE IN CHANNEL FLOWS USING LAGRANGIAN CONCEPTS

A DISSERTATION

SUBMITTED TO THE GRADUATE FACULTY

in partial fulfillment of the requirements for the

Degree of

DOCTOR OF PHILOSOPHY

By

CHIRANTH SRINIVASAN
Norman, Oklahoma
2012

INVESTIGATING BASIC CHARACTERISTICS OF TURBULENCE IN CHANNEL FLOWS USING LAGRANGIAN CONCEPTS

A DISSERTATION APPROVED FOR THE
SCHOOL OF CHEMICAL, BIOLOGICAL AND MATERIALS ENGINEERING

BY

_____
Dr. Dimitrios V. Papavassiliou, Chair

_____
Dr. Prakash Vedula

_____
Dr. Jeffrey H. Harwell

_____
Dr. Robert L. Shambaugh

_____
Dr. Alberto Striolo

To my late grandfather, Shri P. V. Sivarama Dikshitar

Acknowledgements

I thank the almighty for the blessings showered upon me. Ability is of little account without opportunity. Little would I have had a chance to showcase my talent and ability if not for this wonderful opportunity afforded to me by Professor Dimitrios Papavassiliou. Professor Papavassiliou, I thank you for believing in me and providing me this opportunity to attend the University of Oklahoma to pursue my Doctorate degree. I thank you for effort and time spent in educating me. I am grateful for your patience and reassurance during the hard times. I am also thankful for your encouragement and appreciation for the work I have done. I am extremely grateful to you for providing me with plenty of opportunities to travel across the United States to different conferences to showcase our work. You have been instrumental in my development and growth as a student, researcher and a person. You have been a great role model and it's been a blessing to have worked for you. You are one of the great persons I have met and I will forever be appreciative of my time working for you. Thank you again for this opportunity.

I thank my committee members, Dr Alberto Striolo, Dr Jeffrey Harwell, Dr Robert Shambaugh and Dr Prakash Vedula for their comments and incites in improving this work. I also take this opportunity to thank all the reviewers of my publications for providing insightful and thorough reviews of the work, enabling me to improve the quality of the work. I would like to thank British Petroleum for their graduate fellowship which helped me with a part of my tuition during my doctoral degree. The financial support of the project by National Science Foundation under CBET-0651180 is gratefully acknowledged. I would also like to thank the TeraGrid for offering

computational support under TRAC TG-CTS080042, TG-CTS090025 grants. The computational resources provided by the OU Center for Supercomputing Education and Research (OSCER) are also appreciated. I thank Dr Henry Neeman and the OSCER team for their continuous help and support.

There have been many individuals, family and friends, who have played a role in me realizing this dream. First and foremost, I thank my grandmother, Sivakamu for her love and encouragement. I thank my parents, Rajalakshmi and Srinivasan, my aunt, Vidya and Uncle, Gangadharan for their love, affection and support. I also want to thank my sister, Sadhvi, for being there for me through thick and thin. I owe a large deal of my education to my Uncle's, Ramanathan and Somasekharan. I thank them for their support. I want to thank my friends, Srivats, Aravinda, Deepthi, Siva and Pratik for their support and help during my education. I want to thank all my undergraduate friends from Vellore Institute of Technology, who have helped me, supported me and guided me through my Doctorate degree. I thank the members in my group, Kalyan, Khoa, Quoc and Ruby, for the many discussions that have helped me learn new things and realize important ideas. I owe thanks to the CBME department at the University of Oklahoma for their help and support at various times during my academic life. Last but not least, I thank the University of Oklahoma for providing me an ideal environment to work and thrive in.

Table of Contents

List of Tables

List of Figures

Abstract

Many examples of turbulent motion of particles in nature can be better perceived through the concept of backwards turbulent dispersion. Some examples include pollutants in atmosphere or oceans reaching populated human or marine life, mixing scenarios where components are moving towards the mixing location, or temperature noise at a certain downwind location. In these scenarios, turbulent dispersion occurs as the particles diffuse towards a particular location. The combined direct numerical simulation/Lagrangian scalar tracking (DNS/LST) approach is used to obtain Lagrangian statistics of turbulent scalar field. This provides a natural and convenient framework to compute statistics for turbulent backwards scalar dispersion. Using this method, the forwards and backwards single particle and relative dispersion statistics are calculated. The rates of dispersion and the principal direction of transport of heat are studied. Four main regions of the channel, namely, viscous sub-layer, transition region, logarithmic region and center of the channel, are studied with interest. The dispersion characteristics are also analyzed for different types of fluids, including but not limited to, Pr = 0.1 (liquid metal regime), Pr = 0.7 (air), Pr = 10 (water), Pr = 100 to 50000 (heavy oils, engine oils). The results of the study show clear differences in the rates and direction of heat transport for the forwards and backwards dispersion. A term called "turbulent dispersive ratio" is established as a parameter to capture the differences in the direction of forwards and backwards scalar transport.

A vast DNS/LST database generated over the years in the cases of different Re and Pr is utilized to propose and verify a scaling parameter to capture turbulent heat transport. This scaling parameters, identified as the location and the value of the

maximum normal turbulent heat flux, capture all the inner scales, which are the scales of turbulent flows in the near wall regions of the channel, while exhibiting universality in capturing the scalar profiles of mean, fluctuations, and scalar flux.

Finally, the versatile DNS/LST particle method is used to translate the theoretical framework of Churchill to calculate the turbulent Prandtl number (Pr_t). The study provides the first-of-a-kind dependency data for Pr_t for different wall normal locations and different molecular Pr. The results reveal a dependence of Pr_t on the Pr, especially very close to the wall.

Chapter 1: INTRODUCTION

Turbulent transport from solid boundaries has a wide variety of natural and industrial applications. Gaining understanding of such turbulent flows, which can in turn help in actively or passively modifying any such flow system, can be of immense technological importance. Turbulent dispersion is one of the defining characteristics of turbulence and plays a major role in industrial applications, such as heat exchange, mixing, flow in reactors or catalyst regeneration units. The trajectories of fluid particles that move erratically due to dispersion can be analyzed, and their statistics can be helpful in characterizing the turbulence in that flow field. Since turbulent dispersion is a result of the turbulence in the flow field, it is also a random or stochastic process. The majority of our knowledge about turbulent dispersion comes from Eulerian measurements, where a frame of reference that is fixed in space is used. However, Lagrangian computations and measurements, where the system of reference follows the motion of individual fluid elements, can lead to valuable insights about the process of turbulent dispersion and in turn about the mechanism of turbulent transport. Since laminar flows provide weak transport mechanisms, turbulent dispersion is quite important for mixing dispersed phases. In fact, one of the defining characteristics of turbulence is the enhancement of mixing [1].

The literature in the case of turbulent flows inside channels has vastly expanded over the past few decades. Numerical experimentation using the direct numerical simulation technique has been implemented by Lyons [2], Kim et al. [3] and later Papavassiliou [4] to understand some of the finer details of turbulent channel flows.

These studies have classified the different regimes in turbulent channel flows based on the velocity profiles while also identifying the presence of a variety of coherent structures that drive these turbulent flows. Many experimental and computational works have focused on turbulent dispersion in isotropic, homogenous turbulence. However, how does turbulent dispersion behave in anisotropic turbulent channel flow? Is there an interlinking between the coherent structures and the characteristics of turbulent dispersion? Research in the area of turbulent dispersion has not focused on these questions.

Understanding how heat or mass is transported due to turbulent dispersion in channels can also be of practical significance in cases where one needs to determine the locations of hotspots and identifying the positions to place thermal sensors inside heat exchangers, and to calculate locations of maximum or efficient mixing inside mixing vessels. Several different experiments and numerical simulations have aimed at identifying dispersion characteristics in wind tunnels, isotropic turbulence, and in wall turbulence. Most of the data obtained have been for dispersion in case of particles of the fluid dispersing from an initial location at a particular initial time. However, it is not always that particles of the dispersing fluid tend to move away from one another in case of turbulent dispersion. For example, in mixing, ensembles of particles of the fluid move towards the point of mixing and the dispersion carries these particles towards the location at a particular final time of reference. It is important to identify the nature of these two types of dispersion. What is the driving force behind these two types of dispersion and how do they differ in characteristics? The results of such a study can be valuable in improving the existing dispersion models available for mixing applications.

Wall bounded turbulent flows with their relevance in turbulent boundary layers and significance in aerospace, naval and other industrial applications have been studied with vast interest. There has been plenty of research in turbulent boundary layer flows and channel flows aimed at understanding unique parameters to scale turbulent flow parameters. Because of the recent availability of extensive databases for different types of flow and flow conditions, several studies over the past few years have investigated scaling of turbulent momentum transport. While the literature related to scaling of turbulent momentum transport grows, rather few studies have aimed at understanding the scaling and dynamics behind turbulent scalar transport. The direct applicability of the wall parameter scaling of turbulent momentum transport to turbulent scalar transport needs considerable deliberation. Studies have recently established the tenuous and rationally unjustified analogy between momentum and heat transport [5]. Other studies [6] have established further proof of failures of some of the basic transport analogies proposed over the years and plenty of questions remain unanswered with respect to the scaling of turbulent scalar transport.

The failures of the theoretically established analogies [7] have increased the interest of researchers to better understand turbulent heat/mass transport. Since most of the past works have restricted themselves to momentum transport and assumed an analogous relationship to heat transport, to this day, relating the scalar fluctuations to the fluctuations in velocity is a major theoretical problem. The challenge remains to essentially calculate the identified parameters like the Reynolds stress, turbulent heat flux, to close the combined system of equations relating both the momentum and heat transfer.

This dissertation aims to answer some of the unanswered questions outlined above, in the area of turbulent flow research. The research work is focused on fully developed turbulent flow inside turbulent channels. The first objective of this dissertation is to understand the concept of turbulent backwards dispersion and differentiate it from the forwards dispersion. The focus is then shifted to study the scaling characteristics of scalar turbulence. Finally, momentum transport is related to heat/mass transport by obtaining the values for the turbulent Prandtl number.

1.1 Turbulent dispersion

Depending on whether one analyzes a single particle or pairs of particles selected from a particle cloud undergoing dispersion, single or relative dispersion, respectively, are of interest. Studying turbulent relative dispersion is of practical importance, since there is a fundamental link between pair dispersion and problems like growth of contaminant clouds in the atmosphere [8, 9], mixing of chemical species in a chemical reactor [10, 11], and even industrial production of nanoparticles [12]. Furthermore, a clear understanding of turbulent dispersion helps in better describing concentration fluctuations of a particular particle cloud [13, 14] and in determining reaction rates in turbulent chemical reactors and in analysis of turbulent combustion [15, 16].

Two different forms of turbulent dispersion can be distinguished. The classification takes into account the timeframe of the dispersion process and the initial and final location of the particles being dispersed. The forwards dispersion is related to how fluid particles, all at the same initial location (point, line or plane) at an initial time, diffuse away from this source; this is, for example, the case of how smoke moves away

from a chimney. On the other hand, if one considers the case of turbulent mixing, it will occur when material from two different locations, carrying fluid with different scalar concentrations, is brought together by turbulent motion. In this case, the dispersion of interest occurs prior to the particles arriving at a particular final location (point, line or plane) at the final time of interest. This process is termed backwards dispersion. Similar to the concept of turbulent forwards and backwards scalar single particle dispersion, one can also study two different cases of turbulent relative dispersion, "forwards relative dispersion" and "backwards relative dispersion".

1.2 Scaling of heat transport – wall turbulence

With the complexity that turbulence poses and its prevalence in a variety of flows, there has always been the need to simply it to capture some of its important characteristics. For example, some of the concepts like similarity analyses, dimensional analysis, scaling analysis, that have been introduced over the years have enabled researchers to identify some of the main variables and study the behavior of flow characteristics with respect to these variables. Such studies can be advantageous as they can help in reducing the number of variables needed to describe a particular flow. The relatively recent two-fold improvement, first, in developing experimental facilities capable of performing high Reynolds number turbulence experimentation [17-27], and second, in manufacturing high performance supercomputers that enable medium to high Reynolds number direct numerical simulation (DNS) studies [3, 28-34], has helped in accumulating a relatively large database of turbulence statistics. Hence, the use of similarity analysis, dimensional analysis, and the scaling of the turbulent flow statistics has been the subject of increasing interest in the past few years.

A review of the literature developed over the years about the "classical" scaling of turbulent flow close to a solid interface, which uses the wall parameters, namely, friction velocity, u^*, and fluid kinematic viscosity ν, has been presented by Gad-el-Hak and Bandyopadhyay [35].The question of the universality of this classical scaling, however, has been open for debate [36-45]. The main issues voiced in these works and the key points behind these differing opinions have been succinctly summarized by Marusic et al. [46]. While various studies establish the scaling characteristics of momentum transport, there has been a relative lack of studies that aim to understand the same for heat transport (from hereon, any reference to heat transport in the rest of the dissertation will also apply to mass transport. The dimensionless number, Prandtl Number, *Pr*, for heat transport, will automatically correspond to the dimensionless number, Schmidt Number, *Sc*, in case of mass transport). One can trace this lack of extensive scaling studies of heat transport to the establishment of empirical analogies that relate momentum to heat transport. Researchers have long believed that the established analogies can help in easily identifying heat transport scaling from the corresponding momentum transport scaling. However, studies have recently shown that the various momentum-heat transport analogies are not always true and sometimes break down [5, 6].

A first-of-a-kind comprehensive, semi-empirical correlation for the mean temperature profile was derived by Kader [47]. The Kader correlation utilized the classical scaling to predict the mean temperature as a function of the Prandtl number (*Pr*) in turbulent flow between infinitely long parallel plates as follows

$$T^+ = \Pr y^+ \exp(-\xi) + \left\{ 2.12 \ln\left[\left((1+y^+) \frac{1.5\left(2 - y^+/h^+\right)}{1+2\left(1-y^+/h^+\right)^2} \right) \right] + \beta(\Pr) \right\} \exp\left(-\frac{1}{\xi} \right) \quad (1.1)$$

where y^+ is the dimensionless distance from the wall, and h^+ represents the dimensionless half-channel height. The dimensionless temperature in wall units, T^+, is defined as

$$T^+ = \frac{T}{T^*} = \frac{T \rho c_p u^*}{q_w} \quad (1.2)$$

where q_w is the wall heat flux, ρ is the fluid density, c_p is the fluid heat capacity, Γ_w is the wall shear stress, $u^* = \sqrt{\frac{\Gamma_w}{\rho}}$ is the friction velocity, and y^+ is given as $y^+ = \frac{y u^*}{\nu}$.

The Prandtl number of the fluid is given by $\Pr = \frac{\mu c_p}{k}$, where μ is the dynamic viscosity of the fluid, and k is the thermal conductivity of the fluid. The use of the friction velocity, the viscosity and the wall heat flux is the essence of the classical scaling, or also known as "viscous" or "wall" scaling. This approach is referred to as classical scaling in the remainder of the dissertation. In Equation (1.1) the parameters β and ξ are given as follows:

$$\beta(\Pr) = \left(3.85 \Pr^{1/3} - 1.3\right)^2 + 2.2 \ln \Pr \quad (1.3)$$

and

$$\xi = \frac{10^{-2} \left(\Pr y^+\right)^4}{1 + 5 \Pr^3 y^+} \quad (1.4)$$

It is important to mention here that the Kader's temperature profile is semi-empirical and it was derived under the assumption that temperature scales with a single parameter in the overlap region between the inner and outer regions of the channel. The region

close to the wall is called the "inner region", while the region in the center of the channel is called the "outer region". Equation (1.1) is a significant result as it helps to completely describe the temperature profile through the entire height of the channel.

1.3 Turbulent boundary layer parameter – turbulent Prandtl number

The uncertainty associated with calculating the momentum and heat flux in the momentum and heat transport equations make it hard to solve the latter in case of turbulent wall bounded flows. The important fundamental parameter that relates these two quantities is the turbulent Prandtl number (Pr_t) (or turbulent Schmidt number, Sc_t), which relates the eddy diffusivity of heat (or eddy diffusivity of mass) to eddy diffusivity of momentum. Regarding turbulence modeling, the prediction of Pr_t is necessary to close the system of equations for heat transfer when eddy viscosity-based models (such as $\kappa-\varepsilon$ models) are utilized. Churchill [48], in his AIChE Institute Lecture, stated that "The development of a comprehensive predictive correlative expression for the turbulent Prandtl number is the principal remaining challenge with respect to the prediction of turbulent forced convection." In analogy to its molecular counterpart, the Pr_t is defined as the ratio of eddy diffusivity of momentum, ν_t to eddy diffusivity of heat, α_t, while the Sc_t is defined as the ratio of eddy diffusivity of momentum to eddy diffusivity of mass (recall that any reference to Pr_t and to heat transfer applies to the case of mass transfer and for Sc_t)

$$\mathrm{Pr}_t = \frac{\nu_t}{\alpha_t} \tag{1.5}$$

The Pr_t is given as

$$\mathrm{Pr}_t = \left(\frac{\overline{u'v'}\dfrac{\partial T}{\partial y}}{\overline{T'v'}\dfrac{\partial U}{\partial y}} \right) \tag{1.6}$$

Where, u' and v' are the velocity fluctuations in the streamwise, x, and normal, y, directions, respectively. T' is the fluctuation temperature, $\overline{u'v'}$ and $\overline{T'v'}$ is the Reynolds stress and turbulent flux, respectively. The evaluation of Pr_t at any point in the turbulent flow field requires the measurement of four quantities, i.e., the turbulent Reynolds stress, the velocity gradient, the turbulent heat flux, and the temperature gradient at that point. The difficulty of determining these four quantities accurately and concurrently at any given point makes data for Pr_t scarce. Most prior studies have reported that the Pr_t strongly depends on the Pr. In addition, for cases of turbulent flow through ducts, pipes or channels, the Pr_t has shown strong dependence on the distance from the wall.

Chapter 2: REVIEW OF LITERATURE

2.1 Turbulent dispersion

2.1.1 Single particle turbulent dispersion

The dispersion of particles by molecular means (i.e., Brownian motion) from the source in *x*-direction has been described in Einstein's work [49], who formulated the following relation:

$$\frac{d\overline{X^2}}{dt} = 2D \tag{2.1}$$

where D represents the molecular diffusivity and $\overline{X}$ is the particle displacement. For dispersion of fluid particles from a point source in a homogenous, isotropic turbulence, Taylor [50] proposed the following equation, in analogy to Einstein's Brownian movement correlation:

$$\frac{d\overline{X^2}}{dt} = 2\overline{u^2}\int_0^t R^L(\tau)d\tau \tag{2.2}$$

where, $\overline{u^2}$ is the mean square of the *x*-component of the velocity of fluid particles and R^L is the Lagrangian correlation coefficient. According to Taylor, the coefficient R^L takes into account the history of the particle motion. The value of the Lagrangian correlation coefficient is close to one at very small times, and, as a result, the dispersion $\overline{X^2}$ increases with time to the second power. The value of R^L becomes zero at larger times, and the dispersion increases linearly with time. At large times, the dispersion rate is a constant given by

$$\frac{d\overline{X^2}}{dt} = 2\overline{u^2}\tau^L \tag{2.3}$$

where the Lagrangian time scale is defined as

$$\tau^L = \int_0^\infty R^L(\tau)d\tau \tag{2.4}$$

Early reviews by Batchelor and Townsend [51], Monin and Yaglom [52], and Hinze [53] discussed the advances in studies of dispersion since Taylor. Recent reviews by Sawford [54], Warhaft [5] and Dimotakis [11] discussed the importance of understanding turbulent dispersion in analyzing turbulent mixing. The review by Warhaft [5] detailed the study of turbulent mixing using passive scalars. Dimotakis [11] reviewed turbulent mixing by classifying it into three main categories, namely, level-1 mixing, which is similar to mixing of passive scalars, level-2 mixing, akin to coupled dynamic mixing, and level-3 mixing, which produces changes to the mixing fluids. Sawford [54] reviewed the stochastic modeling, two-point closures, and kinematic simulation approaches to model turbulent relative dispersion. The review also entailed the connection of relative dispersion to turbulent mixing.

Corrsin obtained results [55, 56] for line source diffusion in homogenous shear flows with constant mean velocity gradient in which the Lagrangian dispersion in the direction of the flow, *x*, was different than the dispersion in the direction of the velocity gradient, *y*, which is described by Taylor's analysis.

Describing the dispersion of scalars instead of fluid particles turbulence introduces additional complications. This happens because the trajectory of a scalar marker in the flow field does not coincide with the trajectory of a fluid particle, since scalar markers can move off (due to molecular diffusion) of the fluid particle on which

they travel. Therefore, fluids with different *Pr* exhibit different behavior. A further advancement in the theory of dispersion came through Saffman [57], who defined the *material autocorrelation function*, R_d^L, and showed that

$$\overline{X^2} = 2\overline{u^2}\int_0^t (t-\tau)R(\tau)d\tau + 2Dt \qquad (2.5)$$

with

$$R_d^L(\tau) = \frac{1}{3}\frac{\overline{V_i(\vec{x}_0,t_0)V_i(\vec{x}_0,t_0+\tau)}}{\overline{u^2}} \qquad (2.6)$$

where, $V_i(\vec{x}_0,t_0)$ is the ith component of the fluid velocity at the location $\vec{X}(\vec{x}_0,t_0)$ of a marker that was released at location $\vec{x}_0$ at t = 0. The main difference between the material autocorrelation and the Lagrangian correlation is that the former correlates fluid velocity components along a scalar marker trajectory, instead of along the trajectory of fluid particles. The theories developed by Taylor and Saffman were for homogenous and isotropic turbulence. Turbulent dispersion in a wind tunnel has been studied by Shlien and Corrsin [58], while Fackrell and Robins [59] have studied turbulent mass dispersion using propane gas as the tracer.

The behavior of a large number of passive scalar markers, as described by Saffman, is fundamental to passive scalar transport using the Lagrangian framework. For the case of turbulent heat transfer in wall turbulence, Hanratty [60] devised a methodology using Taylor's theory, in which he used the dispersion of heat particles from an infinite number of continuous line sources of heat at one wall to describe a hot plane and an infinite number of continuous line heat sinks along the other wall to describe a cold plane.

2.1.2 Turbulent relative dispersion

The concept of relative dispersion, which involves studying the dispersion of a particle with respect to another particle, was introduced by Richardson [61]. Richardson studied the mean squared separation of particle pairs and concluded that only eddies that are comparable in size with the separation of these particle pairs are effective in increasing dispersion. The mean squared relative displacement of two fluid elements in a static flow dominated by molecular diffusion can be described by the expression provided by Einstein [49] as

$$\frac{d\left(\overline{\Delta X^2}\right)}{dt} = 2D \tag{2.7}$$

where D is the molecular diffusivity and ΔX is the relative separation of the fluid elements. Early studies [62] of mean squared relative dispersion in homogenous turbulence showed varied behavior in different intervals of time. Batchelor also found that, at very large times, the particle pairs move independent of each other and the rate of increase of mean squared displacement is not dependent on time. However, at intermediate times, Batchelor [62], Ogura et al. [63], and Obukhov [64], independently, derived an expression for the rate of mean squared relative displacement in homogenous turbulence, given as

$$\frac{d\left(\overline{\Delta X^2}\right)}{dt} = 3g\varepsilon t^2 \tag{2.8}$$

The term g is called the Richardson constant, and ε is the rate of dissipation of the turbulent kinetic energy. Comprehensive details of the development of various relative dispersion models have been well documented in the classical text of Monin and Yaglom [65]. Following the works of Richardson, Batchelor and Obukhov,

considerable amount of research has been done to document the behavior of relative dispersion in different flow regimes. A review of the various stochastic models implemented to understand the behavior of relative dispersion can be found in the work of Sawford [54]. A complementary review by Salazar and Collins [66] focused recently on various experimental and simulation data of turbulent relative dispersion based on the different scaling regimes. These reviews highlight the importance of DNS and laboratory experiments in obtaining pertinent relative dispersion data.

Relative dispersion plays a vital role in characterizing the concentration fluctuations in a smoke cloud or the temperature variance in a heat exchanger or a reactor. In these cases, however, the focus is on the scalar statistics rather than the fluid element. Modeling the motion of scalar markers adds an additional complication, as these passive markers can move off a fluid element due to molecular diffusion. Batchelor [67, 68], derived the equations describing the scalar relative dispersion. These equations, relating scalar statistics with the displacement of a passive scalar, have also been derived by Egbert and Baker [69], Lundgren [70] and Borgas et al. [71]. Observations from these studies point out the difference between concentration statistics of scalars with non-zero and zero diffusivity that are a direct result of the corresponding difference between the displacement statistics of the diffusing scalar and the fluid particle. At high *Re* and high *Sc*, the difference in the mean concentration has been found to be negligible [57]. Even at high *Re* and high *Sc* the concentration variance is marginally different, since the dissipation of scalar fluctuations is influenced by the molecular diffusivity.

Though plenty of research has been aimed at understanding relative dispersion [54, 66], rather few studies have focused on the rates of mean squared relative displacement when the forwards and backwards perspectives of relative dispersion are considered separately. Bernard and Rovelstad [72] were the first to perform direct numerical simulation to study single-particle backwards dispersion in a turbulent channel flow. They looked at an ensemble of fluid particles having common end points and studied the scalar transport correlations. Not until recently, the first effort to study the differences between forwards and backwards relative dispersion was made by Sawford et al. [73]. Lagrangian stochastic models and DNS were used in stationary, isotropic turbulence to calculate forwards and backwards relative dispersion statistics. Even at low *Re*, where there is a very small inertial sublayer, they found that the backwards relative dispersion proceeds at a faster rate than its forwards counterpart. The results of Sawford et al. also showed clear differences in the particle separation probability density function (pdf) for the forwards and backwards relative dispersion. Sawford et al. observed that the differences vanish when the fluctuating velocity field is symmetric and Gaussian. Experimental evidence of the differences between forwards and backwards relative dispersion have been reported in the work of Berg et al. [74]. A particle tracking velocimetry (PTV) technique was used to obtain Lagrangian trajectories of fluid elements in water for a flow generated using eight rotating propellers. The results obtained showed that the backwards relative dispersion proceeds twice as fast as the forwards relative dispersion. Berg et al. utilized the DNS data of Biferale et al. [75, 76] to compare their experimental work with a direct numerical simulation and found similar results. Berg et al. concluded that the replication of the

results, considering the physical differences existing between the experiment and DNS, pointed to the robustness of the results and also validated the use of DNS to perform turbulent dispersion studies.

2.2 Coherent structures and primary directions of turbulent scalar transport

A physical description of turbulent transport near channel walls can be achieved by a better understanding of the coherent structures that exist in these regions [24]. Theodorsen [77] and Townsend [78] were pioneers in this area, establishing the existence of organized, statistically important motions in turbulent shear flows. Robinson extensively reviewed the literature about coherent motions and discussed the importance of these coherent structures in sustaining turbulence [79]. Over the years, a lot of research has been dedicated to the understanding and prediction of these coherent structures in turbulent flows [80]. These studies have identified a wide range of structures existing in the turbulent boundary layer starting from hairpin vortices [81], hairpin packets [82], horseshoe vortices [77], funnel vortices [83], and near wall longitudinal vortices [84]. The logarithmic layer and the outer region of channel flow have also been studied to analyze the shape of coherent structures existing in these regions. Hanratty and Papavassiliou [85] found the existence of jet-like sheets while Na et al. [86] found structures that they called 'superbursts', which have also been observed by the Particle Image Velocimetry (PIV) studies of Hutchins et al. [87].

Such experimental [82, 83, 88, 89] and numerical studies [90, 91] have also outlined the interlinking of these different coherent structures and the similarity with which these structures are spatially oriented. Previous works [92, 93] have outlined the importance of these coherent structures in characterizing scalar heat or mass transfer.

The proper orthogonal decomposition (POD) technique, which was first proposed by Lumley [94], has been found to be very useful and effective in extracting the nature of coherent structures. The method involves the decomposition of the fluctuating velocity fields into the sum of mutually orthogonal eigenfunctions of the two-point correlation tensor, weighted by coefficients that can be later determined from these eigenfunctions. The most dominant eddy is obtained from the eigenfunction with the highest eigenvalue. For statistically inhomogeneous turbulence, the Karhunen-Loeve [95, 96] expansion is used to extract coherent structures. The Lumley POD technique was validated by Bakewell and Lumley [97], who applied this principle to find the most energetic eddy structure in the wall region ($y^+ < 40$) of a turbulent pipe flow. Only the streamwise velocity component of the two-point correlation was measured, while the other components were obtained by mixing length assumptions and using the equation of continuity. The results obtained suggested that the largest eddy carried more than 90% of the total turbulent streamwise intensity. Moin [98] performed a numerical simulation of turbulent channel flow using large eddy simulation (LES) techniques and obtained the full correlation tensor. The decomposition of this correlation tensor in one and two dimensions showed that the dominant eddy carried about 64% of the turbulent kinetic energy. Applying POD to an axisymmetric turbulent jet, Glauser et al. [99] established that the dominant eigenfunction carried about 40% of the total streamwise turbulent intensity. Further, the works of Herzog [100] and Moin and Moser [101] also involved the use of POD to find the most dominating eigenvalue.

Few studies have explored scalar transport from the viewpoint of correlation tensors. However, understanding the direction of scalar gradient transport by

decomposing the rate of strain tensor has garnered attention over the years. Kerr [102] obtained correlation statistics between the scalar gradient and the vorticity of the flow in three dimensional, forced turbulence and found a strong de-correlation between the two quantities at relatively high Reynolds number. The work also showed evidence by pictorial representations of the normal orientation of scalar gradient with respect to the vorticity and concluded that the scalar markers are wound around the core of the vortex. Ashurst et al. [103] calculated the probabilities of the orientation of the vorticity and scalar gradient with the three different eigenvectors, α (most extensional), β (intermediate), γ (most compressive), of the rate of strain tensor and found a preferential orientation of the vorticity with the intermediate eigenvector, while also observing the scalar gradient to be oriented with the most compressive eigenvector. Vedula et al. [104] have also found a preferential alignment of the scalar gradient with the most compressive eigenvector of the rate of strain eigenvector. Increasing the Reynolds and Schmidt number in their study showed more favorable shift towards this behavior.

2.3 Scaling of heat/mass transport

2.3.1 Model based on scaling patches

The classical scaling that uses the friction velocity, u^*, and the kinematic viscosity, v, as inner scaling parameters and the half channel height, h^+, as the outer scale parameter, has been used to describe momentum transport. Early works of Afzal [105-107] and Panton [108] established the presence of an overlap region, which has the same inner and outer forms of the mean velocity profile. In trying to understand the classical scaling from a different perspective, Wei et al. [38] and Klewicki et al. [109],

used the classification of the turbulent wall flows into different regions, namely, viscous sub-layer, buffer layer, logarithmic region and wake region based on the mean velocity profile as a starting point. They recognized that accurately identifying the properties of the mean velocity profiles and the extent of the corresponding wall layers can be related to the momentum transport dynamics and their scaling with *Re*. The streamwise mean momentum balance equation for fully developed two-dimensional channel flow normalized by classical scaling variables is given by

$$\frac{1}{h^+} + \frac{d^2U^+}{dy^{+2}} - \frac{d(\overline{u'v'})^+}{dy^+} = 0 \qquad (2.9)$$

Wei et al. and Klewicki et al. focused on the physical mechanisms represented by each term of Equation (2.9). The first term is the normalized pressure gradient, acting as the driving force of transport. The second term is the gradient of the viscous stress, and the third and final term is the gradient of the Reynolds stress. So, using this differential form of the momentum balance equation, they concluded that either all three gradients need to be at a balance or two of the gradients need to balance each other with the third being very small. Plotting the ratio of viscous to Reynolds stress gradients close to the channel walls, they found a thin sublayer where viscous and pressure gradients are dominant, while the Reynolds stress gradients are absent. Outside this thin region, they found a region where there was a near perfect balance between the viscous and Reynolds stress gradients. This stress gradient balance layer extended farther into the logarithmic region with increasing *Re*. For farther distances from the channel wall, the Reynolds stress gradient showed a change in sign with the viscous stress gradients becoming very small in comparison with Reynolds stress and pressure gradients at these distances. So, using these arguments, Wei et al. and Klewicki et al. classified the

turbulent channel into four different layers: Layer I, or viscous/advection balance layer; Layer II, or stress-gradient balance layer; Layer III, or meso viscous/advection balance layer, and Layer IV, or inertial/advection balance layer. Work of Wei et al. [110] extended this meso-layer theory from momentum to heat transport. In addition to the classical scaling parameters for momentum transport, they used a new scaling with (T^*Pe) for temperature instead of just T^*, where Pe is the Peclet number given by $RePr$, and defined a variable Φ given by

$$\Phi = \frac{T_w - T}{PeT^*} = \frac{T_w - T}{h^+ \Pr T^*} \tag{2.10}$$

The scaling with T$^*Pe$ helps in taking into account the effects of both the Reynolds number as well as the Prandtl number. Using this variable, the 2D heat equation for fully developed channel flow is given by

$$\frac{d^2\Phi}{d\eta^2} + \frac{dT}{d\eta} + r(\eta) = 0 \tag{2.11}$$

where, $\eta = y^+/h^+$ and $r(\eta) = U(\eta)/U_B$ and U_B is the bulk velocity calculated as $U_B = \frac{1}{h^+}\int_0^{h^+} U^+(y^+)dy^+$. Similar to the case for momentum transport, Wei et al. split the heat transfer domain using the ratio of molecular diffusion flux to turbulent transport flux, R_{HF}, given as

$$R_{HF} = \frac{\frac{d^2\Phi}{d\eta^2}}{\frac{dT}{d\eta}} \tag{2.12}$$

The layer closest to the channel wall, where the molecular diffusion and mean advection are dominant and the turbulent term is negligible, was termed Layer I (molecular

diffusion/mean advection balance layer). This is followed by Layer II, where the molecular diffusion and the turbulent transport are the main components and they balance each other yielding $R_{HF} = -1$, (heat flux gradient balance layer). The next layer, Layer III (meso-layer) is where all the three terms contribute to the heat equation, and Layer IV (inertial layer) is the layer where the heat balance is between the advection term and the turbulent transport term with the molecular diffusion nearly zero. Wei et al. studied the new scaled temperature, Φ, using DNS data from Kawamura's laboratory [111] and found that for a fixed *Re*, the values of Φ monotonically decrease with increasing *Pe*. Plotting the centerline values of Φ, Φ_∞, as a function of *Pe*, they found that $\Phi_\infty \rightarrow 0$ as $Pe \rightarrow \infty$ and that $\Phi_\infty \rightarrow$ O(1) as $Pe \rightarrow 0$. So, generalizing the Φ_∞ behavior to Φ behavior, Wei et al. reduced the partial differential equation (2.11) to an ordinary differential equation for high *Re* in the case of low *Pr* fluids. However, for high *Pr*, Equation (2.11) reduced to an ordinary differential equation form only outside the narrow wall layer (meso-layer), with Wei et al. proposing a rescaling in this narrow region. This new rescaling, called the mesonormalization, was proposed to be associated to the location of the maximum turbulent heat flux. A collapse of the results of the inner normalization and the "mesorenormalization" of the turbulent heat flux for different *Re* and *Pr* is shown in the work of Klewicki et al. [112]. Previous work [113] in our laboratory has aimed at utilizing our direct numerical simulation/Lagrangian scalar tracking data for Poiseuille channel flow and plane Couette flow to explore the scaling patches proposed by Wei et al. It was found that the location of the extent of the mesolayer was varying with $Pr^{(-1/4)}$ for both Poiseuille and Couette flow. The maximum value of the temperature at the center of the channel (Φ_∞) scaled using the

Wei et al. scaling, was found to change with $Pe^{-0.5}$ both for the Poiseuille and Couette flow cases.

2.3.2 Equilibrium similarity analysis for temperature scaling

George et al. [114] in their early works applied similarity analysis to study forced convection in turbulent boundary layers. They proposed an inner and an outer scaling for the mean temperature profile in turbulent boundary layer flows, but did not study the effects of *Pr* or the adverse pressure gradients in such flows. According to their analysis, the inner and outer length scales for a zero pressure gradient (ZPG) boundary layer turbulence and convection were proposed to scale with $y_{is}^{+} = \frac{\frac{yq_w}{\rho C_p}}{\alpha(T_w - T_\infty)}$ and $y_{os}^{+} = \frac{y^{+}}{\zeta_T^{+}}$, where y_{is}^{+} and y_{os}^{+} are the inner and outer length scales, respectively, and α and ζ_T are the thermal diffusivity and thermal boundary layer thickness, respectively. They obtained the inner and outer scaling for the temperature to be $T_{si} = T_w - T_\infty$ and $T_{so} = (T_w - T_\infty)\frac{St}{C_f/2}$, respectively, where C_f is the friction loss coefficient, and *St* is the Stanton number defined as

$$St = \frac{q_w}{\rho c_p U_\infty (T_w - T_\infty)} \tag{2.13}$$

and, for channel flow, T_∞ and U_∞ are the mean temperature and mean velocity at the center of the channel, respectively. More recent work by Wang and Castillo [115] explored an application of the equilibrium similarity analysis (according to which the scales of both inner and outer flows are dictated by equations of motion and their boundary layer conditions alone) to the case of adverse pressure gradient (APG)

boundary layer flows. They also proposed [36] and utilized the asymptotic invariance principle (AIP), according to which the invariance of the boundary layer equations with the dependence of *Re* as *Re* → ∞ should imply the independence of the scaling parameters with the local *Re*. Similar to their previous ZPG studies [114], for this adverse pressure gradient study they developed an inner and an outer scaling for the mean temperature profile based on the AIP. In terms of the inner and outer variables, the mean temperature profile is a function of the inner and outer length scales and the boundary layer thickness as follows:

$$\frac{T_w - T}{T_{si}} = g_{si}(y_{is}^+; \zeta_T^+) \tag{2.14}$$

and $$\frac{T - T_\infty}{T_{so}} = g_{so}(y_{os}^+; \zeta_T^+) \tag{2.15}$$

Substituting these into the inner and outer boundary layer equations in the limit *Re* → ∞, they obtained the following inner and outer scaling expressions for the mean temperatures:

$$T_{si} = \Pr\sqrt{St}(T_w - T_\infty) \tag{2.16}$$

and $$T_{so} = \frac{\zeta_T^*}{\zeta_T}(T_w - T_\infty) \tag{2.17}$$

The term ζ_T^* in the case of outer scaling stood for the thermal displacement thickness given by the equation $\zeta_T^* = \int_0^\infty \frac{T - T_\infty}{T_w - T_\infty} dy$. The inner and outer similarity length scales were found to be

$$y_{is}^+ = \frac{yU_\infty}{\nu}\sqrt{St} \tag{2.18}$$

and $y_{os}^{+} = \frac{y^{+}}{\zeta_{T}^{+}}$, respectively. (2.19)

To verify the accuracy of the scaling parameters proposed, Wang and Castillo [115] utilized the ZPG and APG experimental data of Blackwell et al. [116], ZPG data of Blom [117], APG experimental data of Orlando et al. [118] and the favorable pressure gradient (FPG) data of Thielbahr et al. [119] to provide a comparative study of the classical Reynolds scaling, the scaling for the ZPG boundary layer flow proposed by George et al.[114] and the new proposed scaling given by Equations (2.16-2.19). For all the three types (ZPG, APG and FPG) of thermal boundary layer flow data, only the proposed inner and outer scaling given by equations (2.16-2.19), which for the sake of simplicity is referred to as the WC (Wang and Castillo) scaling in the remainder of this manuscript, caused the mean temperature profiles to collapse into a single asymptotic curve. Further works of Wang et al. [120] showcased the robustness of the WC scaling by using it to obtain a power law solution for the temperature profile in the overlap region, where it was found to be having 5% less error than using Kader's equation [47] (see 1.1).

2.4 Turbulent Prandtl number

Reynolds [121] provided an extensive review of prior work to determine Pr_t. Kays [122] also discussed available results for Pr_t for different fluid systems (air, water), in a two dimensional boundary layer and in flow through a circular tube or a flat duct. The simplest model for determining Pr_t was proposed by Osborne Reynolds, who assumed that $\nu_t = \alpha_t$, resulting to the value of unity for the Pr_t. This is the well-known Reynolds analogy [123], which is by all means an oversimplification. Several

investigators have pointed out the inadequacy of the Reynolds analogy, including Churchill [6, 124] who examined the numerical and functional errors associated in using the Reynolds analogy and put together a simplified model to overcome its inadequacies. The widely used computational fluid dynamics software FLUENT uses a constant value of $Pr_t = 0.85$ [125], irrespective of the wall distance or the Pr. Notter and Sleicher [126] developed the following correlating expression for Pr_t:

$$\mathrm{Pr}_t = \frac{1 + 90\,\mathrm{Pr}^{3/2}(\nu_t/\nu)^{1/4}}{\left[0.025\,\mathrm{Pr}(\nu_t/\nu) + 90\,\mathrm{Pr}^{3/2}(\nu_t/\nu)^{1/4}\right]\left[1 + \frac{10}{35 + (\nu_t/\nu)}\right]} \qquad (2.20)$$

Azer and Chao [127] put forward a correlation of Pr_t for $0.6 \leq Pr \leq 15$ and another for the case of liquid metal fluids. The correlations predicted a dependence of Pr_t on the Pr, Re and the radial distance from the pipe wall. Jischa and Rieke [128] developed a model for Pr_t from the modeled transport equations for the turbulent kinetic energy and for the turbulent heat flux. They concluded that the dependence of the Pr_t on Re and distance from wall, though possible, is of second order importance and put forth the following simple expression for Pr_t :

$$\mathrm{Pr}_t = 0.85 + \frac{0.015}{\mathrm{Pr}} \qquad (2.21)$$

Among the numerous correlations proposed for Pr_t, two of the most interesting and intuitive correlations were presented by Yakhot et al. [129], and by Kays and Crawford [130]. Yakhot et al. presented an analytical solution for finding Pr_t based on the renormalization group method. The equation given by Yakhot et al. is

$$\left[\frac{\left(\frac{1}{\mathrm{Pr}_{eff}}-1.1793\right)}{\left(\frac{1}{\mathrm{Pr}}-1.1793\right)}\right]^{0.65}\left[\frac{\left(\frac{1}{\mathrm{Pr}_{eff}}+2.1793\right)}{\left(\frac{1}{\mathrm{Pr}}+2.1793\right)}\right]^{0.35}=\frac{1}{\left(1+\frac{\nu_t}{\nu}\right)} \qquad (2.22)$$

where,

$$\mathrm{Pr}_{eff}=\frac{\left(1+\frac{\nu_t}{\nu}\right)}{\left(\frac{\nu_t}{\nu}\frac{1}{\mathrm{Pr}_t}+\frac{1}{\mathrm{Pr}}\right)} \qquad (2.23)$$

Equation (2.22) was suggested to be applicable for all Prandtl numbers, and at high Pr and high values of ν_t/ν it converges to the value 0.85.

The next important breakthrough in the prediction of Pr_t came with the empirical model of Kays and Crawford [130]. The turbulent Prandtl number according to this model is given as

$$\mathrm{Pr}_t=\frac{1}{\left\{0.5882+0.228\left(\frac{\nu_t}{\nu}\right)-0.0441\left(\frac{\nu_t}{\nu}\right)^2\left[1-\exp\left(\frac{-5.165}{\left(\frac{\nu_t}{\nu}\right)}\right)\right]\right\}} \qquad (2.24)$$

Both models presented above indicate that Pr_t is a function of kinematic viscosity and eddy viscosity, and it does not depend on the eddy diffusivity of heat. Kays [122] reviewed the renormalization group theory put forward by Yakhot et al. and concluded that it may be applied only in the region of overlap (the logarithmic regime of the mean velocity profile). Kays proposed an expression for Pr_t that can be written as

$$\mathrm{Pr}_t=\frac{2.0}{\left(\frac{\nu_t}{\nu}\right)\mathrm{Pr}}+0.85 \qquad (2.25)$$

The coefficient 2.0 above was suggested to work better for $Pr < 1$ fluids, while a coefficient of 0.7 is appropriate for higher Pr fluids. This equation indicates that as the Pr increases, the Pr_t decreases and for higher Pr, it approaches the value of 0.85. On the basis of the Pr_t equation developed by Kays and Crawford, as shown in Equation (2.24), Weigand et al. [131] extended the model as follows:

$$\mathrm{Pr}_t = \frac{1}{\frac{1}{2\,\mathrm{Pr}_{t\infty}} + APe_t\sqrt{\frac{1}{\mathrm{Pr}_{t\infty}}} - \left(APe_t\right)^2\left[1-\exp\left(-\frac{1}{APe_t\sqrt{\mathrm{Pr}_{t\infty}}}\right)\right]} \qquad (2.26)$$

where,

$$Pe_t = \mathrm{Pr}\frac{\nu_t}{\nu} \qquad (2.27)$$

and $\mathrm{Pr}_{t\infty}$ is the value of Prandtl number far away from the wall, and $A = 0.3$ is a constant prescribing the spatial distribution of Pr_t vs Pe_t. Also, $Pr_{t\infty}$ was calculated by Weigand et al. by the expression

$$\mathrm{Pr}_{t\infty} = 0.85 + \frac{d}{\mathrm{Pr}\,\mathrm{Re}^{0.888}} \qquad (2.28)$$

According to Weigand et al. the value of d is 100, and when Equation (2.26) is applied, at the wall (where $Pe_t = 0$), $Pr_t \rightarrow 2Pr_{t\infty}$, while at large distances from the wall, where $Pe_t \rightarrow \infty$, it is $Pr_t \rightarrow Pr_{t\infty}$. In the original model of Kays and Crawford as shown in Equation (2.24), $Pr_{t\infty}$ is fixed at a constant value of 0.85, which introduces an undesired behavior into the model. This model was found to do comparatively better in predicting the Pr_t for a range of Pr.

Although much work has been done to study the Pr_t for lower Pr's, very few studies have explored the effects of higher Pr number on the Pr_t. Only recently have

computational results with direct numerical simulation (DNS) or hybrid DNS – large eddy simulation have become available for medium and high *Pr*. Schwertfirm and Manhart [132] have studied cases of $Pr \leq 49$ and observed that in the outer region ($y^+ > 20$), the eddy conductivity is the same irrespective of the *Pr*. They also observed the eddy conductivity to decrease near the wall for higher *Pr*. Kasagi et al. [28, 133] have used Eulerian direct numerical simulations to estimate Pr_t. The recent study of Pr_t by Hasegawa and Kasagi [134] for high *Pr* (namely 1, 100, 200, 400) was focused on the investigation of the asymptotic behavior of the eddy diffusivity close to the wall. It showed that there is an increase of Pr_t for increasing *Pr* in the viscous sublayer, but it did not present the Pr_t behavior far from the channel walls.

2.4.1 Turbulent Prandtl number as a ratio of length scales

Crimaldi et al. [135] proposed a model for Pr_t based on Prandtl's concept of mixing length. The turbulent Prandtl number was calculated as the ratio of the mixing length of momentum to the mixing length of heat, as follows:

$$\mathrm{Pr}_t = \frac{L_M}{L_T} \tag{2.29}$$

where, L_M and L_T stand for the mixing length for momentum and heat transfer, respectively. Le and Papavassiliou [93] used a Lagrangian approach in conjunction with DNS to study the correlation between the velocity and temperature fields in wall turbulence. They obtained characteristic length scales for flow structures that contribute to the transfer of heat away from the wall and characteristic length scales for momentum transfer. Assuming further that these characteristic length scales were proportional to the mixing length scales and the ratio of the proportionality constant is

of order one, they used the Crimaldi et al. interpretation of Pr_t, given by Equation (2.29), to determine the Pr_t. They concluded that the Pr_t showed dependence on distance from the wall. However, they did not find any significant changes of the Pr_t with increase of Pr for higher Prandtl numbers ($Pr \geq 0.7$). The estimate of the values of the Pr_t by Le and Papavassiliou was not claimed to be precise enough to distinguish effects of Pr on Pr_t.

2.5 Scaling considerations and the physical interpretation of the turbulent Prandtl number using Churchill's turbulent transport model

Churchill [7] through his early works has articulated criticisms about the validity of algebraic analogies that link transport of energy with transport of momentum in turbulent channel flows. His concerns were threefold, firstly, in the energy balance equation, the ratio of kinematic viscosity to thermal diffusivity (i.e., the Prandtl number, Pr), appears as an additional parameter, which lacks a corresponding counterpart in the momentum balance equation. Secondly, Churchill recognized the complexities involved in the thermal boundary conditions compared to the momentum transport boundary conditions. For example, Churchill provided examples of momentum transport, where the velocity at each wall was always presumed to be equal to the velocity of the wall. However, in the case of heat transport, the channel walls were assigned either a temperature distribution or a heat flux distribution as the boundary condition. Finally, Churchill cited the variability of the heat flux density distribution based on the velocity distribution and mode of heating, which in turn varied as a function of the distance from the channel walls. Early work by Abbrecht and Churchill [1], based on experiments of flow of air in round tubes, determined the eddy viscosity and eddy diffusivity. On the

basis of the ratio of these two quantities, it was concluded that the Pr_t was only a function of ν_t/ν and Pr. Churchill's goal was to understand and eliminate the empiricisms involved in estimating some of the turbulent flow parameters. The initial efforts in this direction by Churchill et al. [136-138] were aimed at understanding turbulent momentum transport. In these works, Churchill et al. showed that the basic models proposed for the closure of the time-averaged momentum equations, like the κ-ε and the mixing length models, broke down fundamentally in different regions of flow through tubes, parallel plates or annuli. The time-averaged equation for momentum transfer is given by

$$\Gamma_w\left(1-\frac{y^+}{h^+}\right)=\mu\frac{dU^+}{dy^+}-\rho\overline{u'v'} \tag{2.30}$$

Where U^+ is the mean velocity in the streamwise direction, $-\rho\overline{u'v'}$ is the Reynolds stress and u' and v' are the velocity fluctuations in the streamwise, x, and wall-normal direction, y, respectively. Equation (2.30) can be made dimensionless using $\frac{\Gamma_w}{\rho}\left(1-\frac{y^+}{h^+}\right)$ and resulting in the following expression:

$$\left(1-\frac{y^+}{h^+}\right)=\frac{dU^+}{dy^+}-(\overline{u'v'})^{++} \tag{2.31}$$

So, instead of using Γ_w/ρ to make Equation (2.30) dimensionless, Churchill introduced a new dimensionless quantity

$$(\overline{u'v'})^{++}=\frac{(\overline{u'v'})^+}{\left(1-\frac{y^+}{h^+}\right)} \tag{2.32}$$

Based on this line of thought, Churchill [48] [124, 139, 140] developed a theoretical framework, based on turbulence scaling other than the conventional scaling based on *viscous units* (i.e., scaling based on the friction velocity and the friction temperature) to describe turbulent scalar transport. Churchill proposed that the local fraction of shear stress due to fluctuations in velocity is a superior dimensionless variable for the modeling of turbulent flows than using dimensionless velocity obtained by scaling with the friction velocity. This local fraction of the shear stress is defined as

$$(\overline{u'v'})^{++} = -\frac{\rho\overline{u'v'}}{\Gamma} \tag{2.33}$$

The scaling parameter of Equation (2.33) is the local fraction of shear stress at any location due to turbulence. The local fraction of shear stress at any location due to viscous effects is therefore given by $[1-(\overline{u'v'})^{++}]$. Hence, Churchill established a scaling based on turbulence-related parameters rather than the viscous wall units in order to avoid empiricisms and heuristic arguments associated with modeling momentum transfer. The ingenuity and reliability of this model, however, was established further when Churchill [124] seamlessly extended this model to heat (and mass) transfer. In analogy with momentum transfer, Churchill proposed a local fraction of normal (radial in case of pipe flow) heat flux density due to turbulence given by

$$(\overline{T'v'})^{++} = \frac{(\overline{T'v'})^{+}}{\left(1-\frac{y^{+}}{h^{+}}\right)} \tag{2.34}$$

where T' is the temperature fluctuation. Using the above theory, the eddy viscosity to viscosity ratio (ν_t/ν) has to be equal to the ratio of the local fraction of momentum transfer due to turbulent fluctuations, to that due to molecular motions, and, thus, the

eddy viscosity obtained a physical meaning that is independent of its diffusive origin. Similarly, Churchill defined the eddy diffusivity over molecular diffusivity ratio to be equal to the local fraction of heat flux density due to the turbulent fluctuations to that of local heat flux density due to molecular motion. In this way, the eddy diffusivity can also be interpreted as a physical quantity that is independent of its heuristic diffusive origin. Accordingly, the mathematical expressions suggested by Churchill for the eddy viscosity and eddy diffusivity are

$$\frac{\nu_t}{\nu} = \frac{(\overline{u'v'})^{++}}{\left[1-(\overline{u'v'})^{++}\right]} \tag{2.35}$$

where $\left[1-(\overline{u'v'})^{++}\right]$ represents the local fraction of shear stress due to molecular motion, and

$$\frac{\alpha_t}{\alpha} = \frac{(\overline{T'v'})^{++}}{\left[1-(\overline{T'v'})^{++}\right]} \tag{2.36}$$

where $(\overline{T'v'})^{++}$ and $\left[1-(\overline{T'v'})^{++}\right]$ represent the local fraction of heat flux density due to turbulence and the local fraction of heat flux density due to molecular motion, respectively. Finally, the Pr_t in terms of the local fraction of fluctuations is expressed as

$$\frac{\mathrm{Pr}_t}{\mathrm{Pr}} = \frac{(\overline{u'v'})^{++}\left[1-(\overline{T'v'})^{++}\right]}{(\overline{T'v'})^{++}\left[1-(\overline{u'v'})^{++}\right]} \tag{2.37}$$

Within this framework, the Pr_t assumes an interesting and quite intuitive physical meaning. Based on Churchill's interpretation, an estimate of the local fraction of shear stresses due to turbulence and due to molecular motion, along with the local fraction of heat flux density due to turbulence and molecular motion, are the quantities required to predict the values of Pr_t. Equation (2.37) suggests that Pr_t is a function of Pr, and a

function of the distance from the wall, as are the local fractions of transport due to turbulence.

With regards to incite on using this as the scaling parameter, Churchill concluded that this scaling provided a more appropriate model for understanding heat transfer, as the main challenge of developing correlations for α_t/α is replaced by the task of developing predictive correlations for $(\overline{u'v'})^{++}$ and Pr_t. Utilizing these scaling arguments further, Churchill derived expressions for the Nusselt number (*Nu,* which incorporates the heat transfer coefficient) in terms of Pr_t and $(\overline{u'v'})^{++}$ noting that the resulting expressions showed deviations from those obtained using standard momentum and heat transfer analogies. Comparing with the simplest analogy between momentum and heat transfer, i.e., the Reynolds analogy, it was shown that it matches Churchill's formulation only in the special case where $Pr = Pr_t \approx 0.86$ and even then by only accounting for an error factor. Churchill revisited some of the analogies that are based on simplistic empiricisms (like the Colburn analogy and the Prandtl-Taylor analogy). He also considered analogies like the one proposed by Kader and Yaglom that was based on the correlating equations of the velocity and temperature profiles, and analogies that were derived based on the differential energy balance (like that of Von Karman and of Martinelli). The resulting comparisons presented in detail the inadequacies of such well-known turbulent transport analogies.

The scaling based on the fraction of the heat flux that is due to turbulence, as proposed by Churchill, also established a firm connection between momentum and heat transfer: the proposed choices for momentum and heat transfer scales led to simpler and more transparent formulations than previous models, and also helped in completely

eliminating empirical or heuristic formulations. They also brought to light the actual analogy that existed between the momentum and heat transport in turbulent wall bounded flows, and provided a sound interpretation of Pr_t based on physical arguments. A parametric sensitivity analysis [141] of the Churchill model with respect to the various parameters showed that the values were insensitive to changes in $(\overline{u'v'})^{++}$ but appeared to depend on the accurate prediction of the Pr_t.

Prior work in our laboratory utilized DNS and Lagrangian scalar tracking (LST) as tools to generate statistical data for turbulent flow and heat transport [142] and to validate Churchill's theories [143]. Comparisons showed that the case of using DNS/LST data for both $(\overline{u'v'})^{++}$ and Pr_t provide good predictions for the mean temperature profile. Using the empirical correlations of Danov et al. [144] for $(\overline{u'v'})^{++}$ and Kays [122] for Pr_t, however, led to large percentage errors in the mean temperatures values, especially for the cases of high Pr ($Pr \geq 100$), suggesting a high sensitivity of the mean temperature profile to the values of $(\overline{u'v'})^{++}$ and Pr_t.

Chapter 3: NUMERICAL METHODOLOGY

3.1 Direct numerical simulation

The direct numerical simulation (DNS) technique is used to solve numerically the Navier-Stokes equation by resolving the different spatial and temporal scales existing in a turbulent flow [3, 28, 145, 146]. Lyons et al. [29] used a pseudospectral algorithm to determine the turbulent velocity field and the results obtained have been validated with experiments by Gunther et al. [147]. In this algorithm, the rotational form of the Navier-Stokes equation was first made dimensionless by using the wall variables, i.e., the kinematic viscosity, v, and the friction velocity, $u^* = (\Gamma_w/\rho)^{1/2}$. The rest of the variables, like the length, time etc, were expressed in terms of these wall variables, and hence these quantities were scaled with the so-called viscous wall units. Another interesting case considered here was the plane Couette flow, where the walls of the channel move relative to each other. The algorithm of Lyons et al. was suitably modified to account for the wall behavior [148-150]. The fluid in both cases was considered to be an incompressible Newtonian fluid with constant density, constant viscosity and constant thermal conductivity. The assumption that the viscous heating effects and the body forces are negligible was also made. The mean pressure gradient acted as the driving force for the Poiseuille channel flow, while the motion of the channel walls in opposite directions (which generates a region of constant shear stress) acted as the driving force for flow in plane Couette flow. The streamwise component of the velocity vector at the channel walls, which was set to zero in Poiseuille flow due to

stationary walls, is set to ± 17.74 for the case of plane Couette flow. The bottom wall moved in the negative x direction, while the top wall moved in the positive x direction.

In Poiseuille channel flow, the simulation was carried out in a computational box with dimensions ($4\pi h^+$, $2h^+$, $2\pi h^+$), where $h^+ = 150$ or 300 viscous wall units, in the x, y and z directions. The box was meshed to carry out numerical calculations in the x, y, z directions with 128 × 65 × 128 and 256 × 129 × 256 mesh points, respectively, for $h^+ = 150$ and 300, respectively. The Reynolds number for the Poiseuille channel was 2660 and 5320, for $h^+ = 150$ and 300, obtained using the mean centerline velocity and the half channel height. Simulations carried out in plane Couette flow have reported [150] longer flow structures in the streamwise direction. Hence, the length of the box is doubled in the x direction, with the computational box in the case of plane Couette flow measuring $8\pi h^+$, $2h^+$, $2\pi h^+$ in x, y and z directions, respectively, with 256 × 65 × 128 grid points for $h^+ = 150$. The Re in this case, measured using half the relative velocity of the wall and half channel height, was 2660, which was the same as that of the lower Re Poiseuille channel flow case. In both Poiseuille and Couette flow cases, the channel was simulated as infinitely long in the streamwise and spanwise directions by imposing periodic boundary conditions. The transport equations were expanded in terms of Fourier series in these two directions. The periodicity lengths (χ_x, χ_z) were $4\pi h^+$, $2\pi h^+$ in the x, z directions, respectively for Poiseuille flow, while they were $8\pi h^+$, $2\pi h^+$ in the x, z directions, respectively for plane Couette flow. The no-slip, no-penetration boundary conditions were imposed at the walls of the channels and the vertical velocity and pressure head were expanded in terms of Chebyshev polynomial series. Variety of time steps were used to advance the simulation, ranging from $\Delta t^+ = 0.125$, 0.15, 0.2 and 0.25

in viscous wall units. The Figures 3.1 and 3.2 depict the picture of turbulent Poiseuille and plane Coeutte flow, respectively. The general description of the DNS is universal to all the studies in this dissertation. Some of the specific details of each study will be described briefly in the corresponding Chapter.

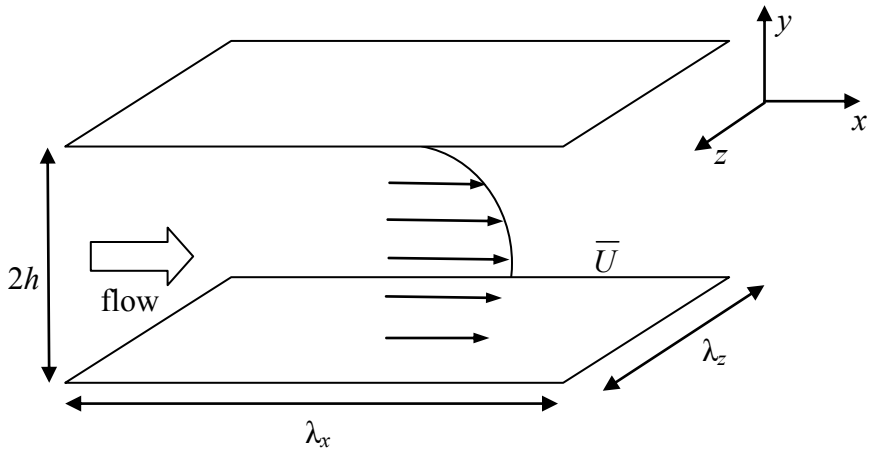

Figure 3.1: Plane Poiseuille flow configuration

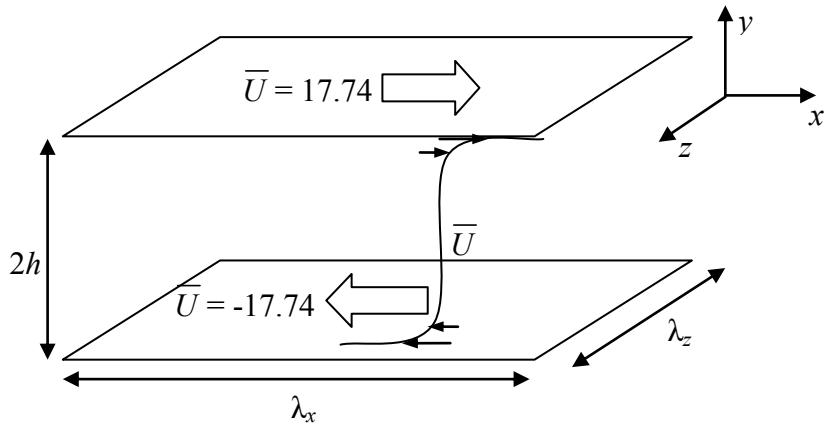

Figure 3.2: Plane Couette flow configuration

3.2 Lagrangian scalar tracking (LST)

Turbulent diffusion in the Lagrangian framework, was described by Taylor [50] as the dispersion of fluid particles from a point source in homogenous, isotropic turbulence. An extension to this theory was provided by Saffman [57] in the case of heat or mass markers by considering that the markers can move off of a fluid particle as a results of molecular diffusion. The basic framework of the Lagrangian scalar tracking was constructed by imagining a heated surface to be formed by an infinite number of continuous sources of heat markers, such as those described by Saffman, and a cooled surface to be formed by an infinite number of continuous sinks of heat, or, alternatively, sources of cold (i.e., negative) heat markers. Hanratty [60] introduced this concept to describe theoretically the transfer of heat from a hot to a cold wall in a turbulent channel flow. Papavassiliou and Hanratty [151] used a direct numerical simulation in conjunction with the tracking of scalar markers to study heat transfer based on direct calculations of the behavior of such wall sources. Further details regarding the validation and implementation of the LST methodology can be found in works of Papavassiliou and Hanratty [151], Ponoth and McLaughlin [152], Papavassiliou [153], Mito and Hanratty [154], Mitrovic and Papavassiliou [155]. However, since LST is not a mainstream, widely used approach, a brief description of the method will be presented here for completeness of this dissertation.

The method of stochastic tracking of heat or mass markers in a turbulent flow field, and the statistical post-processing of the results to obtain scalar profiles is termed as Lagrangian scalar tracking (LST). The passive scalar markers released into the flow field are assumed to be point markers with no size and mass. There are no interactions

between the markers. Hence, the trajectory of a marker does not affect the trajectories of other markers, and it does not affect the flow. Therefore, the case of what is called "passive scalar transport" is simulated. A direct numerical simulation in conjunction with the tracking of scalar markers, LST, has been used in our laboratory (and elsewhere) to study scalar transfer based on direct calculations of the behavior of such sources [72, 154, 156, 157], [148, 158-160]. The tracking algorithm of Kontomaris et al. [159] was used to trace the trajectories of heat markers in the flow field created by the DNS. A mixed Lagrangian-Chebyshev interpolation scheme was used to calculate the velocity between the grid points. The marker motion was split into two parts, namely a convective part and a molecular diffusion part. The convective part was determined by the velocity of the fluid at the marker position, yielding for the equation of the marker motion $\vec{V}(\vec{x}_0,t)=\left[\partial\vec{X}(\vec{x}_0,t)\right]/\partial t$, where the Lagrangian velocity of a marker released at location $\vec{x}_0$ is given as $\vec{V}(\vec{x}_0,t)=\vec{U}\left[\vec{X}(\vec{x}_0,t),t\right]$ ($\vec{U}$ is the Eulerian velocity of the fluid at the location of the marker at time *t*). Molecular diffusion effects follow from Einstein's theory of Brownian motion (Equation 2.1), and were simulated by adding a 3D random walk on the particle motion at the end of every convective step. A Gaussian distribution with zero mean and standard deviation $\sigma^+=\sqrt{2(\Delta t^+)/\mathrm{Pr}}$ in viscous wall units was used to decide the size of the random jumps in each of the three space directions. The *Pr* effects on the process were therefore studied by changing the value of σ^+. Thus, the LST methodology can be used to simulate flows with an extensive range of *Pr* [142, 149].

Besides the common error due to discretization, the numerical error with the LST methodology can be caused by the number of markers considered. Papavassiliou and Hanratty [156] and Papavassiliou [153, 157] have addressed this issue by

examining the statistics of marker trajectories with databases of 16,129 markers and repeating the calculations with the half the number of markers. They have found that results of acceptable accuracy can be obtained with half the number of markers. Mitrovic [161] had further the investigation with a set of 16,129 markers and a set of almost one order of magnitude larger, 145,161 markers. The study showed that the average difference in the statistical behavior of runs with the same *Pr* and different number of markers is less than 1.5%. The study stated that the use of samples with an order of 10^4 markers can provide accurate results for the generation of first order statistics. A balance between the computational cost that is associated with the creating of large data sets and acceptable accuracy of the results should be considered when employing the LST methodology. In each study, different *Pr*'s and different number of scalar markers are released. Also, the orientation of the release is unique to the different studies. Hence, a brief description of the flow and marker parameters, specific to the particular study, has been provided in the corresponding Chapters. In the rest of the dissertation, in most of the cases, temperature is the scalar under discussion and the Prandtl number, *Pr*, is used as the dimensionless number associated with the temperature field. All the corresponding discussion applies to the case of turbulent mass transfer without any chemical reaction (i.e., the case where there is no production or consumption of mass). In that case, concentration would replace the temperature as the scalar field, and the Schmidt number would take the place of *Pr*.

Chapter 4: BACKWARDS AND FORWARDS TURBULENT SINGLE-PARTICLE DISPERSION*

4.1 Simulation parameters and procedure

For this study, the DNS flow field was obtained for Poiseuille channel flow at Re_τ = 150. Simulations for heat transport included Pr = 0.1, 0.7, 6, 10, 50, 100, 500 and 1000. The simulation time step was Δt^+ = 0.125. A total of 145,161 markers were released instantaneously and randomly from a plane normal to the flow direction (i.e., on the *yz* plane) at the entrance of the channel. The initial positions of the markers where distributed uniformly and randomly across this plane. A schematic of the computational box is shown in Figure 4.1. The simulation was allowed to run for 900 viscous wall time units. To explore the differences between the backwards and forwards dispersion, the material autocorrelation coefficients for the backwards and forwards dispersion were determined in all three *x, y* and *z* directions. Figure 4.2 provides a view of the *x*-*y* cross section of the turbulent channel and depicts the concept of forwards and backwards dispersion with the process of the markers being captured and released, respectively, in vertical bins. Using Saffman's definition of the material correlation, the material autocorrelation coefficient was calculated as follows:

$$R_{V_iV_i}(t,t_0) = \frac{\overline{V_i'(t-t_0)V_i'(t_0)}}{\left(\overline{V_i'^2(t-t_0)}\right)^{\frac{1}{2}}\left(\overline{V_i'^2(t_0)}\right)^{\frac{1}{2}}}, \quad i = x, y, z \qquad (4.1)$$

* Most of the material in this Chapter has been published in the International Journal of Heat and Mass Transfer, 53, 1023-1035 (2010)

The overbar denotes the ensemble average over the selected number of markers in the flow field, and the prime denotes the Lagrangian velocity fluctuations, $V_i'(t) = V_i(t) - \overline{V_i}(t)$.

The study was carried out at four locations in the flow, each one at a different distance from the channel wall. The height of the channel, which was $2h^+ = 300$ in viscous wall units, was divided into 101 equal bins, as shown in Figure 4.1. The four chosen locations were the bins that included (a) the edge of the viscous sub-layer ($y^+ = 5$); (b) the transition region between the viscous sub-layer and the logarithmic layer ($y^+ = 37$); (c) the logarithmic layer ($y^+ = 75$); and (d) the center of channel ($y^+ = 150$). For example, at the logarithmic layer, the markers in bins 26 and 75 were used to determine the correlation coefficient as follows: the forwards correlation coefficient was determined by tracking these markers in time for 300 viscous wall time units, while the backwards correlation coefficient was calculated by tracking the markers backwards for 300 viscous wall time units. (The value 300 was determined based on previous results for elevated sources of heat in the channel [148] where the Lagrangian material timescale was found to be less than 300 t^+.) Since the total simulation time was 900 t^+, the markers that were traced forwards were those found in bin 51 at simulation times 0, 100, 200, 300, 400, 500, and 600, while those traced backwards in time were those found in bins 26 and 75 at simulation times 300, 400, 500, 600, 700, 800, and 900. This procedure was repeated at each different location studied.

For Prandtl numbers of 0.1, 0.7, 6, 10, 100, and for the viscous sub-layer, transition and logarithmic region, six values of the correlation coefficients were obtained by tracking markers moving in bins located below the center of the channel.

Six more values were obtained using the markers in bins located symmetrically above the center of the channel, so that twelve total values of the correlation coefficient were obtained from data generated with $\Delta t^+ = 0.125$. For the center of the channel, only six values of the correlation coefficients were calculated for the above mentioned Prandtl numbers. Additional values of the correlation coefficients were calculated using the database that had been previously developed by Nguyen and Papavassiliou [162] with $\Delta t^+ = 0.25$ (six additional values for the center of the channel and twelve additional values for the other three flow regions). Thus, the reported correlation coefficients are an average of twenty four values, in the case of the viscous sub-layer, transition and logarithmic region, while they are an average of twelve values for the center of the channel. For Prandtl numbers of 50, 500 and 1000, only the Nguyen and Papavassiliou data were used, so the reported results are an average of twelve calculations in the case of the viscous sub-layer, transition and logarithmic regions, and an average of six values for the center of the channel. On average, around 34800 markers were considered for the viscous sub-layer, transition and logarithmic regions, in calculating the correlation coefficients for Prandtl numbers of 0.1, 0.7, 6, 10, 100, while on average, 17400 markers were used for the center of the channel. The higher Prandtl numbers of 50, 500, 1000 involved 8700 and 17400 markers, in the center of the channel and in the other three regions, respectively.

4.2 Results and discussion

4.2.1 Correlation coefficients

The material autocorrelation coefficients for the scalar markers were determined first, according to Equation (4.1). The correlation coefficients for the velocity in the *x*, *y* and *z* directions, R_{uu}, R_{vv}, R_{ww}, at different heights are shown in Figures 4.3 to 4.6. The forwards and backwards correlation coefficient for the markers at the center of the channel ($h^+ = 150$) are shown in Figures 4.3(a)-(c). This is the region of channel flow that is more akin to isotropic turbulence. For the correlation coefficient in the *x*-direction, R_{uu}, the forwards correlation coefficient (which is represented by R_{uuf} from here on) is lower than the backwards correlation coefficient (which is denoted by R_{uub}), for $Pr < 6$. Increase in *Pr* increases the value of both R_{uuf} and R_{uub} up to what appears to be an upper limit. For $Pr \geq 50$ the changes in R_{uuf} are not noticeable, while for $Pr \geq 6$ the changes in R_{uub} are not noticeable. This shows that the markers get correlated the same way, irrespective of the Prandtl number for high *Pr*. For any *Pr*, the tail of the R_{uub} coefficient is always longer and higher compared to R_{uuf}. The molecular diffusion effects, which differentiate the behavior of markers at different *Pr*, is small for $Pr \geq 6$ and the markers follow a correlation that is similar to that for fluid particles. From this point on only the graphs for the low *Pr* and one high *Pr* are presented, in order to avoid clutter when presenting the results on the Figures. The lines for $Pr > 6$ are all represented by the line for $Pr = 1000$. The tail of the forwards correlation coefficient R_{vvf} for the *y*-direction velocity is higher than the backwards correlation

coefficient R_{vvb}. For the velocity in the *z*-direction, the R_{wwb} is slightly higher than the R_{wwf} for low *Pr*, but this behavior is reversed for high *Pr,* where the R_{wwf} becomes higher than R_{wwb}.

The comparison between the forwards and backwards correlation coefficient for markers captured and correlated in the logarithmic layer (y^+ = 75) is shown in Figures 4.4(a)-(c). The R_{uuf} is clearly less than the R_{uub} for the correlation coefficient of the *x*-velocity. Increasing the Prandtl number causes an increase in the value of the correlation coefficient till *Pr* = 6, after which it remains constant. The R_{vvf} is slightly higher than R_{vvb} for the correlation coefficient of the *y*-velocity, and the same trend is observed for the *z*-direction for higher *Pr* where the correlation coefficient R_{wwf} is higher than the R_{wwb} coefficient, while for *Pr* of 0.1 and 0.7, we find negligible differences.

The forwards and backwards correlation coefficients for markers captured and correlated in the location between the viscous sub-layer and the logarithmic layer (y^+ = 37) are shown in Figures 4.5(a)-(c). The R_{uuf} is clearly less than the R_{uub} and an increasing *Pr* causes an increase in the value of the correlation coefficient up to *Pr* = 6, beyond which the correlation coefficients do not change. The R_{vvf} is higher than R_{vvb} and, like in the case for y^+ = 75, the correlation coefficient of the z-velocity forwards in time, R_{wwf}, is higher than the correlation coefficient backwards in time R_{wwb}.

The comparison between the forwards and backwards correlation coefficient for markers captured and correlated at the edge of the viscous sub-layer (y^+ = 5) is

presented in Figures 4.6(a)-(c). The R_{uuf} is clearly less than the R_{uub}, but the difference is smaller when compared with the difference between R_{uuf} and R_{uub} for the logarithmic layer and for the transition region between the viscous sub-layer and the logarithmic layer. Increasing *Pr* causes an increase in value of the correlation coefficient up to *Pr* = 50, beyond which there are no notable differences between different *Pr*. We find that the differences between R_{vvf} and R_{vvb} are small for low *Pr*, while for the *Pr* = 1000 R_{vvf} is less than R_{vvb} for the correlation coefficient of the *y*-velocity. The forwards correlation coefficient R_{wwf} is less than the backwards R_{wwb} for the *z*-velocity for all *Pr*.

4.2.2 Dispersion time scales

The correlation coefficients as calculated above provide an outline of the behavior of forwards and backwards dispersion at different regions of the flow. A more comprehensive picture of the forwards and backwards dispersion is obtained by evaluating the timescales associated with the correlation coefficients. A timescale, say in the *x*-direction, can be calculated as

$$\tau_x = \int_{t_0}^{\infty} R_{uu}(t, t_0)dt \qquad (4.2)$$

This timescale can be called the *material timescale* to differentiate it from the term Lagrangian timescale, which is usually reserved for the timescales of fluid particles moving without molecular diffusion effects. The material timescales for both forwards and backwards dispersion are presented in Figures 4.7(a)-(c), for markers correlated at different layers in the turbulent channel. For all cases, the material timescale increases

with *Pr* for both forwards and backwards dispersion, and appears to reach a constant value at very high *Pr*.

For the streamwise velocity, the material timescales for the forwards and backwards dispersion show minimum difference at the center of the channel. The center of the channel is the area of the channel flow field that is closer to Gaussian turbulence than any other region of the channel flow, so this finding is expected given the findings for Gaussian isotropic turbulence by Sawford et al. [73] The maximum difference between the material timescales for the forwards and backwards dispersion appears in the transition region (between the viscous sub-layer and the logarithmic layer), followed closely by the logarithmic region. In all cases, however, the material timescale for the forwards dispersion is less than that for the backwards dispersion.

For the *y*-velocity, at the center of the channel, the forwards and the backwards material timescales are nearly equal, while in the logarithmic region, at lower *Pr* (0.1, 0.7) the timescales are the same, while for the higher *Pr* (≥ 6) the forwards timescales have higher values. In the transition region, for lower $Pr = 0.1$, the forwards timescale is larger, while for higher *Pr*, the timescales have very small differences. However, at the viscous sub-layer, the material timescale for the backwards dispersion is slightly higher than that for the forwards for $Pr \geq 6$, while for $Pr = 0.1, 0.7$, the timescales are nearly the same.

Considering the spanwise velocity, at the center of the channel the material timescales for the forwards and backwards dispersion are very close to one another. In the logarithmic region, except for *Pr* 0.1, where there is no difference in the timescale, the forwards timescale is higher than the backwards timescale. The forwards timescales

are also higher in value than the backwards timescales in the transition region. At the edge of the viscous sub-layer, the material timescale for the forwards dispersion is less than that for the backwards dispersion.

The material timescale defined using the streamwise velocity is larger than the material timescale in the other two directions [see the scale used in Figures 4.7(a)-4.7(c)]. The smaller material timescale is observed in the direction normal to the channel walls, indicating the highly anisotropic character of the dispersion in channel flow. This is true for both the forwards and the backwards dispersion.

The ratios of the values of the material timescales for the forwards to the backwards dispersion are shown in Table 4.1, which is a summary of the behavior of the forwards and backwards timescales relative to each other for all three velocities. In all three directions of the flow at the center of the channel, the ratio is nearly one for all *Pr*. The τ_f / τ_b ratio for the streamwise directions in the other regions, namely, logarithmic region, transition region and viscous sub-layer is well below one. In the normal direction, in the logarithmic region, the ratio τ_f / τ_b is greater than one. It is almost one in the transition region and is smaller than one at the edge of the viscous sub-layer. In the spanwise direction, the ratio τ_f / τ_b is close to one in the logarithmic region, it is above one in the transition region and below one in the viscous sub-layer.

The material timescales in the streamwise and spanwise directions for both forwards and backwards dispersion increase with increasing distances from the wall. This trend becomes more evident when the forwards and backwards dispersion material timescales for $Pr \geq 6$ are grouped together and averaged (since we found that the timescales do not change much for $Pr \geq 6$ an average like this is more meaningful than

examining individual values), the forwards and backwards material timescales increase with increasing distance from the wall. The trend is consistent to the trend observed by Mito and Hanratty [154] and by Le and Papavassiliou [148] but not with the results of Bernard and Rovelstad [72]. The backwards timescale in the streamwise direction, however, exhibits a maximum at $y^+ = 37$. This is likely due to the contributions of strong and well-correlated ejection and sweep coherent structures that contribute to the movement of markers towards that location, while structures that move markers to the center of the channel are not so well correlated.

The behavior of the Lagrangian timescales determines the rate of dispersion for fluid particles in homogenous, isotropic turbulence, as shown in Equations 2.2 and 2.3, but, in the present study, where the flow is anisotropic and molecular effects contribute to dispersion in addition to convection, the material timescales cannot be solely used to determine the rate of forwards and backwards dispersion. The mean square marker displacement can be used to directly visualize the dispersion rate. The difference between the forwards and the backwards dispersion in the y direction as a function of forwards or backwards time is presented in Figures 4.8(a)-(d) for the markers captured in different regions of the channel. Table 4.2 is a summary of the findings of this analysis, and it includes the results for the other two directions. Looking at Figure 4.8, the difference between forwards and backwards dispersion is very small at the center of the channel for $Pr = 0.1$, while for higher Pr, the mean square displacement for backwards dispersion is larger than that for the forwards dispersion. In the logarithmic region, for $Pr \geq 0.7$, forwards mean square dispersion is higher, as is the case for the transition region and the viscous sub-layer.

4.2.3 Effects of the velocity field structure on forwards and backwards scalar dispersion

Examining Table 4.2, one can see where the departure from the behavior for isotropic turbulence occurs: it occurs where the forwards dispersion is higher than the backwards. In the streamwise direction, for all *Pr*, the forwards dispersion is larger compared to the backwards dispersion in the center of the channel and in the logarithmic layer. In the vertical direction, for *Pr* higher than 0.1 and for all locations other than the center of the channel, the forwards dispersion is larger. Similar results are found for the dispersion in the spanwise direction. However, the difference between the forwards and the backwards dispersion is much smaller as a percentage of spanwise dispersion, than the difference in the vertical direction. The obvious question that arises now is how can the dominance of either forwards or backwards dispersion at particular regions in the turbulent flow field be explained?

Sawford et al. [73] found out that, for homogenous isotropic turbulence, the backwards relative dispersion was several times larger than the forwards relative dispersion. This finding was true when the turbulence was not Gaussian, while for Gaussian turbulence there did not appear any difference between the backwards and forwards relative dispersion. Furthermore, asymmetry of the probability density function (pdf) of the particle separation distances was found to cause the differences in the backwards and forwards dispersion. One can then speculate that the fact that turbulence is non-Gaussian in the case of channel flow can result in differences in backwards and forwards dispersion. Combining this speculation with the observations of the previous paragraph leads to the need for a close examination of the probability

density function of the fluctuating velocity fields, and specifically the skewness of the pdf, which is a measure of the pdf asymmetry. Coherent flow structures, like ejection and sweep events, characterize the flow close to the wall and affect the pdf skewness. Further motivation for the need to examine the pdfs of the velocity fields arises when one considers that dispersion characteristics for intermediate and high *Pr* ($Pr \geq 6$) do not appear to change much. At these *Pr*, the convective effects dominate transport compared to molecular diffusion effects.

The backwards dispersion is related to the "history" of the markers or, in other words, their memory of the structure of the velocity field at the point from where they originated before they arrived at a particular location. The forwards dispersion is related to the "future" of the markers. In order to examine the history and future of the markers, the average position from which the markers originate (designated as a trajectory in negative time) and the average position to which the markers disperse forwards (a trajectory in positive time) in the vertical direction, $\overline{Y}$, is presented in Figures 4.9(a)-(d).

As seen in Figure 4.9(a), the markers at the center of the channel on average arrive there from origins that are very close to the center of channel. The forwards dispersion is higher in the streamwise direction, because the forwards dispersing markers have higher initial velocities with which they move out, since the maximum mean velocity is at the center of the channel. The markers arriving at the center region originate from regions that have smaller mean velocities. Considering the vertical and spanwise direction there is no mean velocity to drive the markers, and the skewness of the velocity fluctuation pdf is zero in the vertical and spanwise direction (see Figure

4.10). In the case of backwards dispersion, the markers arrive from locations above or below the center of the channel, where they have some finite skewness. This finite skewness (indicating asymmetric velocity fluctuations) helps in dispersing the markers faster than compared to the forwards dispersion. Hence we find that for higher *Pr*, backwards dispersion is higher in the vertical and spanwise direction. For $Pr = 0.1$, the convective and molecular diffusion effects are nearly comparable; the pdf of the velocity fluctuations in this case does not play a dominant role in the dispersion, and the backwards dispersion is only slightly higher than the forwards dispersion (see Fig 4.8(a)).

The average normal positions from where the markers arrive and leave the logarithmic region is seen in Figure 4.10(b) as a function of time. In the streamwise direction, for $Pr = 0.1$, the markers arrive from $y^+ \approx 102$, while for $Pr \geq 0.7$, the markers arrive on average from $y^+ \approx 93$. The mean velocity is still an important factor at this region of flow. The mean streamwise velocity decreases as the markers reach the logarithmic region. So the dispersion reduces as the markers decelerate in the streamwise direction. On the other hand, markers dispersing away from the logarithmic region move on average towards regions of higher mean velocity. The markers accelerate in this case, explaining why forwards dispersion is higher than backwards dispersion in this region. In the vertical direction, in the logarithmic region, backwards dispersion is higher for $Pr = 0.1$, while for $Pr \geq 0.7$, the forwards dispersion is higher. For $Pr \geq 0.7$, a look at Table 4.1 shows that τ_f / τ_b is greater than one. This means that the forwards moving markers are correlated for a longer time. Also, as seen in Figure 4.9(b), the forwards dispersing markers advance to locations farther from the wall,

experiencing larger velocity fluctuation spikes (since they move to area of higher negative skewness). As a result of all these contributions the forwards dispersion is higher than the backwards dispersion. For $Pr = 0.1$, the markers come on average from higher locations compared to forwards dispersion due to large molecular diffusion and due to the presence of the wall, so that backwards dispersion is higher than forwards dispersion. Considering the spanwise direction, there is no wall to affect the dispersion forwards, so the forwards dispersion is higher as the markers move to regions of more asymmetric velocity fluctuations.

In the transition region, in the streamwise direction, coherent structures in the form of sweep and ejection events start playing a vital role. The skewness of the velocity pdfs experienced by the markers arriving at this location has higher magnitude compared to those that originate from this location. Added to this effect, the higher length and frequency of the sweep events (which are defined as fluid structures that move faster than the mean velocity and move fluid from the outer regions towards the wall regions, [163]) compared to the ejection events (which are defined as fluid structures that move low momentum fluid away from the wall region) cause the backwards dispersion to be higher than the forwards dispersion. (Quantitative characteristics of the ejection and sweep events close to the wall for the presently simulated field can be found in Spencer et al. [164]). In the vertical direction, for $Pr = 0.1$, it is seen in Figure 4.9(c) that the markers move on average to the same location where they come from. In addition, molecular diffusion effects are large, diminishing the effects of the convective transfer and causing the dispersion to be almost equal in both directions. For $Pr \geq 6$ the markers arrive on average from the same location to

which they move out. Also as Table 4.1 indicates, the ratio τ_f / τ_b is nearly one, indicating that the markers dispersing forwards stay together the same amount of time as the markers arriving to the transition region. Considering the skewness of the velocity fluctuations of the arriving markers, it decreases as they arrive at the transition region, while the forwards markers move away with increasing skewness. Since these markers are correlated for approximately the same amount of time, the forwards markers will experience higher velocity fluctuation spikes (higher skewness) and disperse to a larger extent as compared to the backwards dispersing markers. In the spanwise direction, for all *Pr*, the forwards dispersion is larger, as the markers stay closer together and allow turbulence to disperse them for longer times indicated by the fact that τ_f / τ_b is greater than one.

In the viscous sub-layer, the backwards dispersion is higher than the forwards dispersion in the streamwise direction, for all *Pr*. Coherent structures, which are frequent in this region determine the dispersion. The sweep events, which have a higher mean length and frequency over the ejection events [164], cause the backwards dispersion to be higher than the forwards dispersion. In the vertical direction the material timescales are really small, so that the distances from where the markers arrive and where they disperse are nearly the same. Markers arriving to the viscous sub-layer slow down considerably and the skewness becomes smaller as they approach the channel walls [see Figure 4.10(b)]. The forwards dispersing markers, as seen in Figure 4.9(d), move on average towards the transition region, where they find higher asymmetry of velocity fluctuations, as evidenced by the higher magnitude of skewness. This causes the forwards dispersion in this region to be higher than the backwards

dispersion. In the spanwise direction, the skewness is nearly zero in the viscous sub-layer, but $\tau_b > \tau_f$ causing the backwards dispersion to be higher. Only for Pr = 0.1, where the molecular effects are dominant in transferring heat, the forwards dispersion is a higher.

4.3 Conclusions

A combined direct numerical simulation/Lagrangian scalar tracking approach was utilized to study the differences in the behavior of forwards and backwards dispersion in all directions for a turbulent channel flow. The study was carried out at four important regions of the flow, namely the edge of the viscous sub-layer at distance of y^+ = 5, the transition region (between the viscous sub-layer and the logarithmic layer) at y^+ = 37, the logarithmic layer at y^+ = 75, and the center of the channel at y^+ = 150. The simulation runs covered the range of Prandtl numbers, Pr = 0.1, 0.7, 6, 10, 50, 100, 500 and 1000. The analysis involved calculations of the behavior of the material autocorrelation coefficient and of the associated Lagrangian timescales. The mean square dispersion was calculated to study the dispersion.

The material timescales increased with increasing molecular Prandtl number for small Prandtl numbers, reaching constant values for Prandtl numbers larger than six. The simulation results showed that Pr = 0.1 always provides a different scenario compared with the higher Pr (that is $Pr \geq 6$), since molecular diffusion effects are the dominant mechanism of transport. For higher Pr we find that in the streamwise direction, the backwards dispersion is higher near the channel walls, while forwards dispersion becomes higher at the logarithmic layer and the center of the channel. In the

vertical direction, the forwards dispersion is higher for all regions except the center of the channel. In the spanwise direction, the backwards dispersion is higher in the center and viscous sub-layers, while forwards dispersion dominates in the other two regions. For both forwards and backwards dispersion, the material timescale is shorter in the direction normal to the channel walls and longer in the streamwise direction.

In light of the above discussion, there are different cases that arise in the examination of the forwards and backwards dispersion in wall turbulence: The case of the streamwise dispersion, where the difference in the forwards and backwards dispersion is due to the variation of the mean streamwise velocity profile at different distances from the wall, and the case of the vertical and spanwise dispersion. The vertical direction is of particular importance, because this is the direction of transfer when there is heat transfer from or to the wall. The presence of the wall, which limits the range from where markers can arrive at a specific location, in conjunction with the relative importance of molecular versus convective transport, are the main reasons for the observed behavior. When convection is important, the time direction of higher dispersion is the direction in which the material timescale is large and the direction where the velocity skewness is larger.

Table 4.1: Ratio of the forwards material time scale to the backwards material time scale in all three directions of flow for center of the channel, logarithmic region, transition region (between the logarithmic region and the viscous sub-layer) and the viscous sub-layer.

	center of channel			Logarithmic layer			Transition region			Viscous sub-layer		
Prandtl number (*Pr*)	direction			direction			Direction			direction		
	x	*y*	*z*	*x*	*y*	*z*	*x*	*y*	*z*	*x*	*y*	*z*
0.1	0.90	1.00	0.95	0.36	0.97	1.02	0.35	1.30	1.25	0.45	1.18	0.64
0.7	0.92	1.01	0.97	0.29	1.02	1.07	0.19	1.00	1.05	0.36	1.06	0.75
6	0.99	0.98	0.97	0.29	1.08	1.08	0.19	0.99	1.09	0.28	0.96	0.65
10	0.93	1.00	0.99	0.32	1.07	1.03	0.19	0.98	1.12	0.28	0.77	0.69
50	1.00	0.99	1.00	0.29	1.06	1.02	0.20	1.00	1.14	0.31	0.85	0.76
100	1.03	1.01	0.99	0.29	1.05	0.97	0.20	1.00	1.15	0.32	0.83	0.69
500	0.99	0.98	1.05	0.28	1.09	0.99	0.21	1.02	1.18	0.33	0.96	0.83
1000	0.99	1.03	1.04	0.29	1.04	0.96	0.21	0.98	1.19	0.32	0.89	0.67

Table 4.2: Summary of findings about whether forwards or backwards dispersion is higher at different regions in the channel flow at very long times. (The Pr = 1000 here summarizes the results of all Pr including 10, 50, 100, 500 and 1000.)

Direction	Pr	$y^+ = 150$	$y^+ = 75, 225$	$y^+ = 37, 263$	$y^+ = 5, 295$
Streamwise	0.1	Forwards	Forwards	Backwards	Backwards
	0.7				
	6				
	1000				
Vertical	0.1	Backwards	Backwards	Forwards ≈ Backwards	Forwards
	0.7		Forwards	Forwards	
	6				
	1000				
Spanwise	0.1	Backwards	Forwards	Forwards	Forwards
	0.7				Backwards
	6				
	1000				

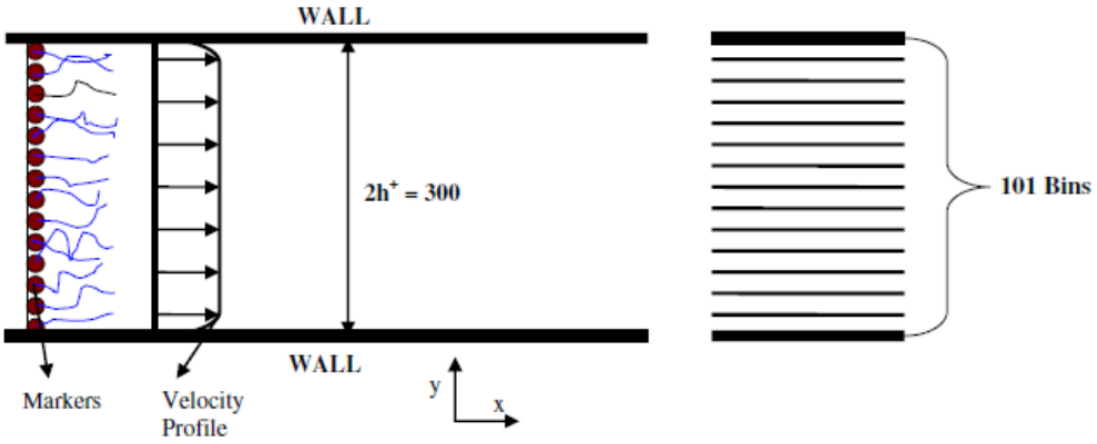

Figure 4.1: Schematic showing the *xy* cross-section of the simulation box, with markers uniformly and randomly released from one plane, as well as the bins in the vertical direction.

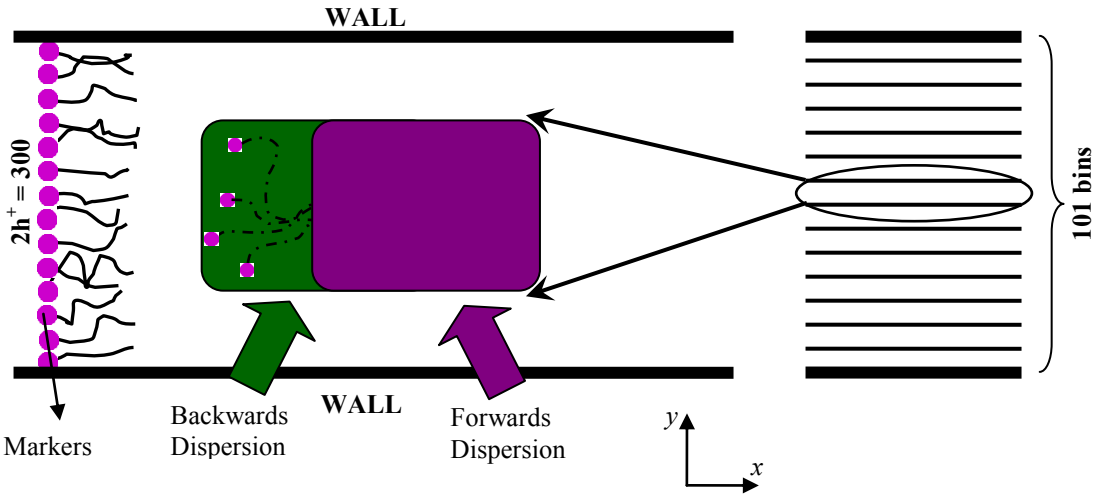

Figure 4.2: Schematic showing the x-y cross sectional view of the simulation box with markers being captured at a particular bin for backwards turbulent dispersion and markers dispersing from the same bin for forwards turbulent dispersion.

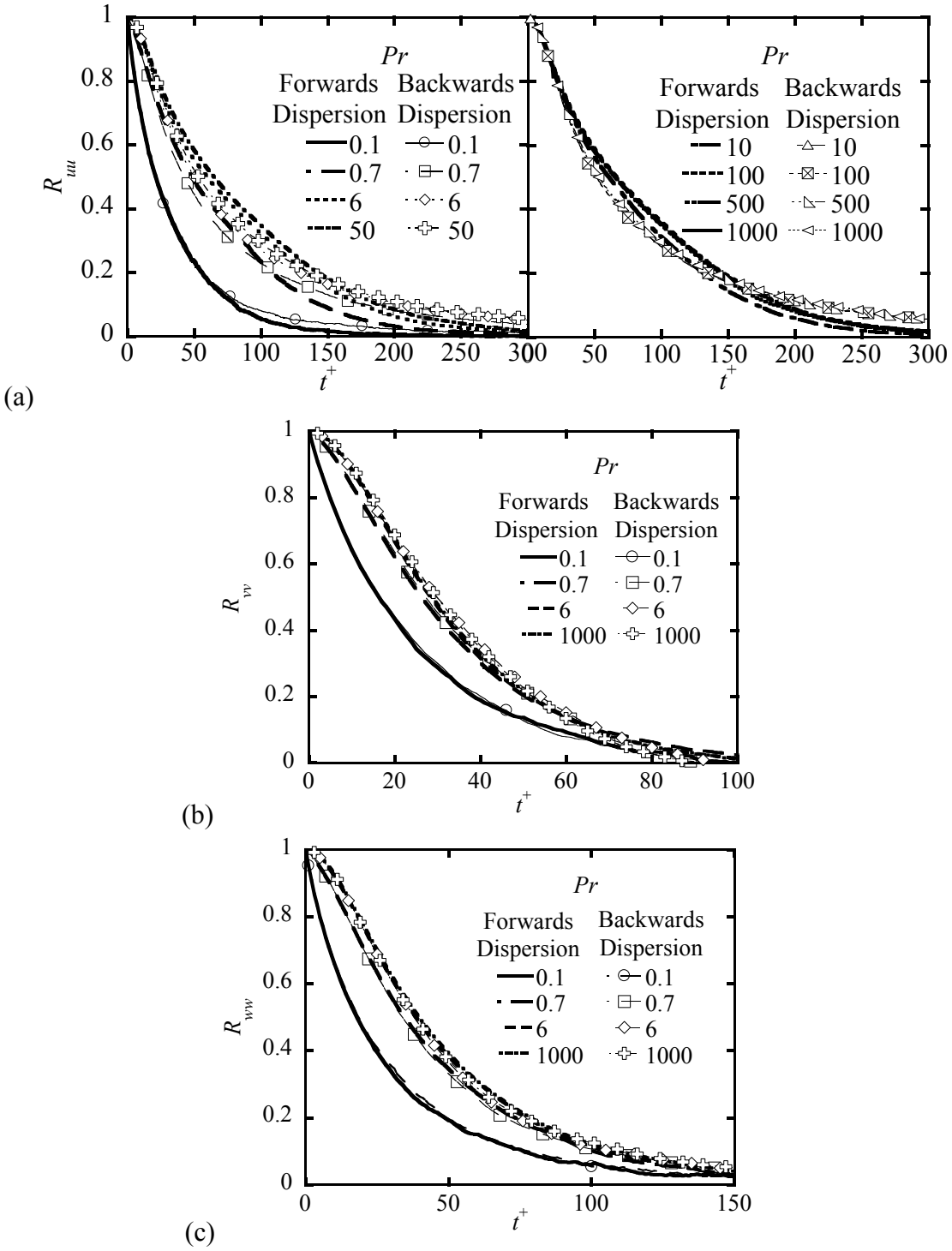

Figure 4.3: Material correlation coefficient as a function of time in cases of forwards and backwards dispersion for markers captured at the center of the channel, and for different Prandtl numbers: (a) Streamwise velocity, R_{uu} ; (b) normal velocity, R_{vv} ; (c) spanwise velocity, R_{ww}. In Figures (b) and (c), the lines for $Pr \geq 10$ are all represented by the line for $Pr = 1{,}000$.

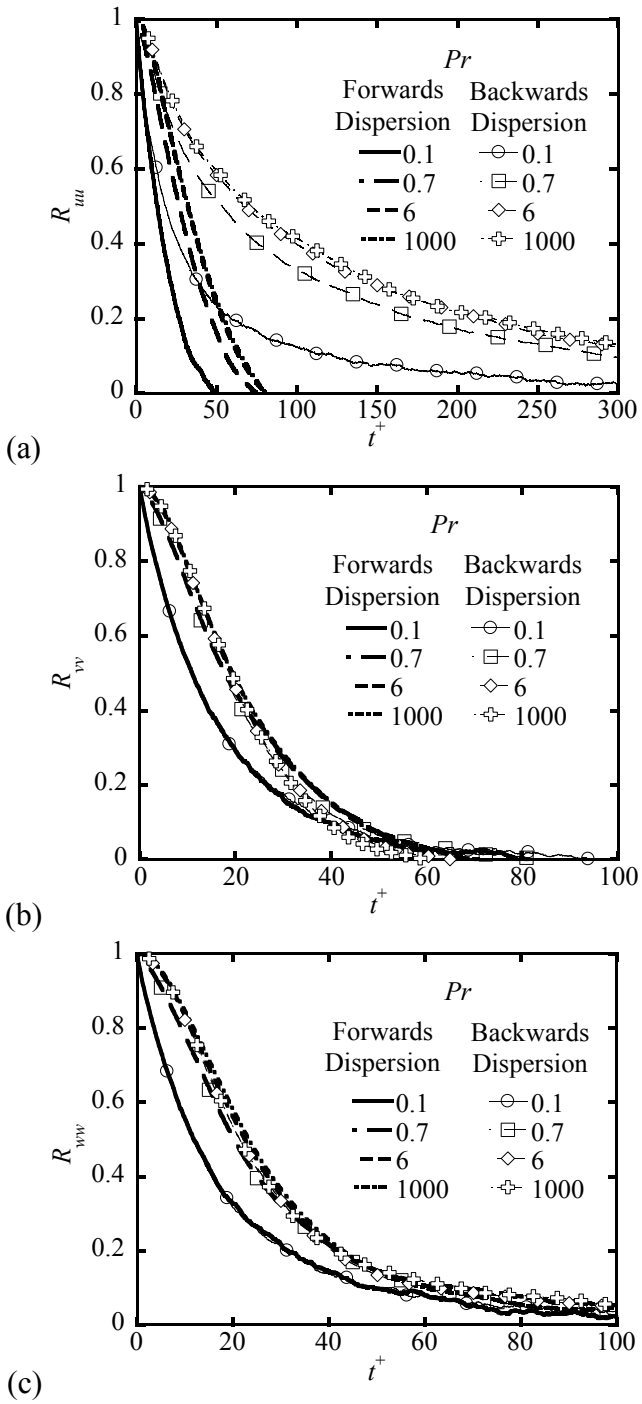

Figure 4.4: Material correlation coefficient as a function of time in cases of forwards and backwards dispersion for markers captured at the logarithmic region of the turbulent channel flow, and for different Prandtl numbers: (a) Streamwise velocity, R_{uu}; (b) normal velocity, R_{vv}; (c) spanwise velocity, R_{ww}. In order to clearly present the results, the lines for $Pr \geq 10$ are all represented by the line for $Pr = 1{,}000$.

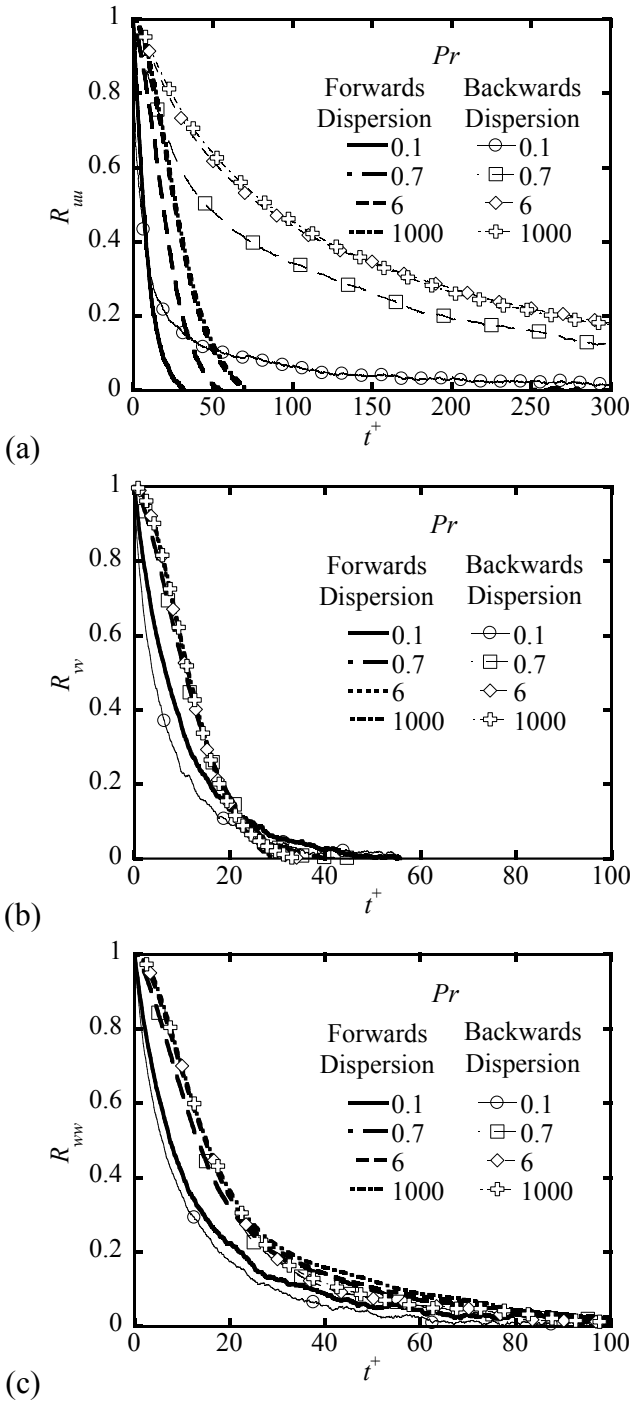

Figure 4.5: Material correlation coefficient as a function of time in cases of forwards and backwards dispersion for markers captured at the transition region between the viscous sub-layer and the logarithmic layer, and for different Prandtl numbers: (a) Streamwise velocity, R_{uu}; (b) normal velocity, R_{vv}; (c) spanwise velocity, R_{ww}. In order to clearly present the results, the lines for $Pr \geq 10$ are all represented by the line for Pr = 1,000.

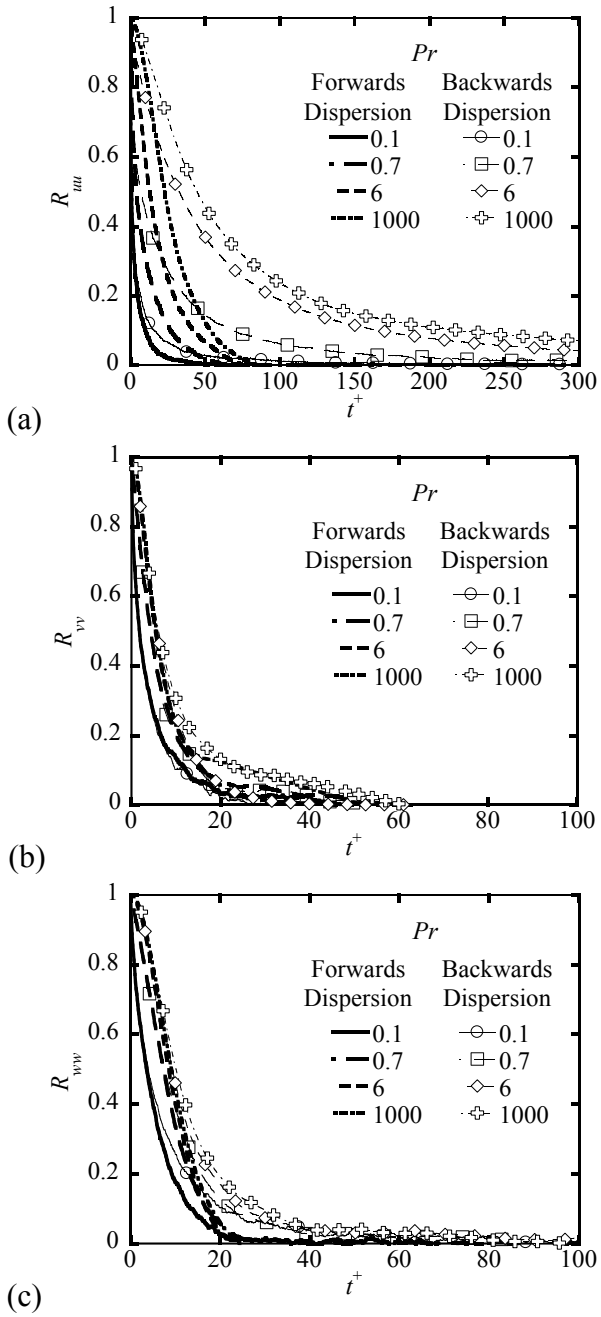

Figure 4.6: Material correlation coefficient as a function of time in cases of forwards and backwards dispersion for markers captured at the edge of the viscous sub-layer, and for different Prandtl numbers: (a) Streamwise velocity, R_{uu}; (b) normal velocity, R_{vv}; (c) spanwise velocity, R_{ww}. In order to clearly present the results, in the streamwise direction, the line for $Pr = 6$ represents the data for $6 \leq Pr < 50$, while the line for $Pr = 1000$ represents the data for $50 \leq Pr \leq 1000$, while in the case of normal and spanwise velocities, the lines for $Pr \geq 10$ are all represented by the line for $Pr = 1{,}000$.

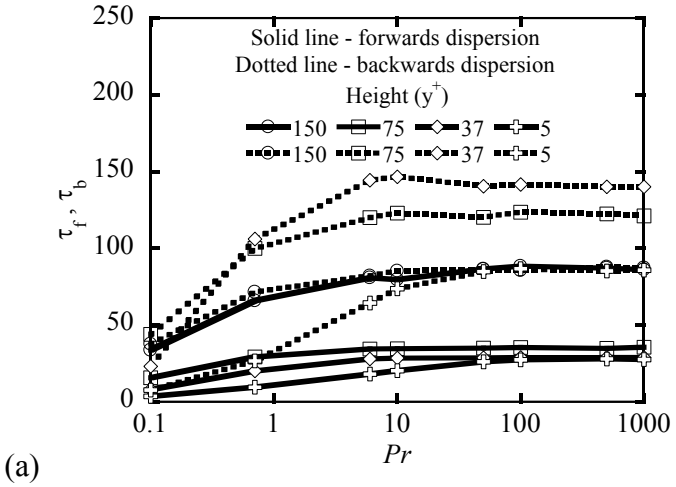

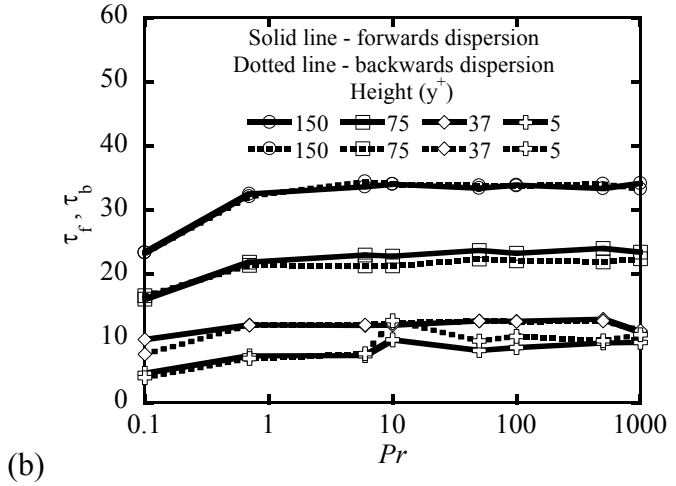

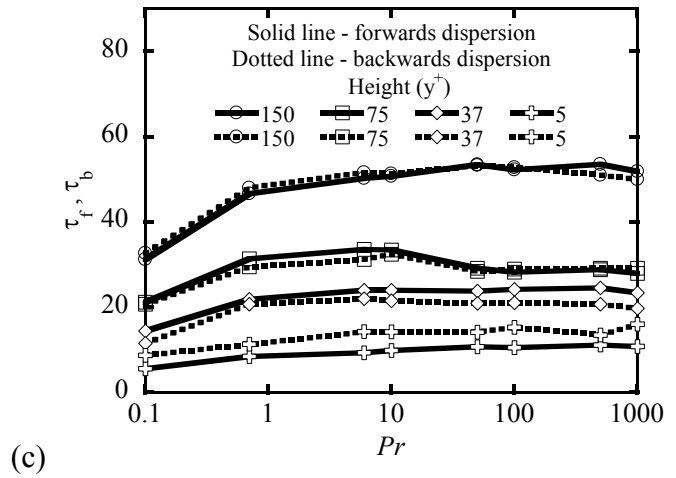

Figure 4.7: Lagrangian time scale as a function of Prandtl number in different regions of the turbulent channel flow for forwards and backwards dispersion: (a) streamwise direction; (b) normal direction; (c) spanwise direction.

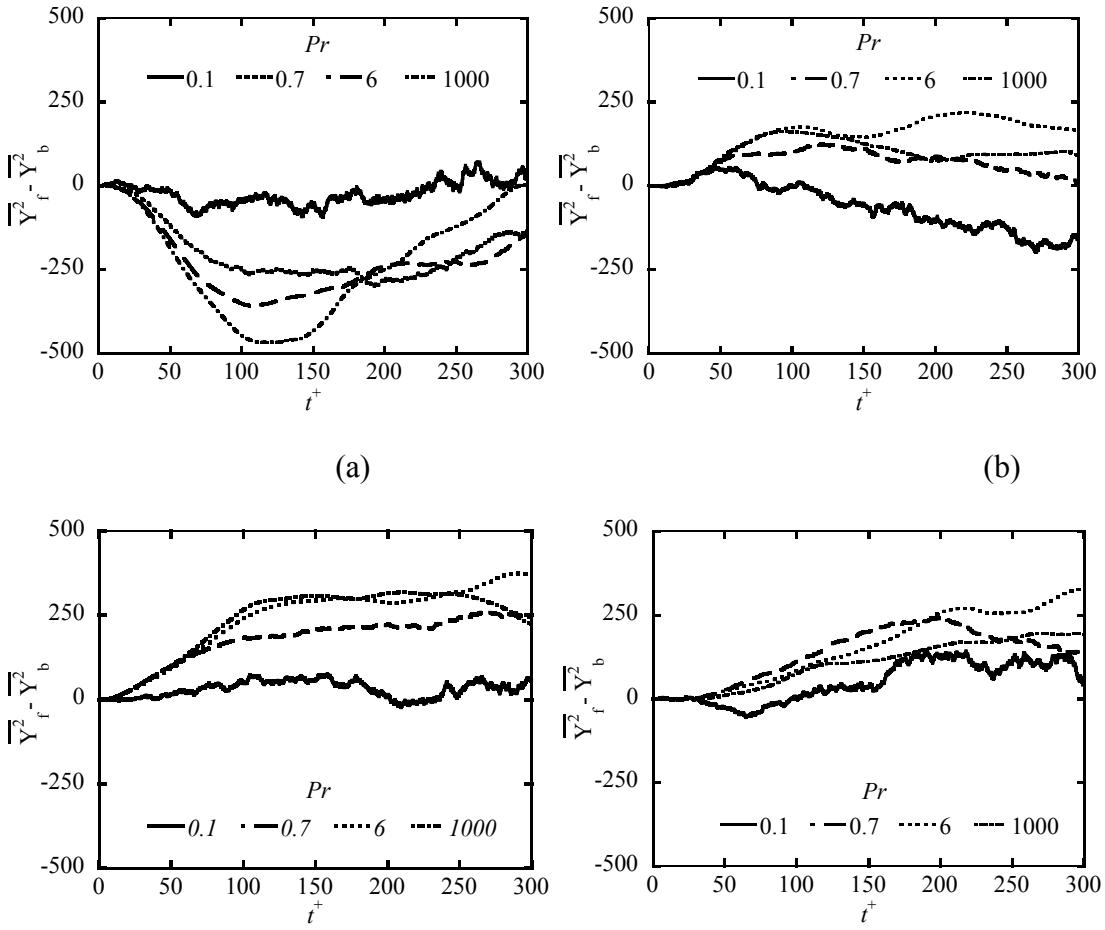

Figure 4.8: Differences between forwards and backwards mean square displacement in the normal direction as a function of time for different Prandtl numbers, in cases of markers captured in different regions of flow (a) center of channel ($y^+ = 150$) ; (b) Logarithmic region of the turbulent channel flow ($y^+ = 75, 225$) ; (c) Transition region of the channel turbulent flow ($y^+ = 37, 263$) ; (d) edge of the viscous sub-layer ($y^+ = 5, 295$).

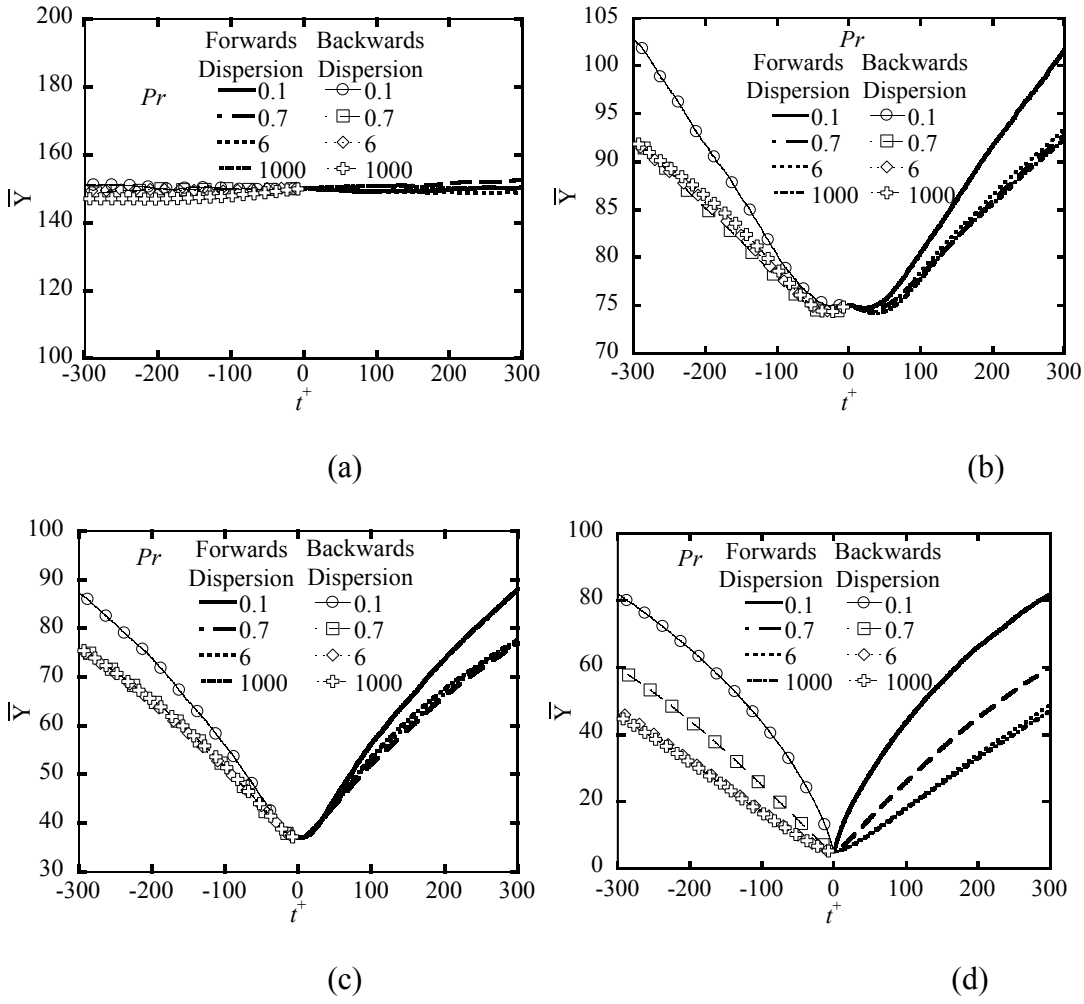

Figure 4.9: Mean vertical position of the markers as a function of time in cases of forwards and backwards dispersion for different Prandtl numbers, and for markers captured in different regions of flow: (a) center of the channel ($y^+ = 150$) ; (b) Logarithmic region of the turbulent channel flow ($y^+ = 75, 225$) ; (c) Transition region of the channel turbulent flow ($y^+ = 37, 263$) ; (d) edge of the viscous sub-layer ($y^+ = 5, 295$).

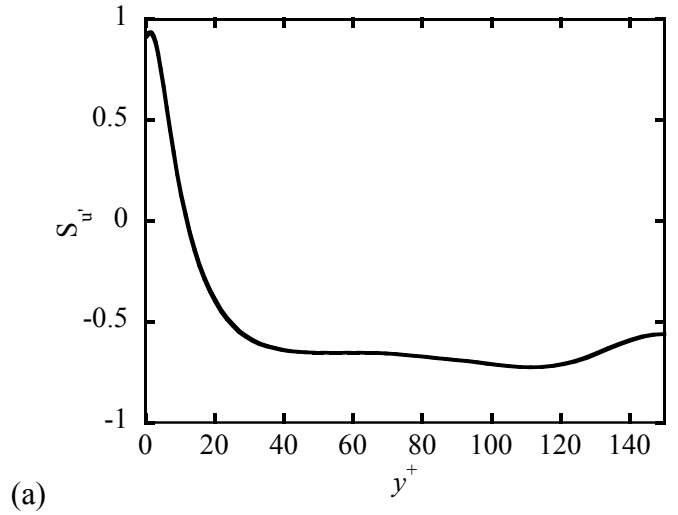

(a)

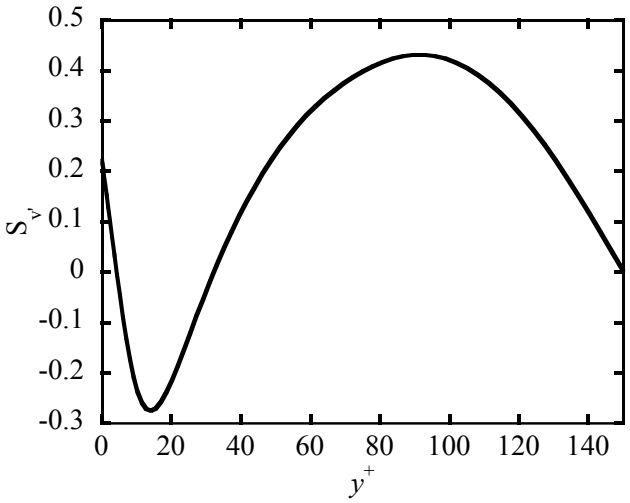

(b)

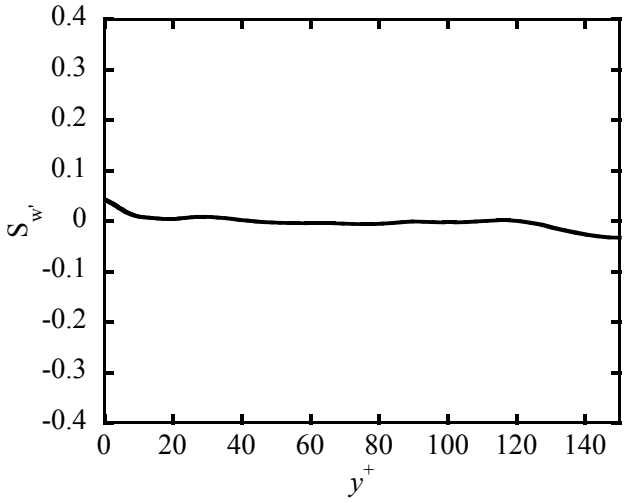

(c)

Figure 4.10: Skewness of the velocity fluctuations as a function of distance from the channel walls: (a) Streamwise; (b) normal direction; (c) spanwise direction.

Chapter 5: FORWARDS AND BACKWARDS RELATIVE SCALAR DISPERSION[†]

5.1 Simulation parameters and procedure

In this Study, the DNS is used to obtain the flow field of Poiseuille channel flow at Re_τ = 300, and for plane Couette flow, at Re_τ = 150. The complementary LST techniques is used to for the simulation of Pr = 0.1, 0.7, 6, 20, 50, in the case of Poiseuille channel flow, and Pr = 0.1, 0.7, 3, 6, 10 in the case of plane Couette flow. The number of scalar markers is 260100 and 145161, and they are released uniformly from an xz plane in the Poiseuille channel and plane Couette flow cases, respectively. The time step with which the simulation is advanced for both cases is $\Delta t^+ = 0.2$ in viscous wall units. Different regions of the channel present different scenarios and different physics in cases of forwards and backwards turbulent dispersion. In order to concentrate on a region, the channel in the vertical direction for Poiseuille flow is divided into 201 equally sized bins, while in the case of plane Couette flow it is divided into 101 bins. Bins corresponding to four regions of turbulent channel flow, the viscous sub-layer, the transition region, the logarithmic region and the center of the channel, are chosen for capturing and tracking of markers. In the Poiseuille flow, the bins chosen are at distances of (a) $y^+ = 5$ (and also at $y^+ = 595$, due to the symmetry of the channel about the center plane at $y^+ = 300$) for the edge of the viscous sub-layer; (b) at $y^+ = 60$ and $y^+ = 540$ for the transition region; (c) at $y^+ = 120$ and 480 for the logarithmic region; and at (d) $y^+ = 300$ for the center of the channel. In the Couette flow, the channel height is half

[†] Most of the material in this Chapter has been published in the International Journal of Heat and Mass Transfer, 55, 5650-5664 (2012)

that of the Poiseuille flow and hence the bins include (a) the edge of viscous sub-layer at $y^+ = 5$ and 295 (due to channel symmetry in this case along the center plane at $y^+ = 150$); (b) the transition region at $y^+ = 37$ and 263; (c) logarithmic region at $y^+ = 75$ and 225 and the (d) center of the channel at $y^+ = 150$. In order to calculate forwards and backwards dispersion statistics, position and velocity of all the markers in the flow field at each time are stored in a database. At a particular time, the time of interest, and a particular bin of interest, the total number of markers present in the bin and the associated marker identity of each marker are determined. The trajectory of each of these markers prior to arriving in the bin can be obtained from previously stored data, and backwards relative dispersion statistics are obtained. The forwards relative dispersion statistics are obtained by tracking the markers captured in the particular bin at the time of interest as they continue to move into the flow field.

In both flow cases, the markers are tracked in time only after they get uniformly distributed in the channel. We determined that the distribution of markers in the vertical direction was uniform when the average vertical marker position was equal to the channel half-height, and when the variance of the distribution of the marker positions in the normal direction was equal to that predicted for a uniform distribution between zero and the channel height, $2h^+$. For a uniform distribution between 0 and $2h^+$, the variance is expected to be $(2h^+-0)^2/12$, i.e., for the low *Re* channel it is expected to be 7500, while for $h^+ = 300$ it is expected to be 30000. The time at which this occurs at time $t^+ = 5000$ and 2000 in case of Poiseuille channel and Couette flow, respectively. The markers are traced for a time period of $t^+ = 300$ (which is much larger than the Lagrangian material time scale obtained in previous results [148, 165]) for both the

cases of forwards and backwards dispersion. For the Poiseuille flow, for each bin, there are several realizations of forwards and backwards dispersion obtained as follows: The time of capture is chosen at $t^+ = 5800$, and then every 100 time units there is a new starting point for dispersion at $t^+ = 5900, 6000, \ldots$ to 7700, thus yielding a total of 20 different realizations. Since there are two bins with identical statistics in the case of the edge of the viscous sub-layer, the transition region, and the logarithmic region due to channel symmetry, as mentioned previously, for these regions the data obtained is a result of average trajectories obtained from 40 realizations. The behavior at the center of the channel has been obtained with only 20 averages. Similarly, for plane Couette flow, the initial time of capture is chosen at $t^+ = 2500$, and then the process is repeated every 100 time units (at $t^+ = 2600, 2700, \ldots$ to 3700) so as to yield 12 averages, which results in 24 averages for the edge of the viscous sub-layer, the transition and the logarithmic regions with symmetry. On an average, 1300 and 1450 markers are captured in Poiseuille channel and plane Couette flow cases, respectively, resulting in about 844350 and 1050525 marker pairs in each respective case. In Poiseuille channel flow, on an average 1.5×10^8 and 3×10^8 marker pairs are used in the calculations for the center of the channel and for the other three regions, respectively. For the plane Couette flow, on an average 1×10^8 and 2×10^8 marker pairs are utilized in the statistical calculations for the center of the channel and the other three regions.

5.2 Results and discussion

5.2.1 Poiseuille flow

In the case of flow restricted by channel walls, the direction normal to the channel walls is the direction of interest. For the remainder of the text, any reference to velocity or distance is always in the vertical direction, perpendicular to the channel walls. The difference between the forwards and backwards mean squared relative displacement in case of Poiseuille channel flow is plotted in Figure 5.1 as a function of time for different *Pr*. Calculating the differences in the mean squared relative displacement in the case of forwards and backwards relative dispersion clearly depicts the differences in the rate of dispersion between these two types of dispersion. It is seen in Figure 5.1 that the difference is positive and is increasing with time for all *Pr* in the case of viscous sublayer, the transition region and the logarithmic region, indicating the higher rate of forwards relative dispersion in these regions of the channel. The center of the channel is the only area of channel flow that can be considered to resemble isotropic turbulence. It is seen that, in this region, the backwards relative dispersion is faster than forwards relative dispersion, in agreement with the results for isotropic turbulence, where Sawford et al. [73] and Berg et al. [74] documented that backwards relative dispersion is faster than forwards relative dispersion. An interesting behavior is also seen in Figure 5.1; the values of the difference between forwards and backwards relative dispersion increase with increasing *Pr* in regions where convection dominates molecular diffusion, while in the viscous sublayer the differences of the relative mean squared displacement increases with decreasing *Pr* highlighting the dominance of molecular diffusion compared to turbulent convection very close to channel walls.

The marker pair separation probability density functions (pdfs) at a particular time for the forwards and backwards relative dispersion are presented in Figures 5.2-5.5. The distribution of the marker pair distance is plotted in Figure 5.2 for the case of the viscous sub-layer with the lower $Pr = 0.1$ behavior plotted in Figure 5.2(a) and the higher $Pr = 50$ behavior plotted in Figure 5.2(b). The marker pair distance distribution for the transition region, the logarithmic region and the center of the channel are shown in Figures 5.3, 5.4 and 5.5, respectively, with $Pr = 0.1$ results as (a) and $Pr = 50$ results as (b). In the viscous sublayer, the transition region and the logarithmic region, and at larger times, there are more pairs with shorter separation distance in case of backwards relative dispersion, while there are more marker pairs with larger separation in case of forwards relative dispersion. This behavior seems to be correlated to the dispersion rate, with faster forwards relative dispersion rates corresponding to more marker pairs that diffuse farther from each other in this type of dispersion. In the center of the channel, however, the higher rate of backwards relative dispersion is reflected in the higher number of largely separated marker pairs for backwards relative dispersion. Comparing the distribution of marker pair distances between different Pr cases, the $Pr = 50$ always has a higher number of marker pairs with smaller separation at all times in all the regions of the flow. The large molecular diffusion for $Pr = 0.1$ (Pr is inversely proportional to the molecular diffusion) causes greater separation of marker pairs and hence the separation distribution of $Pr = 0.1$ is shifted towards higher values of separation of the marker pairs at all times. For a particular Pr, the behavior of the separation pdf with different distances from the channel wall is also interesting, in that the frequency of pairs with small separation decreases with increasing distance from the

channel walls. Such behavior, caused by the differences in *Pr,* for single particle dispersion has been observed and documented in Chapter 4 for Poiseuille channel flow at half the *Re* used herein.

The Poiseuille channel flow data presented here show very consistent differences between the rates of forwards and backwards relative dispersion. So, why do the forwards and backwards relative dispersion exhibit different rates at different regions of the channel for different *Pr*? A starting point to answer this question is to investigate the velocity fluctuations that the markers experience as they disperse in the vertical direction for different *Pr* and to quantify the differences in the marker pair velocity fluctuations. The relative velocity distribution of the marker pairs for different times for the forwards and backwards relative dispersion is plotted for the viscous sub-layer, the transition region, the logarithmic region and the center of the channel, in Figures 5.6, 5.7, 5.8, and 5.9, respectively, for $Pr = 0.1$ in (a) and $Pr = 50$ in (b). The viscous sub-layer, the transition region and the logarithmic region show larger number of marker pairs exhibiting greater velocity differences in the case of forwards relative dispersion, while there are more marker pairs showing smaller velocity differences in the case of backwards relative dispersion.

Motivated by the work of Sawford et al. [73], who found that the "Gaussianity" and symmetry of turbulence caused the differences between forwards and backwards relative dispersion to vanish, the nature of the asymmetry of the pdf of the velocity fluctuations, in other words, the skewness, is also analyzed to possibly explain the differences between forwards and backwards relative dispersion rates. Figure 5.10 is a plot of the skewness of the pdf of the *y*-velocity fluctuations as a function of the

distance from the channel wall. If one traces the variation of the skewness from a y location forwards, it is seen that marker pairs dispersing forwards from that location will travel through areas of pdfs of velocity fluctuations with changing asymmetry, causing them to drift farther from each other. In contrast, marker pairs travelling towards that same y location (as in backwards relative dispersion), start to increasingly experience similar pdfs of velocity fluctuations, causing them to move in concert to each other and closer to each other. This simple but intuitive analysis shows that the inherent imposition of initial and final conditions for forwards and backwards relative dispersion, respectively, plays a major role in the different rates observed in these two cases.

The behavior at the center of the channel is not interpreted by this argument, since backwards relative dispersion at the center of the channel is faster than forwards relative dispersion. It is seen in Figure 5.9, that there is a larger number of marker pairs with larger velocity differences in backwards relative dispersion than in forwards dispersion, in agreement with the finding that there is a larger separation between markers in backwards dispersing pairs than in pairs moving forwards from the center of the channel. So, why would backwards-dispersing markers moving closer towards each other, as they also move towards the center of the channel and as they experience similar skewness of the velocity fluctuation pdf, not disperse slower than their forwards dispersing counterparts? A possible explanation could be the zero skewness (i.e., the symmetric pdf of vertical velocity fluctuations) that the forwards dispersing markers begin to experience as they move out of the center region of the channel (the center is the only region in the channel where the skewness is zero). Another way to interpret this

result is to consider the effect of the coherent structures on particle dispersion, and the differences in the behavior of the coherent structures in this part of the channel compared to the other regions of the channel. It is rather well established that coherent vortical structures, often called ejection and sweep events [79, 163], are generated close to the channel walls and the near-wall region and extend towards the logarithmic layer. Such structures also contribute to the asymmetry of the velocity pdfs. These structures extend only till the edge of the logarithmic regions and become scarce at the center of the channel. Now, correlating this behavior with the relative forwards and backwards dispersion of markers, one can see a consistent pattern in that forwards moving markers from the viscous wall region, the transition and the logarithmic region are aided by these vortical structures in separating from each other. These structures play a role only in transporting markers from the viscous wall region and the logarithmic region towards the center of the channel, in case of backwards relative dispersion. The forwards relative dispersing markers from the center of the channel do not receive any help from these vortical structures due to their absence in the center region of the channel, which is also expressed with the symmetry of the velocity pdf.

This analysis clarifies the reasons behind the differences between the forwards and backwards relative dispersion. However, what is the reason behind the effects of *Pr* on the rates of forwards and backwards relative dispersion? In order to explain this, it is important to consider the effect that the *Pr* has on the rates of scalar dispersion. Earlier work [148, 157] has depicted three *Pr*-dependent zones of scalar dispersion for markers released from the channel walls in case of Poiseuille channel flow, namely, zone 1, a region close to the wall where the molecular diffusion dominates, zone 2, an

intermediate region where there is an interaction between molecular and turbulent diffusion and finally zone 3, a region where turbulent diffusion dominates. So, comparing two cases of *Pr,* such as *Pr* = 0.1 and 50, for markers released at the channel walls or the viscous subregion, the markers with *Pr* = 0.1 spend less time in zone 1 and spend the majority of their time in zone 3. Because molecular diffusion steps are very small for *Pr* = 50 markers, they spend a large amount of time in zone 1, in the molecular diffusion dominated region of the channel, before moving to zone 2 and then 3. Now, the only situation in our study which can be compared to markers released close to the wall is the case of forwards dispersion of markers moving away from the viscous subregion. In that case alone, one finds that the differences between the forwards and backwards relative dispersion are lower for higher *Pr* in agreement with the fact that the higher *Pr* markers spend a lot of time in the viscous subregion before dispersing into different regions of the channel. In the other regions of the channel, since the higher *Pr* markers are already in the turbulence-dominated regimes of the flow, they diffuse faster than the lower *Pr* markers causing increased differences with increased *Pr*.

5.2.2 Plane Couette flow

In this type of flow, the channel walls move relative to each other. This results in a constant stress region, which extends from the edge of the viscous sublayer of the bottom wall to the edge of the viscous sublayer of the top wall, nearly a distance of 220 wall units, similar to the logarithmic region of the Poiseuille channel flow. Thus, this type of flow, which has a very well established logarithmic region and different types of flow structures, compared to Poiseuille channel flow, provides us with a different velocity structure to analyze the differences between forwards and backwards relative

dispersion characteristics. It is important in this context to note that these two flow configurations are not as similar in structure as one might imagine, but are in fact two different types of flow, where the Poiseuille flow is driven by pressure gradient while the plane Couette flow is driven by shear stress due to the motion of the channel walls. Any occurrence of common behavior of relative turbulent dispersion between the Poiseuille channel and plane Couette flow cases will, thus, indicate a universal behavior. The differences in the mean squared forwards and backwards relative displacement, which in turn indicate the rates of dispersion, for the case of viscous sub-layer, the transition region, the logarithmic region and the center of the channel, are presented in Figures 5.11(a), (b), (c) and (d), respectively. The center of the channel and the logarithmic region in the case of plane Couette flow are the same, since the movement of the wall produces an extensive constant stress region, which extends from the transition region of one wall to the other, going through the center of the channel. Hence, the near-isotropic region in the center of the Poiseuille channel is not replicated in plane Couette flow. It is seen that forwards relative dispersion proceeds at a faster rate in the logarithmic region and the center of the channel. In the viscous sublayer and the transition region there is a reversal of this trend with the backwards relative dispersion showing faster rates, on an average, compared to forwards relative dispersion. Since the *Re* is smaller compared to the Poiseuille channel flow case, the values seem to be noisier.

The trend of the skewness plot seems very similar to that of the Poiseuille channel flow, however, the magnitude of the skewness is smaller compared to the Poiseuille flow environment (see Figure 5.12). The marker pair separation distribution

is plotted for the case of viscous sublayer, the transition region, the logarithmic region and the center of the channel in Figures 5.13, 5.14, 5.15 and 5.16, respectively, with data for $Pr = 0.1$ as part (a) and $Pr = 10$ as part (b). It can be seen that in the case of the logarithmic region and the center of the channel, there are more marker pairs with large separation distance in forwards relative dispersion, while there are more marker pairs with smaller separation distance in the case of backwards relative dispersion. This is in agreement with the results that the forwards relative dispersion is faster. This trend is reversed in the cases of the viscous sublayer and the transition region, which show opposite dispersion rate trends compared to the other two regions.

Increase in Pr results in increased differences for the logarithmic region and the center of the channel, as seen on Figures 5.15 and 5.16, and decreased differences for the viscous sub-layer and the transition regions. The marker separation pdfs show similar trends to those observed in Poiseuille channel flow in cases of different Pr, with the $Pr = 0.1$ showing higher large separation frequency and the $Pr = 10$ showing higher small separation frequency. The frequency of small separation also decreases with increase in the distance from the Couette walls.

To interpret these results, as with the case of Poiseuille channel flow, the velocity differences between the marker pairs are studied first. In Figures 5.17, 5.18, 5.19 and 5.20, with data for $Pr = 0.1$ shown in part (a) and $Pr = 10$ shown in part (b) of the figures, we plot the marker distribution of the velocity differences of the marker pairs in different regions of the channel. The logarithmic region and the center of the channel (see Figures 5.19, 5.20) show more pairs with large velocity differences in the case of forwards relative dispersion, consistent with the results of faster forwards

relative dispersion in these regions of the plane Couette flow. The transition region and the viscous sub-layer, however, show more marker pairs with large velocity differences in the case of forwards relative dispersion at some times and at other times show large velocity differences in the case of backwards relative dispersion. At first glance these results seem to be inconsistent with the analysis of velocity differences carried out for the Poiseuille channel flow case. This different behavior can be understood more clearly by considering the root mean squared (rms) y-velocity fluctuation profile in the case of plane Couette flow as a function of the distance from the channel wall, shown in Figure 2 of Papavassiliou and Hanratty [150], and comparing it with that of Poiseuille flow shown in Figure 4 in Moser et al. [30]. This comparison shows that, firstly, the profiles of the rms y-velocity fluctuations are very different in the cases of Poiseuille and plane Couette flows, with Poiseuille flow showing a local maximum of the y-velocity fluctuations closer to the channel walls (in the viscous wall region), while this maximum occurs at the center of the channel for the plane Couette flow. Also, another important observation is that the gradient of the rms y-velocity fluctuation at the center of the channel for Poiseuille flow is non-zero, while it is very close to zero for the plane Couette flow. In fact, for plane Couette flow, the rms velocity fluctuations are almost constant between $y^+ \approx 50$ and $y^+ \approx 250$ at the other half of the channel. Now, relating this observation back to the values of the velocity differences for the forwards and backwards relative dispersion, one can imagine a marker pair undergoing forwards dispersion. Assuming that one of the markers is close to the center and the other marker is at the edge of the viscous wall layer, they have very small velocity differences, due to near zero gradients, but their net separation (and, thus, dispersion) is large. This shows

that the one-on-one correspondence between the differences in velocity fluctuation and the dispersion rates, which existed in the Poiseuille channel flow case, no longer exists in the case of plane Couette flow. Hence, calling on the velocity difference distribution might not help in outlining the differences between the forwards and backwards relative dispersion in plane Couette flow.

The next property to help explain the result is the skewness of the pdf of the *y*-velocity fluctuations. From this, and consistent with the analysis of Poiseuille flow, it is expected that the forwards relative dispersion should show increased rates compared to backwards relative dispersion, as the former type of markers start moving towards regions of increasing differences in velocity pdf compared to the converging markers of backwards relative dispersion, which experience increasingly similar velocity fluctuations as they move towards their common destination. While this analysis works well for the logarithmic region and the center region of the Couette flow channel, it does not apply in the viscous subregion or the transition region. One needs to also consider the coherent structures in Couette flow to explain the near-wall behavior. It has been found that coherent structures in plane Couette flow are different than those of Poiseuille channel flow. Turbulence producing velocity structures existing in plane Couette flow are very large and can extend across the channel from one wall to the other wall [150, 166]. To understand the effect of the large-scale coherent structures in scalar dispersion for plane Couette flow and how it is different from the case of Poiseuille channel flow, an analysis is performed to compare the effect of these structures on the scales of the turbulence close to the channel walls. In Figure 5.21 we plot the average displacement of the mean location of the center of mass of the marker

pairs for forwards and backwards relative dispersion for two *Pr*, *Pr* = 0.1 and 6 in case of Poiseuille flow and *Pr* = 0.1 and 10 in the case of plane Couette flow, as a function of time. The backwards relative dispersion is represented with negative time, indicating the fact that the dispersion occurs prior to the markers arriving at a location. The viscous sublayer is presented in Figure 4.21(a) and the transition region in Figure 5.21(b). The inset numbers in Figure 5.21(a) indicate the corresponding Lagrangian material timescale for that particular case. It is important to understand that the material timescale is correlated with the time a marker spent following a particular flow structure and is related to the distance that the marker traversed with that particular eddy. Obvious from Figure 5.21 are the following facts: (i) For a common *Pr* considered, for both forwards and backwards relative dispersion, the plane Couette flow has higher mean displacements in the vertical directions, indicating the larger and more dominant vortex structures in this particular type of flow; (ii) though not clearly observable, the mean displacement for backwards relative dispersion for higher *Pr*, with $\overline{\Delta y}$ = 76.03 at t^+ = 300, is nearly 7% higher than for forwards relative dispersion, with $\overline{\Delta y}$ = 71.30 at t^+ = 300; and (iii) the Lagrangian material timescale for the backwards relative dispersion is comparatively higher than the forwards relative dispersion for plane Couette flow, while very small differences are found for Poiseuille channel flow. These three results in combination show that the plane Couette flow in effect has large vortical structures extending through the channel, sweeping markers to the near-wall regions. Also, the backwards dispersing markers moving towards the near-wall regions ride on the same velocity structure for a longer duration, hence moving themselves from larger normal distances towards the channel walls compared to the forwards dispersing markers. If

one imagines velocity structures extending through the channel, they would have a two-fold effect: they would help carry forwards dispersing markers away from the center and the logarithmic regions, while at the same time they would be moving backwards dispersing markers towards the channel walls. This is reflected in the rates of forwards and backwards relative dispersion observed for plane Couette flow. Thus, considering coherent flow structures helps in the interpretation of the details of the differences between forwards and backwards relative dispersion.

For both Poiseuille channel and plane Couette flow cases, a comparable number of marker pairs are correlated, but the difference between the forwards and backwards mean squared relative displacement in the plane Couette flow seems to be smaller and more noisier compared to the Poiseuille channel flow. The contributing factors behind these differences appear to be the smaller *Re* in the case of plane Couette flow, and also the smaller skewness values experienced by the markers in plane Couette flow case, causing less asymmetry of the vertical velocity fluctuation pdf compared to the Poiseuille channel flow. In addition, a larger *Re* means larger range of length scales and a wider inertial subrange. At a higher *Re* than the one used here, one would expect even larger differences in the rates of forwards and backwards relative dispersion.

5.3 Conclusions

Computational studies of turbulent relative dispersion have been carried out using a DNS/LST technique for Poiseuille channel and plane Couette flows. The Reynolds number of the turbulent Poiseuille flow is twice of that reported in previous single-particle dispersion studies. Turbulent relative dispersion calculations reveal differences in the values of mean squared relative displacement between forwards and

backwards relative dispersion in the direction normal to the channel walls. The viscous sub-layer, the transition region and the logarithmic region show higher rates of forwards relative dispersion. However, the center of the Poiseuille channel, which is the area that resembles the case of isotropic turbulence the most, shows higher rates of backwards relative dispersion, consistent with prior literature results for isotropic turbulence. The distribution of marker pair vertical velocity difference, the skewness of the pdf of vertical velocity fluctuations, and the nature of the coherent structures existing in such flows help in identifying the underlying reasons behind these differences in the rates of forwards and backwards relative dispersion. In the viscous sub-layer, the transition region and the logarithmic region, the forwards dispersing markers experience different skewness as they disperse in time, while the backwards dispersing markers that move towards a particular region move towards similar velocity structures and experience more and more similar velocity skewness as they approach their common destination. This along with the fact that there are higher number of markers with larger velocity differences and the behavior of the coherent structures that transport the marker pairs from the near-wall regions to the edge of the logarithmic region cause the result of higher number of marker pairs with larger vertical separation in the case of forwards relative dispersion. The center of the channel presents a unique case where the markers dispersing forwards initially experience symmetric pdfs of velocity distributions due to the zero skewness. Also, owing to the absence of coherent structures at the center of the Poiseuille channel flow, and the help that the backwards dispersing markers moving towards the center of the channel receive from the coherent structures that extend from the channel walls, the results show a higher number of marker pairs with large

separation in the case of backwards relative dispersion for the channel center. The rates of forwards relative dispersion increase with increasing *Pr* in the transition and logarithmic regions, while they decrease with increasing *Pr* in the viscous sub-layer. The rate of backwards relative dispersion increases with increasing *Pr* at the center of the channel.

The rates and behavior of dispersion are different in the case of plane Couette flow, owing to the different nature of that flow compared to the Poiseuille channel flow. The forwards relative dispersion proceeds at a faster pace in the case of logarithmic region and the center of the channel in plane Couette flow. The backwards relative dispersion, however, occurs at faster rates in the viscous sub-layer and transition regions. The marker pair velocity differences, which helped in explaining the differences for Poiseuille flow, do not do justice in explaining the results for the plane Couette flow. This is attributed to the fact that the gradient of the vertical velocity fluctuations in this case is very small from the edge of the viscous wall layer from the lower to the upper part of the channel. The asymmetry of the pdf of the vertical velocity fluctuations having small skewness values because of the small *Re* simulated also does not help in explaining the results observed. It is the coherent structures of the velocity, in the case of plane Couette flow, that help in understanding the differences between forwards and backwards relative dispersion. The large scale structures extending through the outer region of the channel to the channel walls help in transporting the forwards dispersing markers for the center of the channel and the logarithmic region, while aiding in the relative dispersion of the backwards dispersing markers for the transition and the viscous subregion. Finally, an increase in *Pr* causes increased

differences between the forwards and backwards relative dispersion. Results from the two different *Re* used in the study indicate that a higher *Re* flow exhibits more consistent trends and accelerated rates of turbulent relative dispersion mainly due to a larger range of length scales.

To summarize, the following important points result from the study:

(i) The imposition of essentially initial conditions for forwards dispersion and final conditions for backwards dispersion on the marker trajectories affects the rate of dispersion experienced by the markers in the case of anisotropic turbulent flow.

(ii) This is true irrespective of the type of flow, the *Re* and the *Pr* of the flow.

(iii) The results show that in Poiseuille flow the pdfs of the vertical velocity fluctuation is sufficient to provide valuable insights into the rate of dispersion, while they fail in cases like the outer region in plane Couette flow, where there is a zero gradient in the rms of the vertical velocity fluctuations.

(iv) The skewness of the pdf of the vertical velocity fluctuations in combination with the nature of coherent structures traipsing the flow, irrespective of the type of flow, help in providing an interpretation of the behavior of the dispersion.

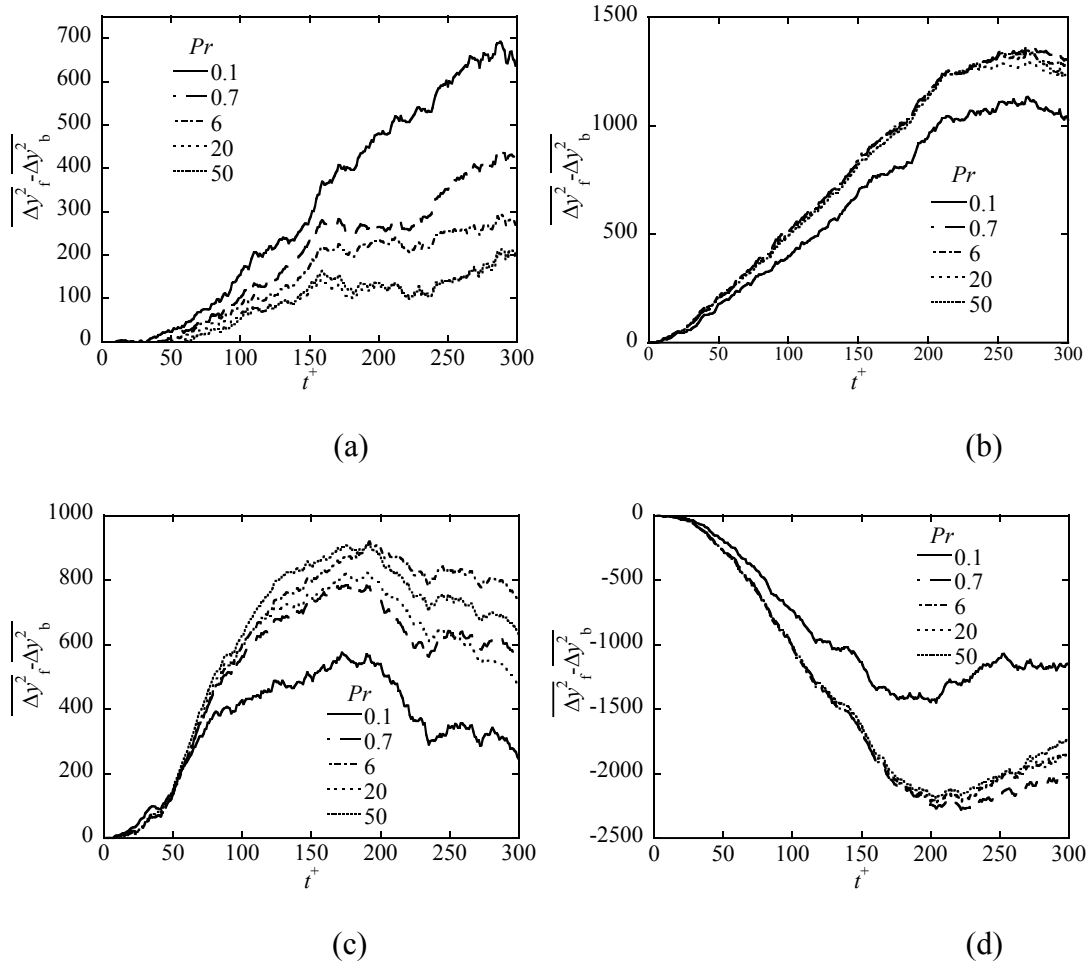

Figure 5.1: Difference between mean squared forwards and backwards relative displacement in the normal direction as a function of time for different Prandtl numbers, in cases of markers captured in different regions of Poiseuille channel flow (a) viscous sub-layer ($y^+ = 5$ and 595); (b) transition region ($y^+ = 60$ and 540); (c) logarithmic region ($y^+ = 120$ and 480): (d) center of the channel ($y^+ = 300$).

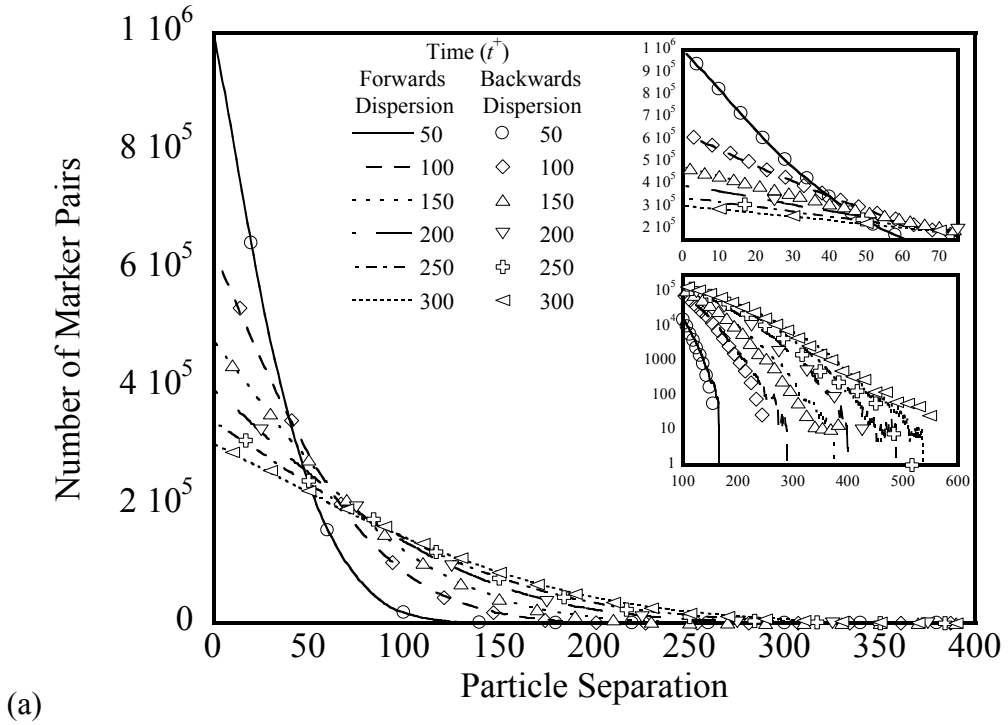

(a)

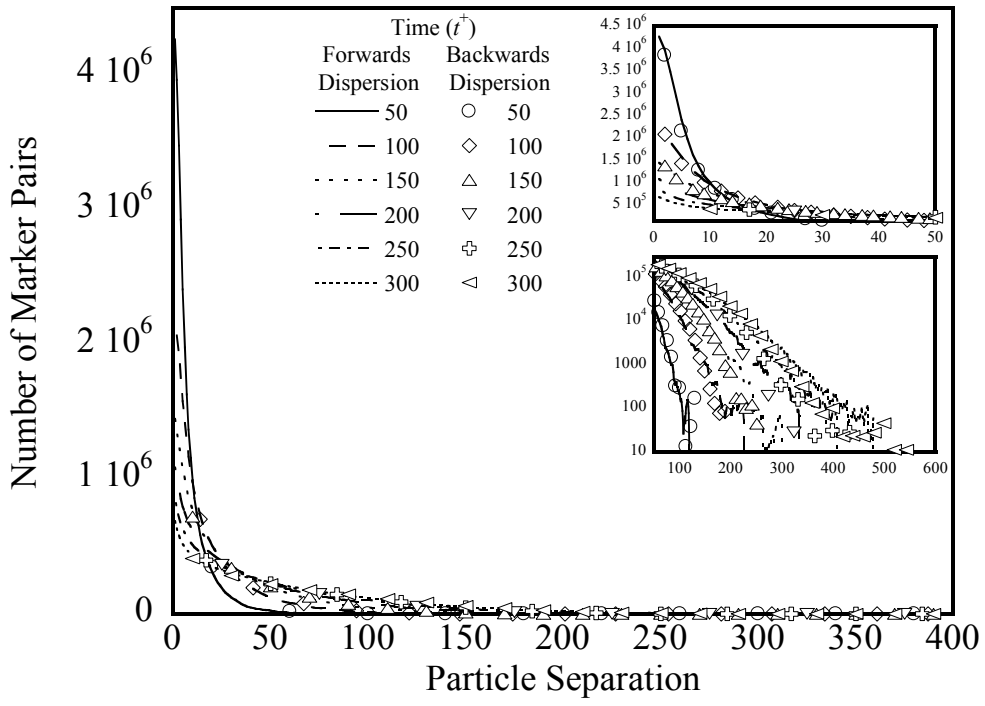

(b)

Figure 5.2: Marker pair distribution based on the marker pair vertical separation, in the case of forwards and backwards relative dispersion, for those markers captured in the viscous sub-layer, plotted at different instantaneous time of dispersion in Poiseuille channel flow for different Prandtl numbers: (a) Pr = 0.1; (b) Pr = 50.

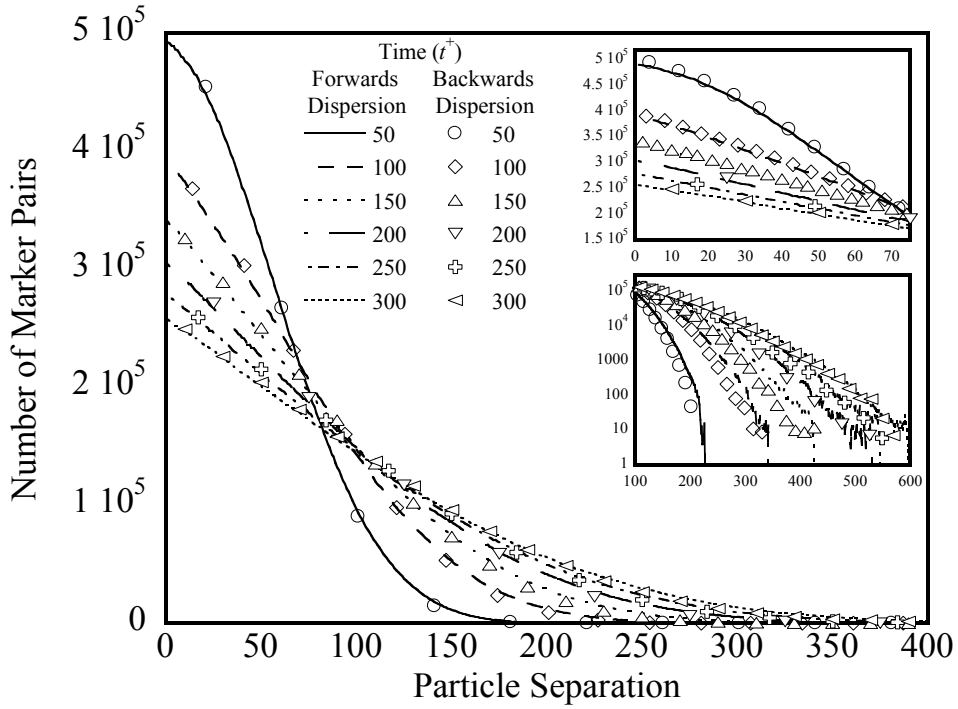

(a)

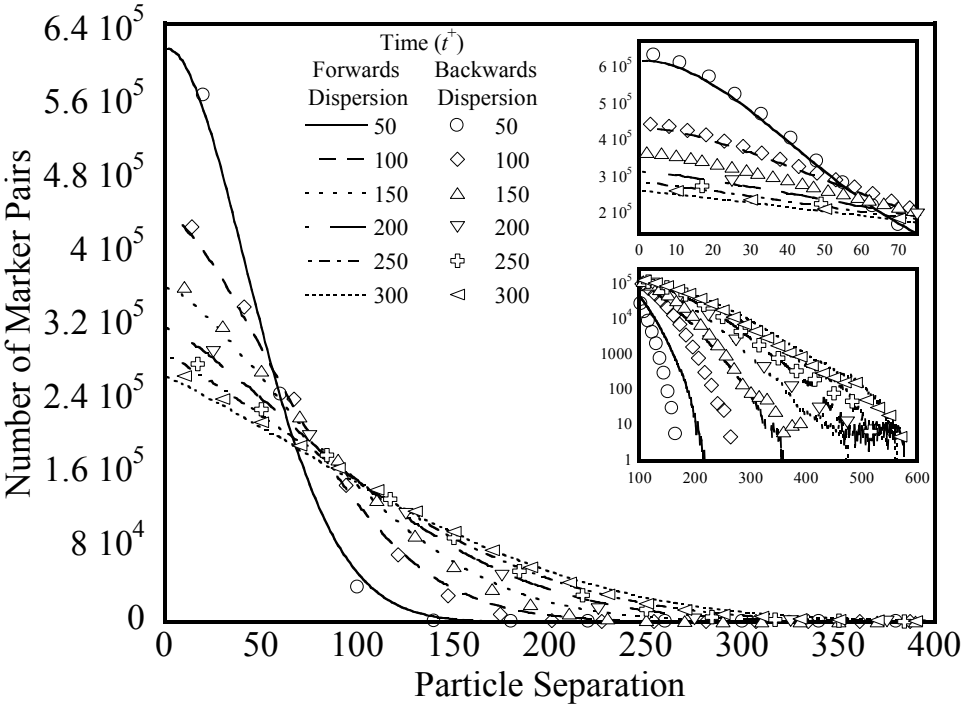

(b)

Figure 5.3: Marker pair distribution based on the marker pair vertical separation, in the case of forwards and backwards relative dispersion, for those markers captured in the transition region, plotted at different instantaneous time of dispersion in Poiseuille channel flow for different Prandtl numbers: (a) $Pr = 0.1$; (b) $Pr = 50$.

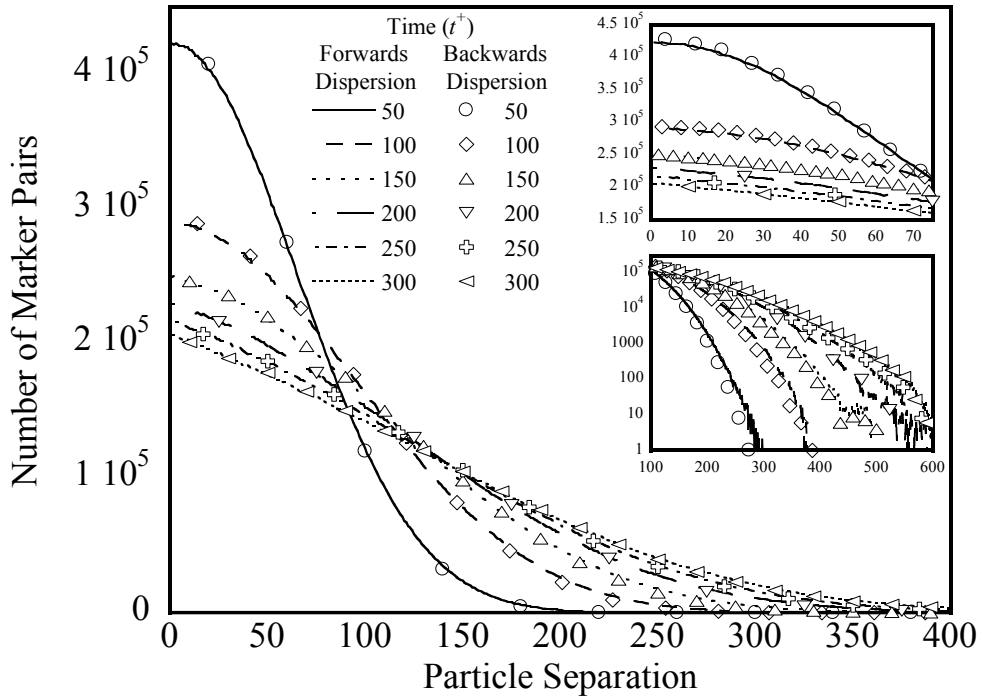

(a)

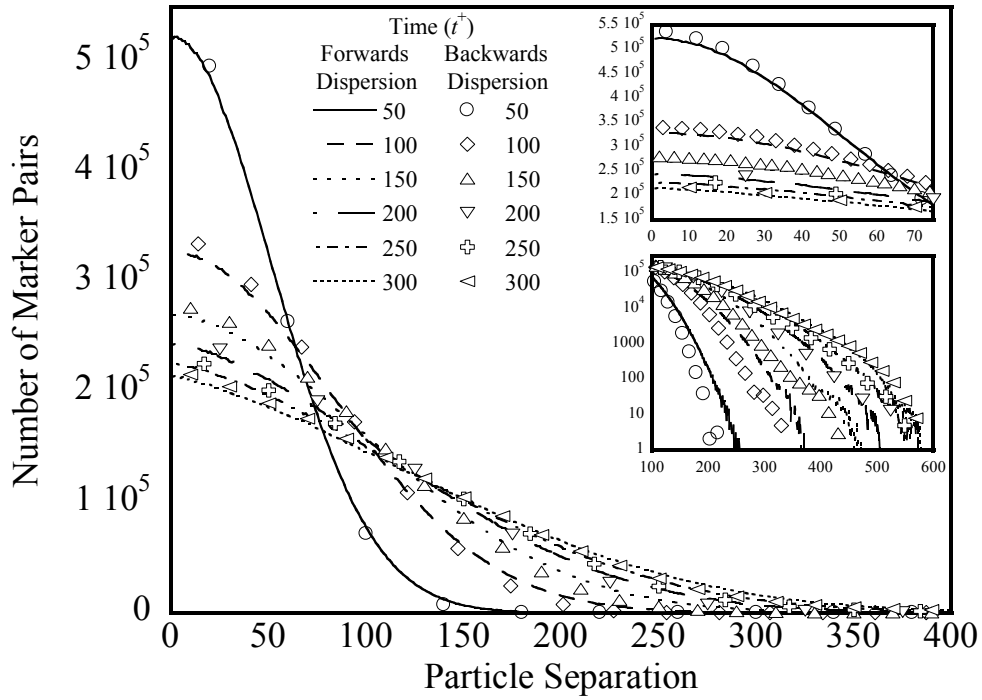

(b)

Figure 5.4: Marker pair distribution based on the marker pair vertical separation, in the case of forwards and backwards relative dispersion, for those markers captured in the logarithmic region, plotted at different instantaneous time of dispersion in Poiseuille channel flow for different Prandtl numbers: (a) $Pr = 0.1$; (b) $Pr = 50$.

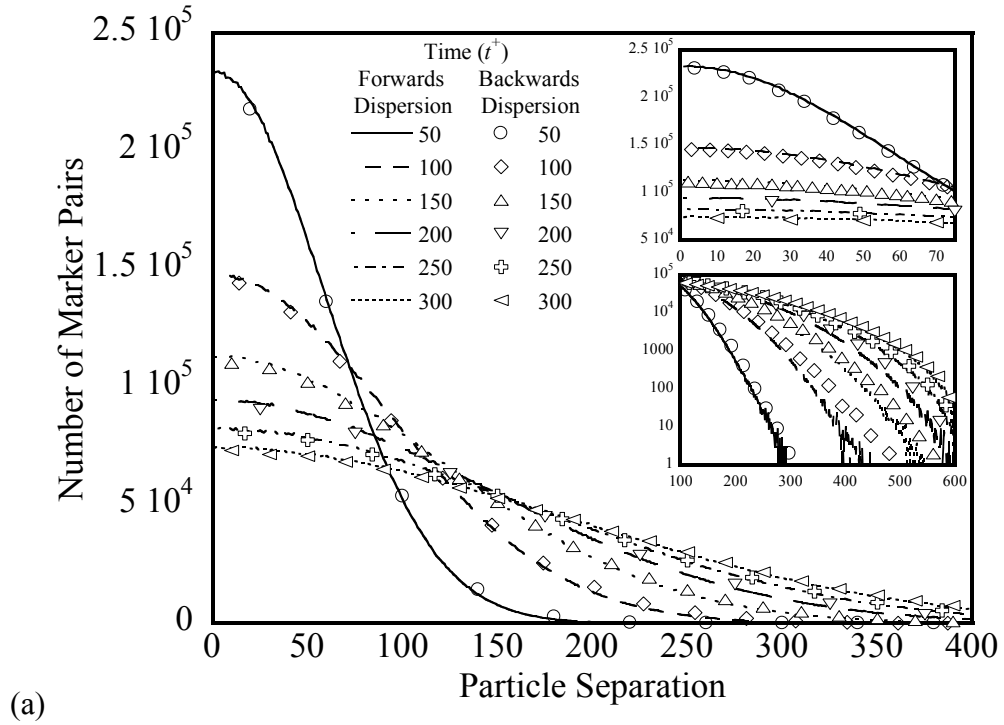

(a)

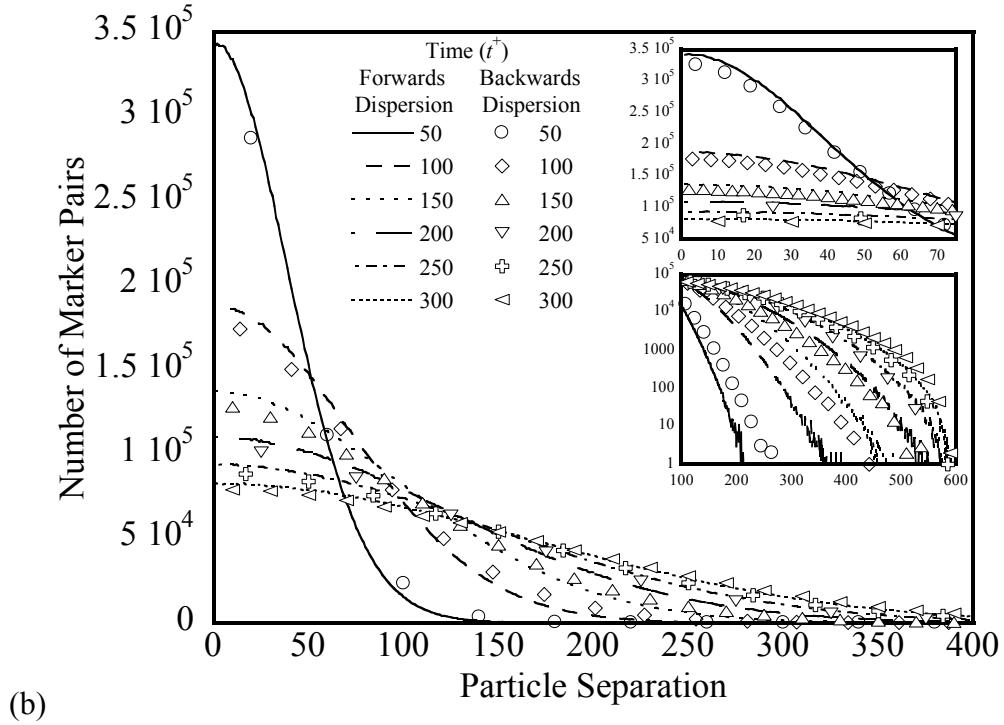

(b)

Figure 5.5: Marker pair distribution based on the marker pair vertical separation, in the case of forwards and backwards relative dispersion, for those markers captured in the center of the channel, plotted at different instantaneous time of dispersion in Poiseuille channel flow for different Prandtl numbers: (a) $Pr = 0.1$; (b) $Pr = 50$.

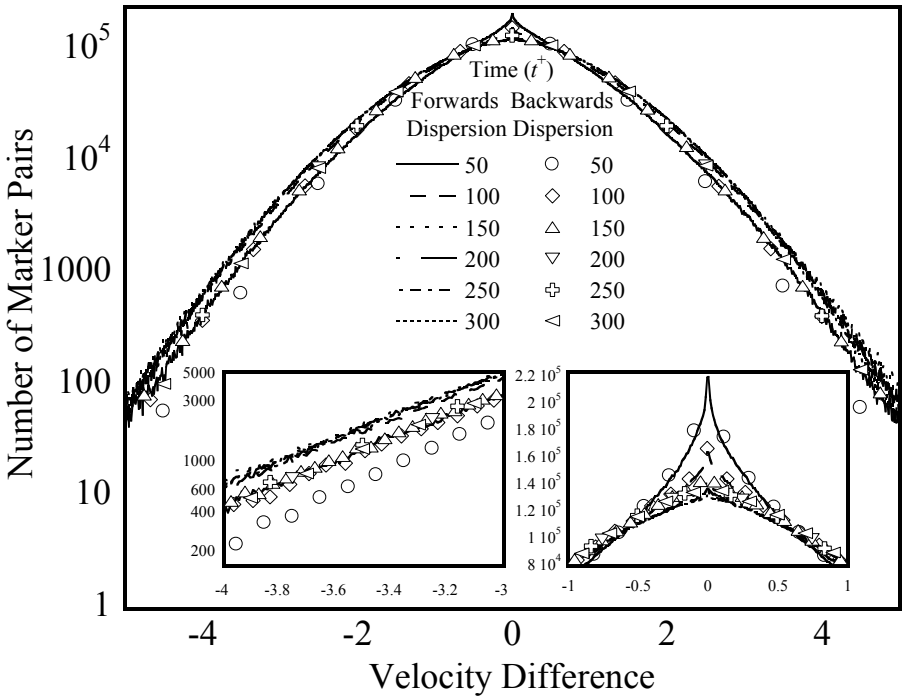

(a)

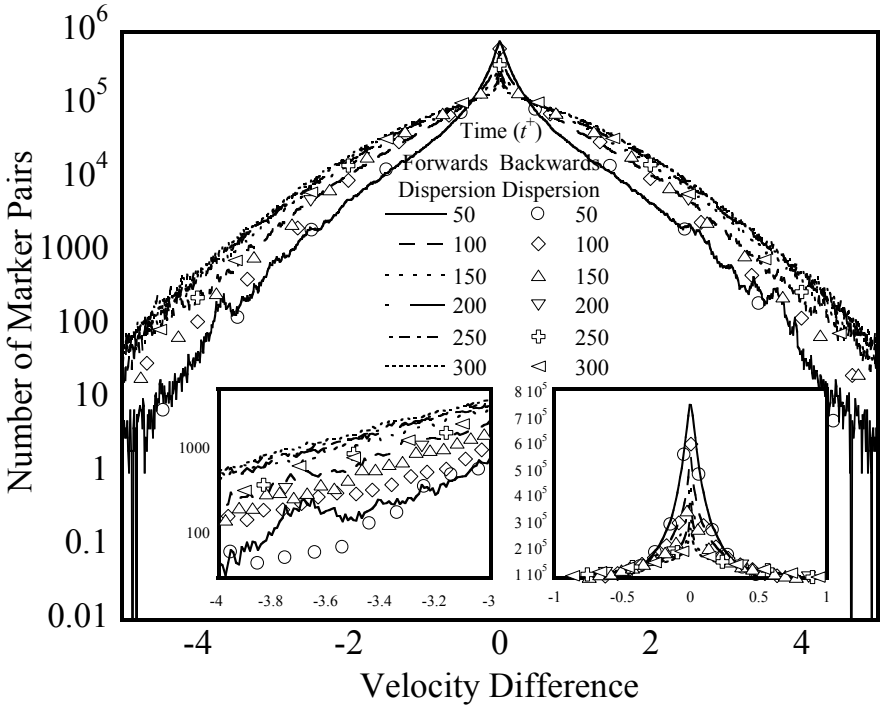

(b)

Figure 5.6: Marker pair distribution based on the vertical velocity difference of the marker pair, in the case of forwards and backwards relative dispersion, for those markers captured in the viscous sub-layer, plotted at different instantaneous times of dispersion in Poiseuille channel flow for different Prandtl numbers: (a) $Pr = 0.1$; (b) $Pr = 50$.

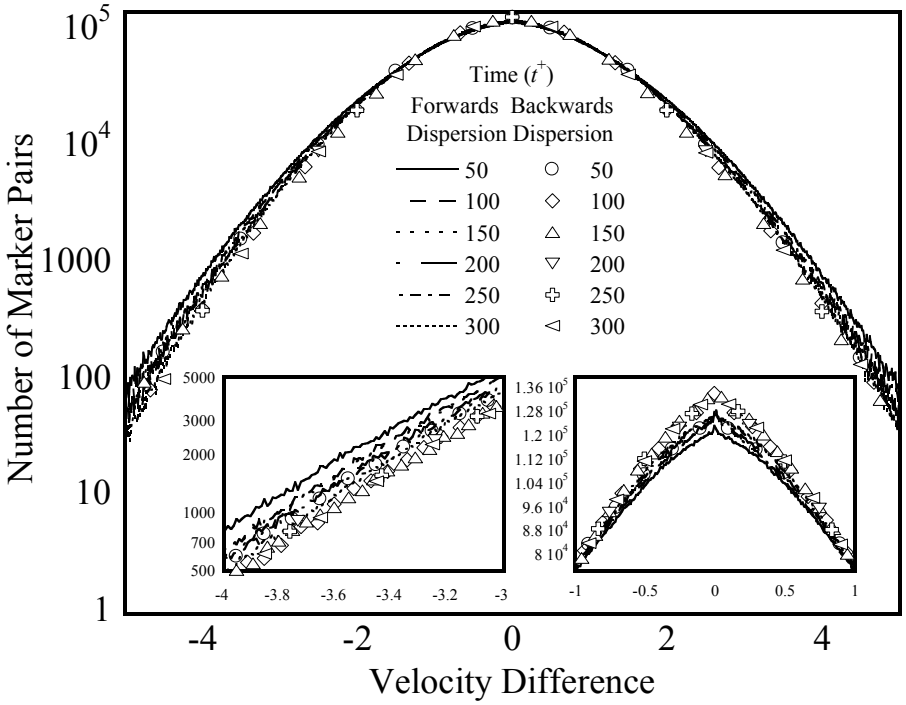

(a)

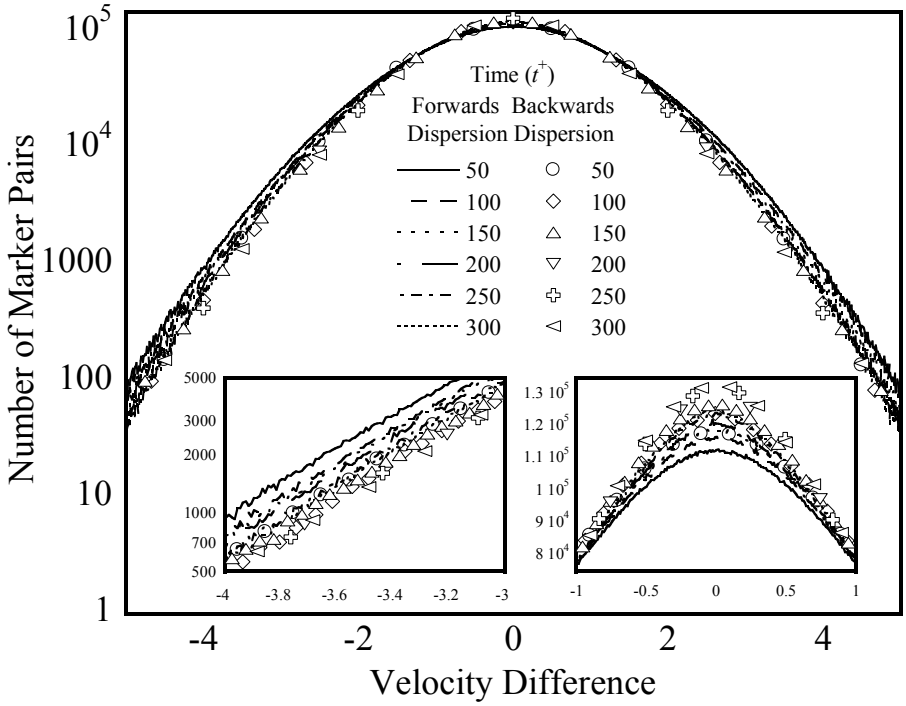

(b)

Figure 5.7: Marker pair distribution based on the vertical velocity difference of the marker pair, in the case of forwards and backwards relative dispersion, for those markers captured in the transition region, plotted at different instantaneous times of dispersion in Poiseuille channel flow for different Prandtl numbers: (a) $Pr = 0.1$; (b) $Pr = 50$.

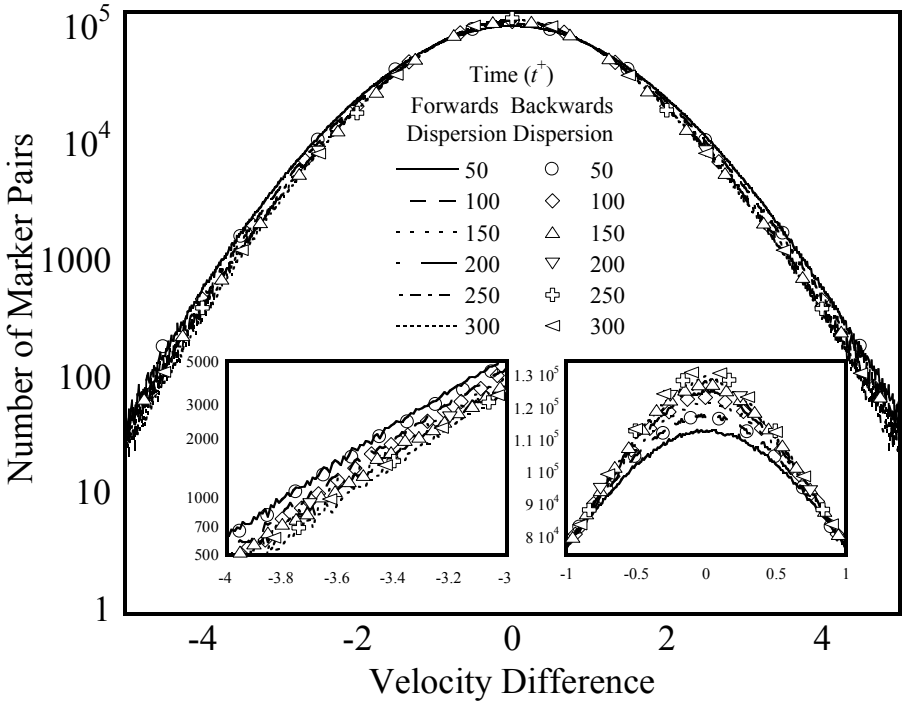

(a)

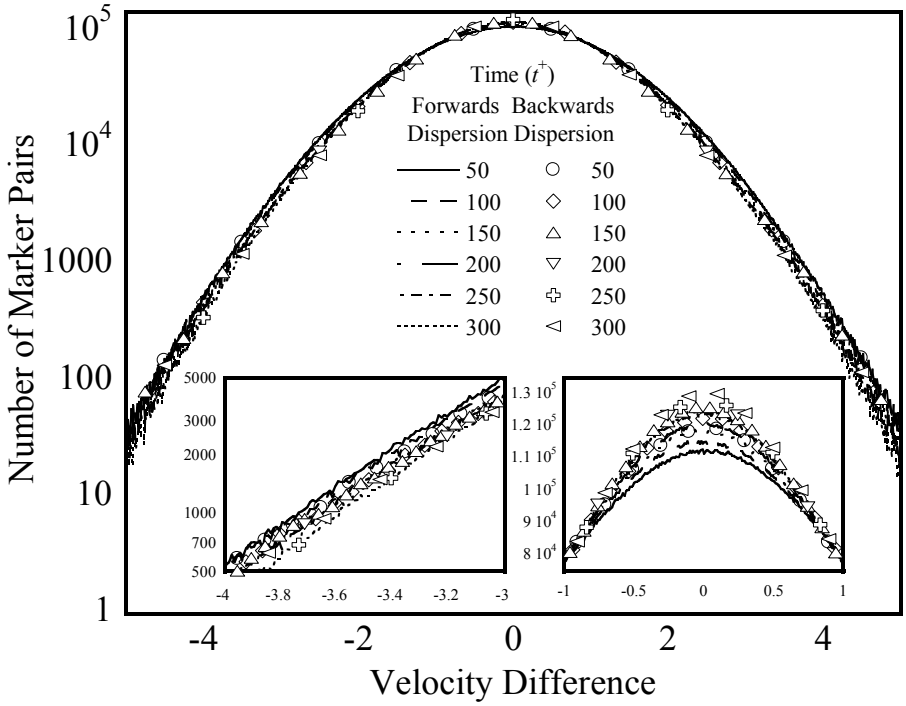

(b)

Figure 5.8: Marker pair distribution based on the vertical velocity difference of the marker pair, in the case of forwards and backwards relative dispersion, for those markers captured in the logarithmic region, plotted at different instantaneous times of dispersion in Poiseuille channel flow for different Prandtl numbers: (a) $Pr = 0.1$; (b) $Pr = 50$.

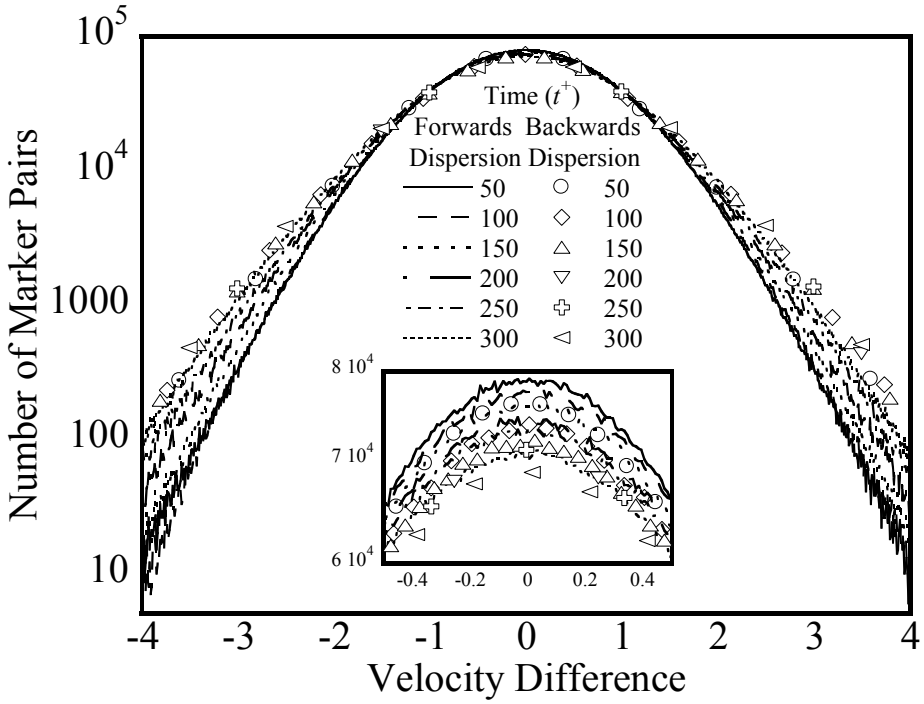

(a)

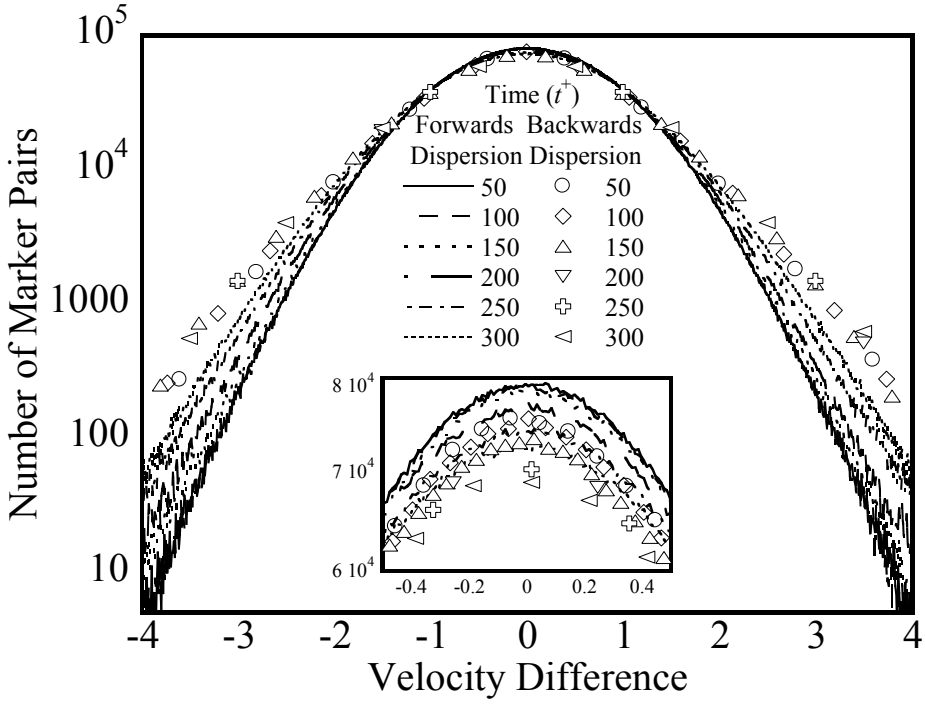

(b)

Figure 5.9: Marker pair distribution based on the vertical velocity difference of the marker pair, in the case of forwards and backwards relative dispersion, for those markers captured in the center of the channel, plotted at different instantaneous times of dispersion in Poiseuille channel flow for different Prandtl numbers: (a) $Pr = 0.1$; (b) $Pr = 50$.

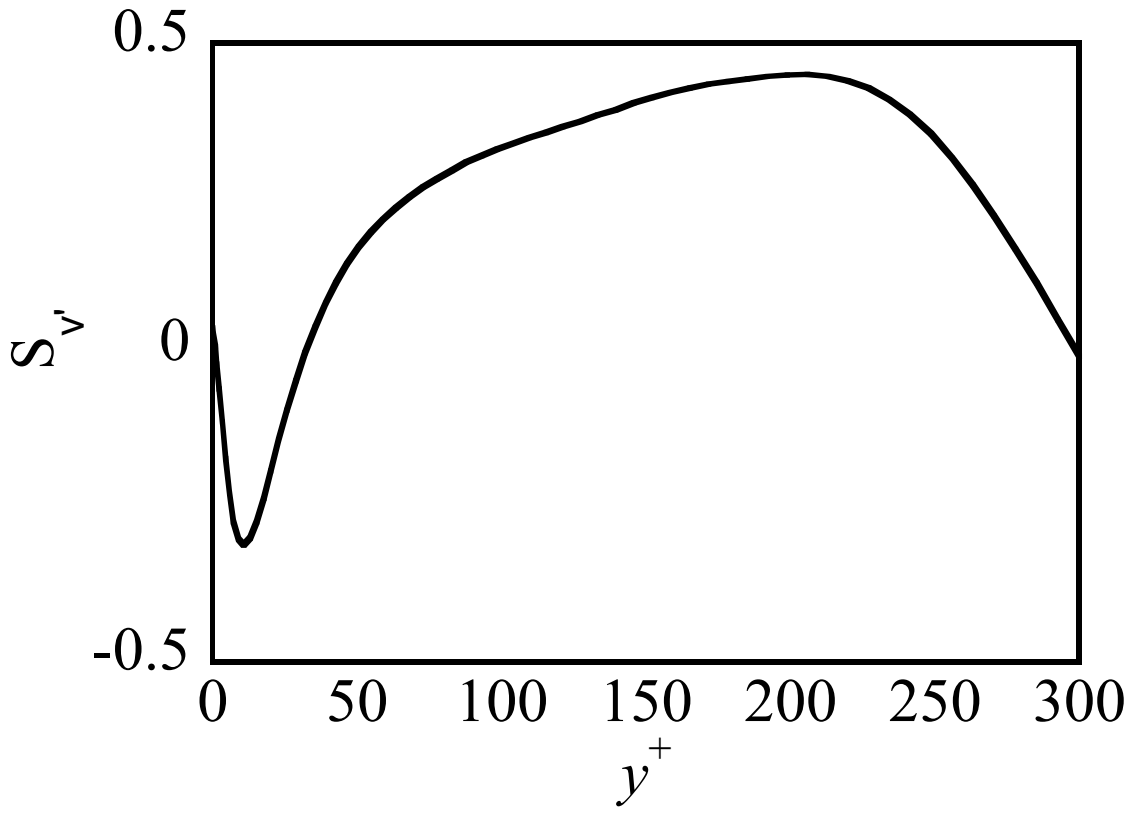

Figure 5.10: Skewness of the velocity fluctuations in the vertical direction as a function of the normal distance from the channel wall in the case of Poiseuille channel flow.

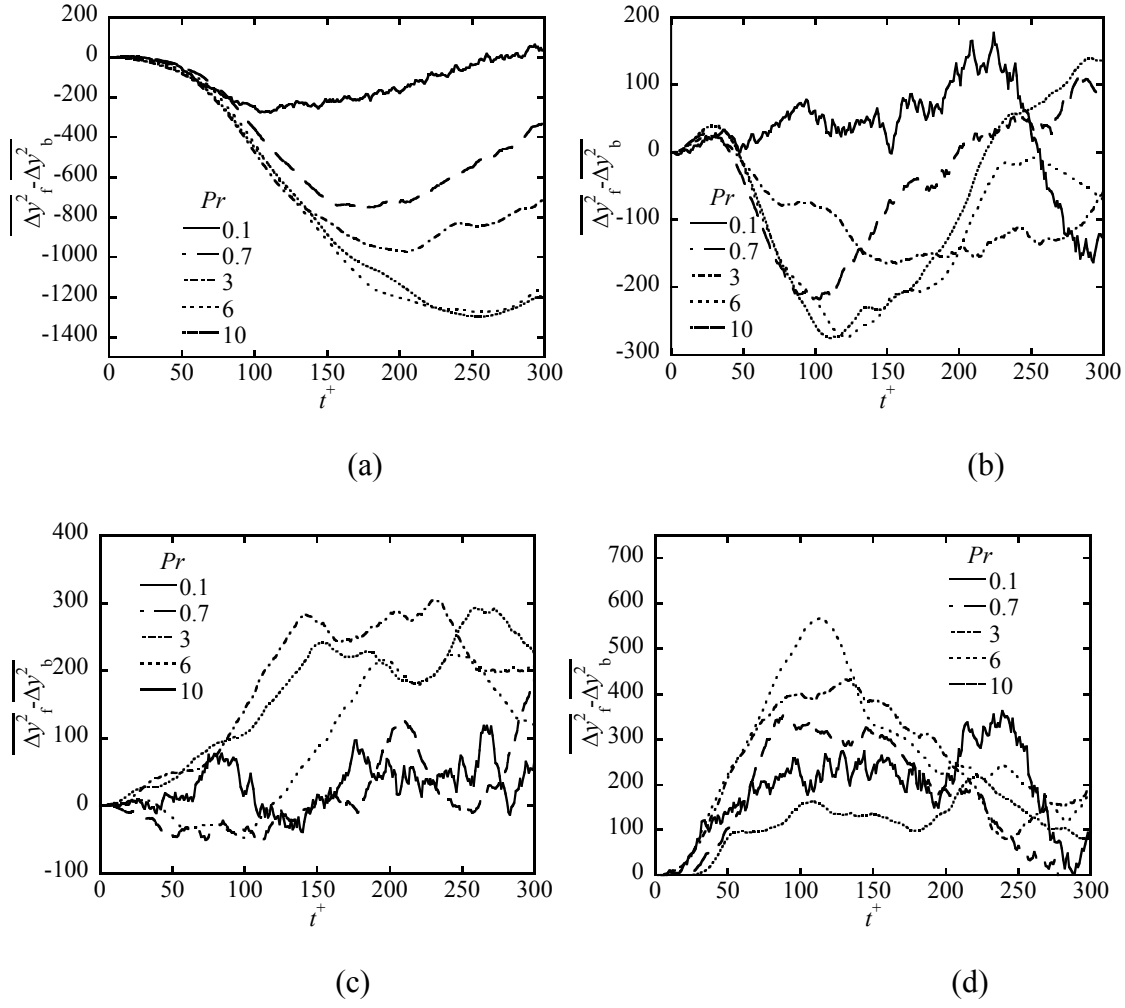

Figure 5.11: Difference between mean squared forwards and backwards relative displacement in the normal direction as a function of time for different Prandtl numbers, in cases of markers captured in different regions of plane Couette flow: (a) viscous sub-layer (y^+ = 5 and 295); (b) transition region (y^+ = 37 and 263); (c) logarithmic region (y^+ = 75 and 225): (d) center of the channel (y^+ = 150).

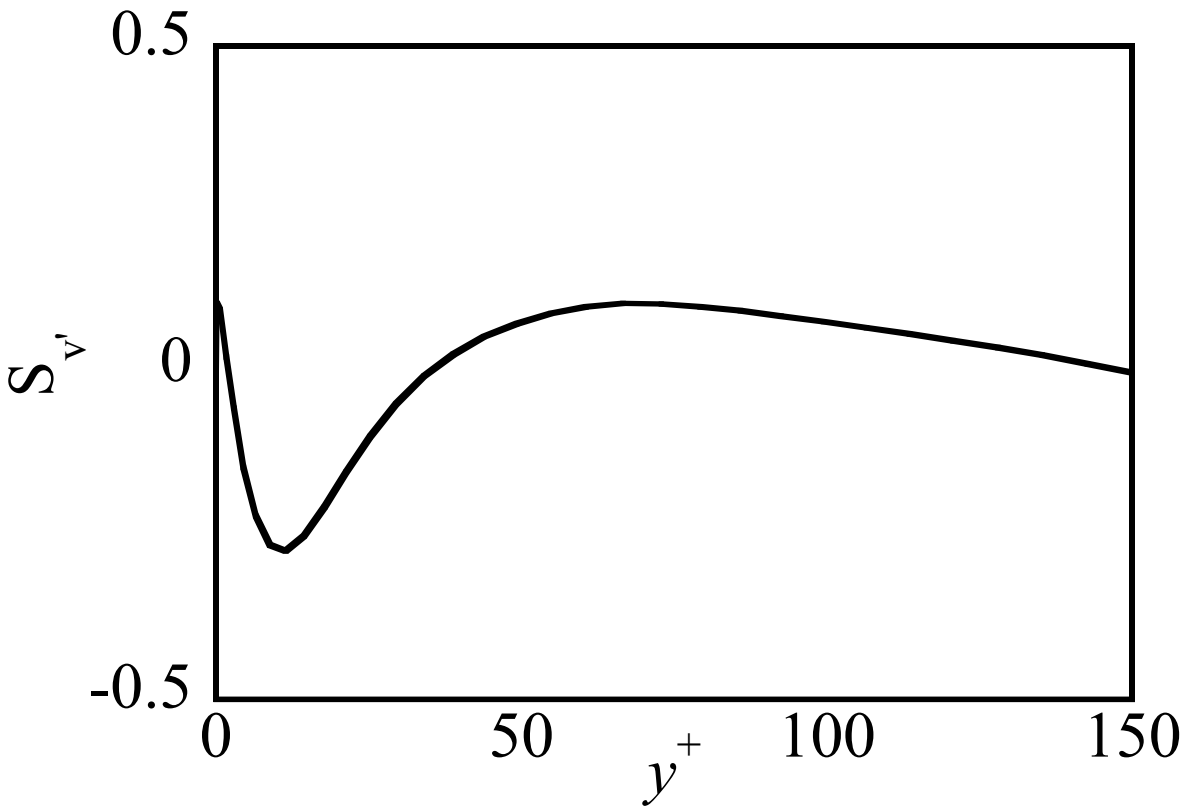

Figure 5.12: Skewness of the velocity fluctuations in the vertical direction as a function of the normal distance from the channel wall in the case of plane Couette flow.

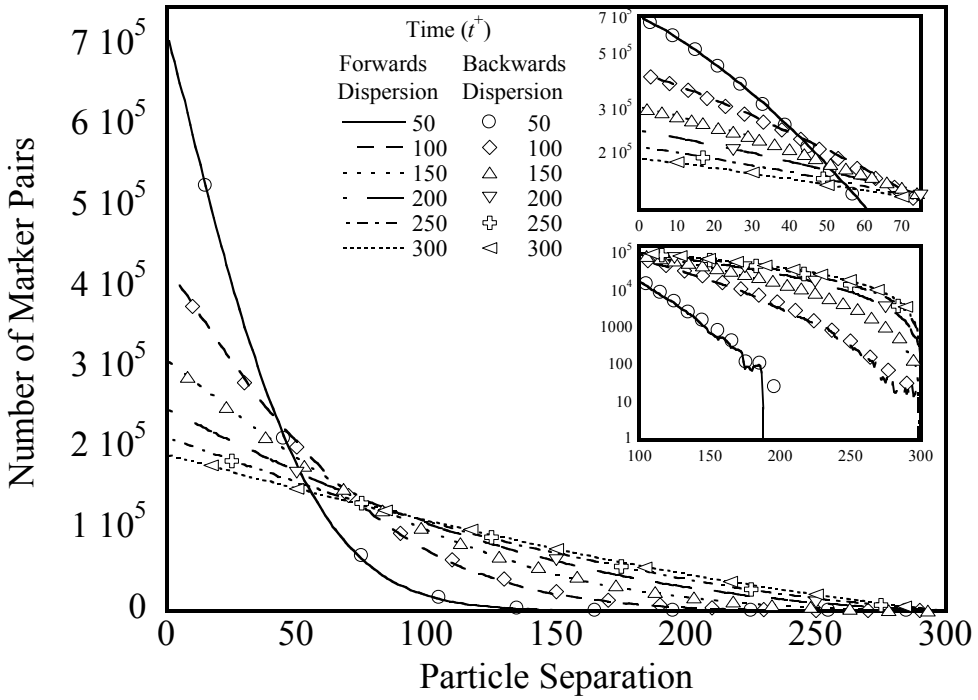

(a)

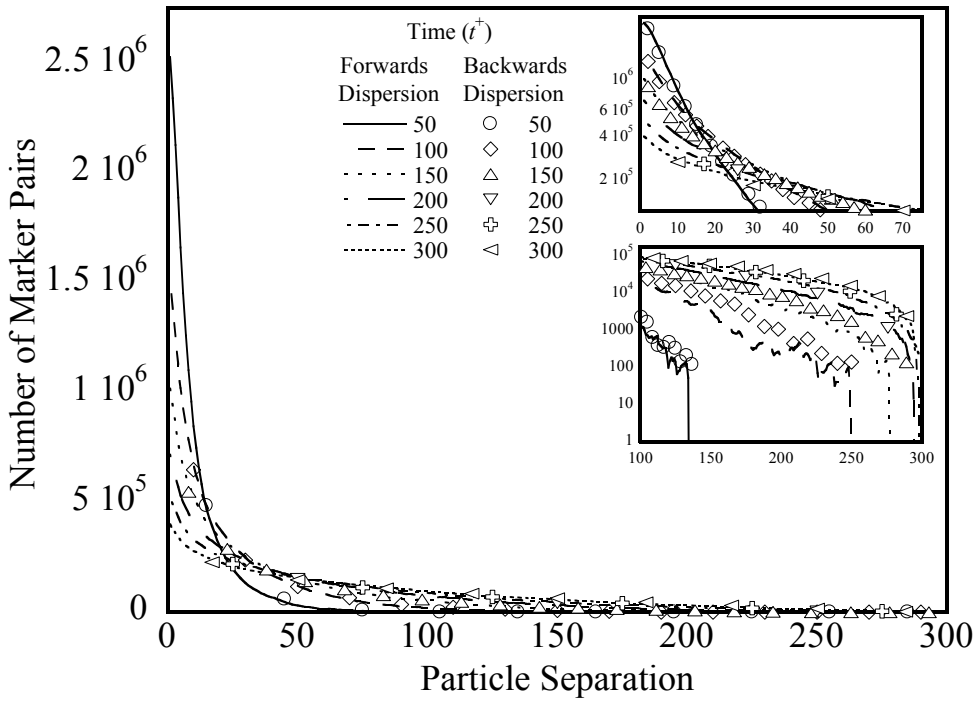

(b)

Figure 5.13: Marker pair distribution based on the marker pair vertical separation, in the case of forwards and backwards relative dispersion, for those markers captured in the viscous sub-layer, plotted at different instantaneous time of dispersion in plane Couette flow for different Prandtl numbers: (a) $Pr = 0.1$; (b) $Pr = 10$.

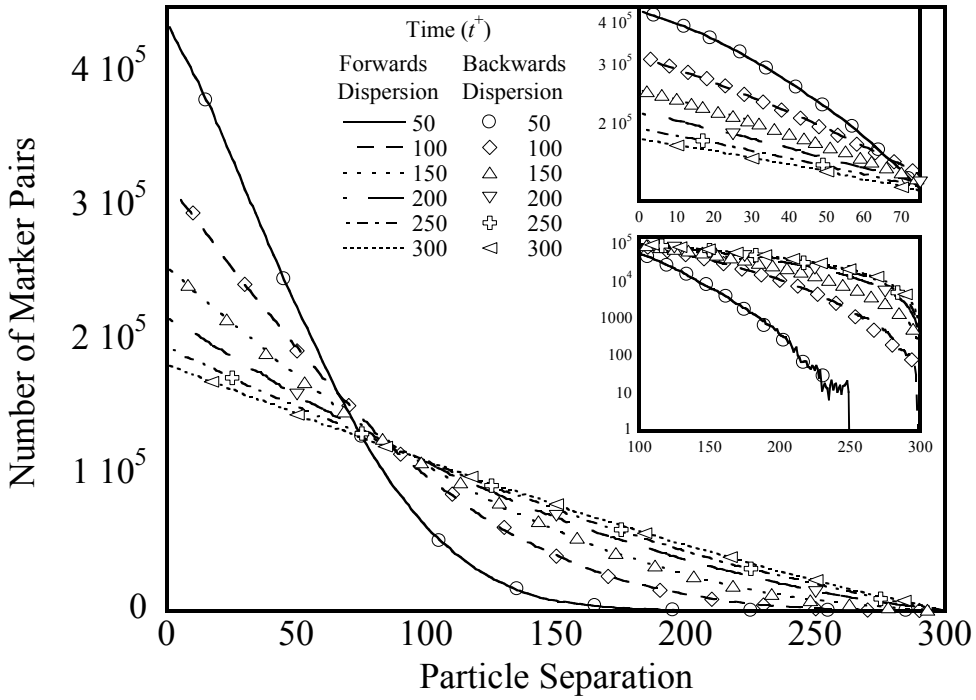

(a)

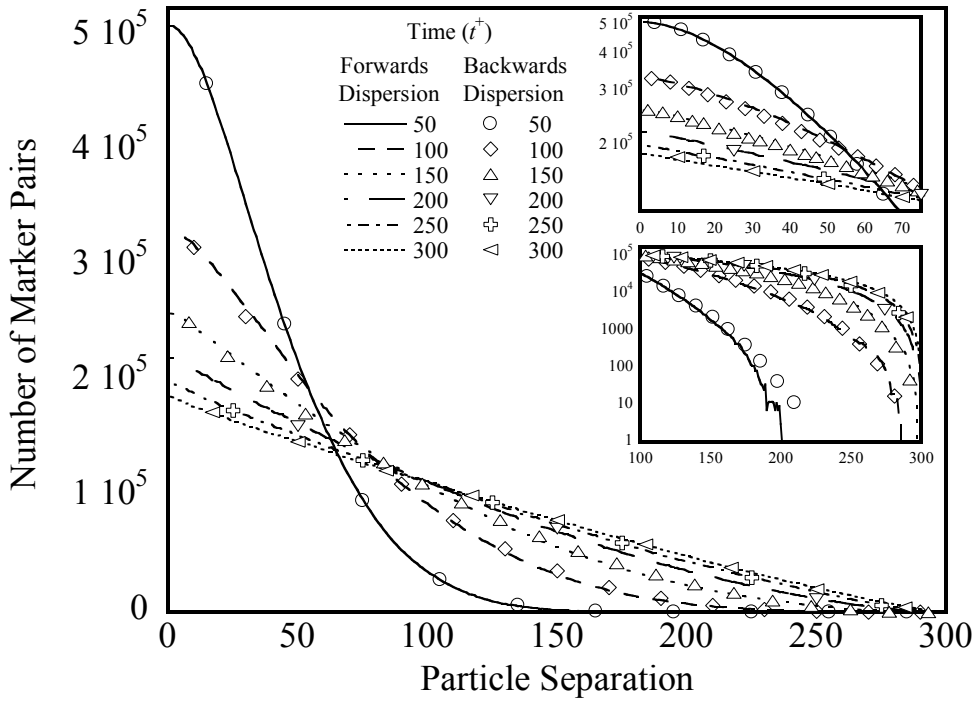

(b)

Figure 5.14: Marker pair distribution based on the marker pair vertical separation, in the case of forwards and backwards relative dispersion, for those markers captured in the transition region, plotted at different instantaneous time of dispersion in plane Couette flow for different Prandtl numbers: (a) $Pr = 0.1$; (b) $Pr = 10$.

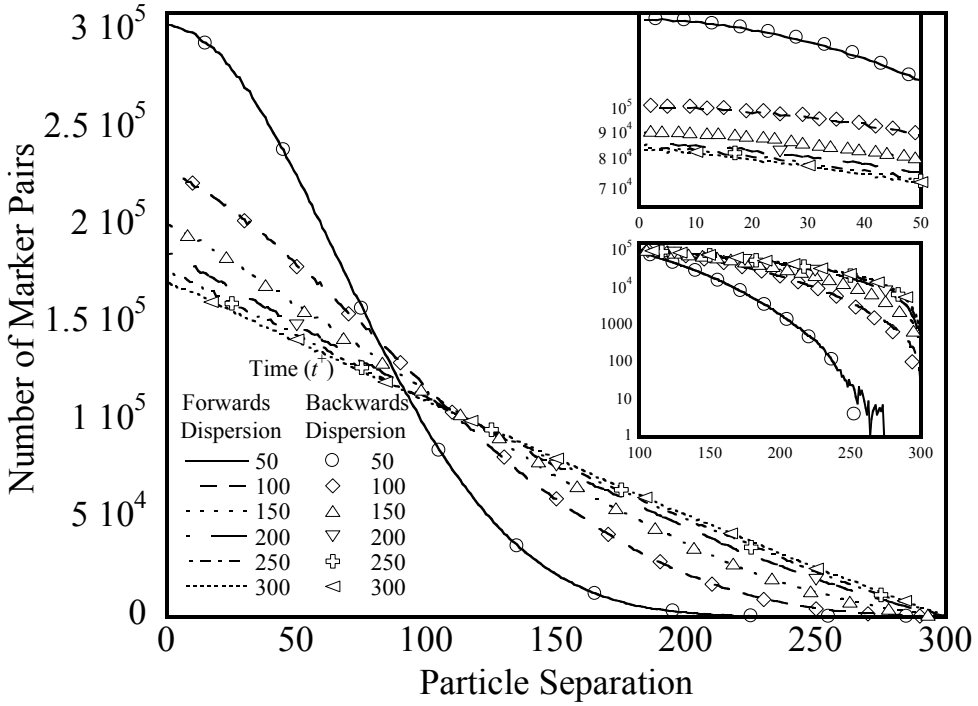

(a)

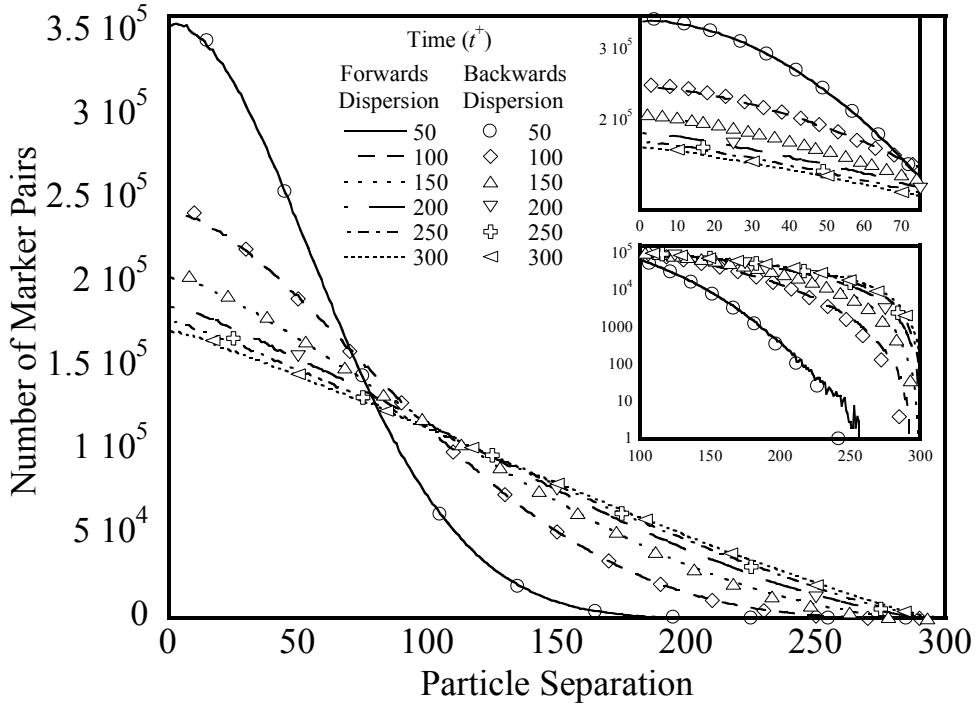

(b)

Figure 5.15: Marker pair distribution based on the marker pair vertical separation, in the case of forwards and backwards relative dispersion, for those markers captured in the logarithmic region, plotted at different instantaneous time of dispersion in plane Couette flow for different Prandtl numbers: (a) $Pr = 0.1$; (b) $Pr = 10$.

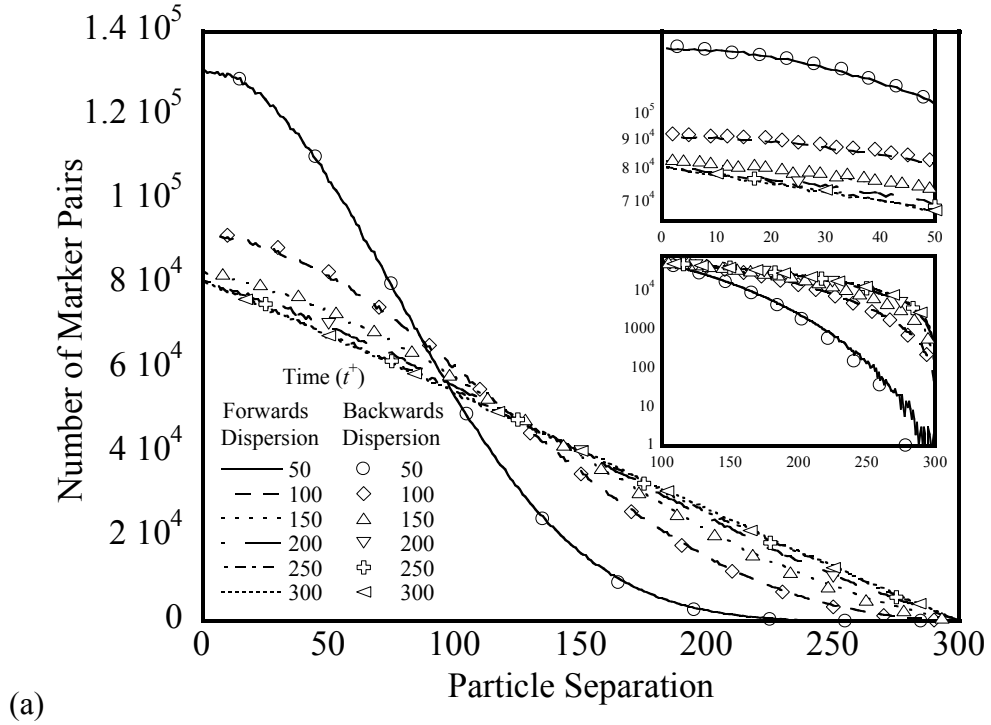

(a)

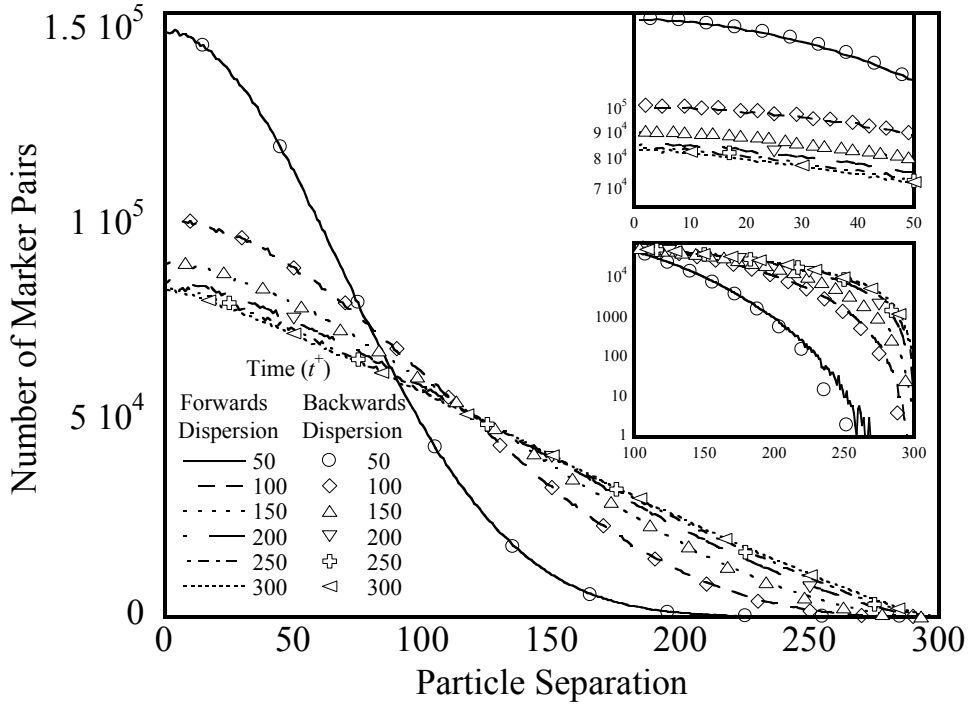

(b)

Figure 5.16: Marker pair distribution based on the marker pair vertical separation, in the case of forwards and backwards relative dispersion, for those markers captured in the center of the channel, plotted at different instantaneous time of dispersion in plane Couette flow for different Prandtl numbers: (a) $Pr = 0.1$; (b) $Pr = 10$.

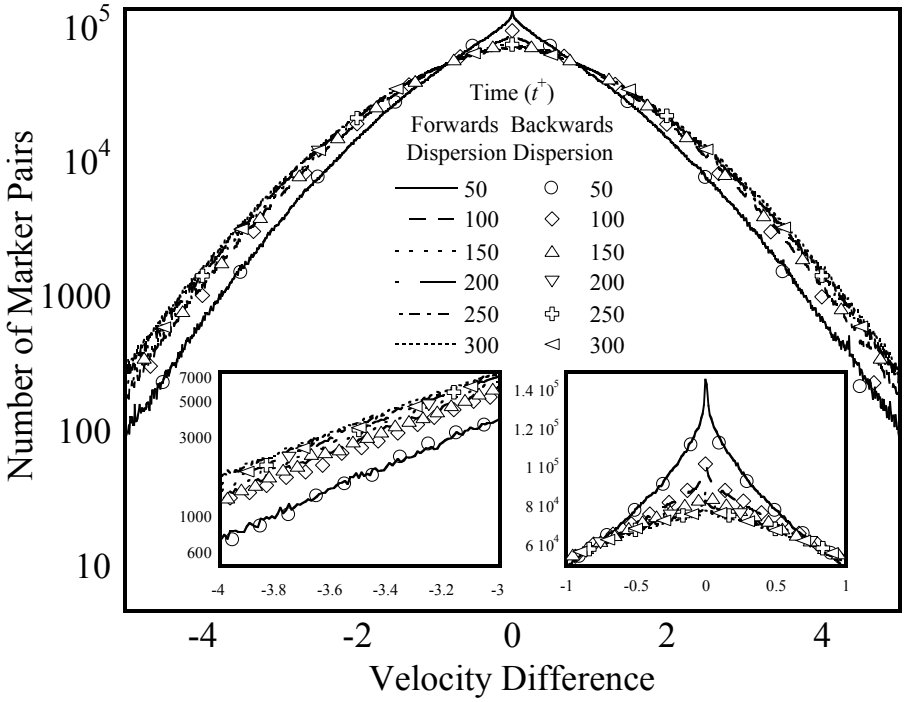

(a)

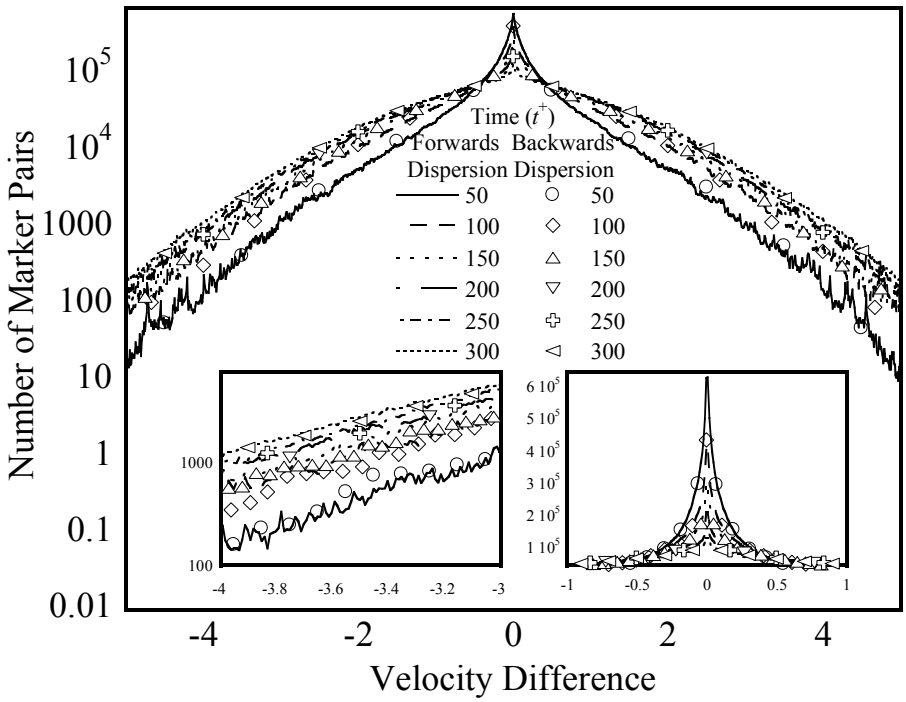

(b)

Figure 5.17: Marker pair distribution based on the vertical velocity difference of the marker pair, in the case of forwards and backwards relative dispersion, for those markers captured in the viscous sub-layer, plotted at different instantaneous times of dispersion in plane Couette flow for different Prandtl numbers: (a) $Pr = 0.1$; (b) $Pr = 10$.

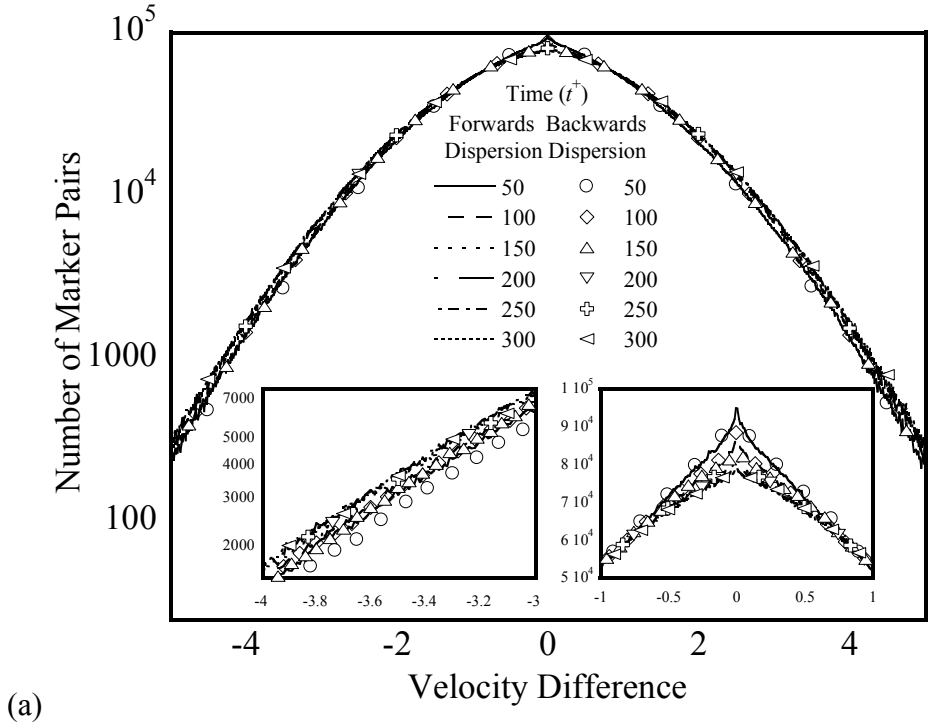

(a)

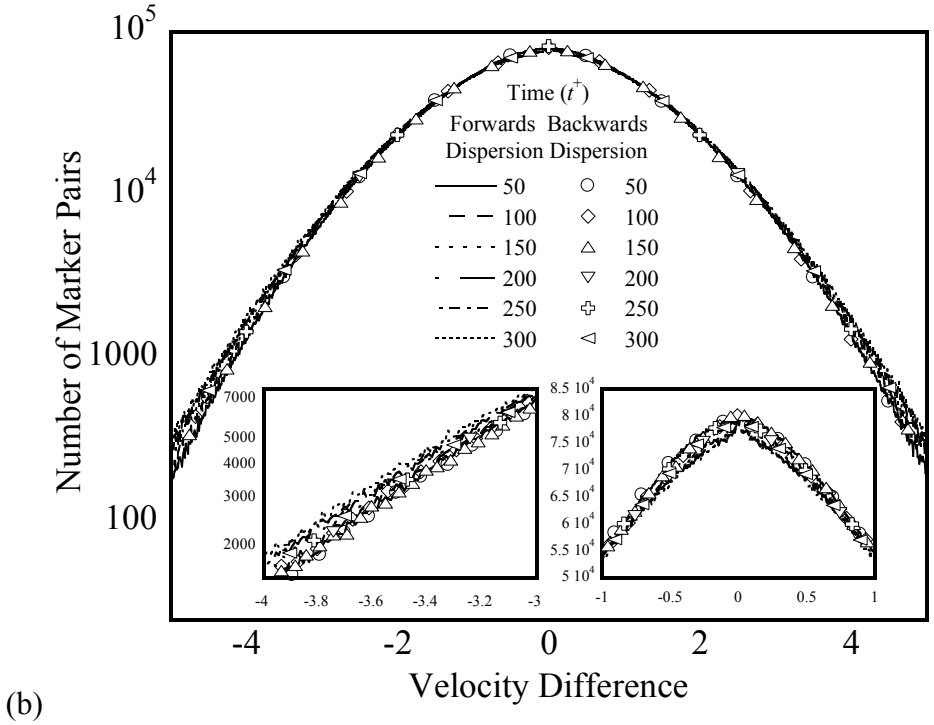

(b)

Figure 5.18: Marker pair distribution based on the vertical velocity difference of the marker pair, in the case of forwards and backwards relative dispersion, for those markers captured in the transition region, plotted at different instantaneous times of dispersion in plane Couette flow for different Prandtl numbers: (a) $Pr = 0.1$; (b) $Pr = 10$.

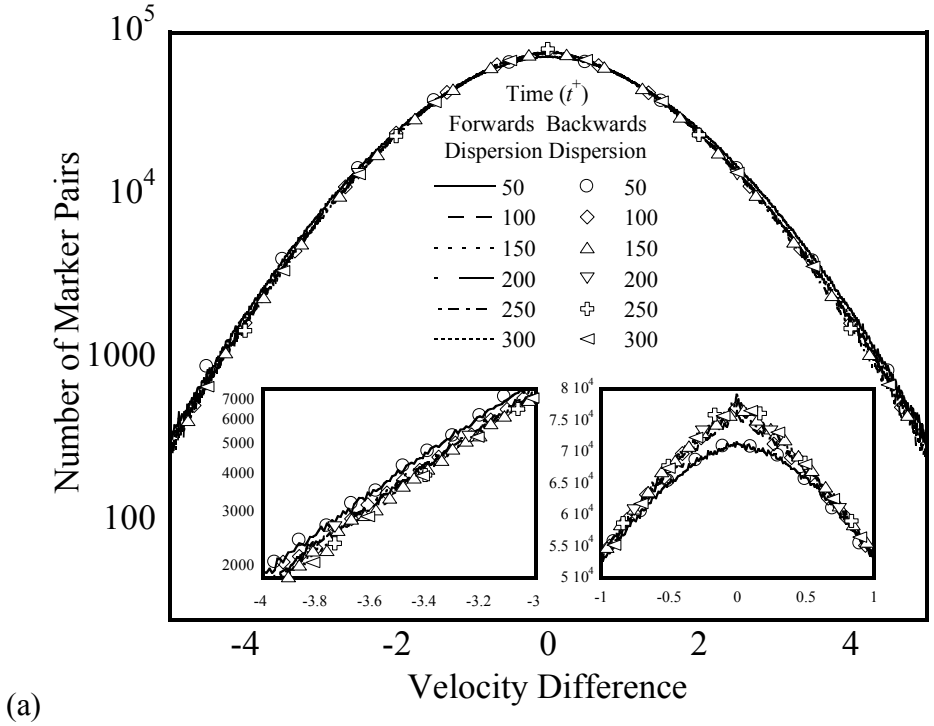

(a)

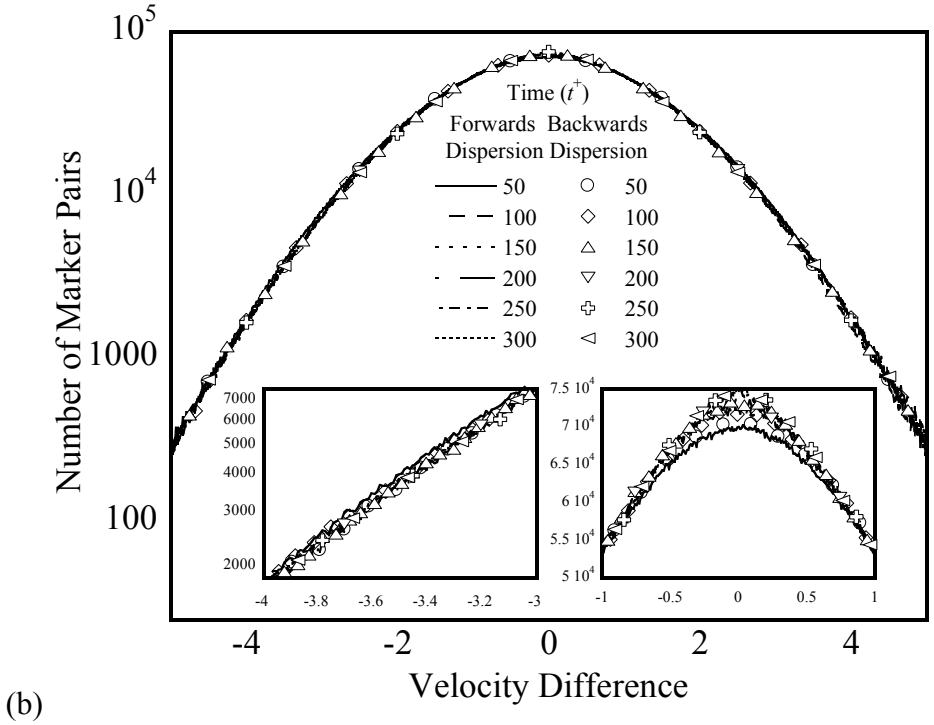

(b)

Figure 5.19: Marker pair distribution based on the vertical velocity difference of the marker pair, in the case of forwards and backwards relative dispersion, for those markers captured in the logarithmic region, plotted at different instantaneous times of dispersion in plane Couette flow for different Prandtl numbers: (a) $Pr = 0.1$; (b) $Pr = 10$.

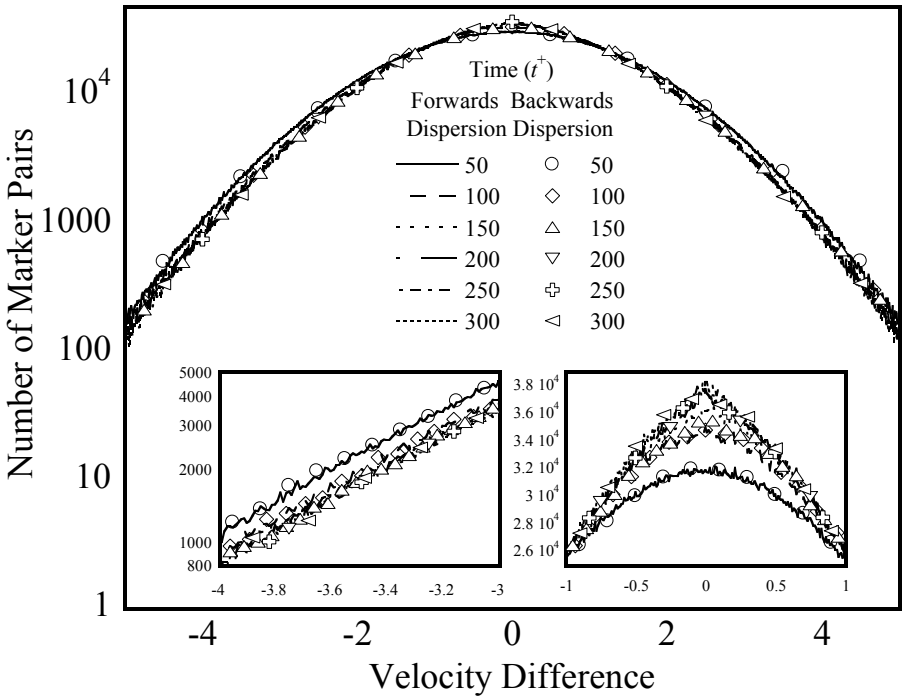

(a)

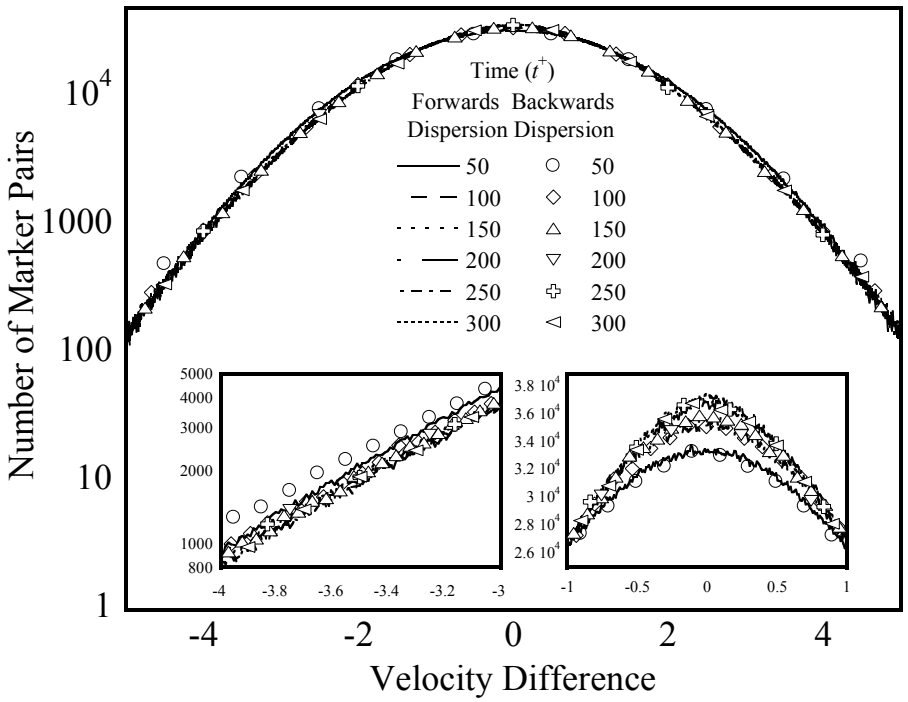

(b)

Figure 5.20: Marker pair distribution based on the vertical velocity difference of the marker pair, in the case of forwards and backwards relative dispersion, for those markers captured in the center of the channel, plotted at different instantaneous times of dispersion in plane Couette flow for different Prandtl numbers: (a) $Pr = 0.1$; (b) $Pr = 10$.

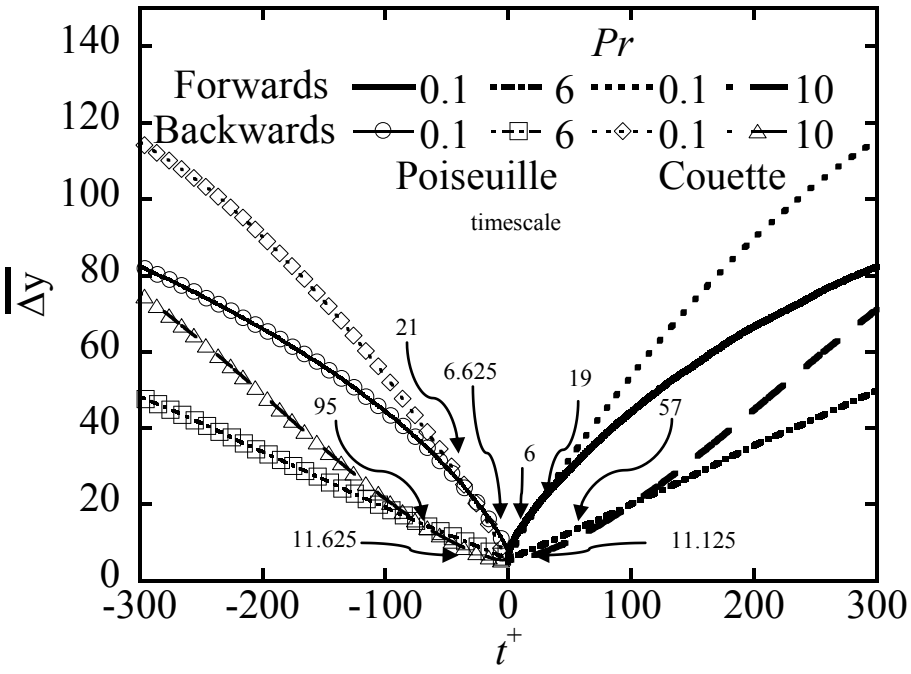

(a)

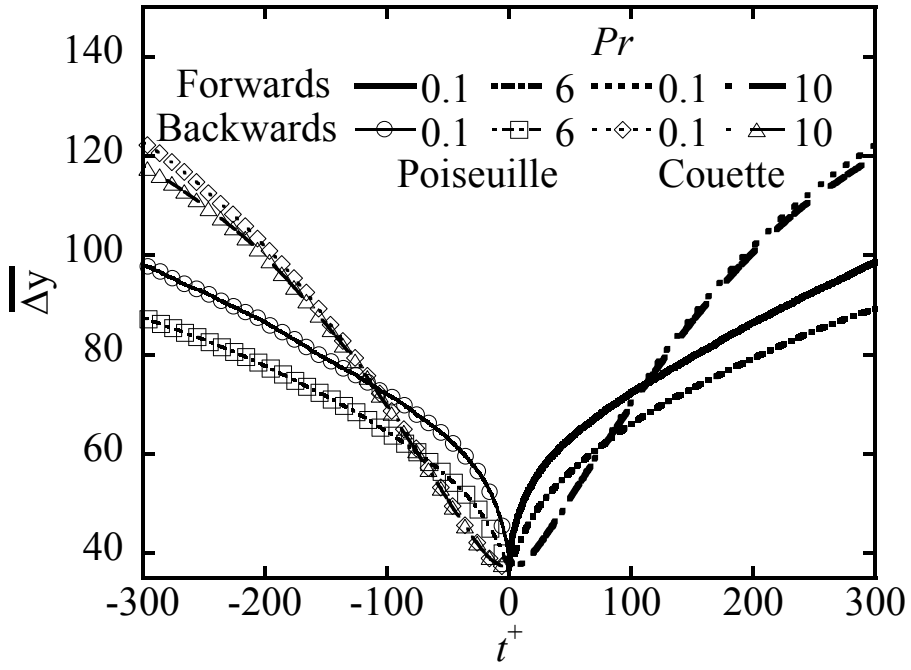

(b)

Figure 5.21: Average displacement of the mean location of the center of mass of the marker pairs as a function of time for forwards and backwards relative dispersion for (a) Pr = 0.1 and 6 in case of Poiseuille flow, and (b) Pr = 0.1 and 10 in the case of plane Couette flow. (a) Viscous sublayer – the arrows and numbers appearing on the figure indicate the Lagrangian material time scale. (b) Transition layer.

Chapter 6: DIRECTIONS OF SCALAR FORWARDS AND BACKWARDS SINGLE PARTICLE DISPERSION[‡]

6.1 Simulation parameters and procedure

In this study, the DNS flow field is obtained for both Poiseuille channel and plane Couette flow at Re_τ = 150. Variety of Pr = 0.1, 0.7, 6, 10, 50, 100, 500, and 1000 for Poiseuille channel flow case and Pr = 0.1, 0.7, 3, 6, 10, 200, 500, 2400, 7500 and 15000 for the Couette flow case are simulated for this particular study. Four different sets of simulations are carried out to obtain the data for the various case of Pr: (a) lower Pr for Poiseuille channel flow (Pr = 0.1, 0.7, 6, 10 and 50), (b) higher Pr for Poiseuille channel flow [162] (Pr = 50, 100, 500 and 1000), (c) lower Pr for plane Couette flow (Pr = 0.1, 0.7, 3, 6 and 10), and (d) higher Pr for plane Couette flow [149] (Pr = 200, 500, 2400, 7500 and 15000). These four sets are simulated with different initial velocity fields, but within each set the initial velocity is common for all Pr within that set. It takes approximately 1400CPU hours on a single processor of an SGI altix (cobalt at national center for supercomputing applications (NCSA)), to simulate one of the sets of 5 different Pr (0.1, 0.7, 6, 10 and 100), for Poiseuille channel flow. The simulation timestep (Δt^+) is 0.125 and 0.2 for Poiseuille and for Couette flow, respectively.

A technique that is loosely similar to Lumley's POD technique (see Section 2.2) is used herein to obtain the directions of scalar transfer in a turbulent channel flow. The directions of scalar transport in different regions of the turbulent channel flow, which are known to contain different types of coherent structures, namely, the viscous sub-

[‡] Most of the material in this Chapter has been published in the Physics of Fluids, 23, 115105 (2011)

layer, the transition region, the logarithmic region and the center of the channel, are studied. In turbulent plane Couette flow, the same regions, except for the center of the channel (since the logarithmic layer extends through the center of channel), are investigated. In all cases, single particle dispersion is considered. The direction of scalar transport both from a point forwards in time and towards a point (i.e., backwards in time), is considered. The differentiation in the directions of scalar transport between the two types of dispersion can help in better understanding the nature of coherent structures that are dominant in the transport of heat. The simulations also cover a range of five orders of magnitude of Prandtl number fluids ($0.1 \leq Pr \leq 15{,}000$).

The heat markers, in our study, drifting in the flow field, can be useful in understanding the scalar transport directions in space. The velocity correlation coefficient of a heat marker, obtained as a function of time in a particular direction, indicates the extent the velocity influences the motion of that heat marker in that direction as the flow field develops. The material time scale, which can be determined from this correlation coefficient, is a measure of the time period during which the heat marker is effectively transported in that particular direction, due to turbulence. To identify the primary direction of scalar transport of heat, with the fluctuating velocities in the x, y and z directions, the nine material auto and cross-correlation coefficients are determined. The 3×3 material correlation coefficient matrix is then decomposed to find the eigenvalues and the corresponding eigenvectors. Now, borrowing ideas from POD, the eigenvector corresponding to the highest eigenvalue would represent the direction of maximum transfer of heat and is presented as the principal direction of scalar transport of heat.

The release of the scalar markers is initiated from points between the grid nodes in the *x*-*z* plane, for a total of 145161 markers at time $t^+ = 0$. The simulation is allowed to run for 4000 viscous wall time units for both plane Poiseuille flow cases. After the markers moving into the flow field get uniformly dispersed (which is at 2000 viscous wall time units), the marker velocities are correlated in time to calculate various parameters. To determine the direction of scalar heat or mass transport, the material auto and cross-correlation coefficients are initially determined for both forwards and backwards dispersion in all three directions *x*, *y* and *z*. Using a material correlation coefficient similar to Saffman, the material correlation coefficients are determined using the equation

$$R_{V_i V_j}(t, t_0) = \frac{\overline{V_i'(t - t_0) V_j'(t_0)}}{\left[V_i'^2 (t - t_0)\right]^{\frac{1}{2}} \left[V_j'^2 (t_0)\right]^{\frac{1}{2}}}, \qquad i, j = x, y, z \qquad (6.1)$$

The ensemble average over the selected number of markers is denoted by the overbar, while the prime denotes the Lagrangian velocity fluctuation $V_i'(t) = V_i(t) - \overline{V}_i(t)$.

The channel is binned in the vertical direction with 101 bins and four different regions are considered for the study. The edge of the viscous sub-layer ($y^+ = 5$, which also includes $y^+ = 295$ since the channel is symmetrical about the center plane), the transition region between the viscous sub-layer and the logarithmic region ($y^+ = 37$ and 263), the logarithmic region ($y^+ = 75$ and 225) and the center of the channel ($y^+ = 150$) are the four regions under study. The markers captured at a particular instant of time, at one of the bins that include the above locations in the vertical direction of the channel, for any *Pr*, lying anywhere in the *xz* plane are correlated both forwards and backwards in time. The procedure is repeated after times of 100, 200, 300, 400, 500, 600 wall time

units allowing us to capture a fresh set of markers travelling through that particular region. A similar procedure is carried out for the upper half of the channel, in order to take advantage of the symmetry of the channel. Complete details of the modeling for channel Poiseuille flow have been presented in Chapter 4. The Couette flow analysis is carried out in a similar way, for example, in the logarithmic region, in case of forwards dispersion, the markers in bins 26 and 75 at viscous wall times of 2500, 2600, 2700, 3000, 3100, 3200, 3500, 3600, 3700 are traced forwards and backwards in time to determine the correlation coefficients. The procedure is similarly repeated for other regions of study. As in the channel flow case, around 1500 markers are captured in each timestep. Following the above procedure, we obtain eighteen values of the correlation coefficients. So, on an average, 27000 markers are correlated in the forwards and backwards direction for these three regions of flow.

The material auto- and cross-correlation coefficients are estimated in all three directions x, y and z of the turbulent channel and Couette flow to construct the complete correlation coefficient matrix

$$\underline{\underline{R}} = \begin{bmatrix} R_{uu} & R_{uv} & R_{uw} \\ R_{vu} & R_{vv} & R_{vw} \\ R_{wu} & R_{wv} & R_{ww} \end{bmatrix} \tag{6.2}$$

(The more convenient notation of u, v, w is used above instead of V_x, V_y, and V_z, respectively) This matrix is then decomposed to find out the eigenvalues and respective eigenvectors.

$$\underline{\underline{R}} \bullet \vec{G} = \lambda \vec{G} \tag{6.3}$$

where, λ and $\vec{G}$ are the eigenvalue and corresponding eigenvector of the velocity correlation coefficient matrix. The eigenvalues and the eigenvectors are determined, to find out the dominant direction of transfer of heat (λ_1, λ_2 and λ_3 are the three eigenvalues in decreasing order of magnitude). In addition, the correlation coefficient is also utilized to determine the turbulent scalar spectra. The Lagrangian scalar spectrum (represented in this study as E) is also calculated from the Fourier transform of the material correlation coefficients.

6.2 Results and discussion

6.2.1 Cross-correlation coefficients for Poiseuille flow

The results obtained for the cross-correlations in all three directions for Poiseuille channel flow, at $y^+ = 5$ are shown in Figures 6.1(a) – 6.1(f) (The diagonal components of the autocorrelation coefficient have been reported in Chapter 4 and are not repeated herein). It should be noted here that even though it would be more natural to represent the results for backwards dispersion as time increases from negative values to zero, the latter corresponding to the time the markers get captured in the bin, all the figures for backwards dispersion in this current study are plotted with a positive time axis after reflection around time 0, to facilitate pictorial comparisons with forwards dispersion data. Out of the 6 cross-correlations determined at this distance, namely, R_{uv}, R_{vu}, R_{uw}, R_{wu}, R_{vw}, R_{wv}, only the R_{uv} and R_{vu} seem to produce a significant result with the rest having values of zero, or very close to zero, for both forwards and backwards dispersion. The markers captured in different regions, in cases of both forwards and backwards dispersion have equal probabilities to move in positive or negative spanwise

directions. So, correlating the spanwise velocity of these markers to either the streamwise or vertical velocity produces cross-correlation coefficients that are on an average close to zero. The cross-correlation coefficients of the markers captured and correlated in the transition region, logarithmic region and the center of the channel of turbulent Poiseuille flow, for different *Pr*, as a function of time are presented in Figures 6.2, 6.3 and 6.4 respectively. The graphs of R_{uv} are presented, as Figures 6.2(a), 6.3(a), and 6.4(a), while the graphs of R_{vu} are presented as Figures 6.2(b), 6.3(b), and 6.4(b), since the rest of the cross-correlations are effectively zero.

Except for the case of outer layer flow at the center of the channel, the R_{uv} and R_{vu}, for a particular *Pr*, are equal and show values in between -0.4 and -0.5 at the time of capture for both forwards and backwards dispersion, in agreement with previous data [167] in the literature. As seen in Figure 6.1(a), the cross-correlation coefficient, R_{uv}, for forwards dispersion in the viscous sub-layer, exhibits a behavior consistent with transport due to quadrant 2 (Q2) or quadrant 4 (Q4) flow events (i.e., $u' < 0$, $v' > 0$ or $u' > 0$, $v' < 0$). For backwards dispersion, the markers seem to be carried towards the viscous sub-layer by quadrant 1 (Q1) or quadrant 3 (Q3) events (i.e., $u' > 0$, $v' > 0$ or $u' < 0$, $v' < 0$) at large times and by Q2/Q4 events at small times. The *Pr* has an effect on the behavior of R_{uv} for both forwards and backwards dispersion. Increasing *Pr* causes an increase in the transition time (time at which the cross-correlation coefficient shifts from Q2/Q4 to Q1/Q3 quadrants) for backwards dispersion. It is interesting to note that, even though *Pr* of 0.1, 0.7, and 6 has slightly differing behaviors, the higher *Pr* ($Pr > 6$) all follow the same trend, as is observable in Figure 6.1(a) for both forwards and backwards dispersion. Earlier results in Chapter 4 have also indicated that the higher *Pr*

behaviors are all clustered together. To avoid clutter, in the rest of the figures, having discovered that the higher Pr (> 6) all have similar behaviors, only four cases (i.e., Pr = 0.1, 0.7, 6 and 1000) are presented. The data for Pr = 1000 in essence represent the behavior of all cases for Pr > 6. The cross-correlation coefficient, R_{uv}, for markers captured in the transition and logarithmic regions shows a reversal in trend, with backwards dispersion predominantly showing Q2/Q4 events, while there is a transition from Q2/Q4 at initial times to Q1/Q3 for forwards dispersion, as seen in Figures 6.2(a) and 6.3(a).

These differences can be attributed to the characteristics of the flow structures and vortices that dominate the viscous sub-layer, the transition and the logarithmic regions of flow, combined with the contrasting dynamics that arise when observing dispersion from the viewpoint of transport of markers towards or away from a region of the channel flow. In channel flow, it has been previously [85, 86, 168] observed that the viscous sub-layer is mainly agitated by quasi-streamwise vortices that carry low velocity fluid away from the wall or high velocity fluid towards the wall, hence causing Q2/Q4 quadrant dominance for forward dispersing markers in these regions. However, the backwards dispersion markers are mainly transported to the viscous sub-layer by the downward traveling vertical structures, which, by notions of continuity, compensate for transport away from the wall. The existence of superbursts, identified in channel flows [86], as one of the salient features in pumping fluid towards the transition and logarithmic regions, support the existence of backwards dispersion R_{uv} correlations in the Q2/Q4 regions. The forwards dispersion is dictated by flow structures existing in the transition and the logarithmic regions, which are known [168] to be large vortices,

primarily oriented in the streamwise direction, leading to smaller cross-correlation of R_{uv} in this case. The increase in *Pr,* which can be associated with lesser effect of molecular diffusion and more vigorous turbulent transport of these markers by the associated vortical structures, causes a variation in the values of R_{uv}.

The velocity cross-correlation coefficient R_{vu} shows uniform trend for all flow regions for both forwards and backwards dispersion, as seen in Figures 6.1(b), 6.2(b) and 6.3(b). The dynamics of the flow structures in the various regions are once again important in the behavior observed. The transport of the passive scalars in case of backwards dispersion is the result of sweeping by high velocity structures transporting fluid towards the wall, in the case of viscous sub-layer, and the bursting of low velocity streaks carrying fluid away from the wall, in the case of the logarithmic layer. In the case of forwards dispersion, the vortices observed in the channel have large streamwise length scales [168] and even though at initial times the markers are transported by the Q2/Q4 events, due to prolonged streamwise transport, they get eventually caught by Q1/Q3 events.

It is also quite interesting to note that the transition times slightly increase as the distance of capture of these markers increases, indicating a larger length of the structures that aid in transport at larger distances from the channel wall. The data of R_{vu} for the lower *Pr* clearly show the possibility of transport structures that are comparatively smaller than those for the higher *Pr*. The difference in values of R_{vu} between forwards and backwards dispersion in absolute value is higher for higher *Pr*. The difference in absolute values between the forwards and backwards dispersion R_{vu} also increases as the distance from the channel wall increases, so the viscous sub-layer

exhibits the least, while the logarithmic region exhibits the highest difference, for a specific *Pr*. The center of the channel is the location that can be considered to be the closest to the case of isotropic turbulence. The value of the cross-correlation coefficient in both cases, for forwards and backwards dispersion, for a variety of *Pr,* is very close to zero.

6.2.2 Cross-correlation coefficients for plane Couette flow

In plane Couette flow, the walls of the channel move relative to each other. The total stress is constant across the channel, creating an extensive constant stress region, similar to the logarithmic region in Poiseuille channel flow. Thus, we can examine the dispersion characteristics in a flow field that has a much better established logarithmic region than that of the plane channel flow, and has flow structures different than those in plane channel flow. If any structures that contribute to dispersion were common, that would indicate a universal behavior. The cross-correlation coefficients, R_{uv} and R_{vu}, are presented as (a) and (b), respectively, in cases of forwards and backwards dispersion for the viscous sub-layer, the transition region and the logarithmic region in Figures 6.5, 6.6 and 6.7, respectively. Figure 6.5(a), is a presentation of R_{uv} for markers captured in the viscous sub-layer for Pr = 0.1, 0.7, 6, 10, 200, 500, 2400, 7500, and 15000. As observed in the case of Poiseuille channel flow, R_{uv} has different trends for Pr = 0.1 and 0.7 and to an extent for Pr = 6. The higher Pr cases correspond to curves that fell exactly over each other. Hence for the other regions of the plane Couette flow, the cross-correlation graphs of $Pr > 6$ are all represented by the case for Pr = 500. The trends for R_{uv} and R_{vu}, observed for forwards and backwards dispersion, for all Pr, in the viscous sub-layer are similar to those obtained for Poiseuille channel flow. There is also qualitative similarity

in the rest of the statistics of R_{uv} and R_{vu} between the two types of flow, for both forwards and backwards dispersion, pointing to the existence of universal structures that help in transport in both of these flow cases.

Summarizing the findings of this Section, in all three regions of both Poiseuille and Couette flow, backwards and forwards dispersion appear to be dominated by different flow structures. Also the behavior observed in both flows seems to be similar, pointing to the universality of these results. The cross-correlation of vertical velocity fluctuations with time to the streamwise velocity fluctuations at initial time, R_{uv}, for markers captured in the viscous sub-layer exhibits a unique behavior, where the strong velocity bursts and sweeps help the scalar transport, for forwards and backwards dispersion. In the other two regions, and in all three regions when considering R_{vu}, the cross-correlation of streamwise velocity fluctuations with time to the vertical velocity fluctuations at initial time, there is a different behavior. In these cases, the Q2/Q4 events help backwards scalar transport while Q1/Q3 events eventually dominate forwards marker transport. The *Pr* also affects the dispersion, especially at $Pr \leq 0.7$.

6.2.3 Direction of heat transport

6.2.3.1 Largest eigenvalues

6.2.3.1.1 Poiseuille flow

The dominant direction of heat transfer is essentially the direction of the eigenvector (primary eigenvector) that corresponds to the highest eigenvalue (primary eigenvalue). Since the values of all the elements of $\underline{\underline{R}}$ have been estimated, the

eigenvalues and the eigenvectors of the matrix can be estimated. The eigenvalue essentially quantifies the amount of turbulent heat transport, while the eigenvector points out the direction of turbulent heat transport.

The primary eigenvalues of the correlation coefficient matrix for the markers captured and correlated at the viscous sub-layer, the transition region and the logarithmic region of the Poiseuille channel flow for both forwards and backwards dispersion are shown in Figures 6.8(a), 6.8(b) and 6.8(c), respectively. The primary eigenvalues for backwards dispersion for a given *Pr* have higher values compared to the forwards dispersion, indicating pronounced amount of turbulent heat transfer for the case of backwards dispersion along the primary direction of transport. Also, the primary eigenvalues for backwards dispersion have significant values for a larger time compared to the forwards dispersion, whose eigenvalues decay to zero relatively quickly with time. The higher *Pr*, as one might expect, show higher values of primary eigenvalues compared to lower *Pr* for both forwards and backwards dispersion. The primary eigenvalues are higher for the logarithmic region compared to the transition region or the viscous sub-layer, indicating higher rates of mixing and hence more effective heat transfer in these regions of turbulent flow.

When one considers these differences in behavior of forwards and backwards dispersion for turbulent heat transport, it is logical to conclude (as with the discussion of cross-correlation coefficient before) that two different types of coherent structures, one headed towards the region and another headed away from the region, might be responsible for the different behaviors observed. The trends of the primary eigenvalues lead to the hypothesis that the markers moving towards a region primarily get

transported by a set of eddies having similar orientation, which are relatively long lived and lengthier, causing pronounced amount of turbulent heat transfer in that direction persistent in time. However, for the case of markers transported forwards, there seems to be a set of short lived, smaller sized eddies, having similar orientation. This leads to a shorter time period of turbulent heat transfer and less turbulent heat transport in this case. The study of the primary eigenvalue at the various regions for forwards and backwards dispersion also shows that as the distance from the channel wall increases, flow structures of larger length and duration are involved in the transport. The behavior of the eigenvalues for markers captured at the center of the channel is different than the rest of the regions, as shown in Figure 6.8(d). The values for forwards and backwards dispersion are very close for $Pr = 0.1$, while for $Pr > 0.1$, the eigenvalues for forwards dispersion are higher up to a time of 110 wall units, after which the backwards dispersion eigenvalues are higher.

6.2.3.1.2 Plane Couette flow

For the case of plane Couette flow, the primary eigenvalues for the case of markers captured and correlated at the viscous sub-layer, the transition region and the logarithmic region are shown in Figures 6.9(a), 6.9(b) and 6.9(c), respectively. At the viscous sub-layer, for $Pr = 0.1$, the values are very close. In this region the turbulent velocity fluctuations are rather small and the molecular diffusion is dominating the dispersion. For the rest of the cases, as with the Poiseuille channel flow, there is universality in the behavior with the primary eigenvalues for backwards dispersion being comparatively larger than for forwards dispersion. Interestingly, when comparing the results in Figures 6.8 and 6.9, the values of primary eigenvalues are always higher

for the case of plane Couette flow compared to Poiseuille channel flow, irrespective of the Pr or the region in the channel for the case of forwards dispersion, while for backwards dispersion, this is true for all $Pr \leq 6$. This can be thought of as the strength of turbulence mixing, which seems to be more intense in the case of plane Couette flow compared to Poiseuille channel flow.

6.2.3.2 Principal directions of heat transfer

The eigenvector directions corresponding to the primary eigenvalues for the case of markers captured in the four different regions, for Pr = 0.1, for Poiseuille channel flow are shown in Figure 6.10. The forwards and backwards dispersion heat transfer directions are shown in Figures 6.10(a) and (b), respectively. At the center of the channel for Pr = 0.1, the direction of heat transfer is predominantly parallel to the z axis for both forwards and backwards dispersion. This is expected, since at the center of the channel there is no preference of the markers to move towards the top or the bottom of the channel. For the case of plane Couette flow, for Pr = 0.1, the direction of eigenvector corresponding to the highest eigenvalue is shown in Figure 6.11 as (a) and (b), for forwards and backwards dispersion, respectively. The directions of heat transfer are mostly oriented at very small angles to the vertical direction, indicating the importance of the normal direction in the role of heat transfer. Comparing the results for the two types of flow, the plane Couette flow with the better established turbulence regime shows more consistent and sustained heat transport over larger time intervals. If one considers the flow field, an eddy will likely transfer heat in the direction that is perpendicular to the axis of the eddy. Coherent structures observed in the turbulent

Poiseuille and plane Couette flows at the transition regions [163, 164], like ejection or sweep events, have structures that have axes with small inclinations to the *xz* plane. Also, the coherent structures observed in the various flow regions [88, 90, 91, 169] are known to be initially oriented with angles of inclination of 45° with the wall. So, these eddies are probably responsible for the heat transfer directions observed in Figures 6.10 - 6.11. Principal heat transport directions for higher *Pr* for both Poiseuille channel flow and plane Couette flow cases can be found in the Appendix B of the dissertation.

The angle of inclination of the primary eigenvectors with the normal to the *xy*, *yz* and *zx* planes, presented as θ_{xy}, θ_{yz} and θ_{zx}, respectively, from here on, and measured with different planes as shown in Figure 6.12, can further help in visualizing the direction of heat transport. One can imagine the angle that the primary eigenvector makes with the normal to the plane for backwards dispersion, to be analogous to the angle of incidence in the case of dispersion of light. Correspondingly, the angle made by the primary eigenvector for the forwards dispersion with the normal to the plane can be imagined as the angle of refraction. A schematic of the analogy between the backwards and forwards dispersion with the physics of optics is shown in Figure 6.13.

The angle of inclination of the primary eigenvectors for both forwards and backwards dispersion as a function of time with the normal to the three different planes, *xy*, *yz* and *zx* are presented as Figures (a), (b) and (c), for the markers captured in the viscous sublayer, the transition region and the logarithmic region of the Poiseuille channel flow in Figures 6.14, 6.15 and 6.16, respectively. In the case of plane Couette flow, these angles for the same three regions are shown in Figures 6.17, 6.18 and 6.19.

Looking at these figures, one can clearly notice differences in the direction of primary eigenvectors between the case of forwards and backwards dispersion.

The spanwise direction, as has been observed in 6.2.1 above and in Chapter 4, plays a minor role in the case of heat transport, which can be observed from the almost parallel inclination of angle of incidence and refraction with the *xy* plane. Some variations from these parallel orientations are observed, especially in the case of lower *Pr* with the angle of incidence. However, these have no significant meaning, and are just a manifestation of the random orientations of the small scale eddies, which seem to be associated with the forwards dispersion and also of the molecular diffusion effects that dominate dispersion for lower *Pr*.

In the viscous sub-layer, the transition and the logarithmic regions, the angles of incidence and refraction with the normal to the *yz* and *zx* planes, in both Poiseuille and Couette flow and for all *Pr*, are at 45° at $t = 0$. Imagining an eddy transferring heat in a direction of 45° with the normal of the *zx* plane, then the axis of the eddy should be perpendicular to this direction (i.e., about 135°, or -45° with the *zx* plane), which matches the orientation of observed coherent structures [88, 90, 91, 169]. For the viscous sub-layer, however, the behavior with time strongly depends on the *Pr*. The lower *Pr* (0.1, 0.7) show random decreases and increases of the angles of incidence and refraction with the *yz* plane and *zx* plane, for both Poiseuille channel and Couette flow. The viscous sublayer is the region that has the smallest turbulent structures than any region of turbulent channel flow, so at lower *Pr*, where molecular diffusion dominates dispersion close to the wall, it leads to a random behavior of the angles. In the case of higher *Pr*, the variation of the angle of refraction of the primary eigenvector with the

normal to the *yz* and *zx* plane, for the viscous sub-layer, the transition and logarithmic region, in both Poiseuille and Couette flow, clearly indicates transport by a rotating eddy extending through that particular region. The interesting part of the study, however, is the differences in these angles when compared to the angles of incidence of the primary eigenvector. The angles of incidence calculated from the average set of markers arriving at a particular location, indicate that these markers move primarily by the same set of eddies which are prevalent in the flow field for a longer time and have stable orientations. Combining these results with those observed for the eigenvalues, it can be concluded that the forwards dispersing heat markers move through a set of short lived eddies that change orientation rapidly with time, while the relatively long lived eddies causing transport for a longer time in a particular direction contribute to backwards dispersion. These results also seem to be consistent with the higher [164] mean length and spacing intervals associated with sweep events as compared to ejection events. In case of Poiseuille channel flow, the angles of incidence and refraction with the *yz* and *zx* plane for Pr = 6, 1000 follow a similar pattern, while in Couette flow, the angles for Pr = 0.7, 6, 500 are grouped together.

However, it is quite puzzling as to why the eddies causing backwards scalar transport show less tumbling and more uniform orientations compared to the eddies causing forwards scalar transport. In the study of single particle dispersion in Chapter 4, it was found that in the vertical direction (where the turbulence is anisotropic) forwards dispersion proceeds at a faster rate compared to the backwards dispersion in the viscous sub-layer, the transition region and the logarithmic region. This is in agreement with the physical picture that the eddies carrying the markers disperse and spread faster during

the process of forwards dispersion, compared to backwards dispersion (which shows a fixed dispersion angle over a longer period of time). The scalar markers moving forwards can be dispersed with Q1/Q3 events in addition to Q2/Q4 events, while markers arriving at one location arrive there predominantly by Q2/Q4 events.

The angles of incidence and refraction of the primary eigenvectors with different planes were presented as a function of dispersion time in the discussion above. One could then examine their relative magnitude using a ratio similar to the ratio of refractive indices used in Snell's law in optics. Since the angles are obtained from turbulent dispersion, this ratio can be named the *turbulent dispersive ratio*. This ratio changes with time, so if one wanted to examine the incidence and refraction angles at a specific time, that time would be the Lagrangian material time scale. One could actually calculate the ratio of the turbulent dispersive indices (forwards dispersion index divided by the backwards dispersion index) from the sine of backwards dispersion primary eigenvector angle to the sine of the forwards dispersion primary eigenvector angle, in analogy to Snell's law for optics. The material scale in the vertical direction calculated from the material correlation coefficient R_{vv} for Poiseuille channel and plane Couette flow is presented in Tables 6.1 and 6.2, respectively. The angles of incidence and refraction at these Lagrangian material time scales, averaged between $\tau_{(f/b)}$-2 and $\tau_{(f/b)}$+2 to obtain better statistics, are presented in Tables 6.3 and 6.4, for Poiseuille and Couette flow, respectively. For Poiseuille channel flow, the turbulent dispersive ratio is presented in Table 6.5, while the same is presented in Table 6.6 for plane Couette flow.

The turbulent dispersive ratio captures the differences between the flow structures that carry scalar markers towards a particular location and at a particular

distance from the wall, which on average have different orientation than the structures that move scalars away from that location. The turbulent dispersive ratio shows a behavior that depends on the *Pr*. However, irrespective of the *Pr*, the calculated turbulent dispersive ratio still helps in envisioning the differences between scalar transport directions for forwards and backwards dispersion.

6.2.4 Lagrangian scalar spectrum

The Lagrangian material correlation coefficient data can be helpful in understanding the behavior of the scalar spectra and estimate any differences that exist between forwards and backwards scalar dispersion. The spectra $E_{vv}(\omega)$ of the vertical material autocorrelation coefficient (R_{vv}) as a function of frequency, ω for markers captured reaching the viscous sub-layer and moving out of the region, in cases of Poiseuille channel and Couette flow, respectively, are shown in Figures 6.20(a) and (b). The spectra presented in Figures 6.21(a) and (b) are obtained from the vertical material autocorrelation coefficient for cases of markers captured in the logarithmic regions for Poiseuille channel and Couette flow cases, respectively. The material autocorrelation coefficient for the case of homogenous, isotropic turbulence is known [154] to have an exponential decay given by $R_{vv} = \exp(-t/\tau)$, where R_{vv} becomes equal to 0.368 when $t = \tau$. The spectrum calculated using this relation for the autocorrelation coefficient (designated as "analytical" in Figures 6.20 and 6.21), when it is plotted along with the spectrum obtained from anisotropic turbulence, demonstrates the effect that the presence of the walls has on the spectrum.

The spectrum close to walls shows variation with *Pr*, while the *Pr* effects seem less pronounced in the logarithmic region, in both Poiseuille and Couette flows. The effect of the anisotropies introduced by the wall is noticed at lower frequencies when comparing the actual spectrum and the spectrum obtained from the analytical correlation, for markers captured at the viscous sub-layer. In the case of markers captured in the logarithmic region, the differences are pronounced even at higher frequency and in case of Poiseuille channel flow, while the differences are negligible in plane Couette flow.

Plotting the Lagrangian scalar spectrum obtained from the auto-correlation coefficient in the three directions, *x, y* and *z*, for different regions of the channel, for all the *Pr*, the slopes at the intermediate frequency range are calculated and tabulated in Tables 6.7 and 6.8, for Poiseuille channel and plane Couette flow, respectively. The Appendix B is presentation of plots of the slope of the spectra as a function of *Pr*. Irrespective of the type of flow or the region of the channel under consideration, the Lagrangian scalar spectrum exhibits a universal behavior with slope $p = -1$, for all $Pr > 0.7$, for both forwards and backwards dispersion. Differences in turbulent scalar transport behavior arising due to different turbulent structures between forwards and backwards dispersion seem to have minimal effects on the turbulent scalar spectrum in these intermediate frequency ranges. For lower *Pr,* ($Pr \leq 0.7$), the spectrum scales with a coefficient greater than -1, in both flow situations. This indicates that at the viscous sub-layer, at lower *Pr*, different turbulent scales contribute to heat transfer when compared to the scales existing in the regions away from the channel walls. This could be intuitively expected as the scales of motion are limited close to the channel walls,

and moreover, at lower *Pr*, molecular diffusion plays a vital role in controlling transport restricting the effect of large scale turbulent structures.

6.3 Conclusions

The predominant direction of turbulent heat transport for forwards and backwards dispersion is comparatively studied for two different types of channel flow, Poiseuille and Couette flow, as a function of the distance from the wall, and for various *Pr* fluids. The dominant direction of heat transport is obtained by calculating the eigenvectors and eigenvalues of the matrix constructed by the velocity auto- and cross-correlation coefficients. After analysis of the results obtained in cases of forwards and backwards dispersion for both flows, it is clear that there is a universality of behavior, irrespective of the type of flow.

The main findings of this analysis are as follows:

(a) Forwards dispersion is different than backwards dispersion and the difference depends on the *Pr* and on the distance from the wall, indicating that forwards and backwards dispersion in anisotropic turbulence exhibit different behavior than they do in isotropic turbulence, where the backwards dispersion is faster for asymmetric turbulence [73].

(b) There are coherent structures that mainly contribute to transport towards a location in the inner region of the flow field, and these are different than the structures that mainly contribute to transport forwards from a location in the flow field. The backwards dispersion is carried out by a set of relatively long-lived, stably oriented flow structures influenced primarily by strong bursting and sweep (Q2/Q4) events, while the

forwards scalar transport is caused by a set of short-lived, constantly tumbling eddies, as the transport is influenced both by Q2/Q4 events and Q1/Q3 events;

(c) The differences in the direction of scalar transport towards a location and away from it can be represented with the help of a newly defined quantity, the turbulence dispersive ratio, which is based on the analogy with optics where the angle at which heat is carried to a point in the flow field by backwards dispersion is considered analogous to the angle of incidence of light, while the angle at which heat is released from a point during forwards dispersion is analogous to the angle of refraction;

(d) Even low *Pr* fluids, where molecular dispersion is dominant close to the wall, have preferred directions of transfer, but more dominant and sustained heat transport, in cases of both forwards and backwards dispersion, is found in all regions of the flow as *Pr* increases. The intensity of heat transport in the direction of the primary eigenvector increases with increasing distance from the channel wall;

(e) The Lagrangian frequency spectrum obtained from the correlation coefficients for high *Pr* and at all regions in the Poiseuille and Couette flows shows the existence of a regime with a slope of -1. This is true for both forwards and backwards dispersion. Only in the viscous sub-layer and at lower *Pr* (*Pr* = 0.1 and 0.7) the slope increases, indicating smaller scales of turbulence that contribute to transport in this region and these *Pr*.

Table 6.1: Lagrangian material time scale in the vertical direction presented for the cases of different *Pr*, at different regions of Poiseuille channel flow, for both forwards and backwards turbulent dispersion.

Pr	Viscous sublayer (y^+ = 5, 295)		Transition region (y^+ = 37, 263)		Logarithmic region (y^+ = 75, 225)	
	forwards	backwards	forwards	backwards	forwards	backwards
0.1	4.6	3.9	9.9	7.6	16.1	16.6
0.7	7.4	6.9	12.1	12.1	21.9	21.4
6	10.3	11.9	12	12.1	23	21.4
1000	11	13	12	12	23	21

Table 6.2: Lagrangian material time scale in the vertical direction presented for the cases of different *Pr*, at different regions of plane Couette flow, for both forwards and backwards turbulent dispersion.

Pr	Viscous sublayer (y^+ = 5, 295)		Transition region (y^+ = 37, 263)		Logarithmic region (y^+ = 75, 225)	
	Forwards	Backwards	Forwards	Backwards	Forwards	Backwards
0.1	4	4	11	10	18	19
0.7	6	7	13	12	20	21
6	9	10	12	14	21	22
500	10	11	10	13	19	19

Table 6.3: Angles of inclinations of the eigenvector directions corresponding to the highest eigenvalue with the normal to the different planes, similar to the angles in optics, at the vertical Lagrangian material scales, for different regions of Poiseuille channel flow for both forwards and backwards dispersion, with changes in *Pr*.

		Angle with normal to the *xy* plane		Angle with normal to the *yz* plane		Angle with normal to the *zx* plane	
	Pr	forwards	Backwards	forwards	Backwards	forwards	Backwards
$y^+ =$ 5, 295	0.1	39	25	64	73	64	73
	0.7	14	88	80	27	80	63
	6	90	89	15	23	75	67
	1000	88	90	15	25	75	65
$y^+ =$ 37, 263	0.1	74	86	69	39	58	51
	0.7	90	89	30	31	60	59
	6	87	88	31	28	60	62
	1000	88	90	32	30	58	60
$y^+ =$ 75, 225	0.1	87	90	28	39	63	51
	0.7	89	88	20	35	70	55
	6	88	89	20	34	70	56
	1000	88	90	22	35	69	55

Table 6.4: Angles of inclinations of the eigenvector directions corresponding to the highest eigenvalue with the normal to the different planes, similar to the angles in optics, at the vertical Lagrangian material scales, for different regions of plane Couette flow for both forwards and backwards dispersion, with changes in *Pr*.

		Angle with normal to the *xy* plane		Angle with normal to the *yz* plane		Angle with normal to the *zx* plane	
	Pr	forwards	backwards	forwards	backwards	forwards	backwards
$y^+ =$ 5, 295	0.1	3	5	90	87	89	87
	0.7	5	86	86	26	88	64
	6	89	87	69	23	87	68
	500	90	89	4	22	88	68
$y^+ =$ 37, 263	0.1	58	90	73	35	83	55
	0.7	89	90	18	29	72	61
	6	88	90	22	26	68	64
	500	90	89	26	27	64	63
$y^+ =$ 75, 225	0.1	88	90	24	34	66	56
	0.7	90	89	24	33	66	57
	6	90	89	24	32	66	58
	500	83	89	21	35	70	55

Table 6.5: Measure of the turbulent dispersive ratio (forwards dispersive index to the backwards dispersive index), obtained from the ratio of sine of the angle of backwards dispersion primary eigenvector to the sine of the angle of forwards dispersion primary eigenvector, with the three different planes, for different *Pr*, at various regions of the Poiseuille channel flow.

	Pr	Turbulent dispersive ratio (with *xy* plane)	Turbulent dispersive ratio (with *yz* plane)	Turbulent dispersive ratio (with *zx* plane)
$y^+ = 5, 295$	0.1		1.06	1.06
	0.7		0.46	0.91
	6	1.00	1.55	0.95
	1000	1.00	1.66	0.94
$y^+ = 37, 263$	0.1	1.04	0.67	0.91
	0.7	1.00	1.02	0.99
	6	1.00	0.93	1.02
	1000	1.00	0.94	1.02
$y^+ = 75, 225$	0.1	1.00	1.36	0.87
	0.7	1.00	1.66	0.87
	6	1.00	1.65	0.88
	1000	1.00	1.55	0.88

Table 6.6: Measure of the turbulent dispersive ratio (forwards dispersive index to the backwards dispersive index), obtained from the ratio of sine of the angle of backwards dispersion primary eigenvector to the sine of the angle of forwards dispersion primary eigenvector, with the three different planes, for different *Pr*, at various regions of the plane Couette flow.

	Pr	Turbulent dispersive ratio (with *xy* plane)	Turbulent dispersive ratio (with *yz* plane)	Turbulent dispersive ratio (with *zx* plane)
$y^+ = 5, 295$	0.1		1.00	1.00
	0.7		0.44	0.90
	6	1.00	0.41	0.93
	500	1.00	5.46	0.93
$y^+ = 37, 263$	0.1	1.18	0.59	0.83
	0.7	1.00	1.61	0.91
	6	1.00	1.17	0.97
	500	1.00	1.03	0.99
$y^+ = 75, 225$	0.1	1.00	1.38	0.91
	0.7	1.00	1.32	0.92
	6	1.00	1.30	0.93
	500	1.01	1.56	0.88

Table 6.7: Measure of the slopes of the Lagrangian scalar spectrum at the intermediate frequency range obtained from the forwards and backwards auto-correlation coefficient in the x, y, z directions, for different Pr, at various regions of the Poiseuille channel flow.

		Slope of $E_{uu}(\omega)$ vs ω		Slope of $E_{vv}(\omega)$ vs ω		Slope of $E_{ww}(\omega)$ vs ω	
	Pr	Forwards	Backwards	Forwards	Backwards	Forwards	Backwards
$y^+ =$ 5, 295	0.1	-0.70	-0.70	-0.77	-0.72	-0.84	-0.86
	0.7	-0.82	-0.85	-0.87	-0.88	-0.99	-1.00
	6	-1.01	-0.98	-0.94	-0.97	-1.08	-1.06
	1000	-0.96	-0.94	-0.91	-0.88	-1.03	-1.01
$y^+ =$ 37, 263	0.1	-0.96	-0.95	-0.92	-0.93	-0.96	-0.93
	0.7	-1.02	-1.00	-1.07	-1.08	-1.04	-1.03
	6	-1.02	-1.01	-1.10	-1.10	-1.07	-1.06
	1000	-0.94	-0.94	-1.03	-1.02	-1.01	-0.98
$y^+ =$ 75, 225	0.1	-0.99	-0.95	-1.00	-0.98	-1.00	-0.96
	0.7	-1.01	-1.02	-1.02	-1.02	-1.05	-1.04
	6	-1.02	-1.02	-1.03	-1.05	-1.03	-1.05
	1000	-0.94	-0.95	-0.96	-0.98	-0.96	-0.96

Table 6.8: Measure of the slopes of the Lagrangian scalar spectrum at the intermediate frequency range obtained from the forwards and backwards auto-correlation coefficient in the x, y, z directions, for different Pr, at various regions of plane Couette flow.

		Slope of $E_{uu}(\omega)$ vs ω		Slope of $E_{vv}(\omega)$ vs ω		Slope of $E_{ww}(\omega)$ vs ω	
	Pr	Forwards	Backwards	Forwards	Backwards	Forwards	Backwards
$y^+ =$ 5, 295	0.1	-0.49	-0.49	-0.58	-0.60	-0.77	-0.76
	0.7	-0.75	-0.74	-0.79	-0.81	-0.93	-0.93
	6	-0.93	-0.91	-0.85	-0.87	-1.00	-0.98
	1000	-0.98	-0.94	-0.86	-0.88	-1.03	-0.97
$y^+ =$ 37, 263	0.1	-0.92	-0.91	-0.85	-0.86	-0.87	-0.85
	0.7	-0.96	-0.95	-0.97	-0.97	-0.95	-0.97
	6	-0.94	-0.95	-1.03	-1.02	-0.97	-0.97
	1000	-0.95	-0.94	-1.02	-1.00	-0.99	-0.96
$y^+ =$ 75, 225	0.1	-0.91	-0.90	-0.89	-0.90	-0.90	-0.92
	0.7	-0.94	-0.94	-0.96	-0.96	-0.95	-0.97
	6	-0.95	-0.94	-0.98	-0.98	-0.98	-0.97
	1000	-0.95	-0.95	-0.97	-1.00	-0.97	-0.97

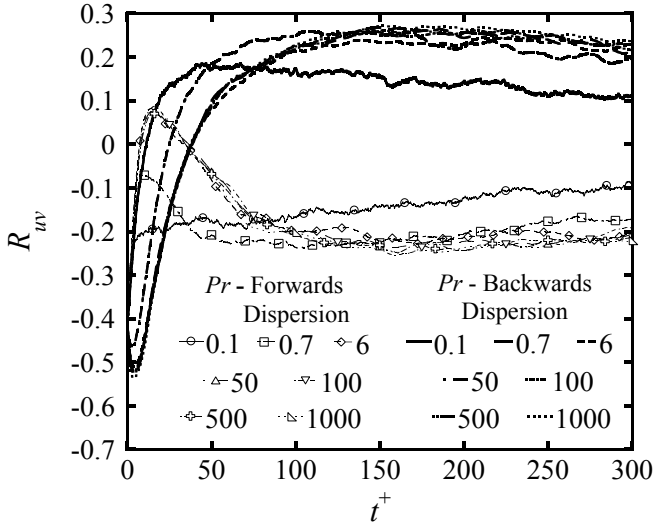
R_{uv}
t^+
Pr - Forwards Dispersion
0.1 0.7 6 50 100 500 1000
Pr - Backwards Dispersion
0.1 0.7 6 50 100 500 1000

(a)

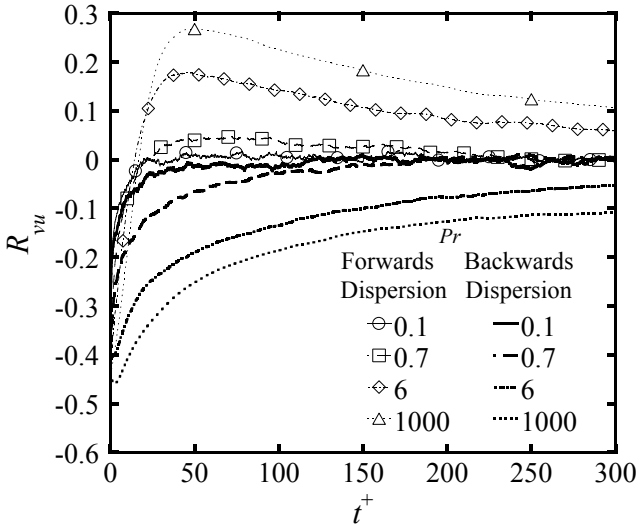
R_{vu}
t^+
Pr
Forwards Dispersion
Backwards Dispersion
0.1
0.7
6
1000

(b)

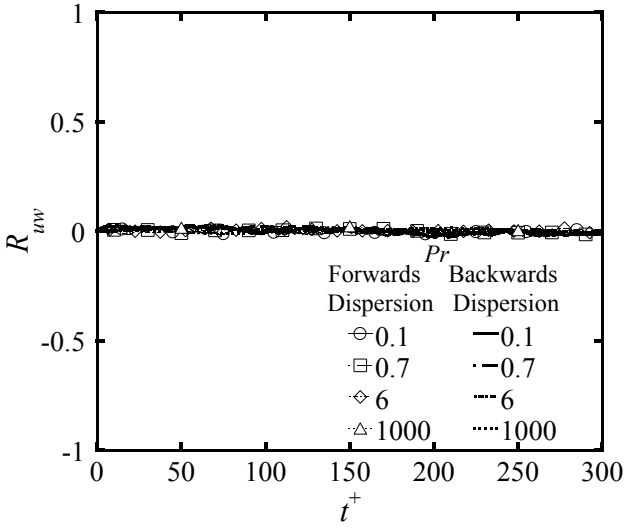
R_{uw}
t^+
Pr
Forwards Dispersion
Backwards Dispersion
0.1
0.7
6
1000

(c)

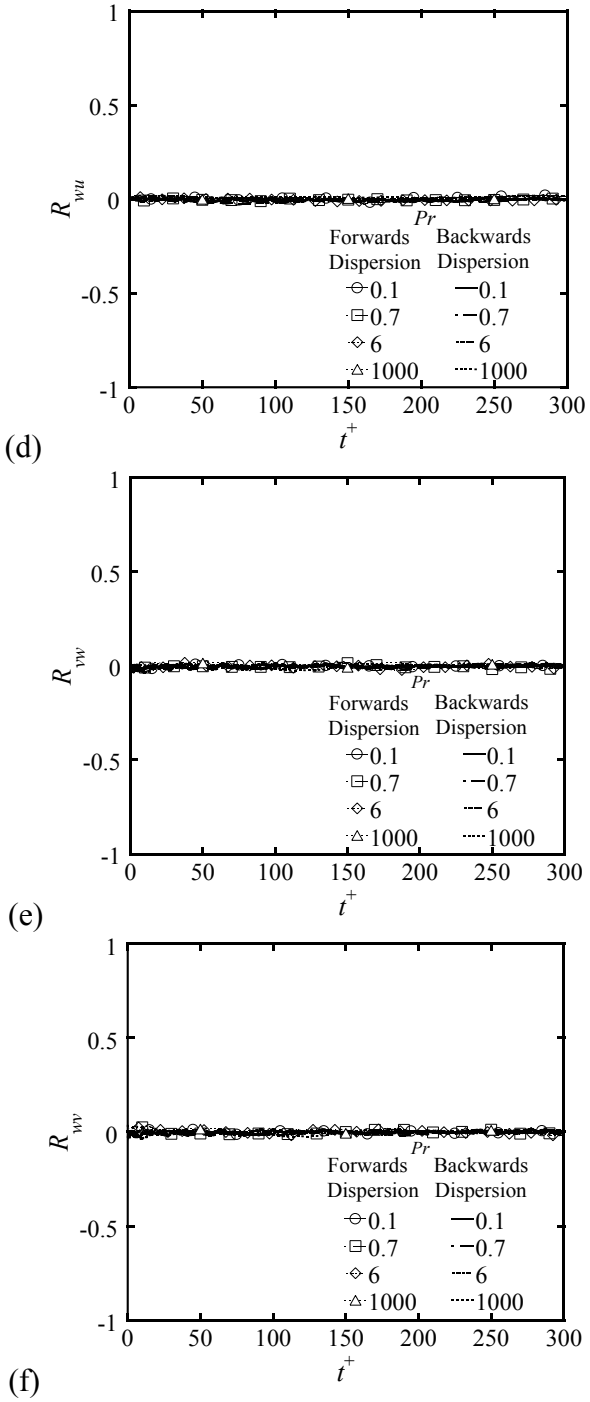

Figure 6.1: Material cross-correlation coefficients plotted as a function of time for different Pr, in cases of forwards and backwards dispersion of markers captured and correlated in the viscous sub-layer of Poiseuille channel flow: (a) R_{uv}, $y^+ = 5$; (b) R_{vu}, $y^+ = 5$; (c) R_{uw}, $y^+ = 5$; (d) R_{wu}, $y^+ = 5$; (e) R_{vw}, $y^+ = 5$; (f) R_{wv}, $y^+ = 5$. In Figures (b) through (f), in order to clearly present the results, the curves for $Pr > 6$ are all represented by the curve for $Pr = 1000$.

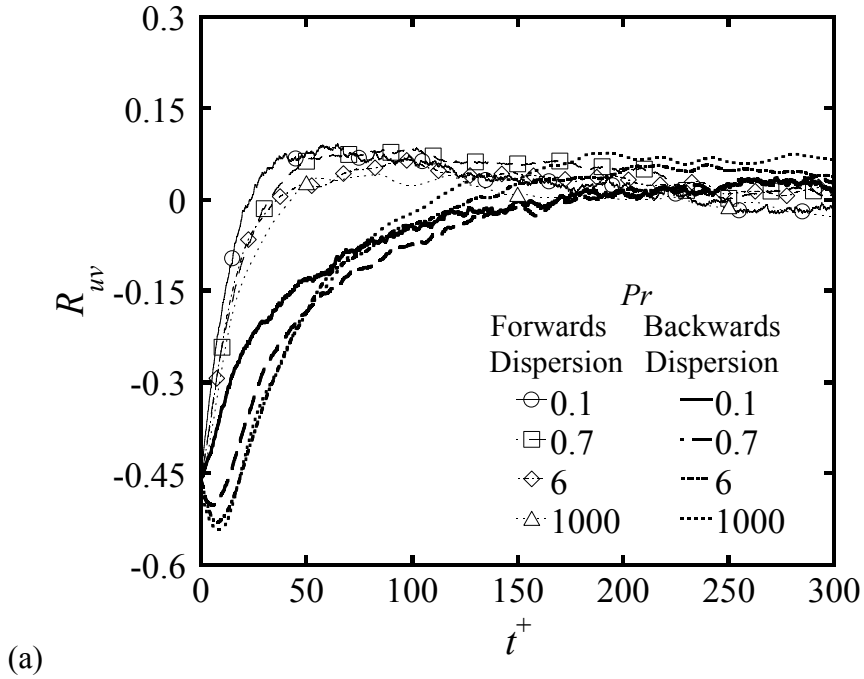

(a)

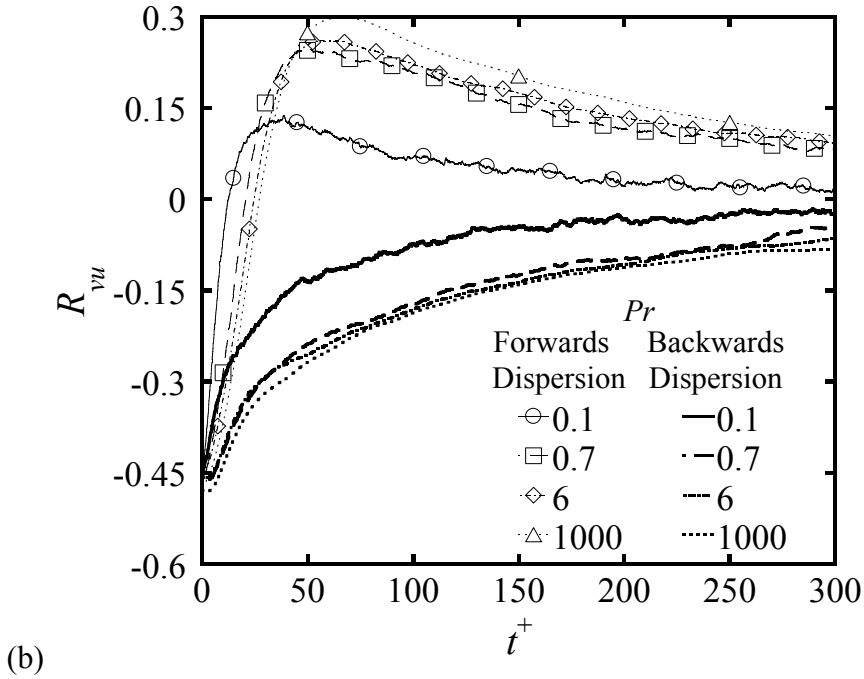

(b)

Figure 6.2: Material cross-correlation coefficients plotted as a function of time for different *Pr*, in cases of forwards and backwards dispersion for markers captured and correlated in the transition region of Poiseuille channel flow: (a) R_{uv}, $y^+ = 37$; (b) R_{vu}, $y^+ = 37$. In order to clearly present the results, the curves for $Pr > 6$ are all represented by the curve for $Pr = 1000$. Also, since the material cross-correlation coefficients obtained from correlations with the spanwise velocities are zero, they are not presented for the transition regions of Poiseuille channel flow.

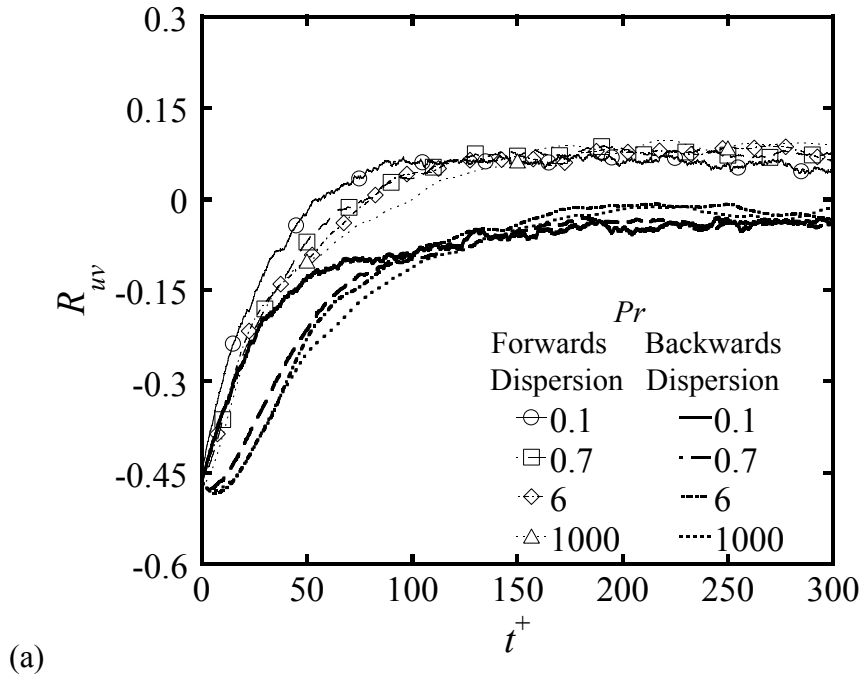

(a)

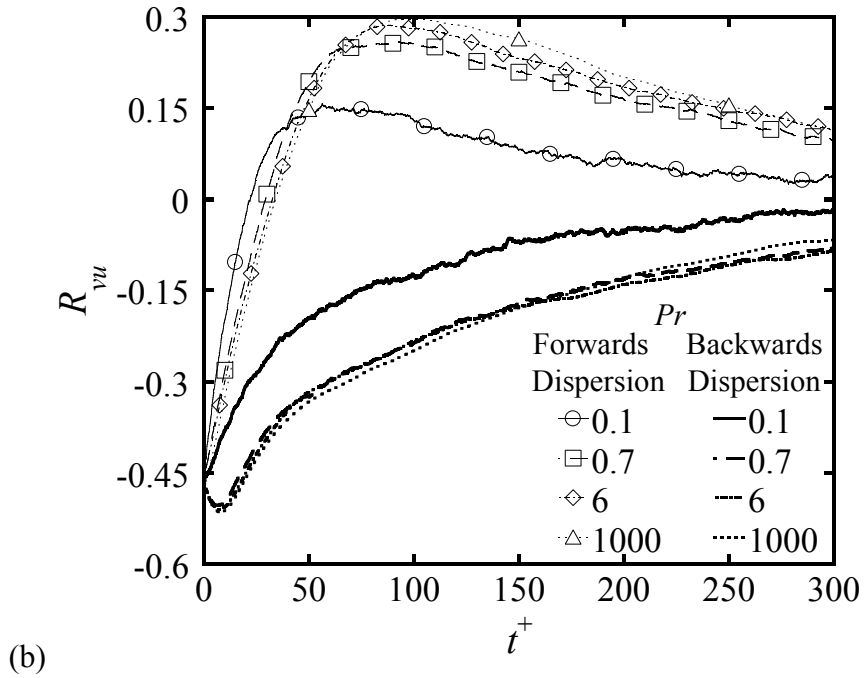

(b)

Figure 6.3: Material cross-correlation coefficients plotted as a function of time for different *Pr*, in cases of forwards and backwards dispersion for markers captured and correlated in the logarithmic region of Poiseuille channel flow: (a) R_{uv}, $y^+ = 75$; (b) R_{vu}, $y^+ = 75$. In order to clearly present the results, the curves for $Pr > 6$ are all represented by the curve for $Pr = 1000$. Also, since the material cross-correlation coefficients obtained from correlations with the spanwise velocities are zero, they are not presented for the logarithmic regions of Poiseuille channel flow.

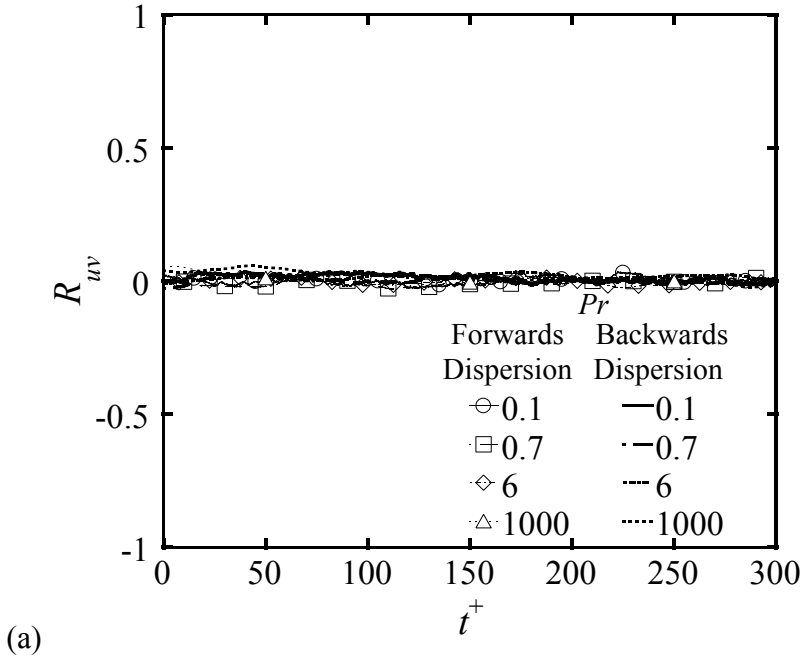

(a)

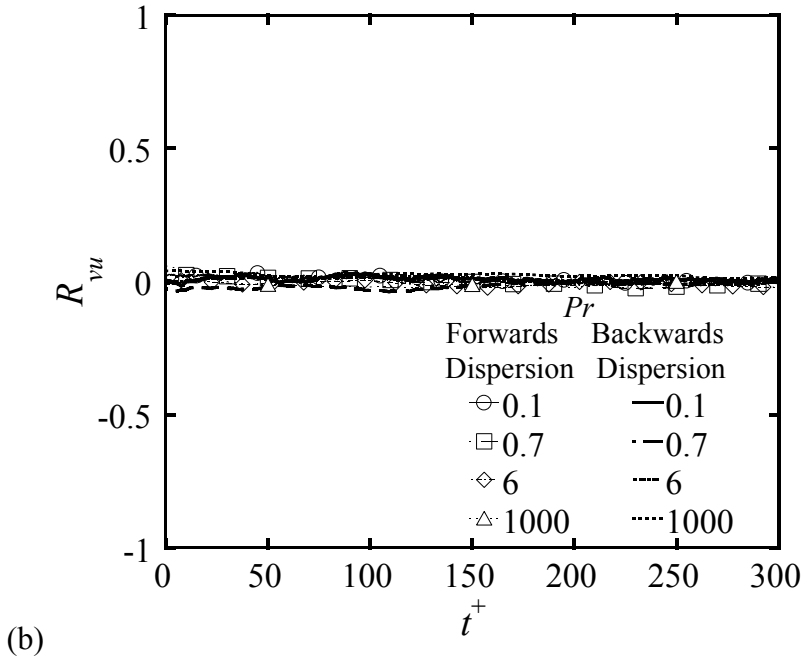

(b)

Figure 6.4: Material cross-correlation coefficients plotted as a function of time for different *Pr*, in cases of forwards and backwards dispersion for markers captured and correlated in the center of the channel for Poiseuille channel flow: (a) R_{uv}, $y^+ = 150$; (b) R_{vu}, $y^+ = 150$. In order to clearly present the results, the curves for $Pr > 6$ are all represented by the curve for $Pr = 1000$. Also, since the material cross-correlation coefficients obtained from correlations with the spanwise velocities are zero, they are not presented for the center of the Poiseuille channel flow.

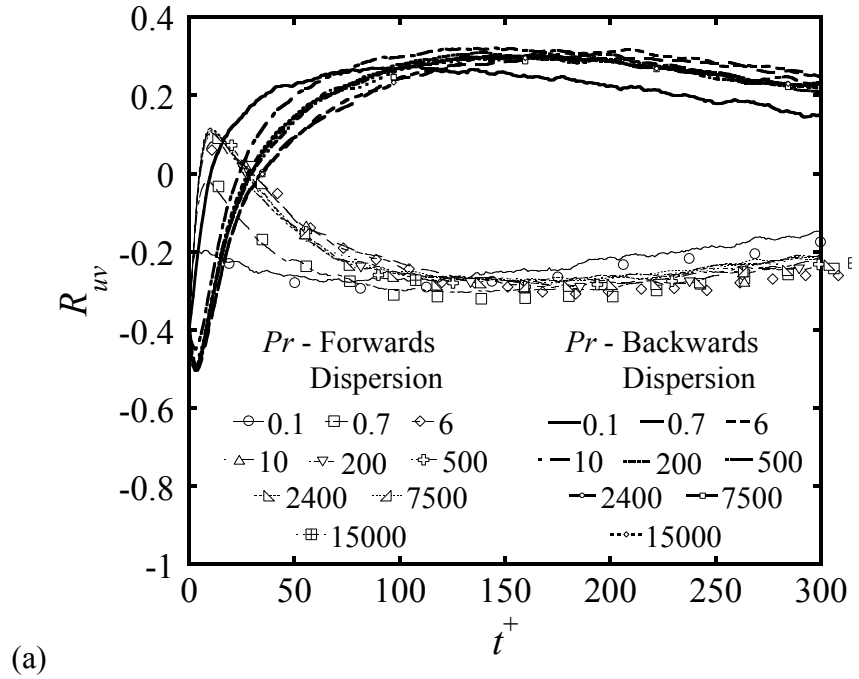

(a)

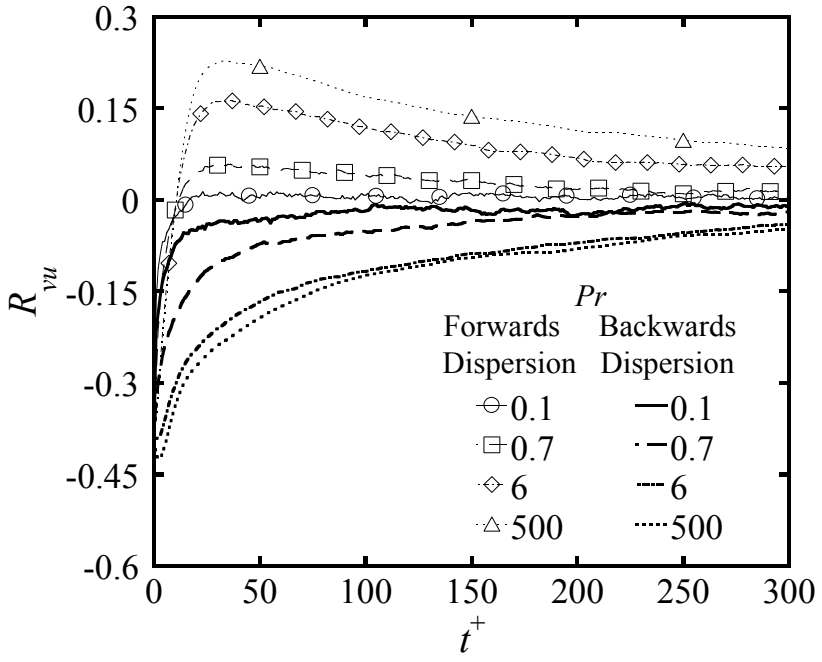

(b)

Figure 6.5: Material cross-correlation coefficients plotted as a function of time for different *Pr*, in cases of forwards and backwards dispersion of markers captured and correlated in the viscous sub-layer of plane Couette flow: (a) R_{uv}, $y^+ = 5$; (b) R_{vu}, $y^+ = 5$. In Figure (b), to clearly present the results, the curves for $Pr > 6$ are all represented by the curve for $Pr = 500$. Also, since the material cross-correlation coefficients obtained from correlations with the spanwise velocities are zero, they are not presented for the viscous region of plane Couette flow.

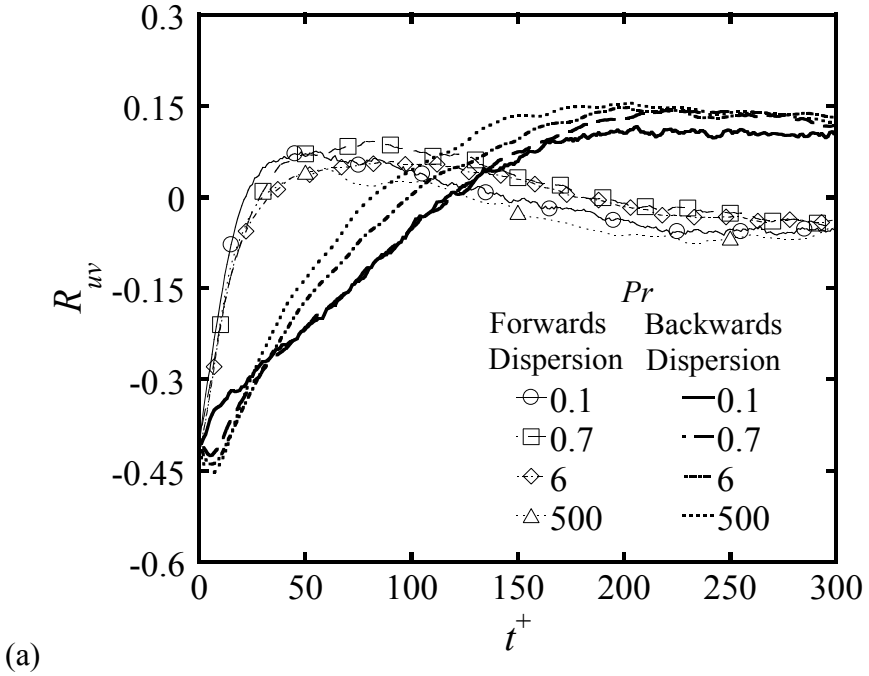

(a)

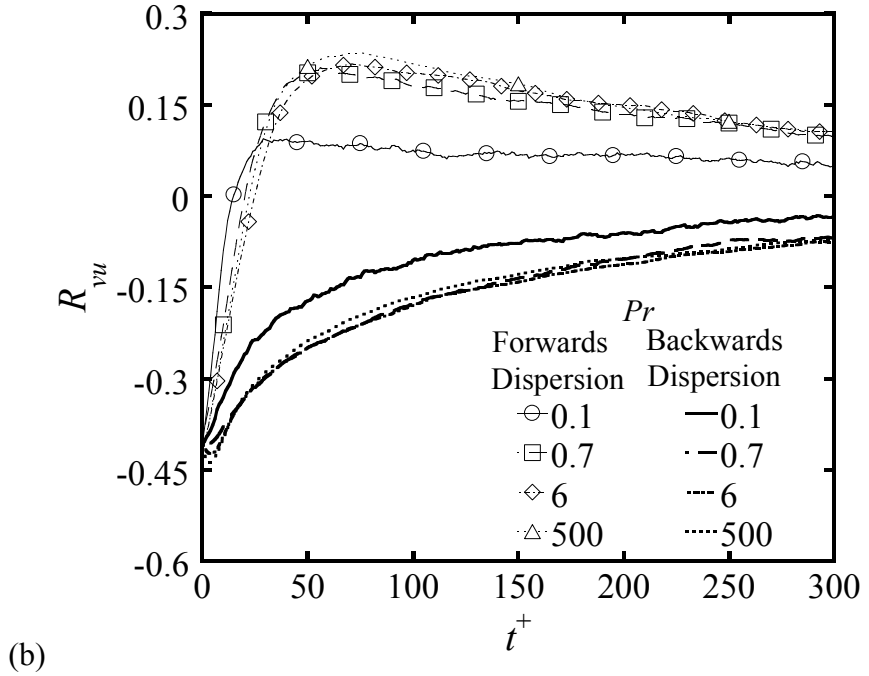

(b)

Figure 6.6: Material cross-correlation coefficients plotted as a function of time for different *Pr*, in cases of forwards and backwards dispersion of markers captured and correlated in the transition region of plane Couette flow: (a) R_{uv}, $y^+ = 37$; (b) R_{vu}, $y^+ = 37$. In order to clearly present the results, the curves for $Pr > 6$ are all represented by the curve for $Pr = 500$. Also, since the material cross-correlation coefficients obtained from correlations with the spanwise velocities are zero, they are not presented for the transition region of plane Couette flow.

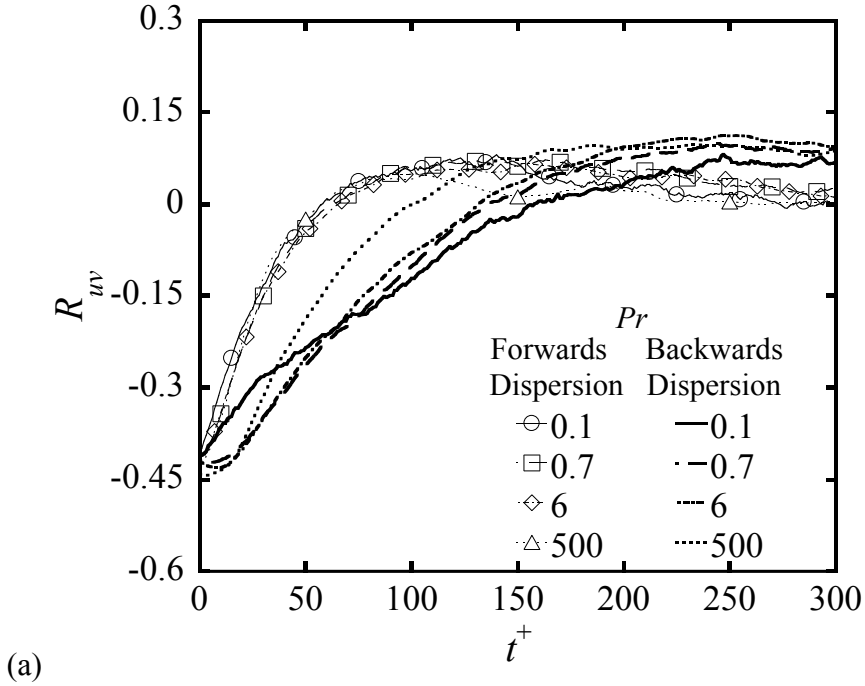

(a)

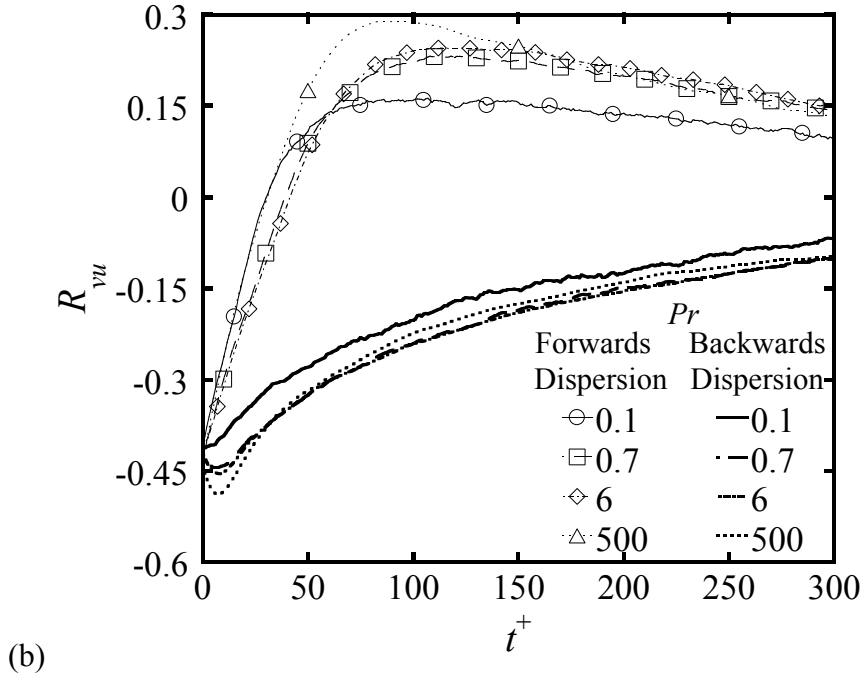

(b)

Figure 6.7: Material cross-correlation coefficients plotted as a function of time for different *Pr*, in cases of forwards and backwards dispersion of markers captured and correlated in the logarithmic region of plane Couette flow: (a) R_{uv}, $y^+ = 75$; (b) R_{vu}, $y^+ = 75$. In order to clearly present the results, the curves for $Pr > 6$ are all represented by the curve for $Pr = 500$. Also, since the material cross-correlation coefficients obtained from correlations with the spanwise velocities are zero, they are not presented for the logarithmic region of plane Couette flow.

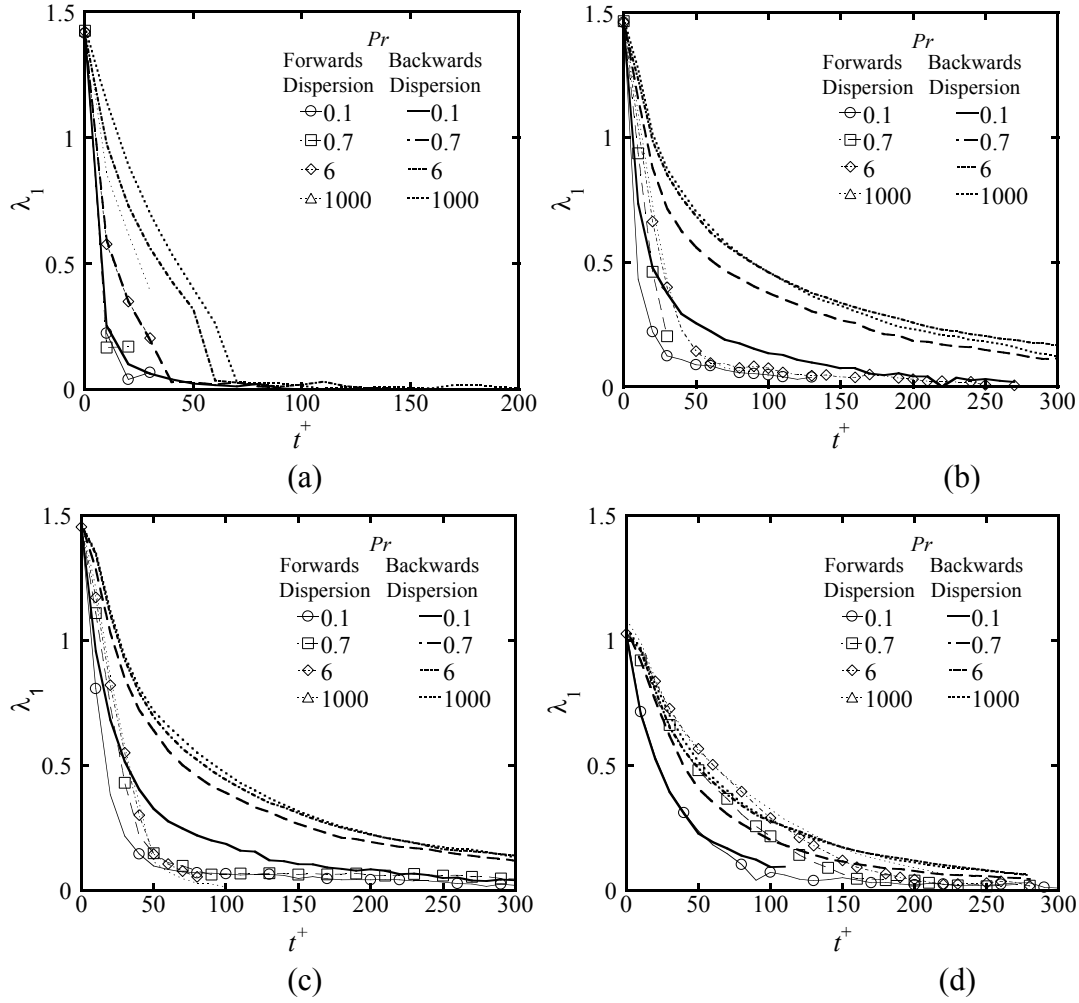

Figure 6.8: Highest eigenvalues obtained from the correlation coefficient matrix for both forwards and backwards dispersion plotted as a function of time for different *Pr* in case of Poiseuille channel flow: (a) $y^+ = 5$; (b) $y^+ = 37$; (c) $y^+ = 75$; (d) $y^+ = 150$. In order to present the plot with clarity, the curves for $Pr > 6$ are all represented by the curve for $Pr = 1000$.

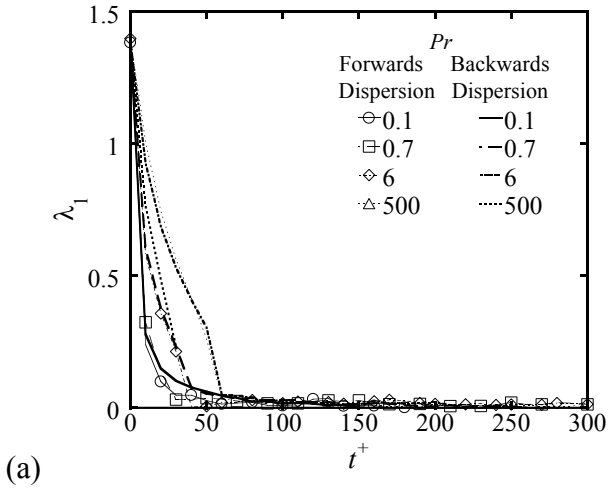

(a)

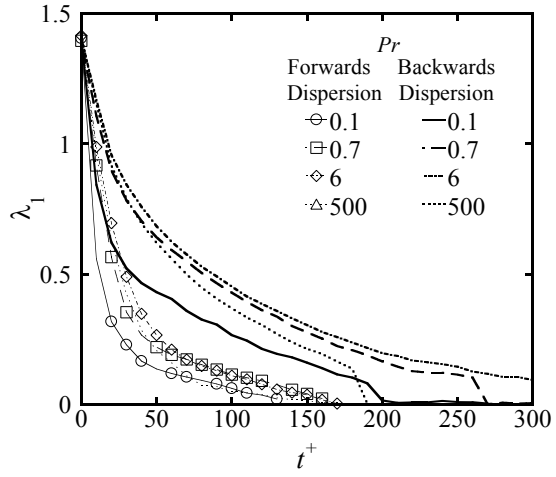

(b)

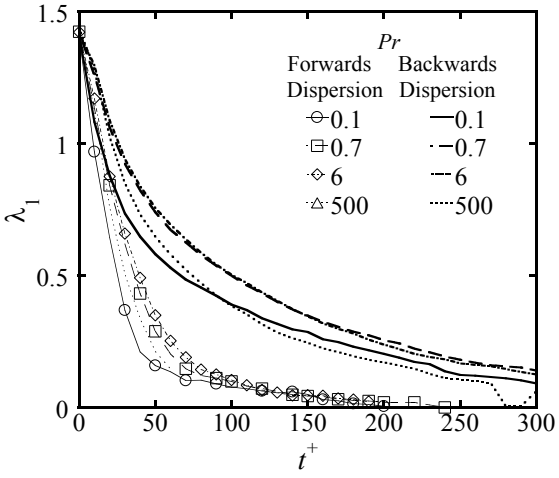

(c)

Figure 6.9: Highest eigenvalues obtained from the correlation coefficient matrix for both forwards and backwards dispersion plotted as a function of time for different *Pr* in case of plane Couette flow: (a) $y^+ = 5$; (b) $y^+ = 37$; (c) $y^+ = 75$. In order to present the plot with clarity, the curves for $Pr > 6$ are all represented by the curve for $Pr = 500$.

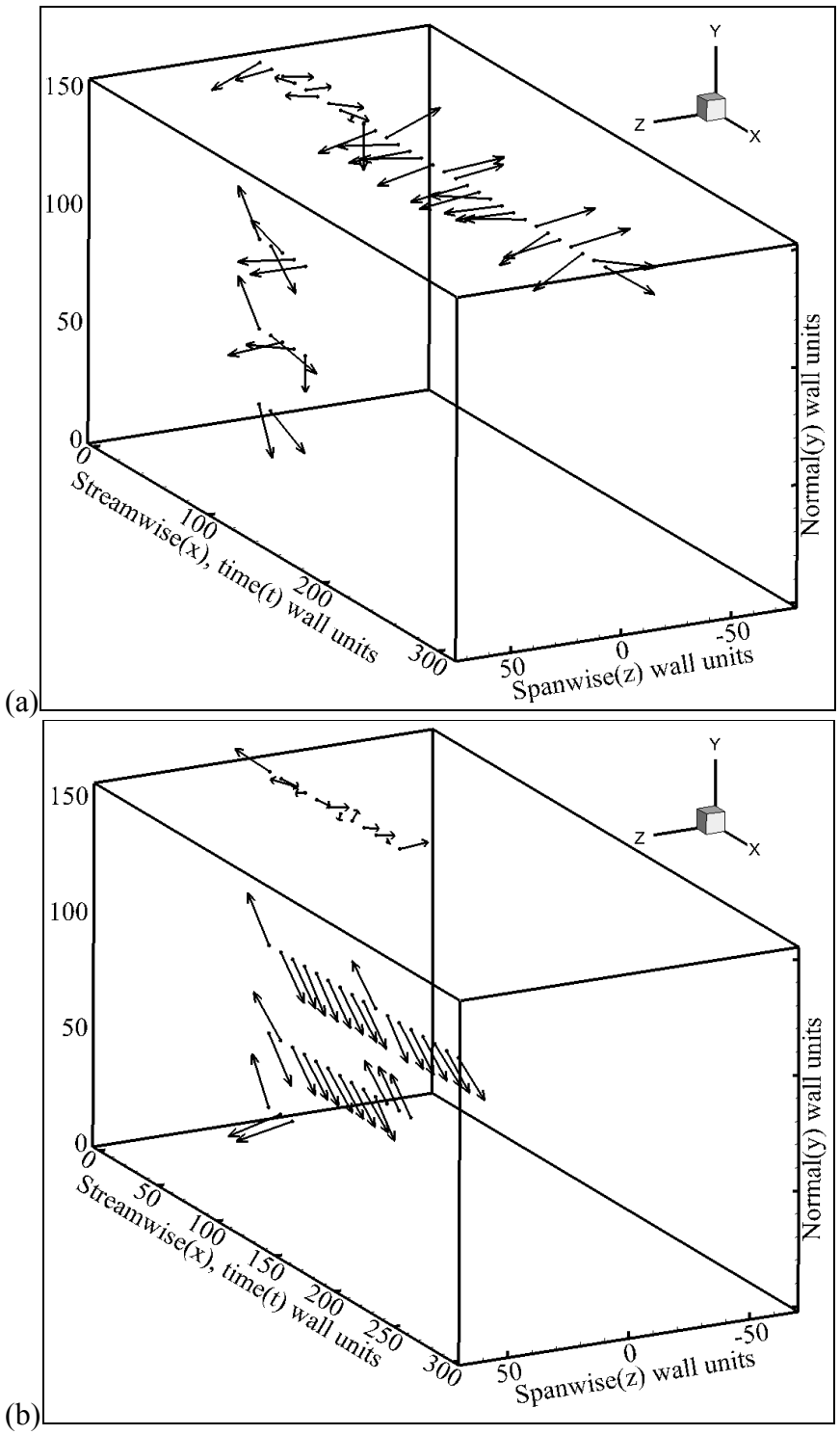

Figure 6.10: Orientation of the eigenvectors corresponding to the highest eigenvalues, plotted in three dimensions in a domain comparable to the computational box, not to exact scale, as a function of time, for a $Pr = 0.1$ in all four regions of Poiseuille channel flow: (a) forwards dispersion; (b) backwards dispersion.

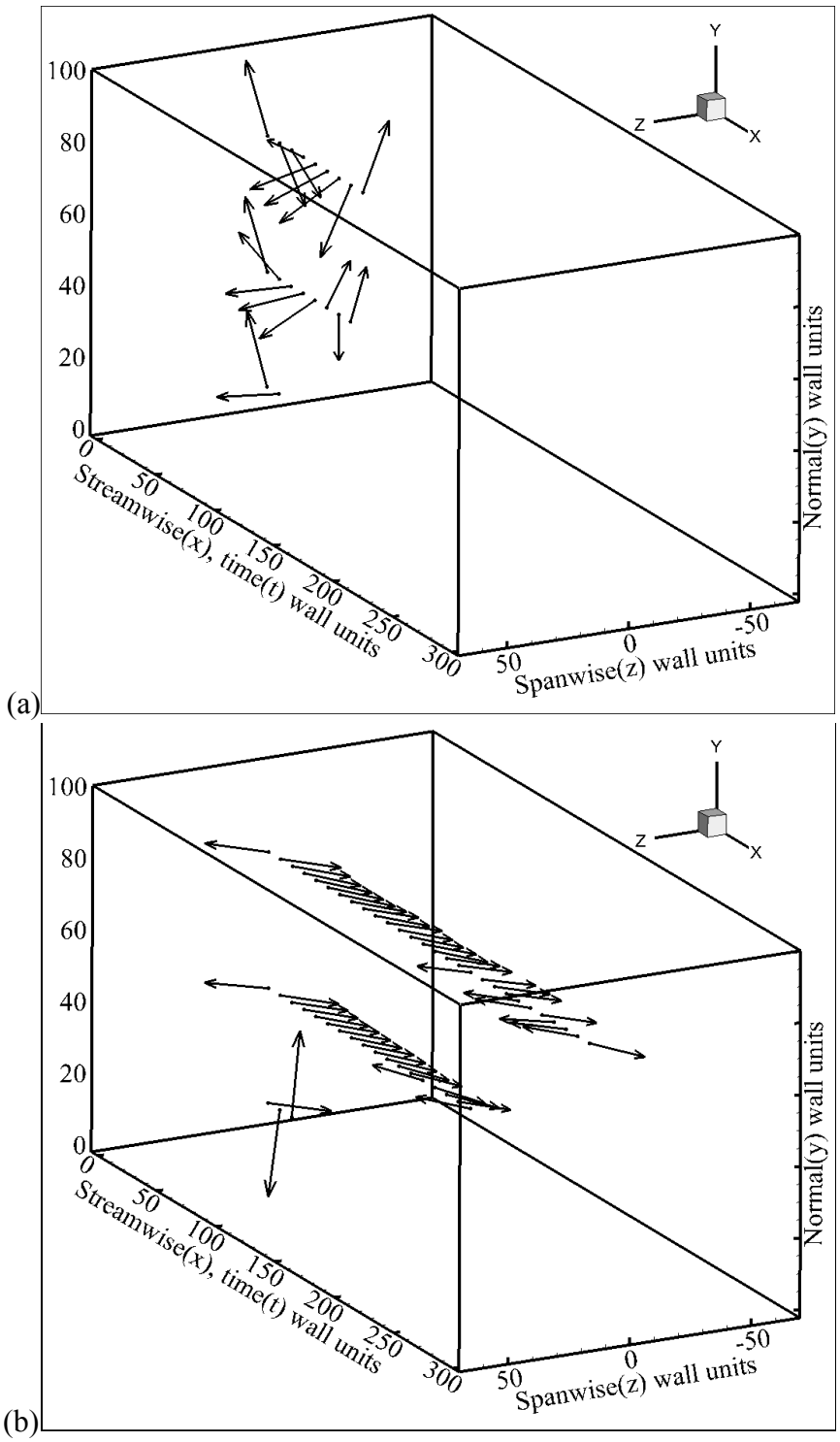

Figure 6.11: Orientation of the eigenvectors corresponding to the highest eigenvalues, plotted in three dimensions in a domain comparable to the computational box, not to exact scale, as a function of time, for a $Pr = 0.1$ in all three regions of plane Couette flow: (a) forwards dispersion; (b) backwards dispersion.

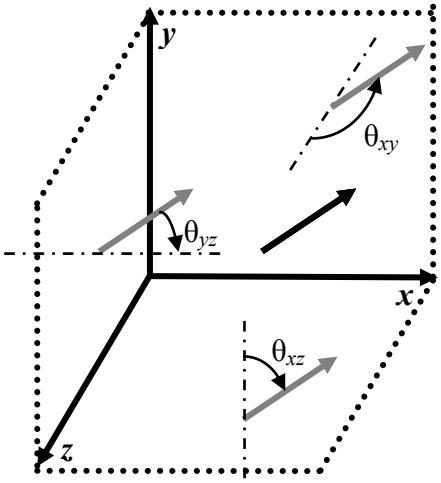

Figure 6.12: Representation of the different angles the primary eigenvector makes with the normal of the three different planes in our current study.

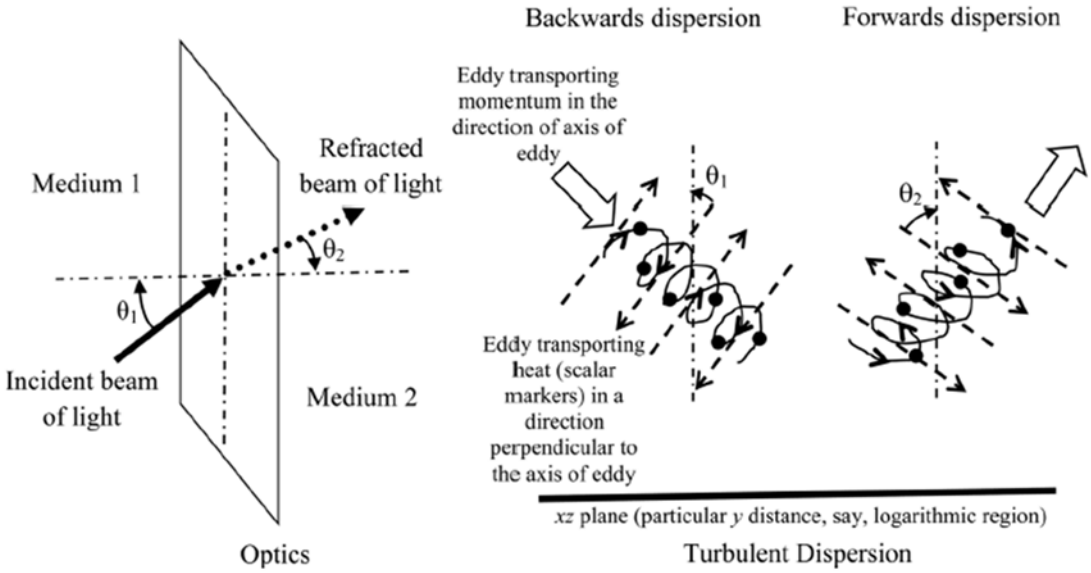

Figure 6.13: Schematic of the suggested analogy between optics and turbulent backwards and forwards dispersion. The angle of incidence of light in medium 1 (θ_1) is similar to the angle that the direction of backwards dispersion of heat makes with the normal of the plane (presented also as θ_1 in the right panel), while the angle of refraction in medium 2 (θ_2) is comparable to that of the forwards dispersion with the normal of the plane (presented as θ_2 in the right panel of the figure).

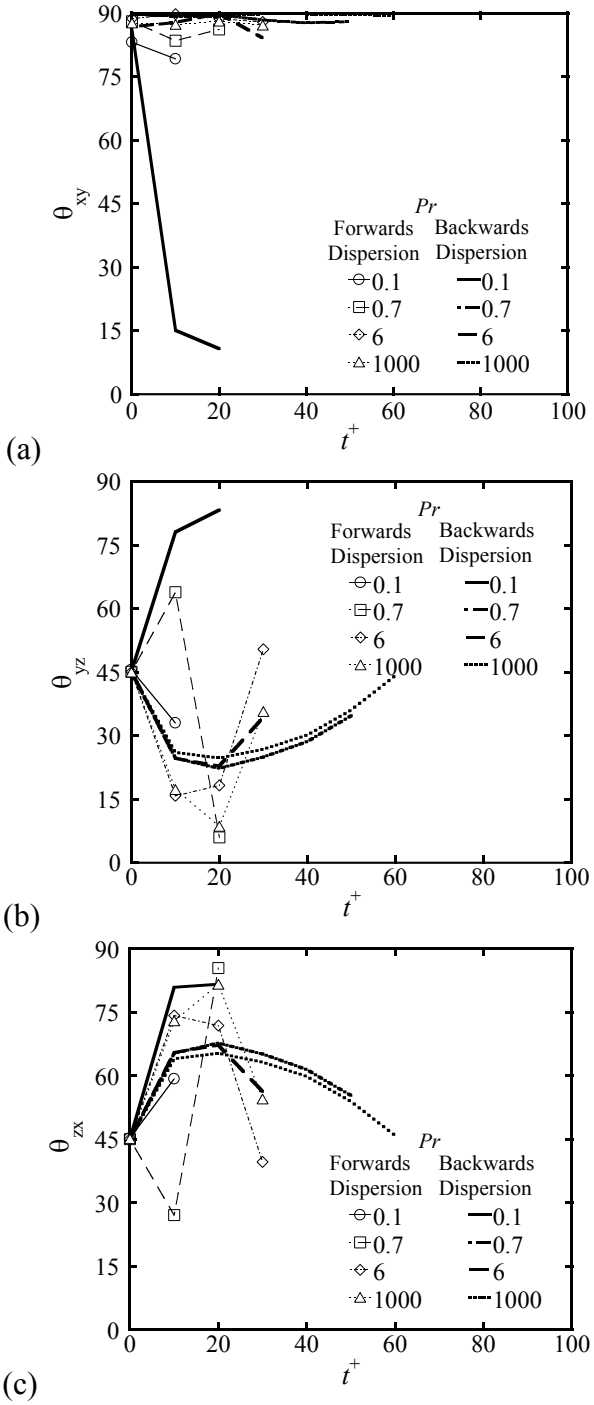

Figure 6.14: Direction of the eigenvector corresponding to the highest eigenvalue obtained for markers captured and correlated in the viscous sub-layer with forwards and backwards dispersion plotted as a function of time, for the case of different *Pr* in Poiseuille channel flow: (a) angle with the *xy* plane; (b) angle with the *yz* plane; and (c) angle with the *zx* plane. In order to present the plot with clarity, the curves for $Pr > 6$ are all represented by the curve for $Pr = 1000$.

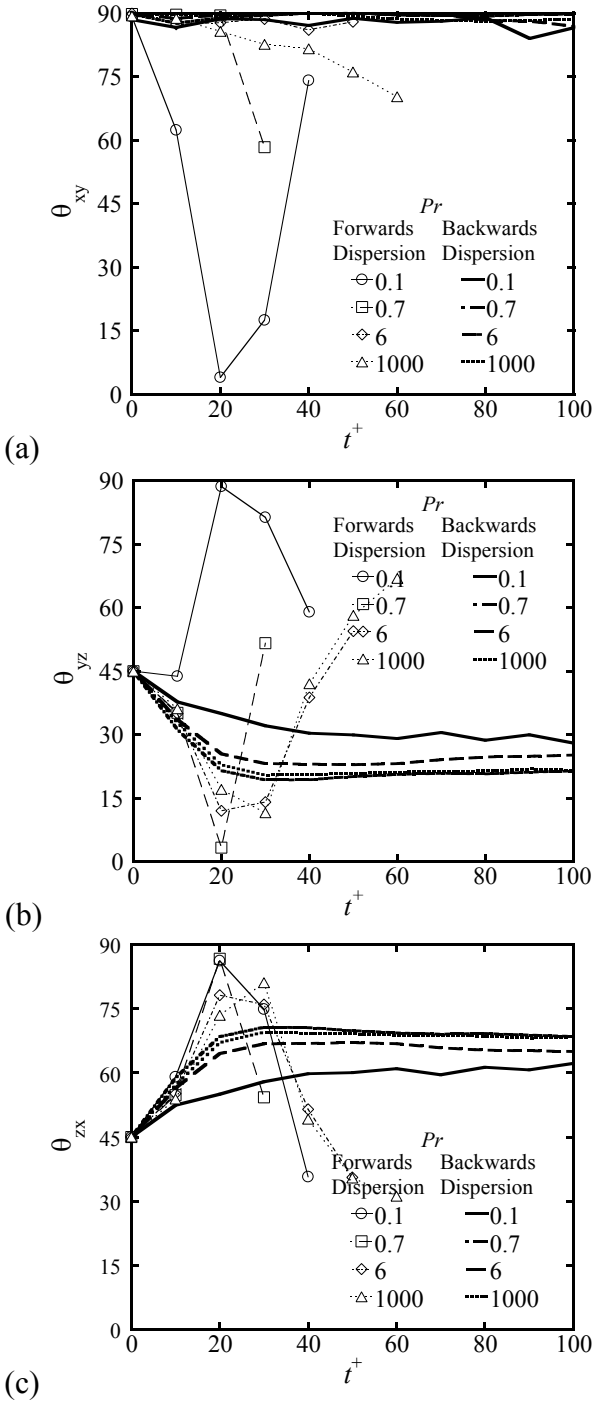

Figure 6.15: Direction of the eigenvector corresponding to the highest eigenvalue obtained for markers captured and correlated in the transition region with forwards and backwards dispersion plotted as a function of time, for the case of different *Pr* in Poiseuille channel flow: (a) angle with the *xy* plane; (b) angle with the *yz* plane; and (c) angle with the *zx* plane. In order to present the plot with clarity, the curves for $Pr > 6$ are all represented by the curve for $Pr = 1000$.

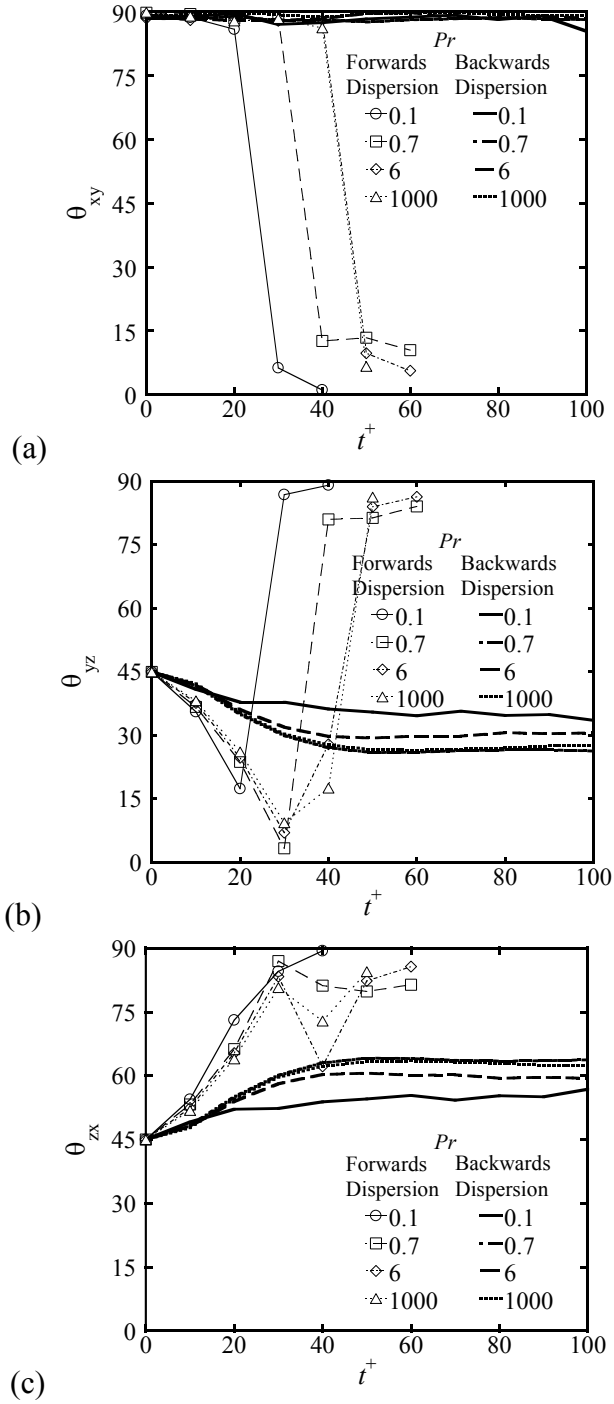

Figure 6.16: Direction of the eigenvector corresponding to the highest eigenvalue obtained for markers captured and correlated in the log-layer with forwards and backwards dispersion plotted as a function of time, for the case of different *Pr* in Poiseuille channel flow: (a) angle with the *xy* plane; (b) angle with the *yz* plane; and (c) angle with the *zx* plane. In order to present the plot with clarity, the curves for $Pr > 6$ are all represented by the curve for $Pr = 1000$.

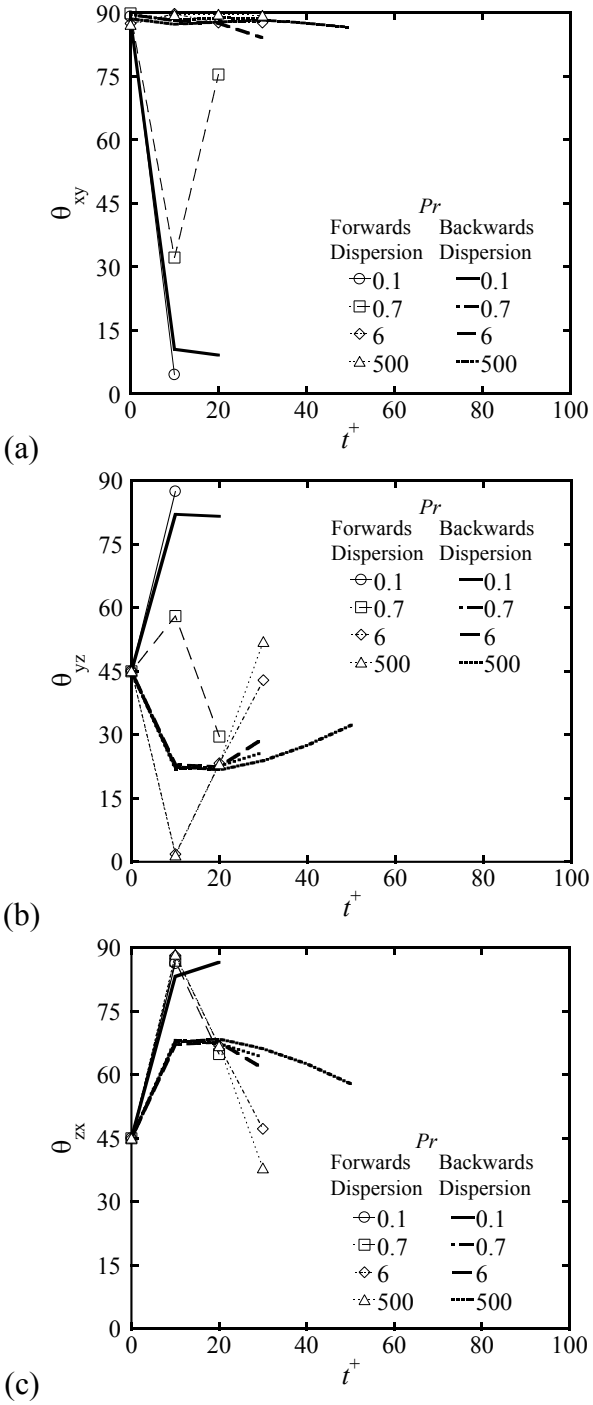

Figure 6.17: Direction of the eigenvector corresponding to the highest eigenvalue obtained for markers captured and correlated in the viscous sub-layer with forwards and backwards dispersion plotted as a function of time, for the case of different *Pr* in plane Couette flow: (a) angle with the *xy* plane; (b) angle with the *yz* plane; and (c) angle with the *zx* plane. In order to present the plot with clarity, the curves for $Pr > 6$ are all represented by the curve for $Pr = 500$.

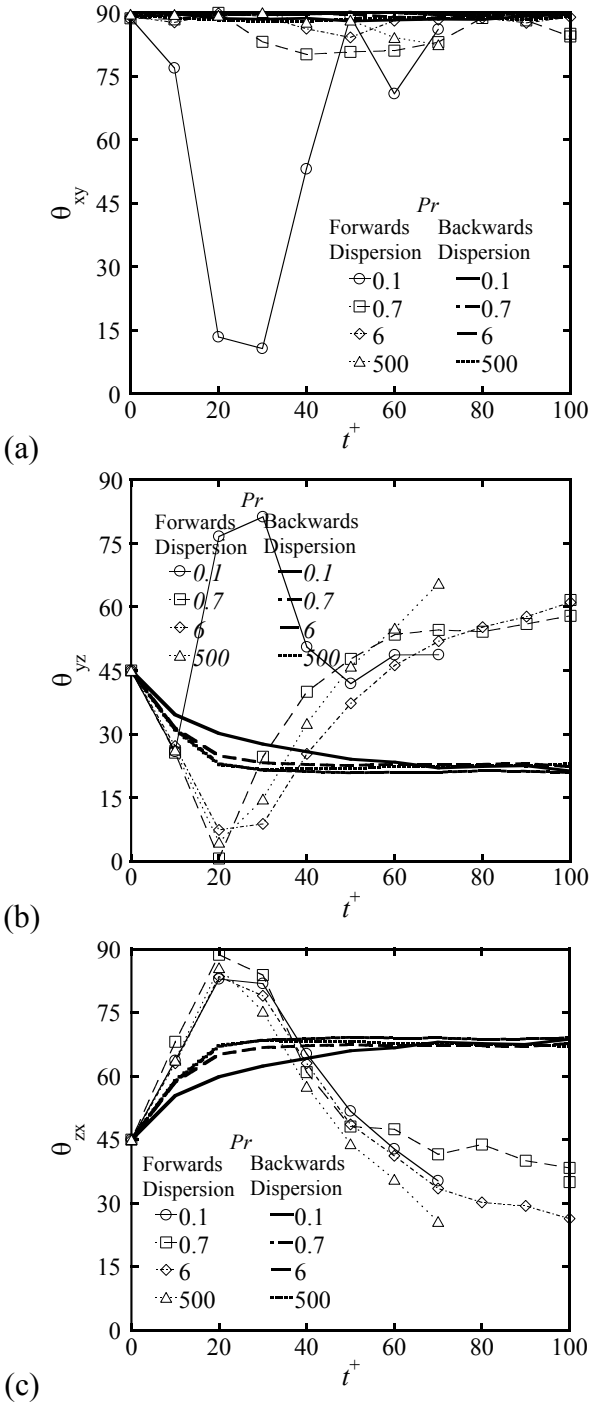

Figure 6.18: Direction of the eigenvector corresponding to the highest eigenvalue obtained for markers captured and correlated in the transition region with forwards and backwards dispersion plotted as a function of time, for the case of different *Pr* in plane Couette flow: (a) angle with the *xy* plane; (b) angle with the *yz* plane; and (c) angle with the *zx* plane. In order to present the plot with clarity, the curves for $Pr > 6$ are all represented by the curve for $Pr = 500$.

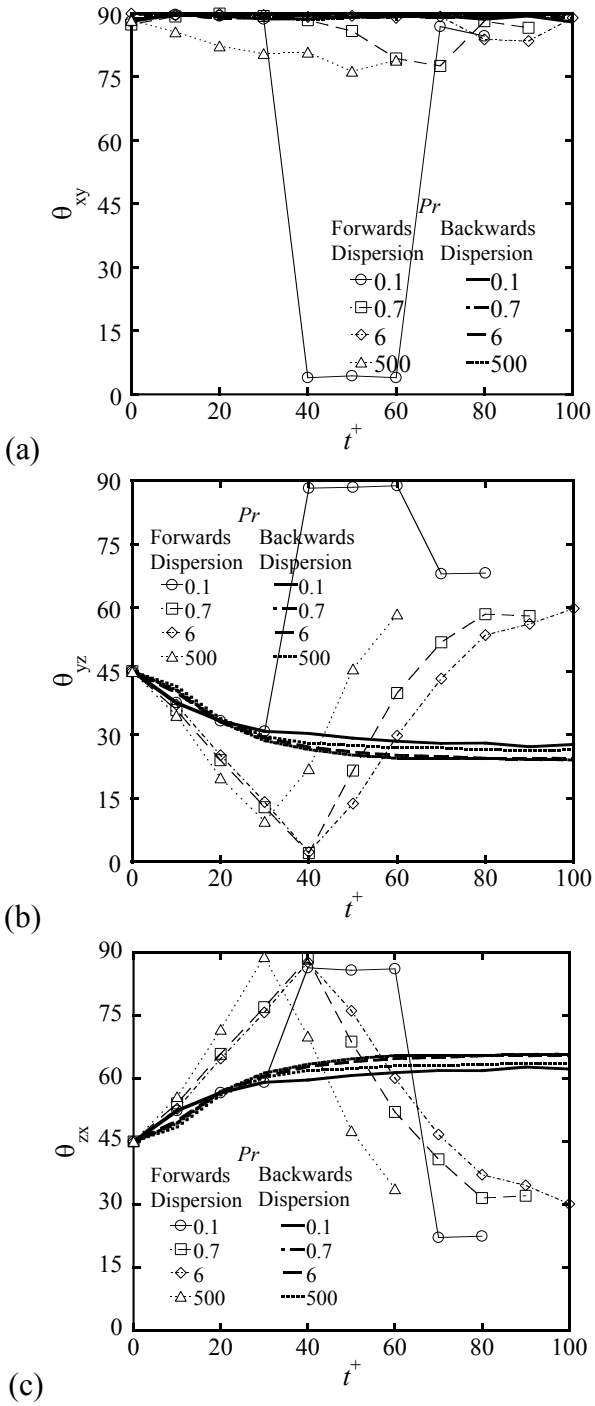

Figure 6.19: Direction of the eigenvector corresponding to the highest eigenvalue obtained for markers captured and correlated in the log-layer with forwards and backwards dispersion plotted as a function of time, for the case of different *Pr* in plane Couette flow: (a) angle with the *xy* plane; (b) angle with the *yz* plane; and (c) angle with the *zx* plane. In order to present the plot with clarity, the curves for $Pr > 6$ are all represented by the curve for $Pr = 500$.

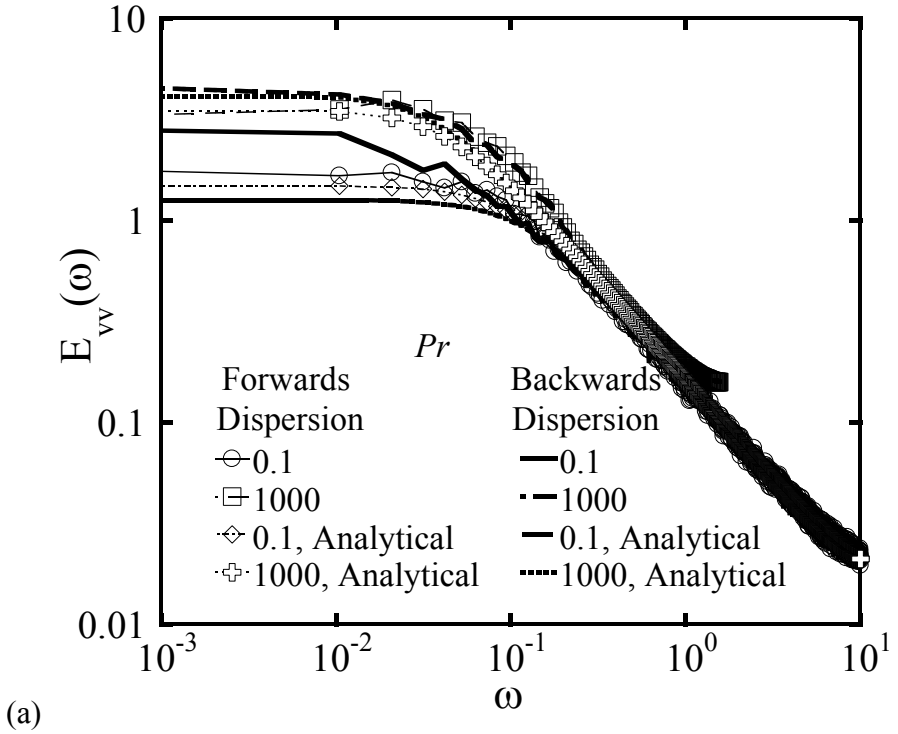

(a)

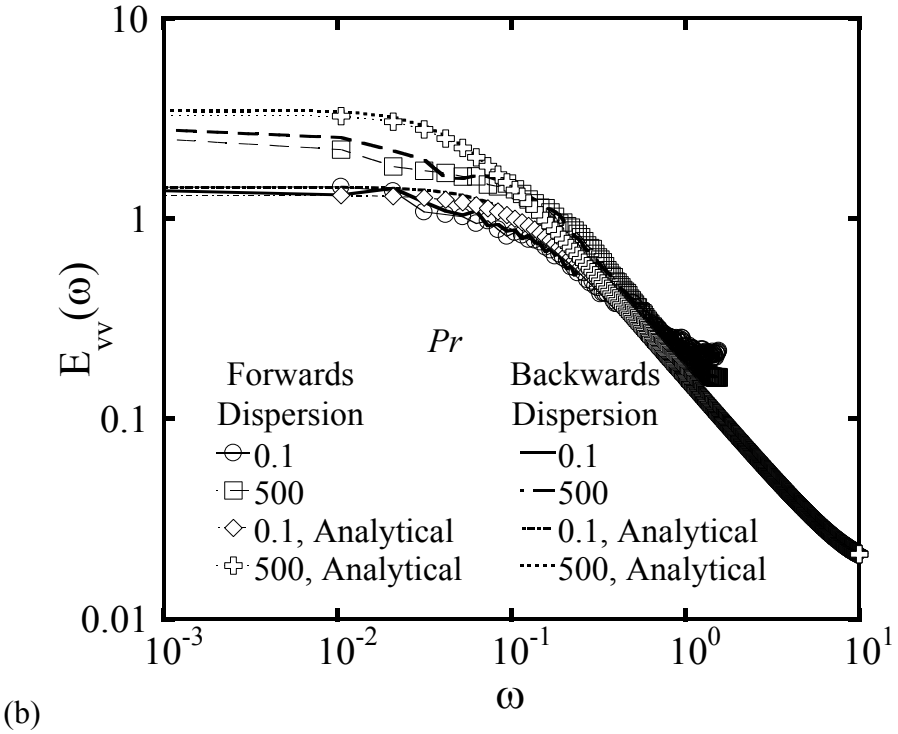

(b)

Figure 6.20: Spectrum of the material autocorrelation coefficient R_{vv} in case of forwards and backwards dispersion of markers captured and correlated in the viscous sub-layer for a low and a high *Pr*: (a) Poiseuille channel flow; (b) plane Couette flow. The lines marked "Analytical" show the spectrum of the material autocorrelation coefficient of $R_{vv} = \exp(-t/\tau_y)$.

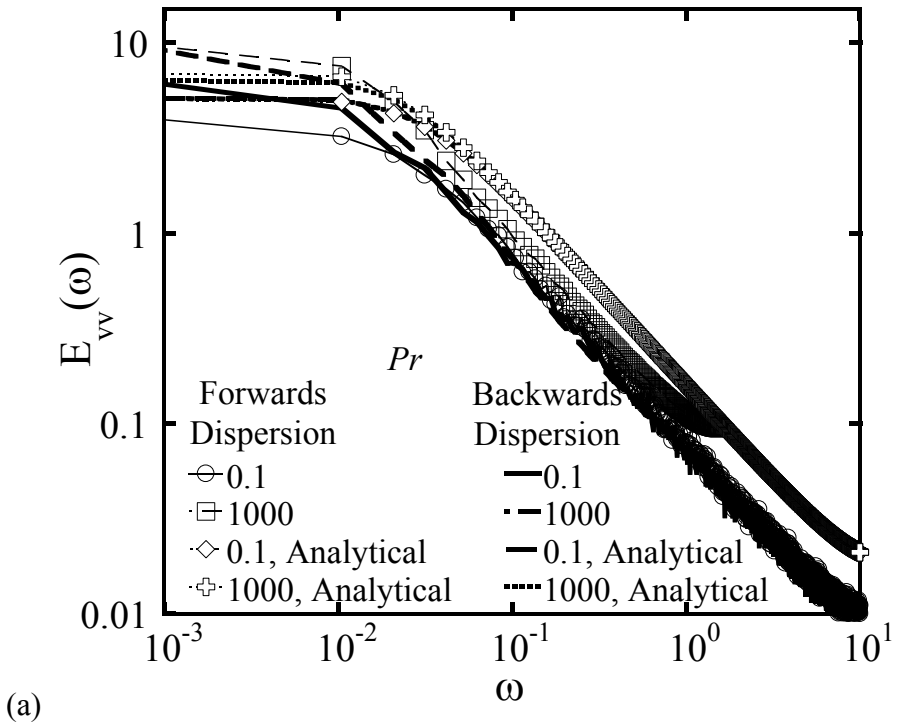

(a)

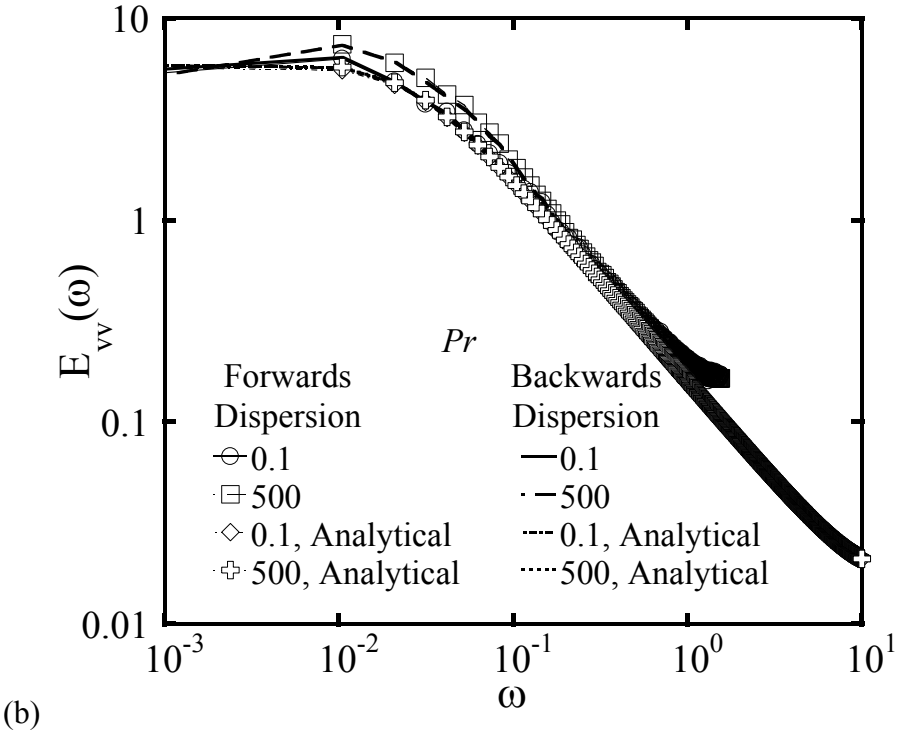

(b)

Figure 6.21: Spectrum of the material autocorrelation coefficient R_{vv} in case of forwards and backwards dispersion of markers captured and correlated in the log-layer for a low and a high *Pr*: (a) Poiseuille channel flow; (b) plane Couette flow. The lines marked "Analytical" show the spectrum of the material autocorrelation coefficient of $R_{vv} = \exp(-t/\tau_y)$.

Chapter 7: SCALING OF HEAT/MASS TRANSPORT

7.1 A new scaling argument

It is apparent from literature review in Chapter 2 that the classical scaling does not do justice in capturing the scales of thermal turbulent transport and that any new scaling proposed must take into consideration the role that turbulence and diffusivity play in altering the turbulence field. Churchill [124] accounted for the turbulence by using the contributing fraction of the turbulent flow to the heat flux, while Wei et al. [110] compartmentalized their scaling by using a term, R_{HF}, which the reflects the ratio of molecular to turbulent fluxes.

In addition, the newly developed scaling parameters from other groups describe mainly the mean scalar profile and also do not take the effects of the fluid diffusivity into account. This work aims at utilizing the extensive database obtained using the DNS/LST approach to propose a scaling that could be universal in capturing both the mean and fluctuating scalar turbulence data. For momentum transfer, Finnicum and Hanratty [170] proposed that the turbulent velocity at the outer edge of the viscous wall region could be scaled with a particular value of the Reynolds stress and they chose the location at which the Reynolds stress is 0.9 of the total stress. Now, understanding that turbulence is a feature of the fluid flow and not of the fluid itself, it is understandable why Finnicum and Hanratty chose the Reynolds stress as the scaling parameter for stress instead of the viscous stress at the wall, Γ_w. In a similar fashion, when considering the case of turbulent heat (or mass) transfer in wall turbulence, the rate at which turbulent heat (or mass) is transported can be used as an appropriate parameter to

capture the scales of turbulence transport. For the case of heat transport in channels with uniform heat flux applied to channel walls, the normal turbulent heat flux has a peak value, $(\overline{T'v'})^+_{\max}$, which accounts for the nature of the turbulent flow, while it includes the effect of the type of fluid on heat transport. It can then be accepted that the different scales of scalar transport in different regions of the channel can be related to this particular maximum value of the normal turbulent heat flux. Hence, a logical scaling parameter for length might be the distance from the wall in the wall-normal direction where the normal turbulent heat flux reaches a maximum, $y^+_{Tv^+_{\max}}$, and a scaling parameter for heat flux can be its corresponding maximum value, $(\overline{T'v'})^+_{\max}$. In cases where the maximum normal turbulent heat flux (MNTHF) has a maximum in the center of the channel (for example in cases of constant wall temperature), one can choose a value at which the normal turbulent heat flux becomes a specified percentage (say 90%) of the total normal heat flux, similar to the choice of Finnicum and Hanratty. For the scaling of the distance from the wall, in addition to the location of the MNTHF, an additional correction is chosen as $St^{\frac{1}{4}}\,\mathrm{Pr}^{\frac{1}{4}}$, where *St* is the Stanton number represented in Equation (2.13). Re-writing this definition using wall variables, the *St* is calculated as

$$St = \frac{q_w}{\rho c_p U_\infty (T_w - T_\infty)} = \frac{q_w}{\rho c_p u^*} \frac{u^*}{U_\infty (T_w - T_\infty)} = \frac{T^*}{(T_w - T_\infty)} \frac{u^*}{U_\infty} = \frac{1}{(T_w - T_\infty)^+ U_\infty^+} \tag{7.1}$$

In our implementation of the scaling, the inner length scaling is given by

$$y^+_{si} = \frac{y^+}{y^+_{Tv_{\max}}} St^{\frac{1}{4}}\,\mathrm{Pr}^{\frac{1}{4}} \tag{7.2}$$

and the inner temperature scaling by

$$T_{si} = \frac{T^+}{T_\infty^+ \left(T'v'\right)_{\max}^+} \tag{7.3}$$

where, the superscript + denotes the variables scaled with the classical viscous wall scaling. It should be noted here that the inner scaling proposed in Equations (7.2) and (7.3) is shown as a function of quantities already scaled in viscous wall units – of course the concept applies when the temperature is scaled any other way.

The newly proposed scaling, which uses the MNTHF as a scaling parameter has some inherent advantages. First and foremost, since turbulence is a feature of the flow, this choice of maximum normal turbulent heat flux, which is a turbulent flow dependent parameter, is an appropriate scaling parameter. Using the MNTHF avoids the explicit use of the *Re* as a scaling parameter, since it is implicitly accounted for within the values of $y^+_{Tv^+_{\max}}$ and $(\overline{T'v'})^+_{\max}$. In addition to this, using MNTHF as a scaling parameter, which is neither a wall-dependent or viscous-based scaling, provides a scaling that is not necessarily restricted to the immediate vicinity of the channel walls. Furthermore, since turbulent heat transport is also dependent on the type of fluid, the maximum normal turbulent heat flux as a proposed scaling parameter can account for the different molecular diffusivities and, thus, successfully help in capturing the thermal field scales of different *Pr* fluids. Finally, the choice of scaling with MNTHF makes this scaling parameter universally applicable to both the mean and fluctuating scalar statistics.

7.2 Simulation parameters and procedure

Calculations using DNS for two Re_τ values (150 and 300) are used for the case of Poiseuille channel flow. In the LST part of the simulation, the cases of *Pr* = 0.7, 3, 6,

10, 200, 500, 2400, 7000, 15000 and 50000 for the low Re_τ case are simulated. The simulation consider Pr = 0.1, 0.7, 6, 20, 50, 200, 2400, 7000, 15000 and 50000 for the high Re_τ case. Each of the simulations is carried out as two sets of simulations, one for the lower values of Pr and the other consisting of higher Pr. The simulations are categorized as A, B, C and D. Complete details of these simulations are provided in Table 7.2. The mean temperature profile in a channel can be obtained by using the combined DNS/LST approach. The basic idea involves the description of the behavior of an instantaneous line source of markers released at the wall of the channel. This behavior is expressed by the joint and conditional probability density function for a marker to be at a location (x, y) in the channel at time t, given that the marker was released at location x_0 at time t_0, $P_1(x-x_0, y, t-t_0 | x_0, t_0)$. The trajectories of all the markers released into the flow field are used as the ensemble to obtain this conditional probability density function, which physically represents a concentration or a snapshot of a cloud of contaminants released from $x_0 = 0$ at t_0. The mean temperature profile in a channel, where heat is added to the fluid from the bottom wall at a constant rate (isoflux condition), can be obtained from P_1 by integrating over time and over the streamwise direction [142, 157]. In discrete form, the integral is:

$$\overline{T}(y) = \sum_{x=x_0}^{x_f} \sum_{t=t_0}^{t_f} P_1(X - x_0, y, t - t_0 | x_0, t_0) \qquad (7.4)$$

Equation (7.4) provides the mean temperature profile at a distance x_f-x_0 downstream from a step change in heat flux at the channel walls at x_0. Also, this mean temperature is with respect to a step change in wall heat flux provided to only one wall (bottom wall in our case) with the other wall kept adiabatic. For simplicity this case is referred to as

Case 1 for the rest of this study. Knowing that the channel is symmetric along the center-plane, one can find the mean temperature profile in the channel for the case of heat flux applied to both top and bottom walls at x_0 by using the following equation, where y=0 is the bottom channel wall:

$$\overline{T}(y^+) = \overline{T}_1(y^+) + \overline{T}_1(2h^+ - y^+) \qquad (7.5)$$

where, T_1 in Equation (7.5) is the temperature calculated using Equation (7.4). This case of both the channel walls being heated with constant uniform heat flux is referred to as Case 2. Combining Cases 1 and 2 with four different simulation cases A, B, C and D, appearing in Table 7.2, leads to 8 different scenarios. It should be noted here, however, that in Cases 2A, 2B, 2C and 2D, the number of markers tracked during numerical simulation is double that of Cases 1A, 1B, 1C and 1D, respectively.

7.3 Results and discussion

In the literature review, the origins of the different temperature scaling ideas that have been proposed over the years, notably in the works of Churchill et al. [124, 138], Wei et al. [110] and Wang et al. [115, 120] have been presented. The different scaling concepts are tabulated in Table 7.1. Each idea, innovative in its own way, has addressed some issues of scaling, while leaving some other questions unanswered.

The framework of Churchill et al. was motivated by the author's philosophy to remove empiricisms associated with the theoretical momentum and heat transport models. This framework accurately prescribes the functional forms of correlating equations for different momentum and heat transport parameters, but as opposed to works of Wei et al. does not explore the dynamics behind the different scales in the

scalar turbulence field. Works of Wei et al. explored the principal layer structure of the thermal field while expounding on the associated flow physics. However, the limitation with this approach is the fact that different principal layer structures emerge for different ranges of *Re* and *Pr*. This necessitates the use of different scaling parameters for different Peclet numbers. In addition, using these scaling parameters, though a clear picture of the dynamics of the thermal field emerges, it does not help in describing the fluctuating thermal quantities. The similarity analysis of Wang et al. addressed the former issue of Wei et al., as they devised inner and outer scaling parameters that help in capturing all the scales of the mean thermal field in one single profile for different pressure gradient flows. Similar to the scaling analysis of Wei et al., however, this scaling analysis is also limited to the mean thermal quantity and it does not take into consideration the effects that *Pr*, as an extra parameter in case of heat transport, adds to the scaling of the thermal field.

The scaling by Churchill et al. and by Wei et al., have been previously addressed in our laboratory [113, 143]. The results of this present work primarily focuses on comparisons of data from the classical scaling, the scaling of Wang et al. and the scaling that has been proposed herein in Section 7.1. As set forth in the discussion in Section 7.1, the normal turbulent heat flux is central to the scaling arguments we put forward in this work. So, the results of the wall-normal turbulent heat flux as a function of normal distance from the channel walls are first presented. The procedure outlined in references [139, 143] is used to obtain the normal turbulent heat flux. Two sets of mean temperature data, from the DNS/LST approach outlined above and from the semi-

empirical mean temperature equation of Kader [47], are used for calculating the normal turbulent heat flux.

In Figure 7.1 we present the variation of normal turbulent heat flux in the vertical direction when one wall (bottom wall) is heated with constant heat flux, for a flow with Re_τ = 150 (referred to as "low *Re*" from here on), with low *Pr*'s, *Pr* = 0.7, 3, 6, 10, 200, Case 1A, plotted in (a), and high Prandtl numbers (*Pr* = 500, 2400, 7000, 15000, 50000), Case 1C, plotted in (b). The normal turbulent heat fluxes become dominant as one travels away from the near wall region towards the channel core, where all the contribution to the total heat flux is from the turbulent heat flux. The diffusive contribution to the total normal heat flux becomes smaller with increasing *Pr,* because of the thinner diffusive sublayers. Due to the constant heating of one wall and the adiabatic nature of the other, the normal turbulent heat flux has a finite value ≈ 0.55 at the center of the channel. In the case of Re_τ = 300 (referred to "high *Re*" from here on), the values of the normal heat flux as the function of normal distance is shown in Figure 7.2, for lower *Pr*'s (0.7, 6, 20, 50), Case 1B, plotted in (a), and higher *Pr*'s (200, 2400, 7000, 15000, 50000), Case 1D, plotted in (b). The data for the high *Re* indicate that all the characteristics of normal heat flux found in the low *Re* flow, are replicated.

The same results for the normal turbulent heat flux for Case 2, where both channel walls are heated with the same heat flux, is presented in Figures 7.3 and 7.4, for low and high *Re*, respectively. The results show the same trends observed in the case of one heated channel wall, with the main difference arising in the center of the channel (where the heat flux balance leads to a zero value of the normal turbulent heat flux). The results for both cases of wall heating, for different *Re* and *Pr* show good agreement

between data from the DNS/LST and from Kader's equation. It is of significance to mention here that the Lagrangian tracking approach of calculating mean temperature profile, just for the low *Pr* (0.7 and 3) cases results in some data noise. Hence, this noise is transferred to the normal turbulent heat flux values through the mean temperature gradients. The curves for the low *Pr*, in the previous figures are thus a polynomial fit of the corresponding data. As a result, there are small deviations in the normal turbulent heat flux values at low *Pr* from Kader's data. Results for the low *Re* data, with uniform heat flux boundary conditions at the channel walls, have also been previously documented in our laboratory [143], as well as in the works of Kasagi et al. [28] and Kim and Moin [171]. The high *Re* results shown here also compare well with the data of Kawamura et al. [172].

It is interesting to comparatively look at Figures 7.1 and 7.2, or Figures 7.3 and 7.4, to notice any effect that the *Re* has on the values of the normal turbulent heat flux. Such a comparison is shown in Figures 7.5(a) and (b), for uniform heat flux applied from one wall and both walls, respectively. In order to notice differences arising for the high *Pr* cases, the graphs are plotted in semi-log scale, with the different *Pr* indicated by the pointed arrows. For low *Pr*'s (0.7 and 6), in the thermal buffer layer, there is clear increase in the values with increase in *Re*. This behavior has been observed previously in the works of Kawamura et al. [172], for *Pr* = 0.025, 0.2 and 0.7, though they used a slightly different set of *Re*, Re_τ = 180 and 395, in their study. For the high *Pr* cases, shown in Figures 7.5(a) and (b), in the thermal buffer regions, one can notice only small differences in the values of the normal turbulent heat flux. As a relative percentage, these differences are very small and do not reflect a trend of the normal

turbulent heat flux with *Re*. The normal turbulent heat flux in the diffusive sublayer shows a clear characteristic behavior with respect to *Re* and *Pr*. At low *Pr*, *Pr* = 0.7 and 6 for Case 1 heating and *Pr* = 0.7 for Case 2, there is a clear increase in normal turbulent heat flux with an increase in *Re*. This result was also reported in the work of Kawamura et al. where they found a slight increase in the slope of the normal turbulent heat flux normalized with the *Pr* and wall-normal distance. The large *Pr* results, *Pr* > 200, for one heated wall and *Pr* > 6 for two heated walls, in the diffusive sublayer, however, show that the normal turbulent heat flux decreases with increasing *Re* in these regions.

The early works of Shaw and Hanratty [173], studying high *Pr*, suggested that the rate of heat transfer, controlled by convective motion, is greatly dampened close to wall surface by the effects of molecular diffusion. They observed that the viscous sublayer acts as a low-pass filter, allowing only the low frequency velocity fluctuations while filtering out the high-frequency velocity fluctuations. The "low-pass filtering effect" has also been reported in the works of Hasegawa and Kasagi [174], and Na and Hanratty [175]. This low-pass filtering effect could be the reason behind the decrease in the normal turbulent heat flux with increasing *Re* in the diffusive sublayer. Comparatively imagining the large and small scales of turbulent transport in the low and high *Re*, the high *Re* would have a higher number of large convective scales compared to the low *Re*. However, these get filtered out by the viscous sublayer resulting in smaller values of normal turbulent heat flux for the high *Re*. Now, the question arises as to why is this behavior observed only for the high *Pr* and not for the low *Pr*? The work of Abe et al. [31] helps shed some light into the results. Studying the

transport near the wall for low *Pr*, *Pr* = 0.025, 0.71, Abe et al. found first that large scale velocity fluctuations are reported mostly in the outer regions of the flow for such small *Pr*. Also, they found that for small *Pr* due to increased molecular diffusion effects, the contribution of turbulent flux to transport in these layers decreases. So, it is understandable that when *Re* increases for the low *Pr*, the convection effects slightly increase causing the normal turbulent heat flux to increase in value.

The balance equation for the total normal heat flux was can be found in Teitel and Antonia [176] for fully developed turbulent channel flow. For the case of one of the channel walls being heated with constant heat flux while the other wall is adiabatic (Case 1), the equation is given as

$$\frac{1}{\mathrm{Pr}}\frac{dT^+}{dy^+}+(\overline{T'v'})^+=(1+\gamma)\left(1-\frac{y^+}{2h^+}\right) \qquad (7.6)$$

In equation (7.6), $(\overline{T'v'})^+$ is the heat flux normalized by the heat flux at the wall, $(\overline{T'v'})^+=\frac{\rho c_p(\overline{T'v'})}{q_w}$ and γ is a small correction term suggested in the works of Churchill et al. [48, 137, 138, 144] to take into account the turbulent velocity profile. The corresponding equation for the case of both channel walls heated with constant heat flux (Case 2) is given by

$$\frac{1}{\mathrm{Pr}}\frac{dT^+}{dy^+}+(\overline{T'v'})^+=(1+\gamma)\left(1-\frac{y^+}{h^+}\right) \qquad (7.7)$$

The maximum normal turbulent heat flux can be theoretically calculated from Equation (7.6) and Equation (7.7), for the respective cases. For simplicity we make two assumptions, first, that the correction term, γ, is negligible and secondly, the mean temperature in the wall-normal regions where the normal heat flux reaches maximum is

assumed to be logarithmic. The second assumption leads to the temperature gradient given as

$$\frac{dT^+}{dy^+} = \frac{1}{V_k y^+} \tag{7.8}$$

where, V_k is the von Karman constant of the mean temperature profile. The normal turbulent heat flux, thus, for Case 1 becomes

$$(\overline{T'v'})^+ = (1+\gamma)\left(1-\frac{y^+}{h^+}\right) - \frac{1}{\mathrm{Pr}\, V_k y^+} \tag{7.9}$$

Now, neglecting γ and differentiating Equation (7.9) yields

$$\frac{d(\overline{T'v'})^+}{dy^+} = \frac{1}{\mathrm{Pr}\, V_k}\frac{1}{y^{+^2}} - \frac{1}{2h^+} \tag{7.10}$$

which leads to the location of the maximum normal turbulent heat flux to be approximately

$$y^+_{Tv^+_{\max}} = \sqrt{\frac{2h^+}{\mathrm{Pr}\, V_k}} = \sqrt{\frac{2\,\mathrm{Re}}{\mathrm{Pr}\, V_k}} \tag{7.11}$$

which then gives the peak value of the normal turbulent heat flux to be

$$(\overline{T'v'})^+_{\max} = 1 - \sqrt{\frac{2}{V_k\,\mathrm{Pr}\,\mathrm{Re}}} = 1 - \sqrt{\frac{2}{V_k Pe}} \tag{7.12}$$

For Case (2) a similar analysis yields

$$y^+_{Tv^+_{\max}} = \sqrt{\frac{\mathrm{Re}}{\mathrm{Pr}\, V_k}} \tag{7.13}$$

and $$(\overline{T'v'})^+_{\max} = 1 - \frac{2}{\sqrt{V_k Pe_\tau}} \tag{7.14}$$

A similar derivation for Case 2 alone has also been presented by Kawamura et al. [172]. However, Kawamura et al. assumed an approximated correction function, γ, from the velocity profile. Neglecting higher order terms arising for the normal turbulent heat flux, they derived that the location of the maximum normal turbulent heat flux should be

$$y^+_{Tv^+_{\max}} = \sqrt{\frac{\mathrm{Re}}{(1-b)\,\mathrm{Pr}\,V_k}} \tag{7.15}$$

where b in their expression was an empirical constant appearing in the correction function with a constant value of 0.4. The peak value of the normal turbulent heat flux was then given as

$$(\overline{T'v'})^+_{\max} = 1 - 2\sqrt{\frac{1-b}{V_k Pe}} - \frac{2b}{1-b}\frac{1}{V_k Pe} + \frac{b}{(1-b)^{\frac{3}{2}}}\frac{1}{(V_k Pe)^{\frac{3}{2}}} \tag{7.16}$$

We present in Figures 7.6 and 7.7 the wall-normal location of the peak turbulent heat flux as (a) and the peak turbulent heat flux as (b) for Cases 1 and 2, respectively, plotted as a function of the *Pr* and for different *Re*. For both cases the results from the theoretical calculation are presented along with the DNS/LST and Kader results. In Case 2, the results from the theoretical calculation of Kawamura et al. are also presented for comparison. For both cases, the locations of the peak normal turbulent heat flux agree very well between the DNS/LST and the Kader data. But there are considerable variations between the DNS/LST data and the theoretically predicted values. A power law fit of the normal location of maximum normal turbulent flux obtained from both DNS/LST and Kader reveals that it varies approximately with $Pr^{-1/4}$ for both cases. However, the theoretically predicted equations from this study and that of Kawamura et

al. show a $Pr^{-1/2}$ variation. The possible reason behind this behavior could be the assumption of the logarithmic behavior of the mean temperature profile.

The values of the MNTHF, for both Re_τ, increase asymptotically with Pr, approaching the value of one as $Pr \rightarrow \infty$. The value of the maximum normal turbulent heat flux shows good agreement between the results of the DNS/LST and Kader's. Also, there is good agreement, especially, for the medium and high Pr, between the DNS/LST results and the values obtained from the theoretical formulae. We list in Tables 7.3 and 7.4 the location of the peak normal turbulent heat flux and its values, respectively, for Case 1, obtained in three different data sets, namely, DNS/LST, Kader's formula and the theoretical formula. The tables also include the percent differences between the DNS/LST and Kader data, and DNS/LST and theoretical formulae. Similar data are presented in Tables 7.5 and 7.6, for Case 2. Clearly observable are the high percent differences between the theoretically predicted values of the location of the peak normal turbulent heat flux and those from the DNS/LST studies. However, for the value of the peak normal turbulent heat flux, even though the low Pr cases show some differences, the percent differences are extremely small for the medium and high Pr cases. This is because varying values of the peak location of the wall-normal turbulent heat flux do not imply changes in the values of the peak normal turbulent heat flux for high Pr.

The mean temperature profile scaled with the viscous wall scaling (T scaled with T^* and y with ν/u^*), for different Pr, with lower Pr cases in (a) and higher Pr cases in (b), for a flow with $Re_\tau = 150$ in the wall heating Case 1 is presented in Figure 7.8. The same case for $Re_\tau = 300$ is shown in Figure 7.9(a) and (b). The same low Re and

high *Re* cases are presented in Figures 7.10 and 7.11 for the wall heating Case 2. The behavior of the mean temperature profile in turbulent channel flow at low *Re* has been documented in previous works from our laboratory [143, 157]. The data for $Re_\tau = 300$, however, are novel, and similar to the low *Re*, show good agreement with Kader's profile. From the profiles shown in Figures 7.8-7.11, it is apparent that using the friction temperature and the friction velocity does not capture the turbulent scalar scales in the flow. The only collapse in the scaling of the temperature variables using classical scaling has been noticed at very close regions to the boundary walls by scaling the variables using Prandtl number [172]. Hence, scaling with the classical scales does not show any collapse in the mean temperature profile in the channel.

In order to understand the nature of the WC scaling, the mean temperature data are used to present the WC inner scaling. In Figure 7.12, with low *Re* in (a) and high *Re* in (b), we show the mean temperature scaled using the WC inner scaling for Case 1, where one wall is heated while the other wall is being adiabatic, for a variety of *Pr*. Results for the WC inner scaling are presented in Figure 7.13 for Case 2. In both Figures, only the DNS/LST data is shown, since it has been clear from the previously presented data that Kader's formula exhibits similar behavior. For both the wall heating scenarios, this WC scaling, keeping in mind that it has been proposed with respect to adverse pressure gradient studies, shows a good collapse of the mean temperature profiles for different *Pr* very close to the channel walls. However, from the buffer region to the outer region of the channel, for both *Re*, the mean temperature profiles show systematic variations with the *Pr* of the fluid. This is reflected in the decrease in the values of scaled mean temperature with the increase in *Pr*. The results indicate that

the WC inner scaling captures the small scales of turbulent scalar transport in the diffusive sublayer, which exhibit similar scales irrespective of the *Pr* of the fluid. However, the scaling fails to account for the variations in scales that become important to heat transfer with the variation in *Pr* in the buffer and outer regions of the channel. So, in effect, even though the WC inner scaling has been shown to account for the effects of ZPG, APG and FPG in the turbulent scalar field [115], in the turbulent regions of the channel, it fails to capture the effects of different fluid *Pr*.

The scaling proposed in this work (i.e, the maximum normal turbulent heat flux, MNTHF, scaling) is presented for Case 1 of wall heating in Figure 7.14 with low *Re* data in (a) and high *Re* in (b). The corresponding Case 2 results are presented in Figure 7.15. From the scaling results, it can be confirmed that the value of maximum normal turbulent heat flux, $(\overline{T'v'})^+_{\max}$, is a viable parameter for capturing the turbulent scalar scales while the location of the normal turbulent heat flux, $y^+_{Tv^+_{\max}}$, with fluid parameters factored in it, can help in doing the same for the turbulent length scales. Utilizing the peak location and the peak values of the normal turbulent heat flux for the scaling, one would expect that they are applicable in regions where there are increased contributions due to the dominance of convective transport. The results here verify this conjecture by showing that the collapse in the mean temperature is very good in the inner and buffer regions of the channel. The average of the scaled mean temperature profiles calculated from all the different cases of *Pr* is represented in Figures 7.14 and 7.15 by an orange dark line and the error bars are represented by the cyan colored lines. Admittedly, in some cases of *Pr*, at some regions of the channel, the values of the scaled mean temperature profile show deviations from the averaged value, with values being outside

the error bars. This could be due to the sensitivity of the scaled data to the peak location and value of the normal turbulent heat flux. To analyze this effect, the data for the peak value and location of the normal turbulent heat flux obtained from the theoretical correlations in Equations (7.14) and (7.15), respectively, just for Case 2, are used to scale the mean temperature. Figure 7.16, with low *Re* in (a) and high *Re* in (b), is a picture of how the mean temperature profiles scaled with these values. Large variations of the scaled data with the effects of *Pr* are observed. In Tables 7.3 and 7.4, when comparing the locations and values of the MNTHF between the DNS/LST and the theoretical correlations, it was seen that there were large variations between the locations of the peak between the two different methods, while the variations between the peak values were comparatively small. This observation combined with the results from Figure 7.16 indicate that the MNTHF scaling proposed in this analysis is sensitive to the location of the peak normal turbulent heat flux more than it is to the values of the peak normal turbulent heat flux. Large variations in the location of the MNTHF, as reported earlier, result in high variations in the scaled mean temperature profile. The mean temperature is also scaled by the results of the location and value of the maximum normal turbulent heat flux obtained from the theoretical correlations of Kawamura et al. [172] given by Equations (7.16) and (7.17), respectively. Figure 7.17(a) and (b) is a plot of the scaled temperature profile for the low and high *Re*. The results again show the poor collapse of the data for this case as expected. This is due to the fact that the values of both the theoretical correlations proposed in this paper and those obtained by Kawamura et al. are very similar and show large deviations from that of DNS/LST data.

Having found that the determination of the location of the maximum normal turbulent heat flux can help in obtaining better scaling results, it is important to represent the DNS/LST values of the predicted location of the maximum normal turbulent flux in a functional form. The variation of the location of the MNTHF as a function of the friction Peclet number is shown in Figure 7.18. By using a power law fit, the equations for the location of the maximum normal turbulent heat flux for Case 1 of heating are given as

$$y^+_{Tv^+_{\max}} = 140 Pe^{-0.24} \tag{7.17}$$

and for the case where both walls are heated (Case 2) by

$$y^+_{Tv^+_{\max}} = 107 Pe^{-0.23} \tag{7.18}$$

Now, using these values for the location of the maximum normal turbulent heat flux and using Equations (7.6) and (7.7), respectively, for Cases 1 and 2, it is possible to estimate the values of the maximum normal turbulent heat flux. Such values are obtained and shown in Tables 7.7 and 7.8 for Cases 1 and 2, respectively. The main observation from this table is the fact that comparisons of the values of the location of the MNTHF from the power law fit with the DNS/LST data show small differences. Even though, there are still differences between the power law fit and the data from DNS/LST, these differences are comparatively smaller than the differences between the DNS/LST data and the empirical correlations for location and values of MNTHF developed in this paper.

The mean temperature profile scaled using the MNTHF scaling is shown in Figures 7.19 and 7.20, for Cases 1 and 2, respectively. As previously, the lower *Re* data are shown in (a), while the higher *Re* data are shown in (b). The results show

remarkably good collapse of the mean temperature profiles in the near wall and buffer regions. This proves that better estimates of the location of the maximum normal heat flux help in better collapse of the scaled results. The lower *Pr* cases (especially *Pr* = 0.7) shows some outlier characteristics. This can be attributed to high fluctuations in data for the normal turbulent heat flux profiles at such low *Pr* using our DNS/LST method. Owing to this, as mentioned before, one needs to fit the profile to obtain a smooth curve for the normal turbulent heat flux and the values of location and values of the MNTHF are not completely accurate. The large percent errors of the maximum normal turbulent heat flux for the low *Pr* case, the *Pr* = 0.7 which demonstrates outlier characteristics, further strengthens the hypothesis that the scaling analysis depends on accurate determination of both the location and the values of the maximum normal turbulent heat flux.

To further examine the scaling of the scalar turbulence statistics, the MNTHF scaling is implemented on the profiles of the normal turbulent heat flux presented previously in Figures 7.1-7.4. The same parameters, the value of MNTHF and the location of the MNTHF obtained from the DNS/LST study and factored by the Stanton and Prandtl numbers to a power of 0.25 are used for the scaling. In Figure 7.21 we show the normal turbulent heat flux for the wall heating Case 1 with (a) presenting the low *Re* data and (b) showing the higher *Re* data. The corresponding case for the wall heating Case 2 is shown in Figure 7.22. Observable from the graphs is the collapse of the normal turbulent heat flux in the regions near the channel walls. One can also notice that the scaling is not as smooth as that for the temperature, with wide error bars shown in some cases. This indicates that the normal turbulent heat flux values are more

sensitive to the peak values and location of the normal turbulent heat flux than the mean temperature.

To explore further the scaling analysis, the same scaling is applied to the root mean square of the temperature fluctuations. The root mean square (rms) of the temperature fluctuations as a function of the normal distance from the channel walls is shown in Figure 7.23. The data shown are Eulerian simulation data from the works of Schwertfirm and Manhart [132] and Dong et al. [177, 178]. The results are for the case of $Re_\tau = 180$, with two channel walls maintained at two different constant temperatures. Now, the normal turbulent heat flux profile behaves in a different manner in the case of constant temperature or constant heat flux boundary conditions [28, 132, 172, 177]. It could be inaccurate to use the normal turbulent heat flux data for the case of constant heat flux conditions to scale the rms of the temperature fluctuations (since the data is from the case of constant temperature boundary conditions). Instead, the normal turbulent heat flux values are obtained from the same work of Schwertfirm and Manhart given in their Figure 5. In the case of constant temperature boundary condition, the normal turbulent heat flux does not show asymptotic decreases after the maximum value. Hence, the point at which the profile attains 90% of the asymptotic value is chosen as the value of the MNTHF. The scaling of the rms of the temperature fluctuations using these values is shown in Figure 7.24. Remarkably, the profiles for the various *Pr* collapse in the near wall and buffer regions of the channel. For the high $Pr = 100$ data, due to the unavailability of normal turbulent heat flux data, the data from our constant wall heat flux condition is used for the location and the value of the maximum turbulent heat flux. This results in a slight deviation of the scaling from the collapse of

other data. These results show that the normal turbulent heat flux is a versatile parameter that can be used to capture not only the mean, but also the fluctuating characteristics of scalar turbulence.

7.4 Conclusions

The DNS/LST method is implemented for Poiseuille channel flow to obtain a wide range of scalar transport data for different Re_τ (150 and 300) and for *Pr* spanning six orders of magnitude. Such data have been obtained for two different wall heating scenarios, first, with just one wall being heated with constant heat flux while the other was maintained adiabatic, and second, with the both walls being heated with constant heat flux. Such a database has enabled us to examine the features of turbulent scalar transport. The normal turbulent heat flux was found to vary with the *Pr* and with the *Re*. Since the normal turbulent heat flux parameter accounts for the variation in the flow and scalar characteristic of turbulence, the location and the value of the peak normal turbulent heat flux were chosen as the two main parameters for scaling the mean temperature, the normal turbulent heat flux, and the root mean square of the temperature fluctuations. The obtained results show that the maximum normal turbulent heat flux, used as a scaling parameter, captures most, if not all, the mean and fluctuating scalar turbulence characteristics. The scaled profiles of the mean temperature, normal turbulent heat flux and the rms of the temperature fluctuations all show good collapse in the near wall and buffer regions of the channel.

A theoretical model inspired by Kawamura et al.[172], has also been presented. The theoretically model for the normal turbulent heat flux does a good job in predicting the values of the maximum normal turbulent heat flux (MNTHF) within reasonable

error percentages. However, prediction for the location of the maximum normal turbulent heat fluxes (MNTHF) deviates from the DNS/LST results.

A sensitivity analysis was performed to size up the effect of the location and values of the MNTHF, on capturing the turbulent scalar behavior. The results show that obtaining the location values of the MNTHF with accuracy is more important while there is less sensitivity of the scaled data to the values of the MNTHF. Using our DNS/LST data for the location and values of the MNTHF for variety of *Pr* and for two different *Re*, a power law fit is obtained for the location of the MNTHF as a function of the *Pe*. The mean temperature profiles are scaled with data for the location of the MNTHF from these power law fits. These values can then be used to determine the values of the MNTHF. The results show good collapse of the scaled data enabling one to use these power law fits to obtain peak locations of the normal turbulent heat flux. Since the normal turbulent heat flux, especially for medium and high *Pr*, occurs closer and closer to the walls, it is important to obtain its value and location with accuracy in order to precisely define the scaling. In addition to the DNS/LST approach utilized here for obtaining the scalar transport characteristics, Eulerian DNS or large eddy simulation data can help in obtaining accurate results of locations and values of maximum normal turbulent heat flux, as they become available for high *Re* and *Pr*.

Table 7.1: Scaling parameters used in different studies for scalar transport in turbulence.

Theory	Length Scale		Temperature Scale	
	Inner Scaling	Outer Scaling	Inner Scaling	Outer Scaling
Classical Scaling	$y\frac{u^*}{\nu}$	$\frac{y}{\zeta_T}$	$\frac{q_w}{\rho c_p u^*}$	$\frac{q_w}{\rho c_p u^*}$
Wei et al. [110]	$y\frac{u^*}{\nu}$		$\frac{q_w}{\rho c_p u^*}\mathrm{Pr}$	
George et al. [36]	$\frac{\frac{y q_w}{\rho c_p}}{\alpha(T_w - T_\infty)}$	$\frac{y}{\zeta_T}$	$T_w - T_\infty$	$(T_w - T_\infty)\frac{St}{C_f/2}$
Wang and Castillo [115]	$\frac{yU_\infty}{\nu}\sqrt{St}$	$\frac{y}{\zeta_T}$	$(T_w - T_\infty)\mathrm{Pr}\sqrt{St}$	$(T_w - T_\infty)\frac{\zeta_T^D}{\zeta_T}$
Srinivasan and Papavassiliou (present work)	$\frac{y^+_{Tv_{\max}}}{St^{\frac{1}{4}}\,\mathrm{Pr}^{\frac{1}{4}}}$		$T_\infty^+ Tv^+_{\max}$	
Churchill et al. [124, 139]	$(\overline{u'v'})^{++} = \frac{-\rho\overline{u'v'}}{\Gamma_w\left(1-\frac{y^+}{h^+}\right)}$			
	$(\overline{T'v'})^{++} = \frac{\rho c_p\overline{T'v'}}{q_w\left(1-\frac{y^+}{h^+}\right)}$			

Table 7.2: Simulation conditions for numerical marker-tracking experiments.

Case	Reynolds Number (Re)	Prandtl Number (Pr)					Number of Markers	time step advancement (Δt)	Simulation time (t)
		a	b	c	d	e			
A	150	0.7	3	6	10	200	145161	0.25	4000
B	300	0.1	0.7	6	20	50	260100	0.2	8000
C	150	500	2400	7000	15000	50000	16129	0.25	13000
D	300	200	2400	7000	15000	50000	260100	0.2	8000

Table 7.3: Values of the peak location of the normal turbulent heat flux obtained using the DNS/LST method, Kader's data and theoretical correlation of Srinivasan and Papavassiliou in equation (7.11) for the case of one channel wall heated with constant heat flux. The corresponding percentage differences between the DNS/LST and Kader's value along with the percentage differences between DNS/LST and values from equation (7.11) are also presented. The two flow cases with Re_τ = 150 and 300 are presented.

	Re_τ = 150					Re_τ = 300				
Pr	DNS/LST	Kader	% difference between DNS/LST and Kader	Eqn (7.11)	% difference between DNS/LST and Eqn (7.11)	DNS/LST	Kader	% difference between DNS/LST and Kader	Eqn (7.11)	% difference between DNS/LST and Eqn (7.11)
0.7	44.500	40.500	8.99	32.331	27.35	53.500	56.500	-5.61	45.723	14.54
3	31.500	25.500	19.05	15.617	50.42					
6	22.500	20.500	8.89	11.043	50.92	34.500	27.500	20.29	15.617	54.73
10	19.500	17.500	10.26	8.554	56.13					
20						20.500	20.000	2.44	8.554	58.27
50						16.500	16.000	3.03	5.410	67.21
200	9.622	8.419	12.50	1.913	80.12	10.606	10.223	3.61	2.705	74.50
500	7.056	6.943	1.60	1.210	82.86					
2400	5.703	4.795	15.92	0.552	90.32	6.482	5.725	11.67	0.7 81	87.95
7000	4.263	3.695	13.33	0.323	92.42	5.408	4.511	16.59	0.457	91.55
15000	4.263	3.195	25.05	0.221	94.82	4.230	3.695	12.66	0.312	92.62
50000	2.985	2.514	15.76	0.121	95.95	3.441	2.732	20.59	0.171	95.03

Table 7.4: Values of the peak normal turbulent heat flux obtained using the DNS/LST method, Kader's data and theoretical correlation of Srinivasan and Papavassiliou in equation (7.12) for the case of one channel wall being with constant heat flux. The corresponding percentage differences between the DNS/LST and Kader's value along with the percentage differences between DNS/LST and values from equation (7.12) are also presented. The two flow cases with Re_τ = 150 and 300 are presented.

	Re_τ = 150					Re_τ = 300				
Pr	DNS/LST	Kader	% difference between DNS/LST and Kader	Eqn (7.12)	% difference between DNS/LST and Eqn (7.12)	DNS/LST	Kader	% difference between DNS/LST and Kader	Eqn (7.12)	% difference between DNS/LST and Eqn (7.12)
0.7		0.814	0.94	0.787	4.20	0.912	0.896	1.77	0.849	6.84
3	0.940	0.917	2.42	0.897	4.57					
6	0.935	0.943	-0.89	0.927	0.78	0.965	0.974	-0.93	0.949	1.67
10	0.947	0.956	-0.92	0.944	0.40					
20						0.969	0.988	-1.00	0.972	0.65
50						0.980	0.994	-0.84	0.982	0.31
200	0.987	0.989	-0.23	0.987	-0.04	0.989	0.994	-0.24	0.991	0.00
500	0.991	0.993	-0.20	0.992	-0.10					
2400	0.995	0.997	-0.16	0.996	-0.14	0.996	0.998	-0.10	0.997	-0.05
7000	0.997	0.998	-0.11	0.998	-0.10	0.998	0.999	-0.07	0.999	-0.05
15000	0.998	0.999	-0.08	0.999	-0.09	0.998	0.999	-0.05	0.999	-0.03
50000	0.999	0.999	-0.05	0.999	-0.06	0.999	0.999	-0.02	0.999	-0.02

Table 7.5: Values of the peak location of the normal turbulent heat flux obtained using the DNS/LST method, Kader's data, theoretical correlation of Srinivasan and Papavassiliou in equation (7.13) and theoretical correlation of Kawamura et al. [172] in equation (7.15) for the case of both the channel walls heated with constant heat flux. The corresponding percentage differences between the DNS/LST and Kader's, DNS/LST and values from equation (7.13) and DNS/LST and values from equation (7.15) are also presented. The two flow cases with Re_τ = 150 and 300 are presented.

	Re_τ = 150							Re_τ = 300						
Pr	DNS/ LST	Kader	DNS/ LST and Kader (%)	Eqn (7.13)	DNS/ LST and Eqn (7.13) (%)	Eqn (7.15)	DNS/ LST and Eqn (7.15) (%)	DNS/ LST	Kader	DNS/ LST and Kader (%)	Eqn (7.13)	DNS/ LST and Eqn (7.13) (%)	Eqn (7.15)	DNS/ LST and Eqn (7.15) (%)
0.7	34.500	31.500	8.70	22.862	33.73	29.514	14.45	48.500	41.000	15.46	32.331	33.34	41.740	13.94
3	18.500	20.500	-10.81	11.043	40.31	14.257	22.94							
6	16.500	17.500	-6.06	7.809	52.67	10.081	38.90	24.500	21.000	14.29	11.043	54.93	14.257	41.81
10	17.500	15.500	11.43	6.049	65.44	7.809	55.38							
20								16.500	15.000	9.09	6.049	63.34	7.809	52.67
50								13.500	12.000	11.11	3.826	71.66	4.939	63.42
200	8.036	7.419	7.67	1.353	83.17	1.746	78.27	10.036	8.582	14.49	1.913	80.94	2.469	75.40
500	6.589	6.037	8.39	0.855	87.02	1.104	83.24							
2400	4.491	4.046	9.91	0.390	91.31	0.504	88.78	5.193	4.801	7.55	0.552	89.37	0.713	86.27
7000	3.469	3.195	7.89	0.229	93.41	0.295	91.49	4.511	3.695	18.10	0.323	92.83	0.417	90.75
15000	2.985	2.732	8.46	0.156	94.77	0.202	93.24	3.695	3.195	13.51	0.221	94.02	0.285	92.28
50000	2.124	2.105	0.89	0.086	95.97	0.110	94.80	2.959	2.305	22.11	0.121	95.91	0.156	94.72

Table 7.6: Values of the peak normal turbulent heat flux obtained using the DNS/LST method, Kader's data, theoretical correlation of Srinivasan and Papavassiliou in equation (7.14) and theoretical correlation of Kawamura et al. [172] in equation (7.16) for the case of both the channel walls heated with constant heat flux. The corresponding percentage differences between the DNS/LST and Kader's, DNS/LST and values from equation (7.14) and DNS/LST and values from equation (7.16) are also presented. The two flow cases with Re_τ = 150 and 300 are presented.

	Re_τ = 150							Re_τ = 300						
Pr	DNS/ LST	Kader	DNS/ LST and Kader (%)	Eqn (7.14)	DNS/ LST and Eqn (7.14) (%)	Eqn (7.16)	DNS/ LST and Eqn (7.16) (%)	DNS/ LST	Kader	DNS/ LST and Kader (%)	Eqn (7.14)	DNS/ LST and Eqn (7.14) (%)	Eqn (7.16)	DNS/ LST and Eqn (7.16) (%)
0.7	0.759	0.822	3.90	0.699	7.89	0.736	2.99	0.849	0.824	2.92	0.787	7.32	0.819	3.60
3	0.884	0.940	1.12	0.855	3.37	0.879	0.59							
6	0.880	0.935	-3.60	0.897	-1.98	0.916	-4.11	0.938	0.944	-0.66	0.927	1.12	0.941	-0.36
10	0.899	0.947	-3.62	0.920	-2.43	0.935	-4.11							
20								0.964	0.969	-0.56	0.960	0.39	0.968	-0.45
50								0.977	0.980	-0.32	0.975	0.25	0.980	-0.28
200	0.961	0.987	-2.21	0.982	-2.20	0.986	-2.59	0.985	0.989	-0.38	0.987	-0.23	0.990	-0.50
500	0.972	0.991	-1.67	0.989	-1.72	0.991	-1.97							
2400	0.981	0.995	-1.35	0.995	-1.41	0.996	-1.52	0.995	0.996	-0.16	0.996	-0.15	0.997	-0.23
7000	0.985	0.997	-1.16	0.997	-1.23	0.998	-1.29	0.997	0.998	-0.12	0.998	-0.12	0.998	-0.17
15000	0.987	0.998	-1.02	0.998	-1.07	0.998	-1.12	0.998	0.998	-0.08	0.999	-0.09	0.999	-0.12
50000	0.991	0.999	-0.77	0.999	-0.81	0.999	-0.83	0.999	0.999	-0.04	0.999	-0.05	0.999	-0.07

Table 7.7: Values of the peak location of the normal turbulent heat flux obtained using a power law fit of the DNS/LST results, shown by equation (7.17), and the corresponding peak values of the normal turbulent heat flux obtained using correlation of Srinivasan and Papavassiliou shown in equation (7.12) for the two different Re, $Re_\tau = 150$ and $Re_\tau = 300$, cases, and for a variety of Pr in the case 1 of one wall of the channel heated with constant wall heat flux. The percentage errors between these value and DNS/LST data are also presented.

	$\mathrm{Re}_\tau = 150$						$\mathrm{Re}_\tau = 300$					
	$y^+_{Tv^+_{\max}}$			$Tv^+_{\max}$			$y^+_{Tv^+_{\max}}$			$Tv^+_{\max}$		
Pr	DNS/LST	Power Fit	% error	DNS/LST	Power Fit	% error	DNS/LST	Power Fit	% error	DNS/LST	Power Fit	% error
0.7	44.500	46.489	-4.47	0.822	0.770	6.26	53.500	39.456	26.25	0.912	0.846	7.23
3	31.500	32.945	-4.59	0.940	0.866	7.94						
6	22.500	27.961	-24.27	0.935	0.892	4.52	34.500	23.731	31.22	0.965	0.943	2.21
10	19.500	24.777	-27.06	0.947	0.908	4.21						
20							20.500	17.848	12.94	0.978	0.963	1.51
50							16.500	14.369	12.92	0.985	0.973	1.28
200	9.622	12.195	-26.74	0.987	0.958	2.90	10.606	10.350	2.41	0.991	0.982	0.96
500	7.056	9.818	-39.14	0.991	0.967	2.44						
2400	5.703	6.773	-18.77	0.995	0.977	1.78	6.482	5.749	11.31	0.997	0.990	0.67
7000	4.263	5.258	-23.33	0.997	0.982	1.45	5.408	4.462	17.49	0.998	0.993	0.56
15000	4.263	4.390	-2.98	0.998	0.985	1.24	4.230	3.726	11.92	0.999	0.994	0.49
50000	2.985	3.302	-10.62	0.999	0.989	0.96	3.441	2.802	18.56	0.999	0.995	0.39

Table 7.8: Values of the peak location of the normal turbulent heat flux obtained using a power law fit of the DNS/LST results, shown by equation (7.18), and the corresponding peak values of the normal turbulent heat flux obtained using correlation of Srinivasan and Papavassiliou shown in equation (7.14) for the two different Re, $Re_\tau = 150$ and $Re_\tau = 300$, cases, and for a variety of Pr in the case 2 of both the walls of the channel heated with constant wall heat flux. The percentage errors between these value and DNS/LST data are also presented.

	$\mathrm{Re}_\tau = 150$						$\mathrm{Re}_\tau = 300$					
	$y^+_{Tv^+_{max}}$			Tv^+_{max}			$y^+_{Tv^+_{max}}$			Tv^+_{max}		
Pr	DNS/LST	Power Fit	% error	DNS/LST	Power Fit	% error	DNS/LST	Power Fit	% error	DNS/LST	Power Fit	% error
0.7	34.500	30.212	12.43	0.759	0.683	9.94	48.500	30.831	36.43	0.850	0.784	7.65
3	18.500	21.459	-16.00	0.884	0.819	7.38						
6	16.500	18.233	-10.50	0.880	0.856	2.67	24.500	18.732	23.54	0.938	0.916	2.34
10	17.500	16.170	7.60	0.899	0.877	2.38						
20							16.500	14.168	14.14	0.964	0.944	2.05
50							13.500	11.455	15.15	0.977	0.958	2.02
200	8.036	7.996	0.50	0.961	0.945	1.65	10.036	8.305	17.24	0.985	0.971	1.45
500	6.589	6.447	2.17	0.972	0.956	1.62						
2400	4.491	4.459	0.73	0.981	0.970	1.12	5.193	4.667	10.13	0.995	0.984	1.07
7000	3.469	3.467	0.06	0.985	0.977	0.83	4.511	3.641	19.29	0.997	0.988	0.89
15000	2.985	2.898	2.89	0.987	0.981	0.68	3.695	3.051	17.42	0.998	0.990	0.79
50000	2.124	2.184	-2.81	0.991	0.985	0.55	2.959	2.308	22.02	0.999	0.992	0.64

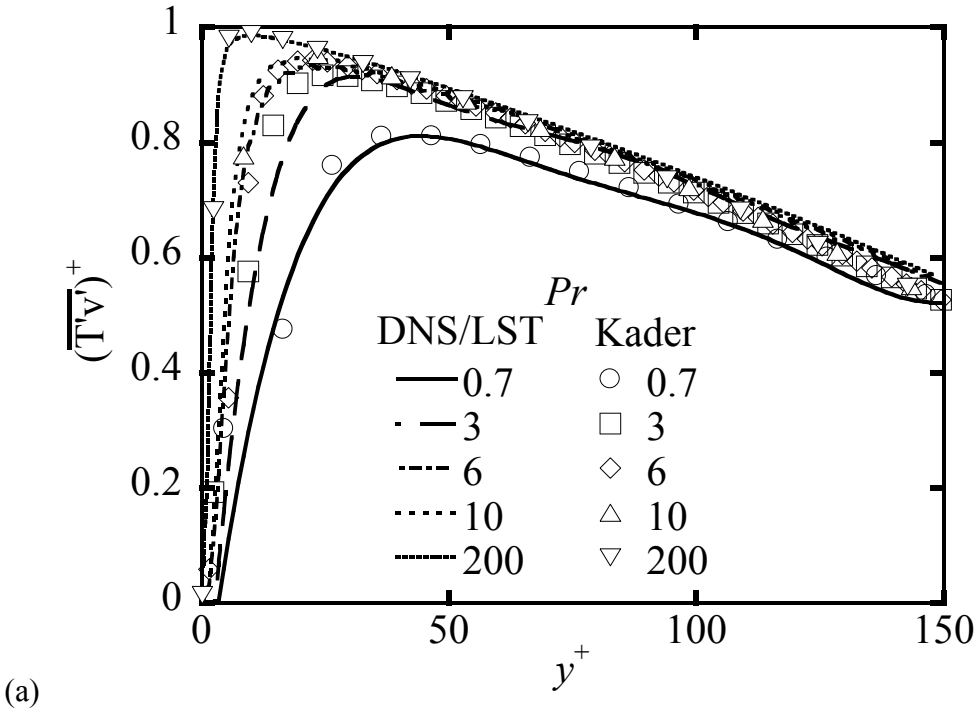

(a)

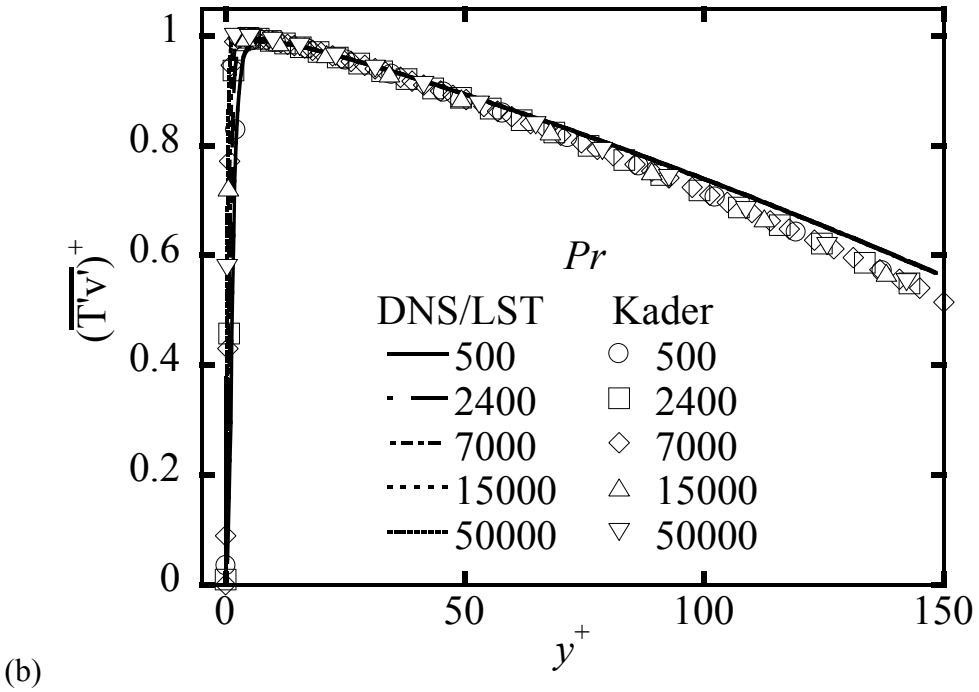

(b)

Figure 7.1: Values of the normal turbulent heat flux as a function of the wall-normal distance with a constant heat flux applied to one channel wall while maintaining the other adiabatic, in flow with $Re_\tau = 150$, obtained from the DNS/LST data and Kader's equation: (a) for small *Pr*, *Pr* = 0.7, 3, 6, 10 and 200 and (b) high *Pr*, *Pr* = 500, 2400, 7000, 15000, 50000.

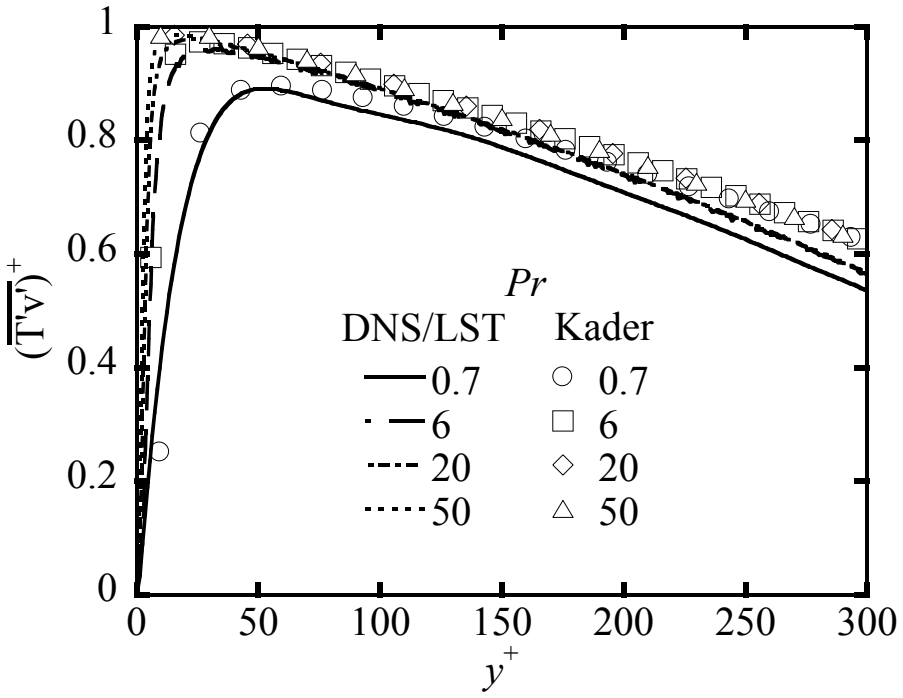

(a)

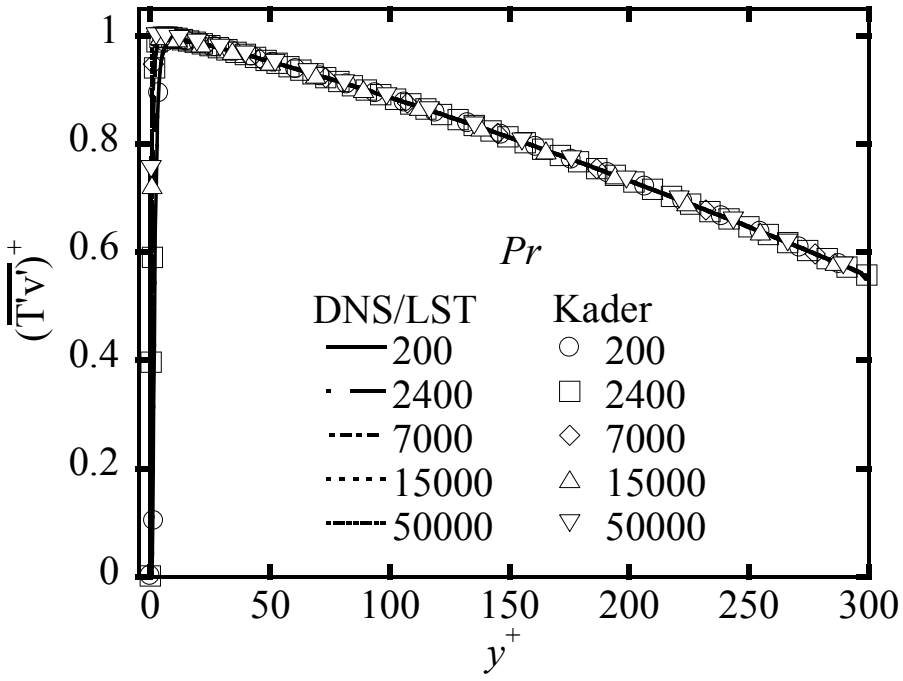

(b)

Figure 7.2: Values of the normal turbulent heat flux as a function of the wall-normal distance with a constant heat flux applied to one channel wall while maintaining the other adiabatic, in flow with $Re_\tau = 300$, obtained from the DNS/LST data and Kader's equation: (a) for small Pr, $Pr = 0.7$, 6, 20 and 50 and (b) high Pr, $Pr = 200$, 2400, 7000, 15000, 50000.

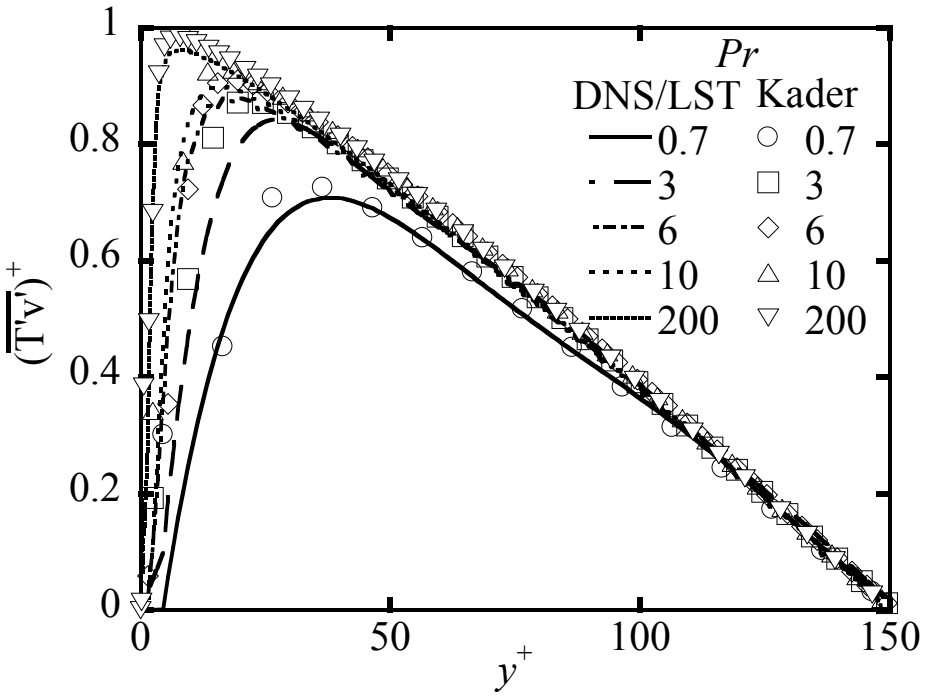

(a)

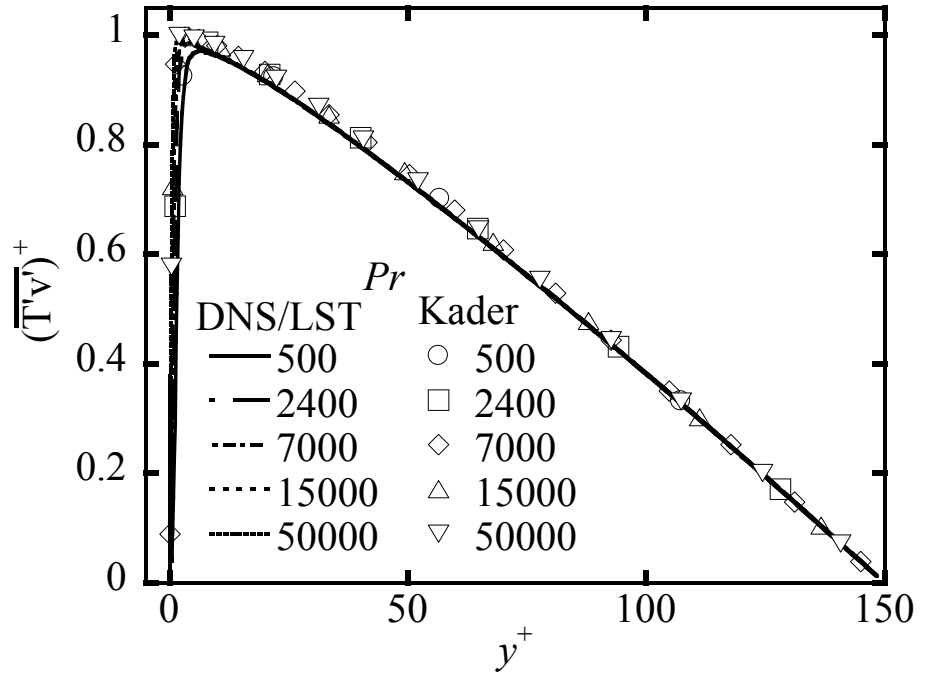

(b)

Figure 7.3: Values of the normal turbulent heat flux as a function of the wall-normal distance with a constant and uniform heat flux applied to both channel walls in flow with Re_τ = 150, obtained from the DNS/LST data and Kader's equation: (a) for small *Pr*, *Pr* = 0.7, 3, 6, 10 and 200 and (b) high *Pr*, *Pr* = 500, 2400, 7000, 15000, 50000.

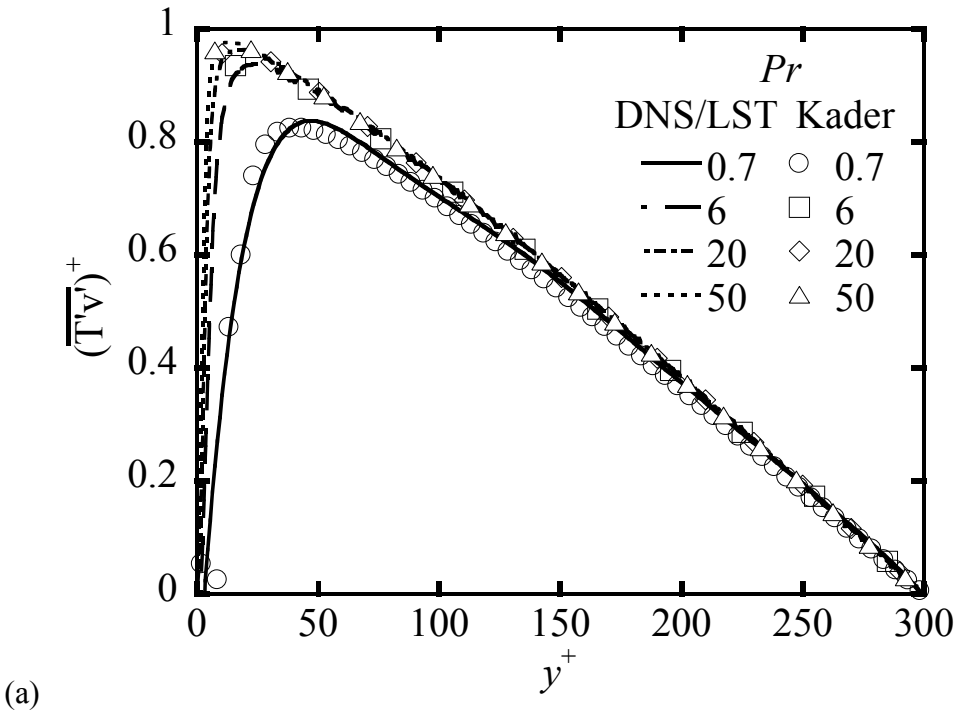

(a)

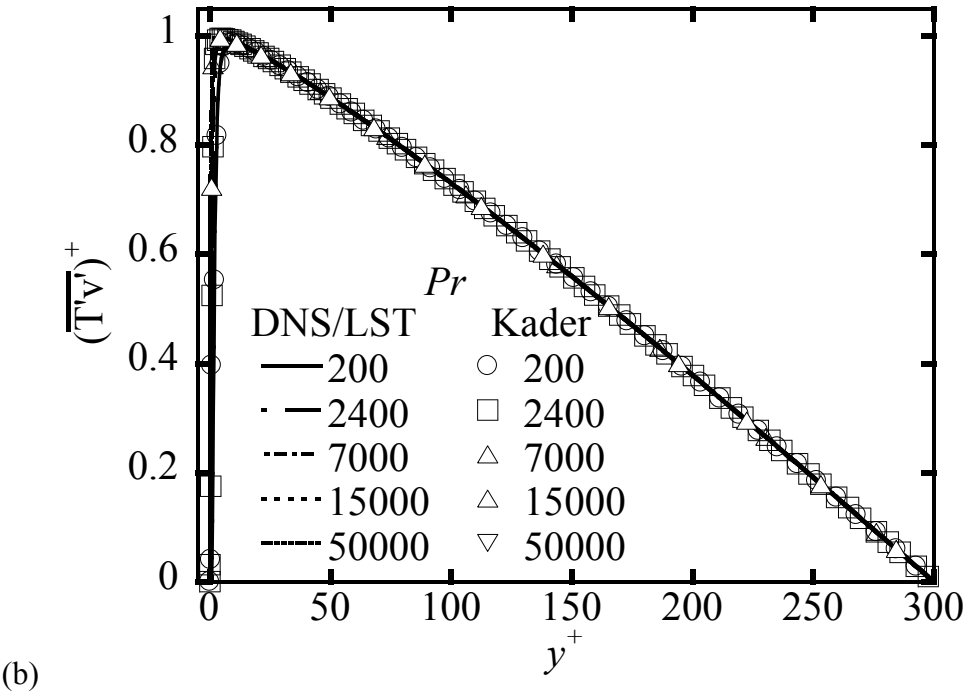

(b)

Figure 7.4: Values of the normal turbulent heat flux as a function of the wall-normal distance with a constant and uniform heat flux applied to both channel walls in flow with $Re_\tau = 300$, obtained from the DNS/LST data and Kader's equation: (a) for small *Pr*, *Pr* = 0.7, 6, 20 and 50 and (b) high *Pr*, *Pr* = 200, 2400, 7000, 15000, 50000.

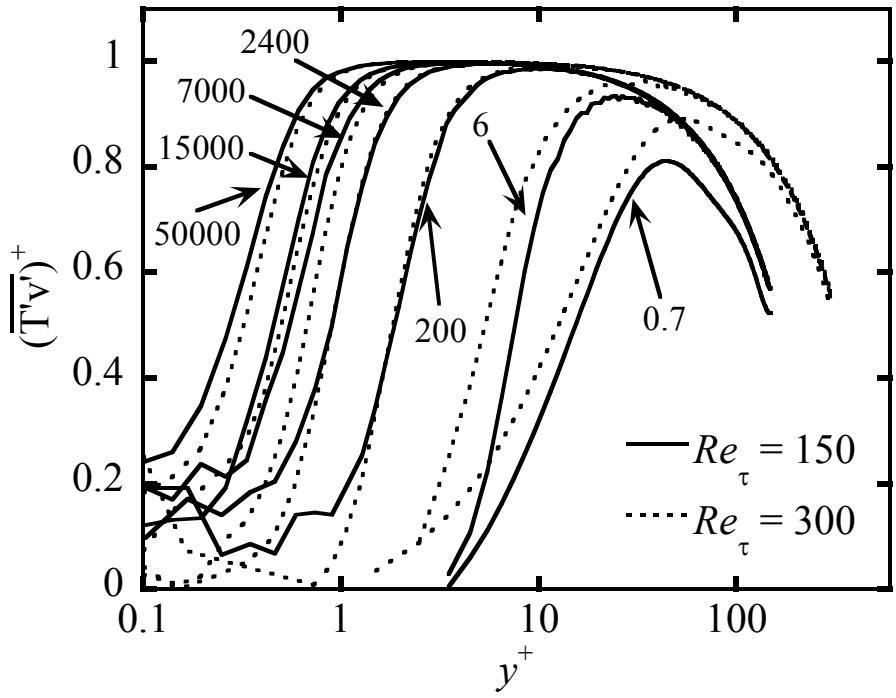

(a)

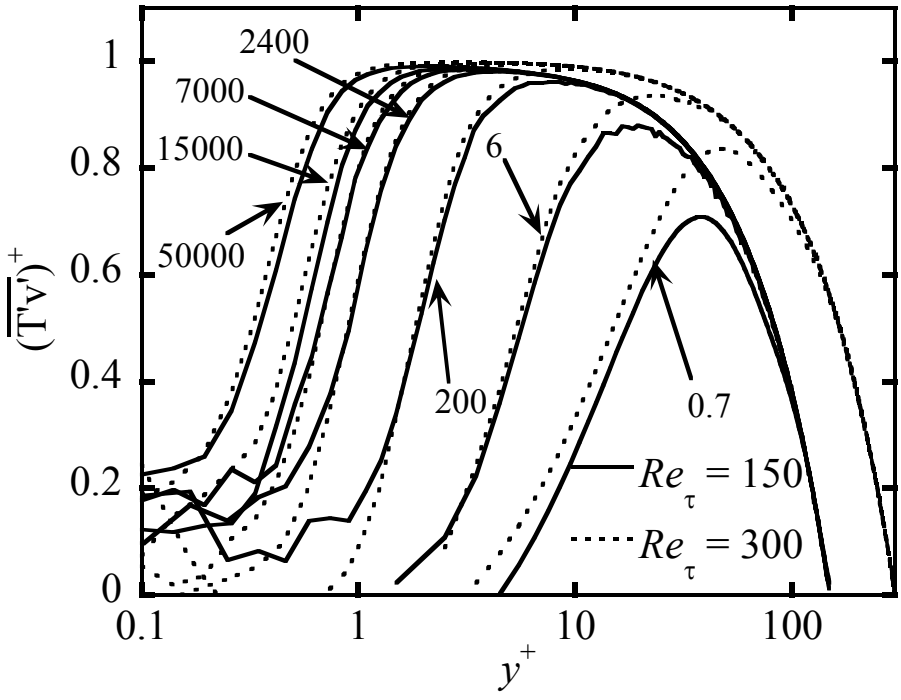

(b)

Figure 7.5: Comparisons of the values of the normal turbulent heat flux as a function of the wall-normal distance for two different *Re*, Re_τ = 150 and 300, for different *Pr*, *Pr* = 0.7, 6, 200, 2400, 7000, 15000 and 50000 with: (a) constant uniform heat flux applied to only bottom wall and (b) constant uniform heat flux applied to both walls.

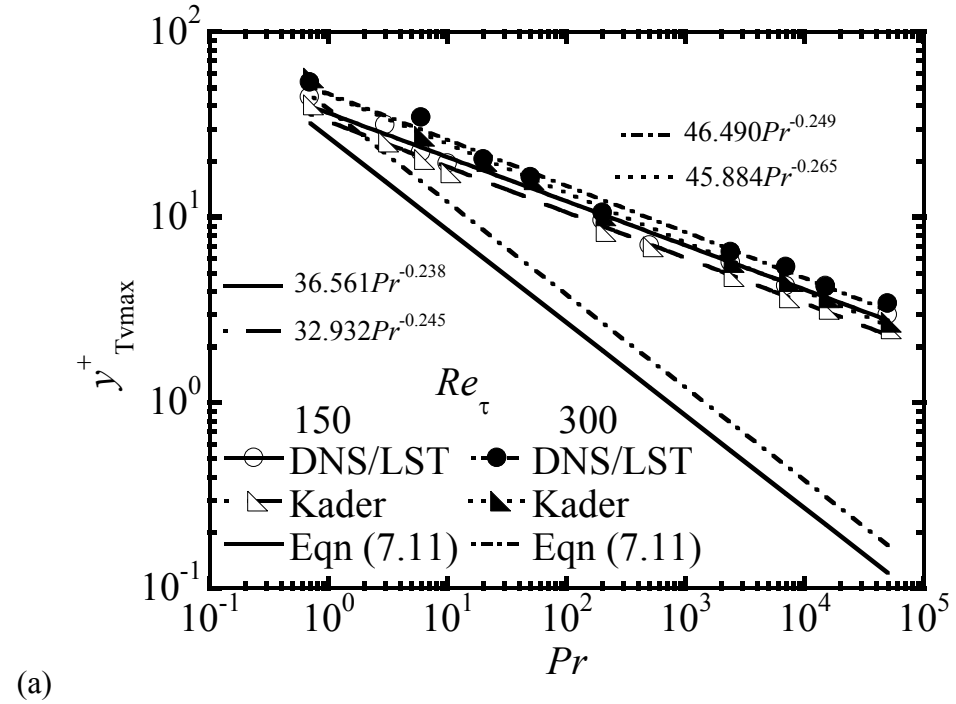

(a)

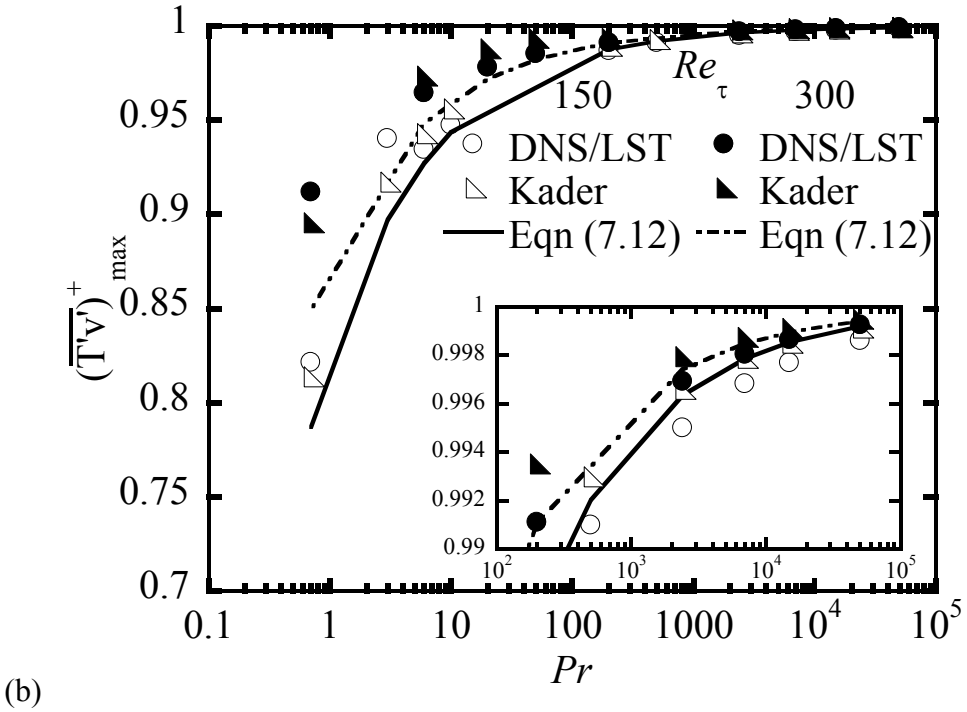

(b)

Figure 7.6: Location and values of the peak normal turbulent heat flux plotted as a function of the fluid *Pr* in two different Re_τ, Re_τ = 150 and 300 cases, obtained using three different methods, namely, the DNS/LST, Kader's and the theoretical correlations of Equations (7.11) and (7.12), for the uniform constant heat flux boundary condition applied to one channel wall represented as (a) peak location and (b) peak value.

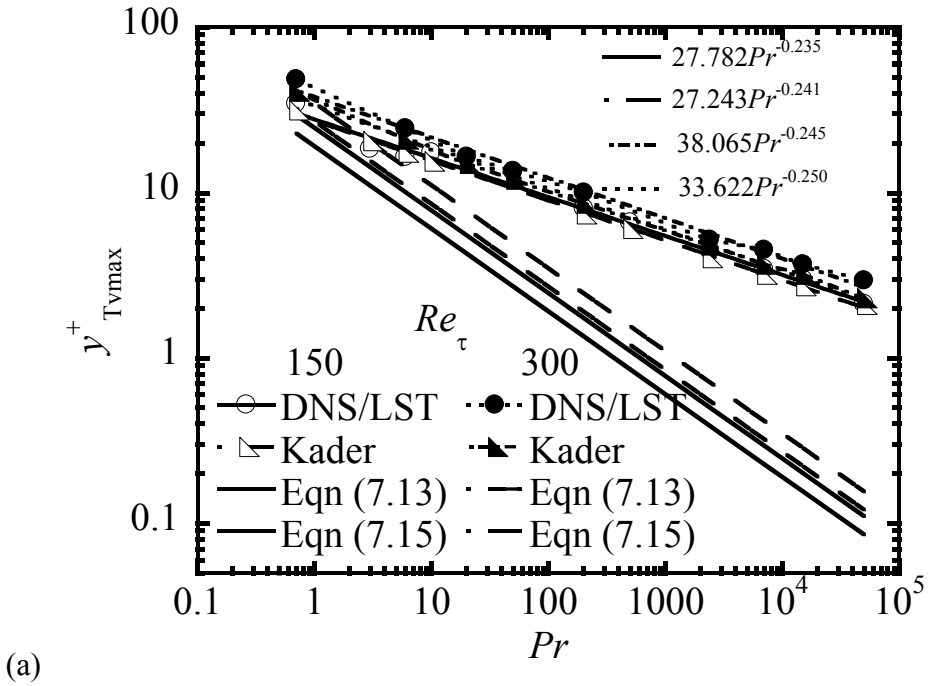

(a)

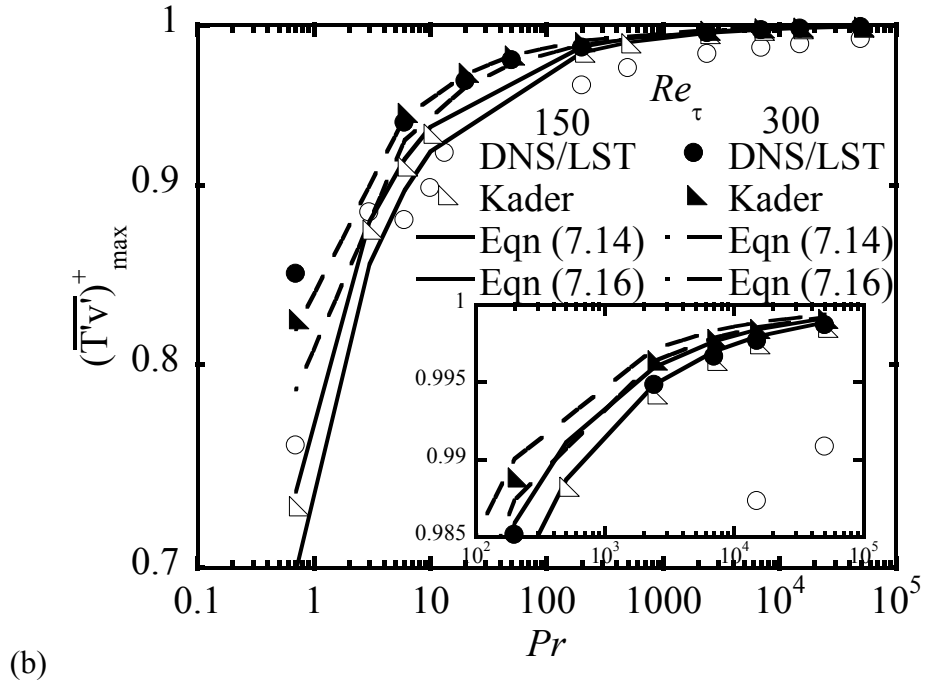

(b)

Figure 7.7: Location and values of the peak normal turbulent heat flux plotted as a function of the fluid *Pr* in two different Re_τ, $Re_\tau = 150$ and 300 cases, obtained using four different methods, namely, the DNS/LST, Kader's and the theoretical correlations of Srinivasan and Papavassiliou given in Equations (7.13) and (7.14), and theoretical correlations of Kawamura et al. [172] given in Equations (7.14) and (7.16), for the uniform constant heat flux boundary condition applied to both channel walls represented as (a) peak location and (b) peak value.

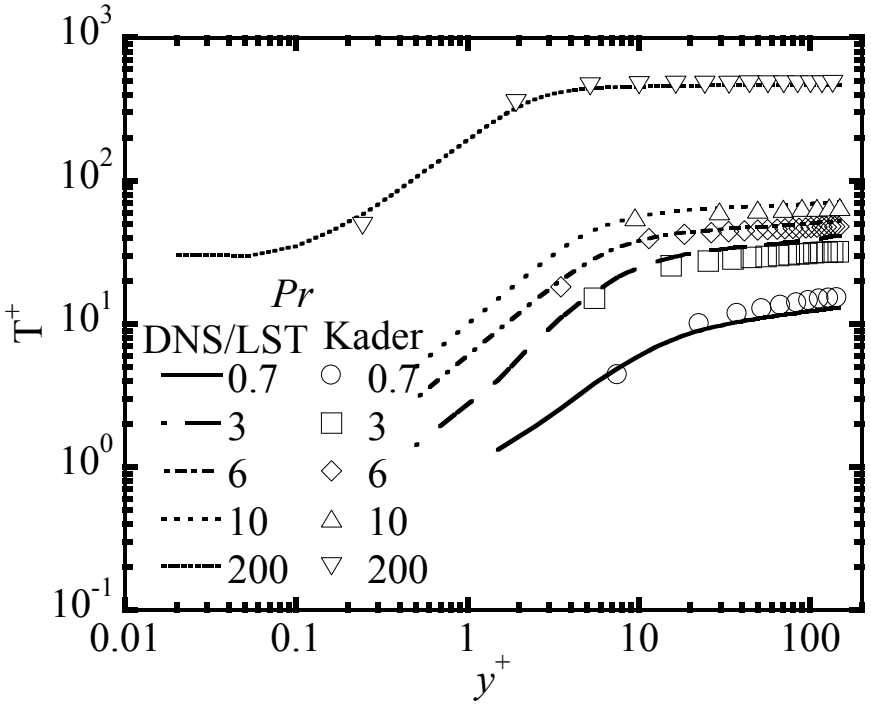

(a)

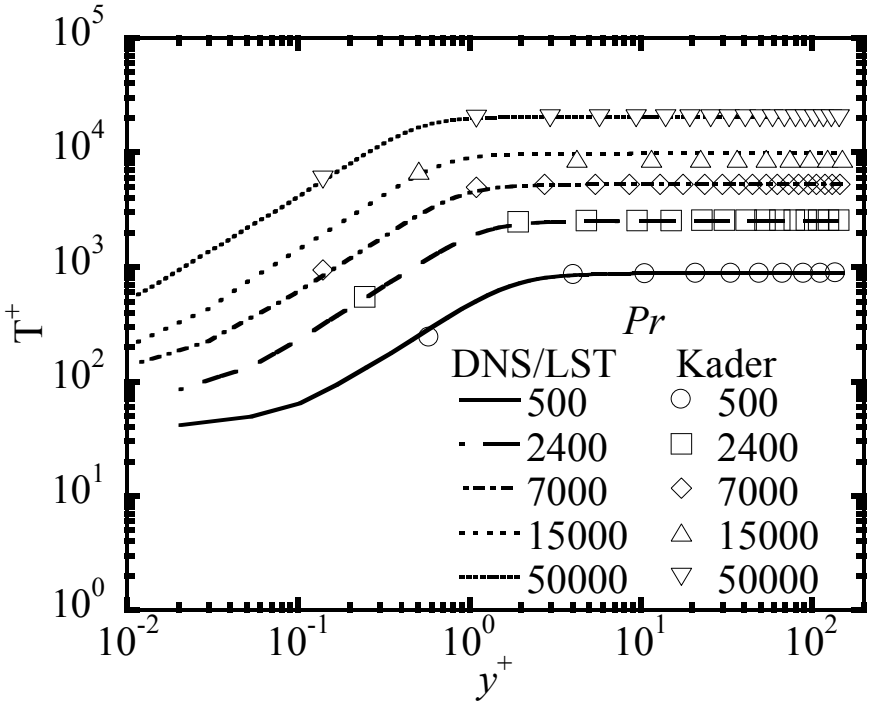

(b)

Figure 7.8: Mean temperature profile plotted as a function of the wall-normal distance for the case of one wall of the channel heated with constant heat flux. Results from DNS/LST and Kader's equation at $Re_\tau = 150$, obtained for different Pr: (a) $Pr = 0.7$, 3, 6, 10 and 200 and (b) $Pr = 500$, 2400, 7000, 15000 and 50000.

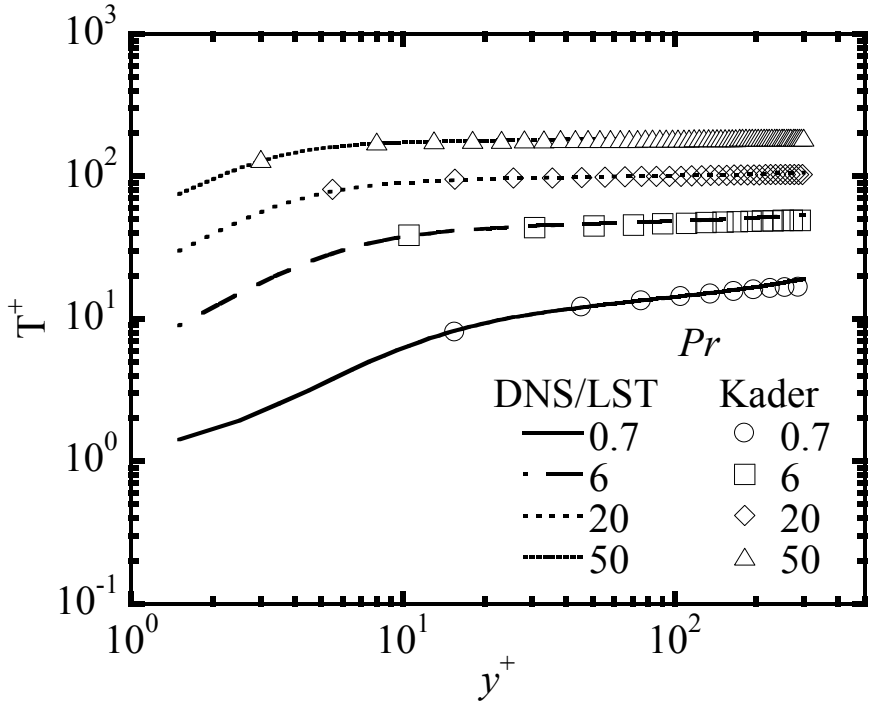

(a)

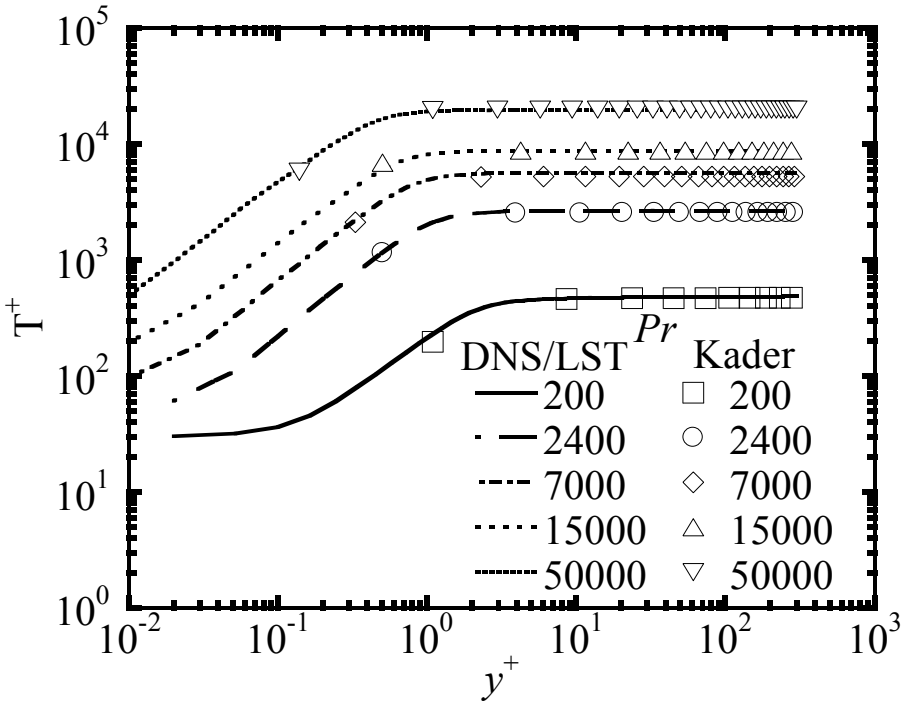

(b)

Figure 7.9: Mean temperature profile plotted as a function of the wall-normal distance for the case of one wall of the channel heated with constant heat flux. Results from DNS/LST and Kader's equation at $Re_\tau = 300$, obtained for different Pr: (a) $Pr = 0.7$, 6, 20 and 50 and (b) $Pr = 200$, 2400, 7000, 15000 and 50000.

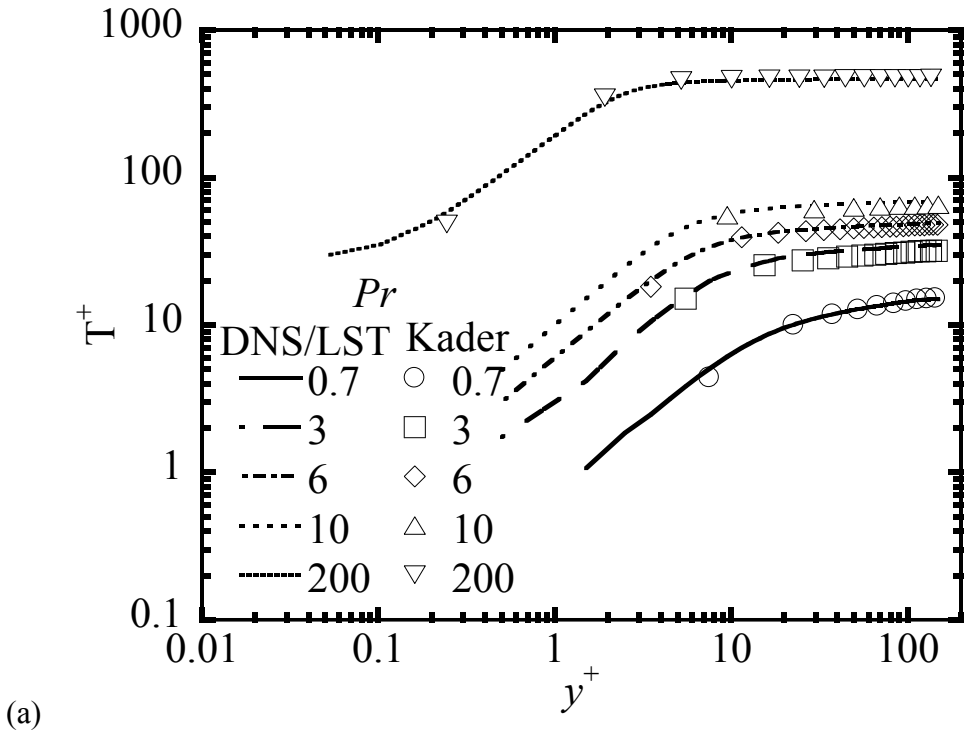

(a)

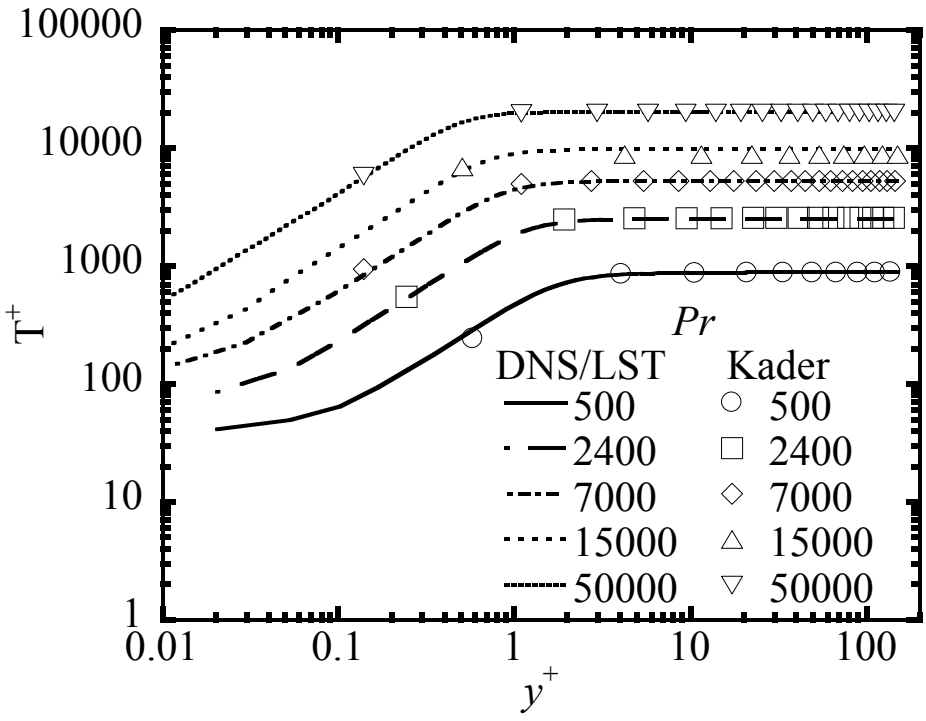

(b)

Figure 7.10: Mean temperature profile plotted as a function of the wall-normal distance for the case of both the walls of the channel heated with constant heat flux. Results from DNS/LST and Kader's equation at $Re_\tau = 150$, obtained for different Pr: (a) $Pr = 0.7$, 3, 6, 10 and 200 and (b) $Pr = 500$, 2400, 7000, 15000 and 50000.

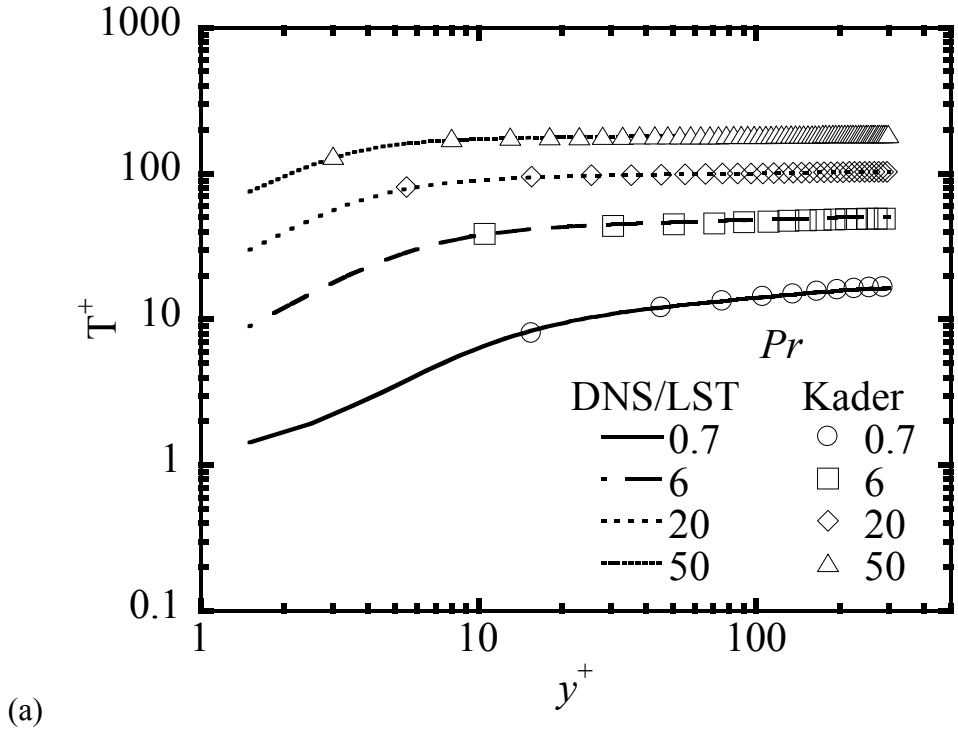

(a)

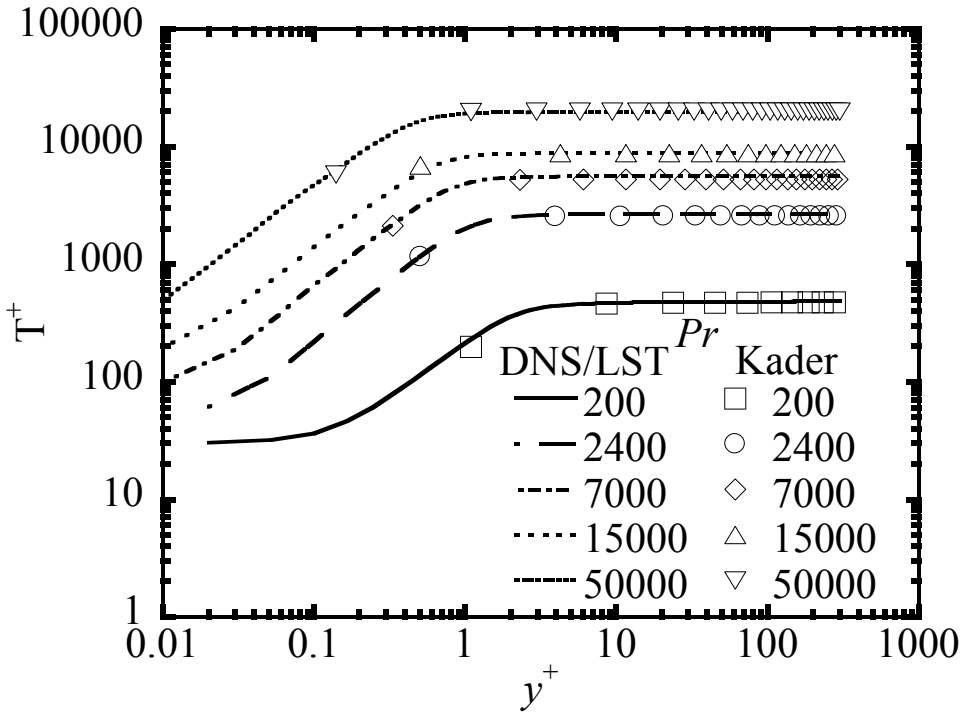

(b)

Figure 7.11: Mean temperature profile plotted as a function of the wall-normal distance for the case of both the walls of the channel heated with constant heat flux. Results from DNS/LST and Kader's equation at $Re_\tau = 300$, obtained for different Pr: (a) $Pr = 0.7$, 6, 20 and 50 and (b) $Pr = 200$, 2400, 7000, 15000 and 50000.

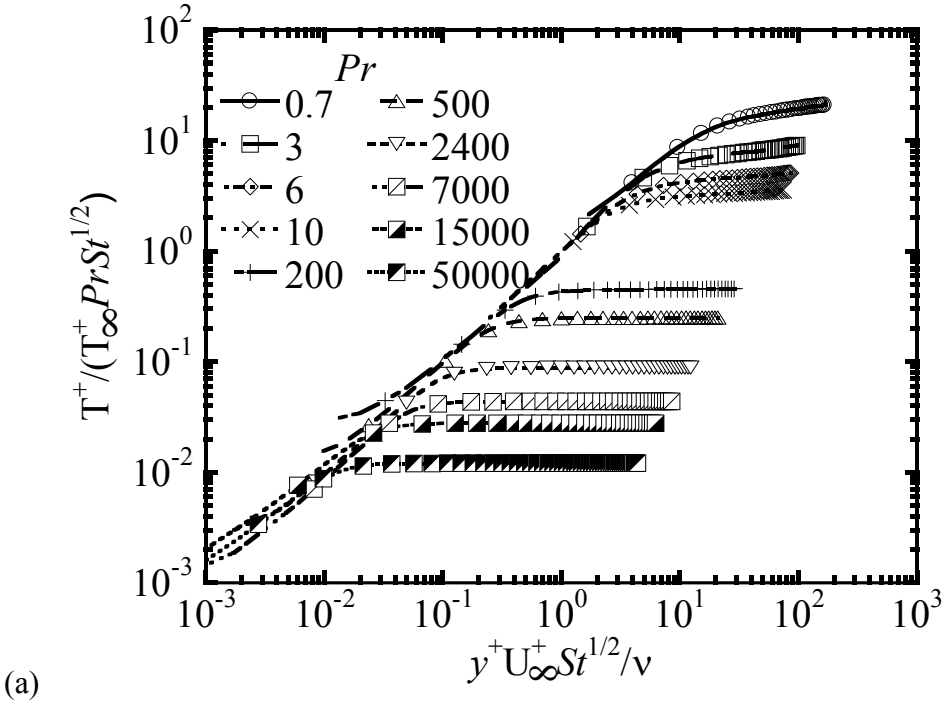

(a)

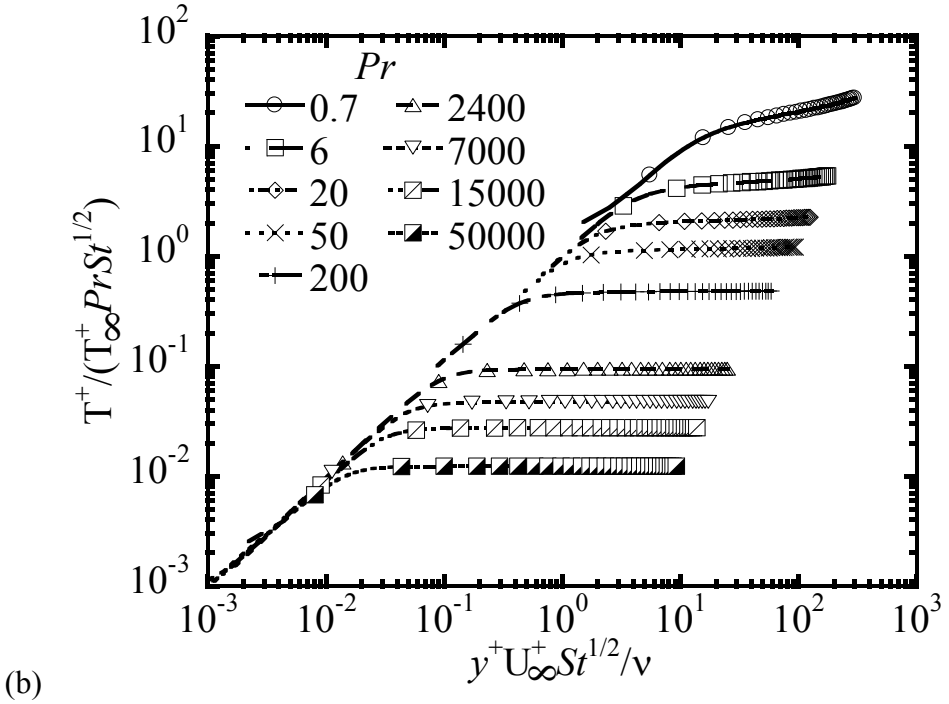

(b)

Figure 7.12: Values of the mean temperature scaled using the Wang et al. scaling plotted as a function of the scaled wall-normal location for the case where one channel wall is heated with constant heat flux, plotted for different *Pr* in flow cases with different Re_τ: (a) $Re_\tau = 150$ and (b) $Re_\tau = 300$.

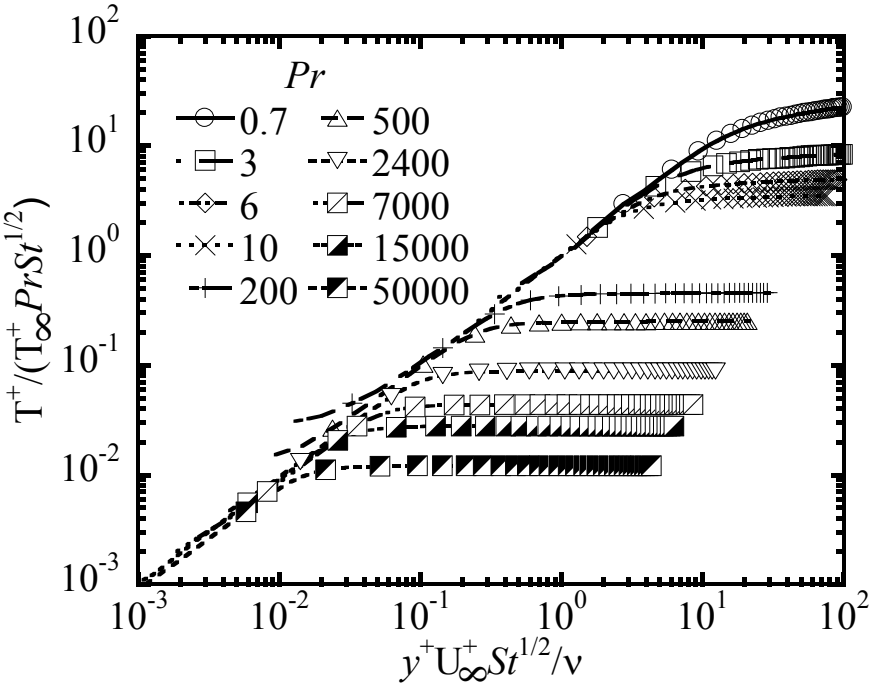

(a)

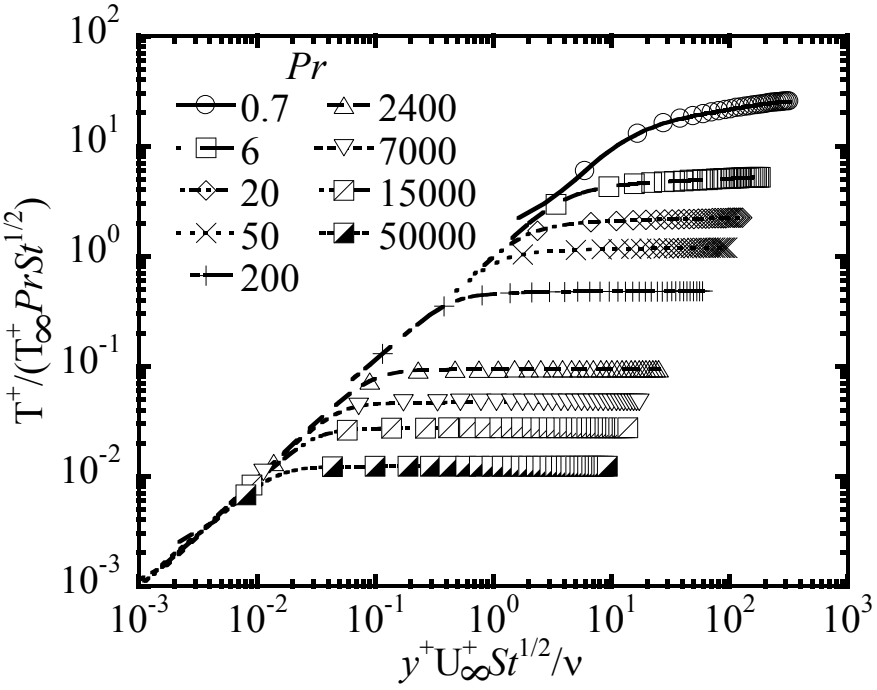

(b)

Figure 7.13: Values of the mean temperature scaled using the Wang et al. scaling plotted as a function of the scaled wall-normal location for the case where both the channel walls are heated with constant heat flux, plotted for different *Pr* in flow cases with different Re_τ: (a) $Re_\tau = 150$ and (b) $Re_\tau = 300$.

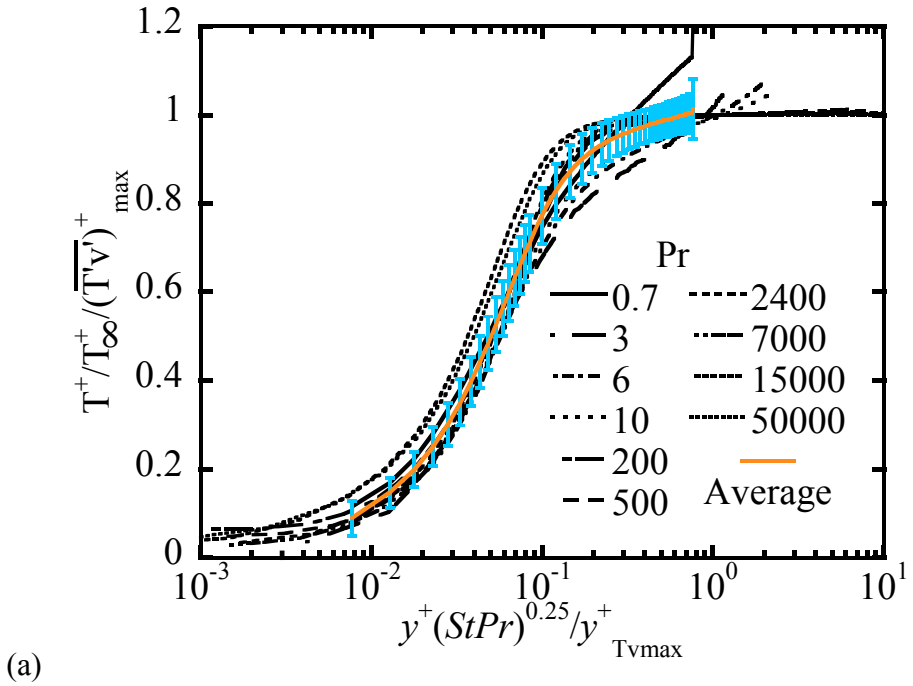

(a)

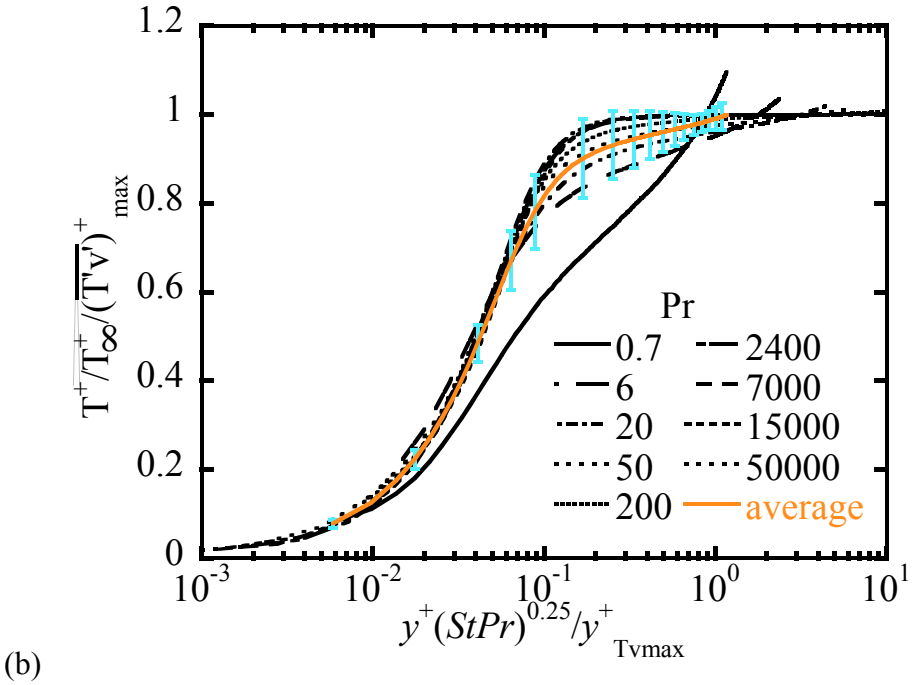

(b)

Figure 7.14: Values of the mean temperature scaled using the Srinivasan and Papavassiliou scaling plotted as a function of the scaled wall-normal location with scaling values of the maximum normal turbulent heat flux obtained from DNS/LST, for the case where one channel wall is heated with constant heat flux, plotted for different *Pr* in flow cases with different Re_τ: (a) $Re_\tau = 150$ and (b) $Re_\tau = 300$. The orange line indicates the average obtained for all the *Pr* data while the blue bars represent the error bars with plus/minus one standard deviation.

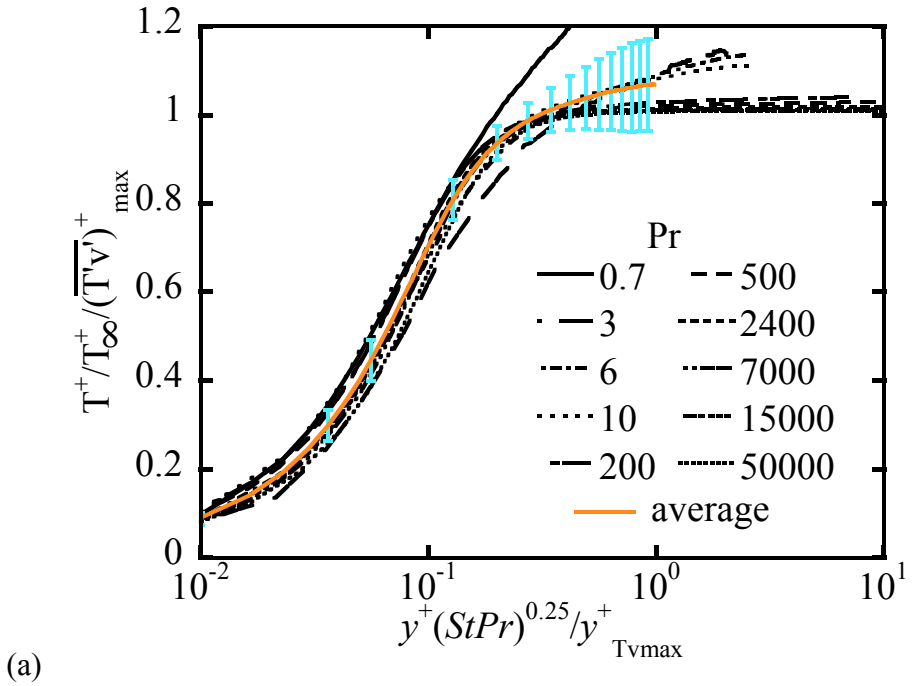

(a)

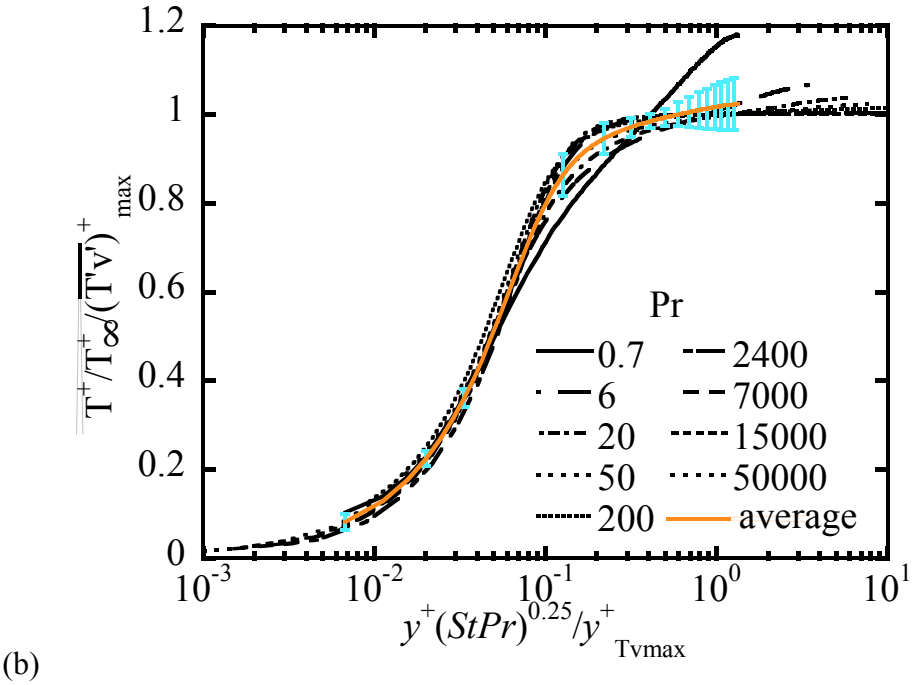

(b)

Figure 7.15: Values of the mean temperature scaled using the Srinivasan and Papavassiliou scaling plotted as a function of the scaled wall-normal location with scaling values of the maximum normal turbulent heat flux obtained from DNS/LST, for the case where both the channel walls are heated with constant heat flux, plotted for different *Pr* in flow cases with different Re_τ: (a) $Re_\tau = 150$ and (b) $Re_\tau = 300$. The orange line indicates the average obtained for all the *Pr* data while the blue bars represent the error bars with plus/minus one standard deviation.

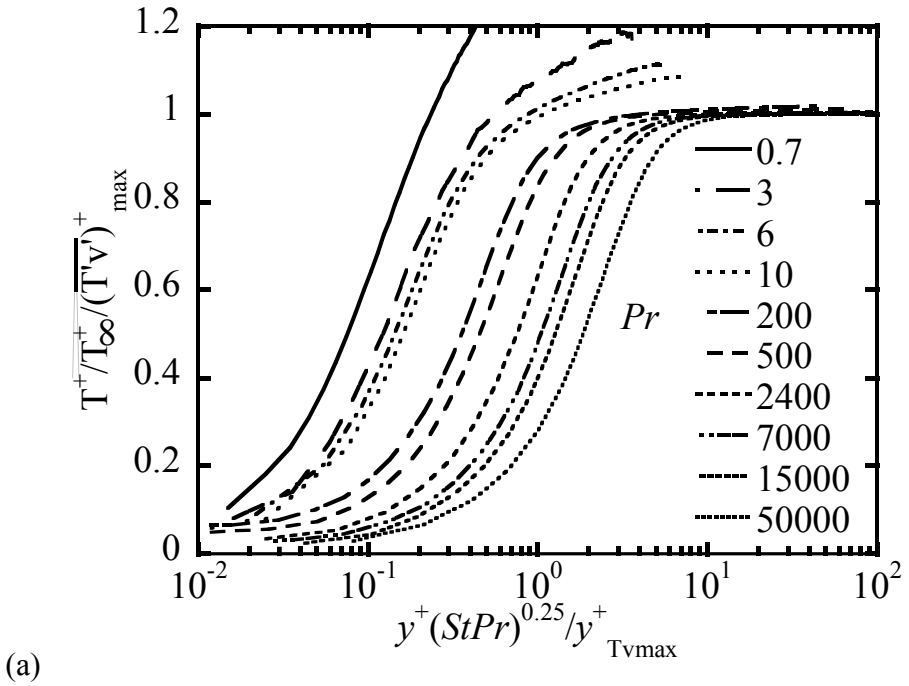

(a)

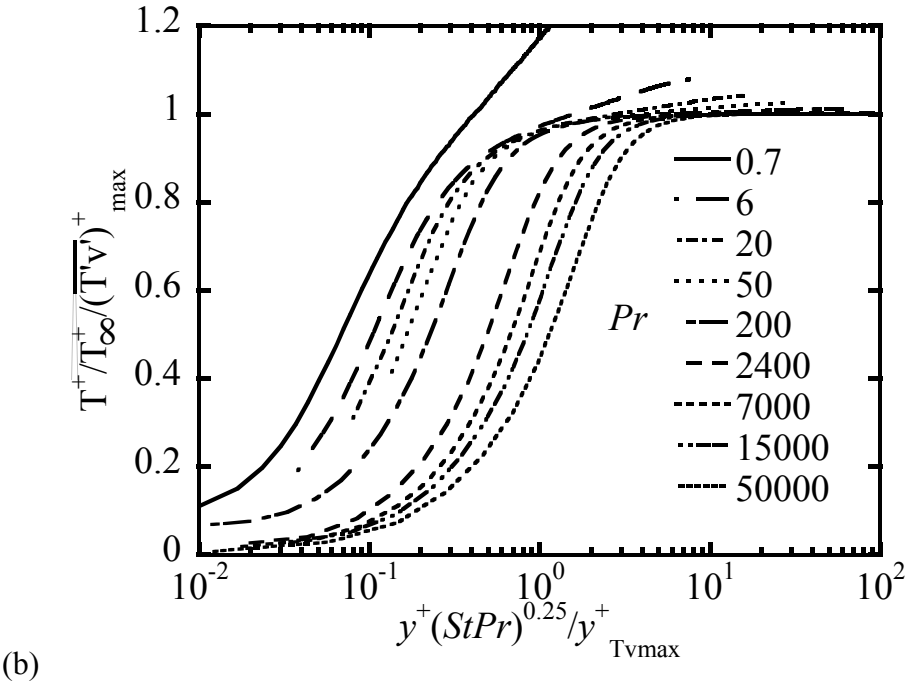

(b)

Figure 7.16: Values of the mean temperature scaled using the Srinivasan and Papavassiliou scaling plotted as a function of the scaled wall-normal location with scaling values of the maximum normal turbulent heat flux obtained from theoretical correlations of Srinivasan and Papavassiliou presented in equation (7.14) and (7.15), for the case where both the channel walls are heated with constant heat flux, plotted for different *Pr* in flow cases with different Re_τ: (a) $Re_\tau = 150$ and (b) $Re_\tau = 300$.

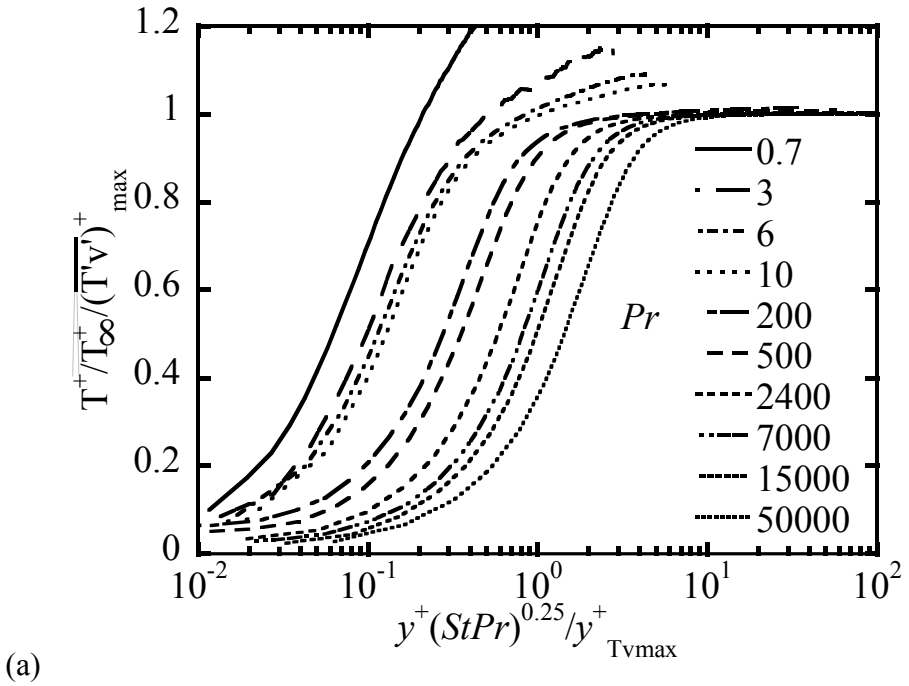

(a)

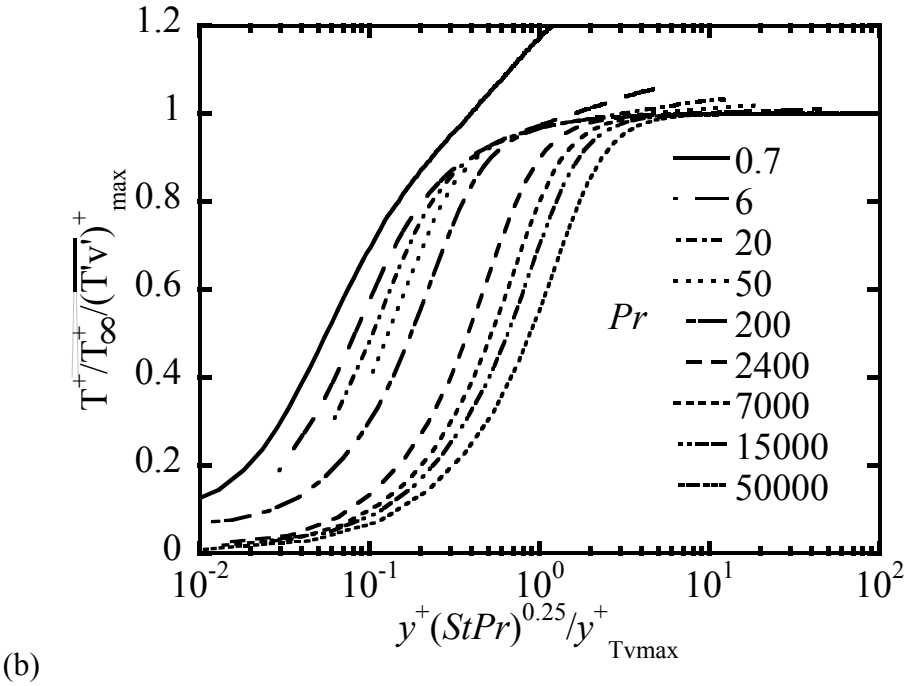

(b)

Figure 7.17: Values of the mean temperature scaled using the Srinivasan and Papavassiliou scaling plotted as a function of the scaled wall-normal location with scaling values of the maximum normal turbulent heat flux obtained from theoretical correlations of Kawamura et al. [172] presented in equation (7.16) and (7.17), for the case where both the channel walls are heated with constant heat flux, plotted for different *Pr* in flow cases with different Re_τ: (a) $Re_\tau = 150$ and (b) $Re_\tau = 300$.

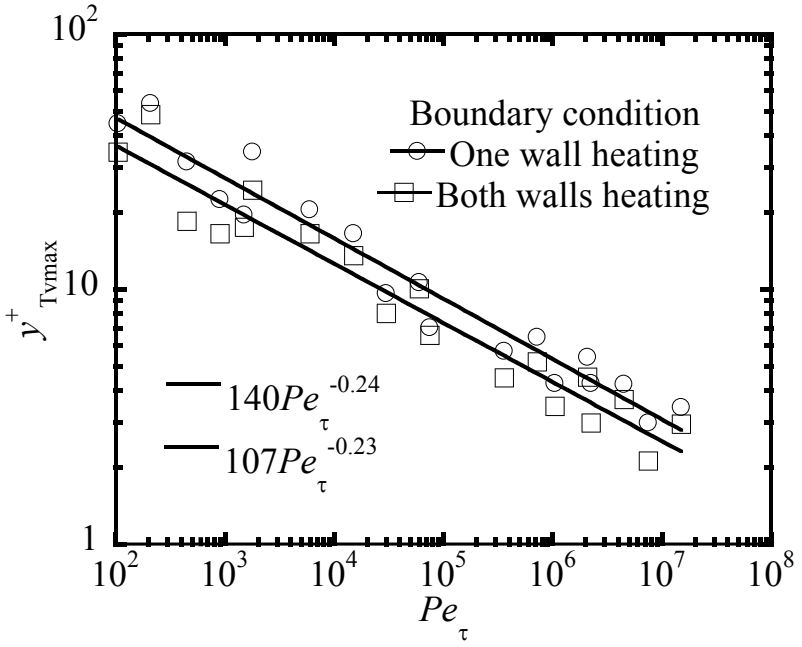

Figure 7.18: Value of the locations of the peak normal turbulent heat flux plotted as a function of the Pe_τ in both the wall heating cases.

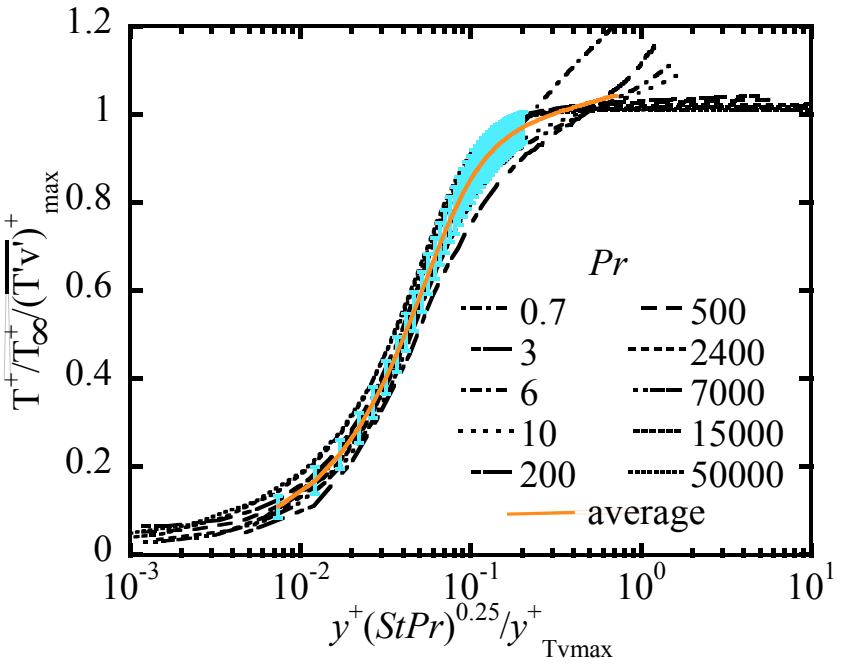

(a)

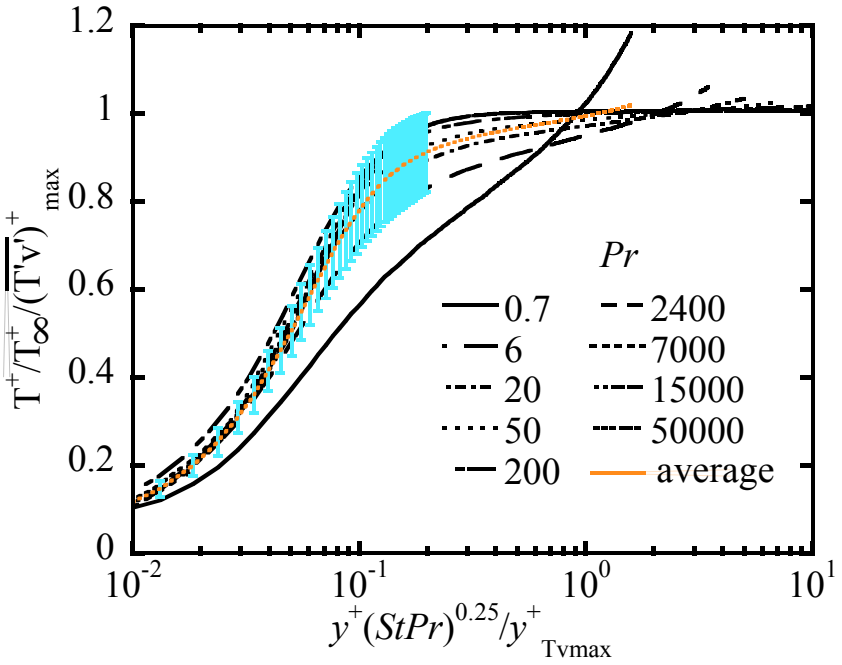

(b)

Figure 7.19: Values of the mean temperature scaled using the Srinivasan and Papavassiliou scaling plotted as a function of the scaled wall-normal location with scaling values of the maximum normal turbulent heat flux used from table 7.7, for the case where one channel wall is heated with constant heat flux, plotted for different *Pr* in flow cases with different Re_τ: (a) $Re_\tau = 150$ and (b) $Re_\tau = 300$. The orange line indicates the average obtained for all the *Pr* data while the blue bars represent the error bars with plus/minus one standard deviation.

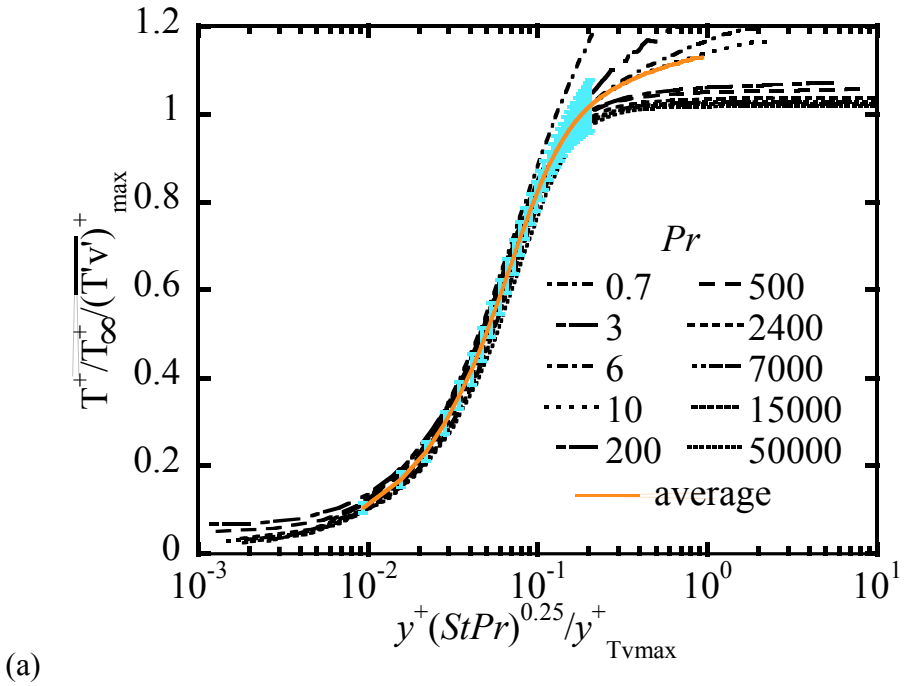

(a)

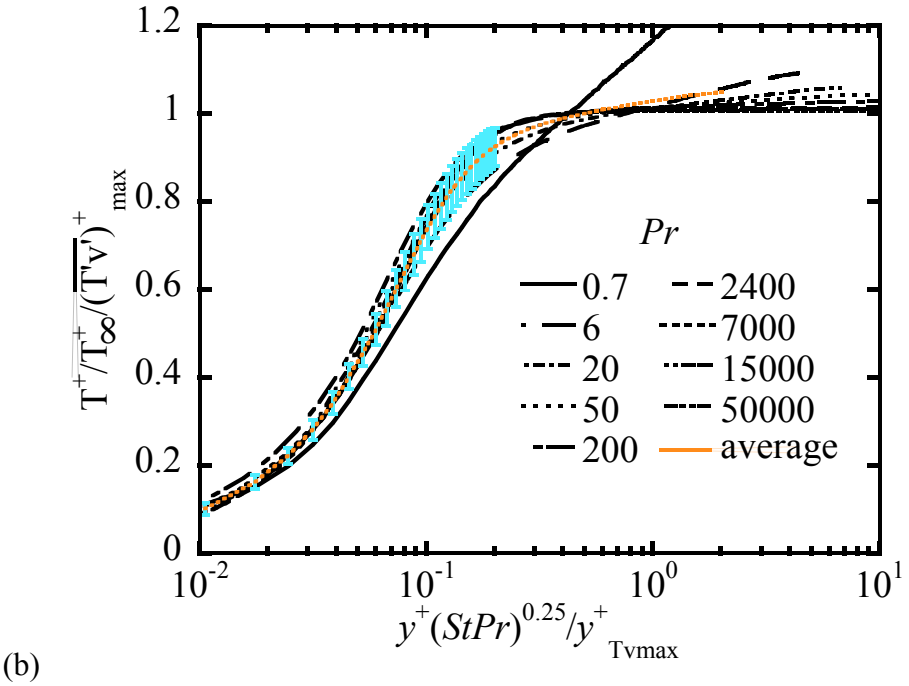

(b)

Figure 7.20: Values of the mean temperature scaled using the Srinivasan and Papavassiliou scaling plotted as a function of the scaled wall-normal location with scaling values of the maximum normal turbulent heat flux used from table 7.8, for the case where both channel walls are heated with constant heat flux, plotted for different *Pr* in flow cases with different Re_τ: (a) $Re_\tau = 150$ and (b) $Re_\tau = 300$. The orange line indicates the average obtained for all the *Pr* data while the blue bars represent the error bars with plus/minus one standard deviation.

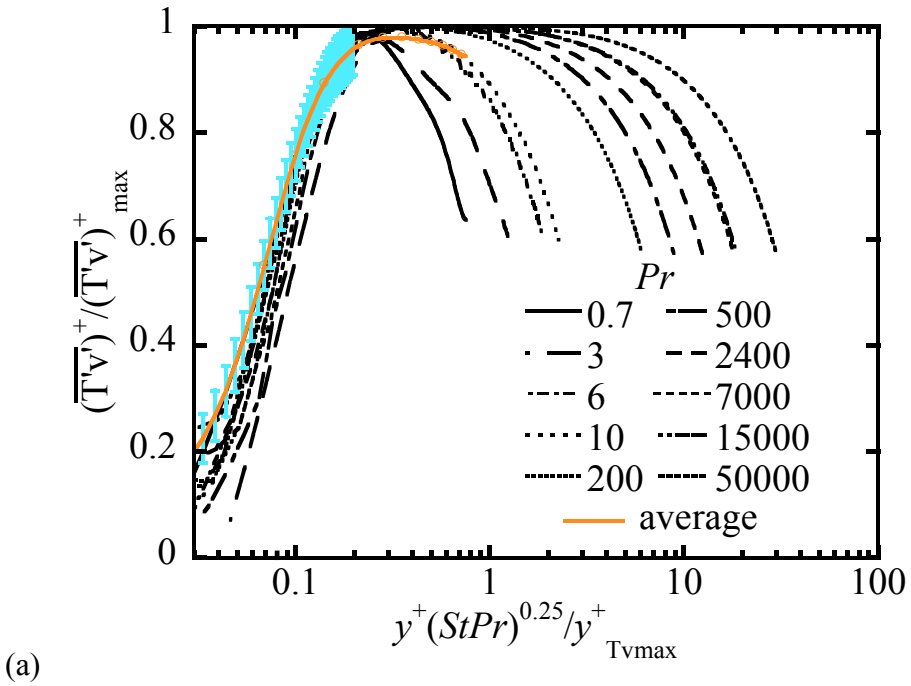

(a)

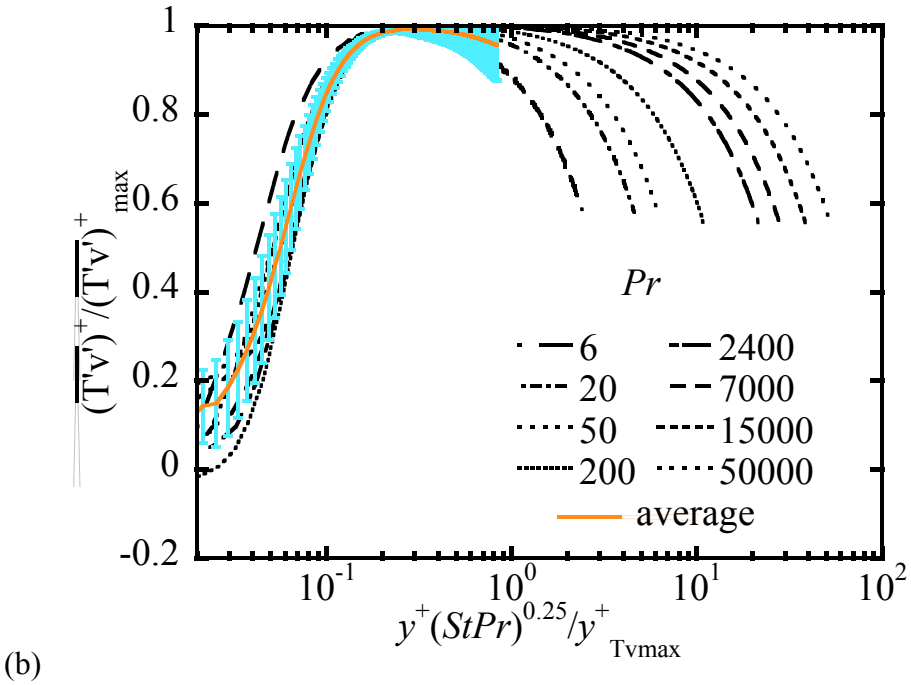

(b)

Figure 7.21: Values of the normal turbulent heat flux scaled using the Srinivasan and Papavassiliou scaling plotted as a function of the scaled wall-normal location with scaling values of the maximum normal turbulent heat flux obtained from DNS/LST, for the case where one channel wall is heated with constant heat flux, plotted for different *Pr* in flow cases with different Re_τ: (a) $Re_\tau = 150$ and (b) $Re_\tau = 300$. The orange line indicates the average obtained for all the *Pr* data while the blue bars represent the error bars with plus/minus one standard deviation.

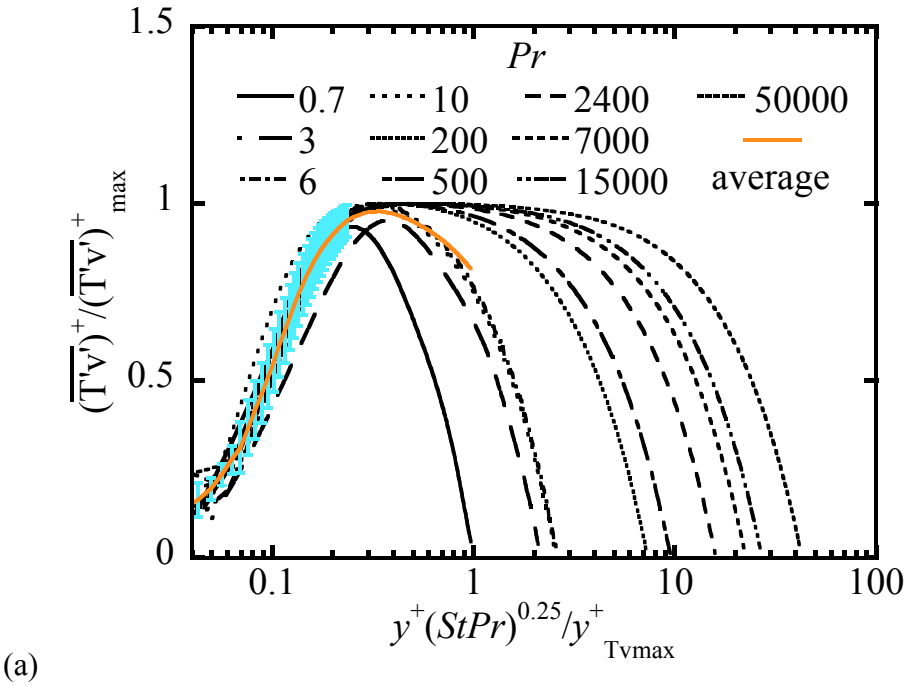

(a)

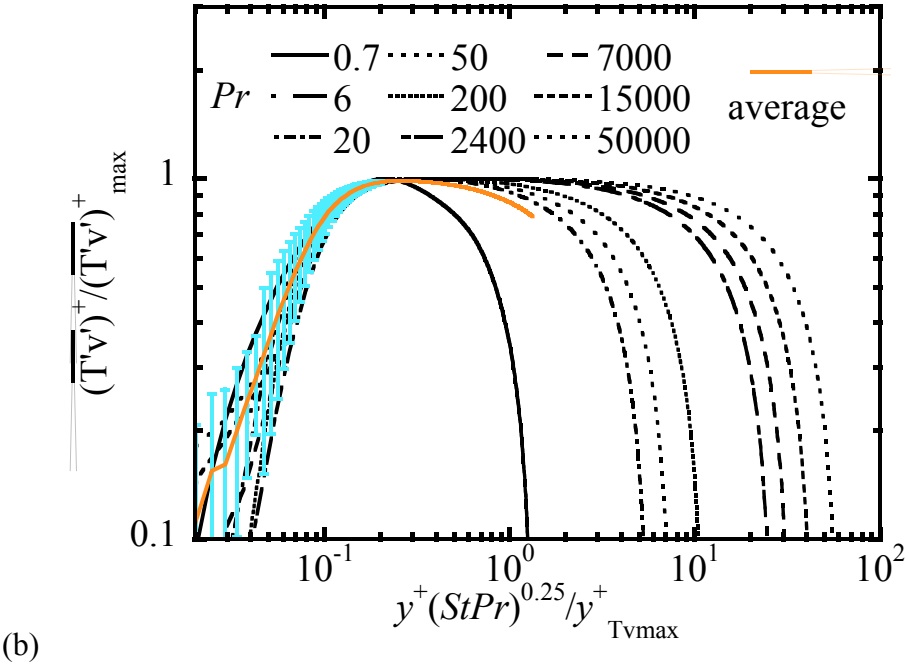

(b)

Figure 7.22: Values of the normal turbulent heat flux scaled using the Srinivasan and Papavassiliou scaling plotted as a function of the scaled wall-normal location with scaling values of the maximum normal turbulent heat flux obtained from DNS/LST, for the case where both the channel walls are heated with constant heat flux, plotted for different *Pr* in flow cases with different Re_τ: (a) $Re_\tau = 150$ and (b) $Re_\tau = 300$. The orange line indicates the average obtained for all the *Pr* data while the blue bars represent the error bars with plus/minus one standard deviation.

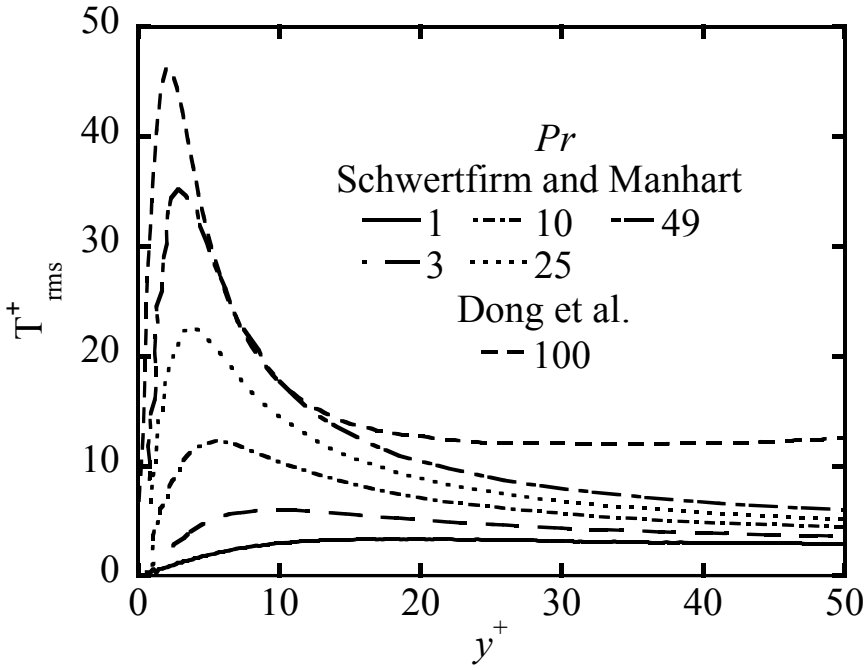

Figure 7.23: Values of the root mean square of the temperature varying as a function of the wall normal distance obtained from works of Schwertfirm and Manhart [132] and Dong et al. [177] for different *Pr* at $Re_\tau = 180$.

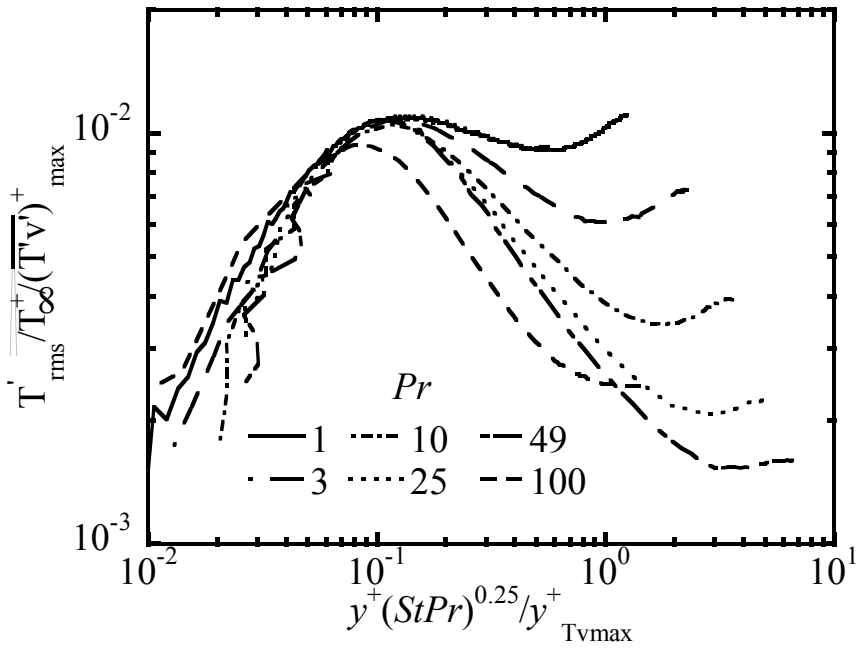

Figure 7.24: Scaled values of the root mean square of the temperature varying as a function of the scaled wall normal distance obtained using the scaling of Srinivasan and Papavassiliou shown for different *Pr* at $Re_\tau = 180$.

Chapter 8: PREDICTION OF TURBULENT PRANDTL NUMBER[§]

8.1 Simulation parameters and procedure

The goal of this work is to determine the Pr_t for different molecular Prandtl number fluids and the behavior of the Pr_t at different distance from the wall. Using DNS and a Lagrangian approach, the Pr_t was calculated using Churchill's [139] interpretation of eddy diffusivities of momentum and heat. The turbulent *Pr* was estimated with different molecular *Pr* and at different distances from the channel walls by two approaches. The first approach utilized the Lagrangian scalar tracking database developed in our laboratory to generate Eulerian type mean velocity and temperature profiles. From these profiles the variation of the local fraction of shear stress due to turbulence $(\overline{u'v'})^{++}$ and the local fraction of heat flux density due to turbulence $(\overline{T'v'})^{++}$ were determined. The details of the simulation can be found in Le and Papavassiliou [143]. The corresponding local fractions of shear stress and heat flux density due to molecular motions were also calculated and from these values the Pr_t was calculated. The other approach involved determining the local fractions of shear stresses and normal heat flux density using the Lagrangian data directly in conjunction with Churchill's physical interpretation without synthesizing any Eulerian temperature profile. This means that Pr_t can be estimated by finding the contributions of turbulent fluctuations to the transport of momentum and heat in the direction normal to the walls. Translating this interpretation in the Lagrangian framework, the number of fluid or heat

[§] Most of the material in this Chapter has been published in the Industrial Engineering and Chemistry Research, 50, 8881-8891 (2011)

markers that arrived at particular distance from the wall (or a bin of appropriate width centered at that location) due to turbulence, would provide an estimate for the turbulence contributions to the transport of momentum or heat, while those that arrived due to molecular motion would help in calculating the molecular contributions to the transport of momentum or heat, respectively. A calculation of the ratio, hence, provided the value of Pr_t.

The DNS is used to obtain the velocity field for the Poiseuille channel and plane Couette flows at Re_τ = 2660. In the first method of determining Pr_t, for Poiseuille channel flow, fluids with Pr of 0.7, 3, 6, 10 and 100 were simulated whereas for plane Couette flow, the Pr was 0.7, 6, 10 and 200. In both Poiseuille channel flow (these were referred to as run E, in Table 1 of Ref. [142]) and plane Couette flow (which were referred to as run A in Ref. [149]), 145,161 markers were released at $y_0 = 0$ at $t^+ = 0$. The time step Δt^+ is 0.25 and 0.2 for the Poiseuille and Couette flow cases, respectively. The complete details to obtain the Pr_t using the second – Lagrangian method is presented below.

8.1.1 Incorporating Churchill's model into the Lagrangian framework – local fraction of normal heat flux

Two sets of simulations were carried out to determine Pr_t, for each of the Poiseuille and Couette flow cases. The first part of the simulation involved finding the local contributions of turbulence and molecular motions to normal heat flux density. The Prandtl numbers of 0.1, 0.7, 6, 10 and 100 were studied for Poiseuille channel flow while for Couette flow Prandtl numbers of 0.1, 0.7, 3, 6, 10 and 200 were studied. In both the Poiseuille channel flow and the plane Couette flow, 145,161 heat markers were

released in the flow field. The time step Δt for the simulation was 0.125 and 0.2 for the Poiseuille and Couette flow cases, respectively. The heat markers were released at y^+ = 0 at t^+ = 0 into the flow field. The channel width was divided in 300 bins, each one of width equal to one viscous unit. After the markers were uniformly dispersed in the y direction, which occurred at large simulation times, the markers that were within each of the 300 bins were identified and captured. Let us denote this time by t_c. Each of the heat markers captured at t_c in a bin contributed to the normal heat flux in that bin; however, there needs to be a way to differentiate the ones that contributed to turbulent heat flux from those that contributed to molecular normal heat flux. The position y_{t_c}, and the velocity, V_{t_c}, of all the heat markers in each of the bins at t_c was known from the DNS/LST simulations as mentioned earlier. Note that only the vertical direction was considered, as the methodology tried to estimate the fraction of heat flux in the direction normal to the wall. As the markers moved during each timestep of Δt, the position $y_{t_c+\Delta t}$ and the velocity $V_{t_c-\Delta t}$ of each heat marker, were also known from the estimates of DNS/LST. The total distance a heat marker moved in that timestep can be estimated as $\Delta y_{tot} = (y_{t_c+\Delta t} - y_{t_c})$. Using values of V_{t_c} and $V_{t_c-\Delta t}$ and substituting them in Equation (8.1) below yields the distance traveled due to convection as shown in Equation (8.2):

$$y_i(x_0, t_{n+1}) = y_i(x_0, t_n) + \left[\frac{3}{2}V_i(x_0, t_n) - \frac{1}{2}V_i(x_0, t_{n-1})\right]\Delta t \qquad (8.1)$$

$$\Delta y_{turb} = y_{t_c+\Delta t} - y_{t_c} = \left[\frac{3}{2}V_{t_c} - \frac{1}{2}V_{t_c-\Delta t}\right]\Delta t \qquad (8.2)$$

The distance the heat marker moved due to turbulence alone can thus be estimated. The motion of each heat marker due to molecular means can be calculated as $\Delta y_{mol} = \Delta y_{tot} - \Delta y_{turb}$. So, the values of Δy_{mol} and Δy_{turb}, for each heat marker, were compared, and depending on which was larger, a marker was labeled as a turbulent or a molecular marker. For example, if there were 2500 turbulent markers and 35000 molecular markers found in one bin, the respective turbulent and molecular distances moved by these markers would be summed up to find the contributions of turbulent and molecular normal heat fluxes, respectively.

Figure 8.1 is a schematic representation of the method used to calculate the local fraction of turbulent normal heat flux for an example of 3 heat markers. The ratio of the turbulent to molecular normal heat fluxes, thus, provided an estimate of $\frac{(\overline{T'v'})^{++}}{1-(\overline{T'v'})^{++}}$. Now, the problem arose with the estimation of the time interval required for these calculations. This time interval was assumed to be related to the Lagrangian time scale associated with the movement of the heat markers, and more specifically it was assumed that it was proportional, i.e., a multiple, of the Lagrangian time scale. In addition, since the different regions of flow in the channel have different time scales, one common time interval for all distances from the channel wall could produce erroneous results. The Lagrangian material time scale provided a good idea of the different time intervals that need to be considered for different vertical location in the channel. The expressions used were those obtained by Le and Papavassiliou [148]

Poiseuille Flow

$$\tau_y^L = (0.98\,\mathrm{Pr}^{0.13})\left[4.59 + 33.04\left(\frac{y_0^+}{h^+}\right)^{0.87}\right] \quad \text{for } Pr \le 3 \qquad (8.3)$$

$$\tau_y^L = \left[4.59 + 33.04\left(\frac{y_0^+}{h^+}\right)^{0.87}\right] \quad \text{for } Pr > 3 \qquad (8.4)$$

Couette Flow

$$\tau_y^L = \mathrm{Pr}^{0.083}\left[1.83 + 24.85\left(\frac{y_0^+}{h^+}\right)^{0.58}\right] \quad \text{for } \mathrm{Pr} \le 3 \qquad (8.5)$$

$$\tau_y^L = \left[1.83 + 24.85\left(\frac{y_0^+}{h^+}\right)^{0.58}\right] \quad \text{for } Pr > 3 \qquad (8.6)$$

As a first approach, the time intervals were calculated with substituting different values of y_0 (corresponding to locations at the center of the bins in the range 0.5 to 149.5) in Equations 8.3 – 8.6. With these values of time intervals, the local turbulent fractions of normal heat flux were determined and compared with Eulerian results for $(\overline{T'v'})^{++}$. Even though the trend observed for the local fraction of normal heat flux due to turbulence matched the results obtained from Eulerian data, there were discrepancies in the actual values. So, a calibration procedure was implemented to determine the time interval over which the movement of a heat marker should be evaluated in order to classify it as molecular or as turbulent. Two *Pr*, 0.7 and 10 for Poiseuille flow, were considered. The time interval was increased to twice and then to three times the Lagrangian material scale to no avail. When the time interval was fixed at four times the Lagrangian material scale, the results matched the Eulerian results. The time interval was further increased to 5 times and then to 10 times the Lagrangian material time scale, but the resulting fraction of turbulent heat flux showed no

variations. So, the time interval was determined to be four times the Lagrangian material scale and, for all other *Pr* and the case of plane Couette flow, the results were also in agreement with Eulerian results. The data used to obtain the results, in case of Poiseuille channel flow, spanned a time t_c of 2900 wall time units to 4100 wall time units, while for Couette flow it was between 3500 and 4500 wall time units . In order to decrease noise, different initial time steps were used within these time ranges. For example, in the case of Poiseuille flow, for Pr = 100, at y^+ = 149.5, the time interval was 150 (4 times 37.5, which is the Lagrangian material time scale at y^+ = 149.5). In this case, 1050 different initial times starting from 2900 to 3950 were used, and the results were then averaged. Similarly, in case of Couette flow, for Pr = 0.1, at y^+ = 134.5, where the time interval was 83 (4 times 20.75), 917 different initial times were used. Also, the channel symmetry along the centerline at y^+ = 150 was utilized, and results for the top half of the channel were added to the results for the bottom half to further reduce statistical noise. It must be noted here that the values of Pr_t calculated were very sensitive to the values of $(\overline{T'v'})^{++}$ obtained using the above procedure, especially for the higher *Pr*. For example, for the case of Poiseuille flow, with Pr = 100, assume that the $(\overline{T'v'})^{++}$ value can be either 0.993 or 0.998, which is a difference of 0.5%. Using a value of $(\overline{u'v'})^{++}$ equal to 0.91, the Pr_t calculated utilizing Equation (2.37) results in values of 7.128 and 2.026, respectively. This indicates that Pr_t given by Equation (2.37) is very sensitive to the values of $(\overline{T'v'})^{++}$, especially for higher *Pr*. This is an important observation, because Churchill's model for turbulent convection is insensitive to reasonable changes in the numerical and empirical functions that appear in the model equations [141]. This finding has been further corroborated with data from

our laboratory [143], but it is true for the prediction of the mean temperature profile. The prediction of Pr_t appears to be very sensitive to even very small changes in $(\overline{T'v'})^{++}$.

8.1.2 Incorporating Churchill's model into the Lagrangian framework – local fraction of shear stress

Is it possible to apply the same methodology to fluid particles (these are similar to heat markers, but their motion was simulated with no Brownian motion), and to determine the local fraction of shear stresses in the normal direction due to turbulent and molecular contributions? To resolve this question, 145,161 fluid markers were released uniformly from the *y-z* plane at time $t^+ = 0$. The timesteps for the Poiseuille channel and plane Couette flow simulations were 0.125 and 0.2, respectively. The channel width was again separated into 300 bins of equal size, and the fluid markers that were found within each one of these bins at time t_c were identified. Similar to the estimation of the local fraction of normal heat flux, the distances traveled by turbulent and molecular fluid markers were summed up and the ratio was used to calculate the local fraction of turbulent shear stress.

However, there were a few details that needed attention before proceeding to the calculation of the local fraction of shear stresses. Firstly, for the motion of fluid markers, there were no diffusion effects, so the criteria to classify turbulent and molecular markers needed modification. In order to address this issue, the assumption made was that if a fluid marker left a particular bin, after moving some distance during an appropriately determined time interval, then it would be considered a turbulent

marker, while if it moved from one location to another within the same bin, it would be assigned a molecular status. Hence, the number of bins (or, in other words, the bin size) is important and should be fixed.

Second, in the previous case, the Lagrangian material scale played a vital role and helped in estimating the appropriate time interval in different vertical locations of the channel. But, the same formulae cannot be applied in the case of fluid markers. This essentially left us in the dark with regards to the time interval needed. To determine the time interval, a calibration approach, as was utilized with the turbulent fraction of heat flux, was implemented. For Poiseuille channel flow, an arbitrary time interval of $\Delta t = 2$ was tried, and, interestingly, the results of the local fraction of shear stress in the normal direction due to turbulence matched those from Eulerian simulations, at about $y^+ = 70.5$. So, for regions at $y^+ \geq 70.5$, the value of 2 wall time units was used to carry out the analysis and determine the local fraction of turbulent shear stress. For distances in the range $0 \leq y^+ \leq 70.5$, the use of a time interval of 2 over-estimated the values; hence, the time interval needed to be smaller when compared to that at $y^+ = 70.5$. In order to determine the different time intervals, the time intervals were reduced, starting from $\Delta t = 2$ at $y^+ = 70.5$, proportional to the Lagrangian material scales for Poiseuille channel flow in the vertical direction. Similarly, it was found that for plane Couette flow a time interval of 2 matched Eulerian results at $y^+ \geq 80.5$. The different ratios of Lagrangian material scales for different y^+ for plane Couette flow were used to determine the time intervals at distances $y^+ < 80.5$. A total of 50 and 250 different initial times for the cases of Poiseuille and plane Couette flows, respectively, were used, and the results averaged to decrease statistical noise. The channel symmetry along $y^+ = 150$ once again was

utilized to further reduce noise. The data obtained for the local fraction of turbulent shear stress for both Poiseuille and plane Couette flows seemed to agree well with the Eulerian results reported by Le and Papavassiliou.

8.2 Results and discussion

8.2.1 Turbulent Prandtl number obtained using Eulerian equations

The local fraction of shear stress due to turbulence, $(\overline{u'v'})^{++}$, can be obtained using the DNS results as follows:

$$\frac{\Gamma}{\Gamma_w}\left[1-(\overline{u'v'})^{++}\right]=\frac{d\overline{U}^{+}}{dy^{+}} \qquad (8.7)$$

where y^+ is the distance from the wall in viscous wall units ($y^+ = yu^*/\nu$), and $\overline{U}^+$ is the dimensionless mean velocity ($\overline{U}^+ = \overline{U}/u^*$). The value of the local fraction of shear stress due to turbulence as obtained using Equation (8.7), for both Poiseuille [164] channel and plane Couette [143] flows is presented in Figure 8.2. It starts from zero at the channel wall and goes up to nearly 1, while reaching a plateau value, at $y^+ \approx$ 55-60.

The local fraction of heat flux density for the case of both walls of the channel being heated is given by

$$\frac{q}{q_w}\left[1-(\overline{T'v'})^{++}\right]=\frac{d\overline{T}^{+}}{dy^{+}} \qquad (8.8)$$

The results obtained can be found in Figures 8.5(a) and (b) in reference [143].

The values of $(\overline{u'v'})^{++}$ presented in Figure 8.2, for Poiseuille and Couette flow with the respective values of $(\overline{T'v'})^{++}$ (from Le and Papavassiliou [143]) are substituted

into Equation (2.37) and the Pr_t is determined as a function of the distance from the channel wall and for a range of Pr's.

The results are presented in Figures 8.3(a) and (b), for Poiseuille channel and plane Couette flow, respectively. For Poiseuille channel flow, the Pr_t does not show any systematic change and has values between 0.8 and 1, at large distances from channel wall, while the value increases above one 1 near the channel wall. Also, the Pr_t increases with increase in Pr near the channel wall. For the case of plane Couette flow, the Pr_t at large distances from the channel wall also does not exhibit systematic change, and it is between 0.7 and 1 for Pr = 0.7 and 200, while it is between 1 and 1.5 for Pr = 6 and 10. At regions close to the channel walls, the Pr_t, shows lower values compared to the values at the center of the channel.

8.2.2 Turbulent Prandtl number using Lagrangian arguments

The local fraction of turbulent shear stresses for Poiseuille and Couette flow calculated using the method described above is shown in Figure 8.2. The values obtained are a little higher than those from Eulerian calculations till y^+ = 5.5 and y^+ = 13.5, for Poiseuille flow and plane Couette flow, respectively. At distances greater than these, the values obtained for the local fraction of turbulent shear stress are always a bit lower than those from Eulerian results. However, the trend is similar for both methods, and, as can be expected, the fraction of turbulent shear stress is higher near the center of the channel when compared to near the channel walls. Interestingly, for Couette flow, the fraction of turbulent shear stress is larger as compared to the Poiseuille channel flow. Such result is in line with the fact that the turbulence intensity (i.e., the root mean

squared of the velocity fluctuations) is higher for Couette flow than for Poiseuille flow at the same *Re*.

The turbulent contribution to the local fraction of normal heat flux is presented in Figures 8.4 (a) and (b), for Poiseuille channel and plane Couette flow, respectively, as a function of normal distance from the channel wall.

The details of the simulation methodology used to obtain these results have been discussed in Section 8.1. The schematic shown in Figure 8.1 is an illustration of the idea behind the calculation of the turbulent heat flux. For both types of flows, there is zero contribution to the local fraction of normal heat flux due to turbulence at the channel walls. So, for all *Pr*'s, the curves rise from zero to values very close to one for medium-high *Pr* ($Pr \geq 3$). It is also observed that the fraction of normal heat flux due to turbulence rises faster to values close to one for higher *Pr*'s, indicating that for these *Pr*'s the normal heat flux is mainly due to turbulence. For lower *Pr*'s, this is true at large distances from the wall, while closer to the wall there are both turbulent and molecular contributions to normal heat flux. As was observed earlier for the transport of momentum, the Couette flow exhibits a higher level of turbulent contribution to the total normal heat flux than the Poiseuille channel flow. Since the Couette flow field is under constant shear stress, it can be viewed as a rather extended logarithmic layer of a turbulent velocity field. It can be, thus, inferred that the logarithmic layer is a region that promotes turbulent mixing.

Figures 8.5(a) and (b) are plots of the Pr_t calculated using the values of the shear stress and heat flux density from the DNS/LST. The Pr_t increases for increasing molecular *Pr* close to the wall in both Poiseuille and Couette flow. This behavior of

increasing Pr_t near the wall with Pr has been observed previously in the DNS results of Schwertfirm and Manhart [132], and Hasegawa and Kasagi [174]. For $Pr \geq 3$, in both Poiseuille and Couette flow, the Pr_t starts from high values near the channel walls (similar to the results of Schwertfirm and Manhart, and Hasegawa and Kasagi) and decreases as the distance from the wall increases. In case of lower Pr (i.e., 0.1, 0.7), the Pr_t starts from lower values. An insight can be obtained by referring to Figure 18 of Bergant and Tiselj [179], which showed the Pr_t profile as a function of distance from the wall, for different boundary conditions. Bergant and Tiselj observed that the Pr_t showed trends of reaching a minimum near channel walls when a constant heat flux boundary condition was utilized. This boundary condition allowed temperature fluctuations at the wall. The value of Pr_t, on the other hand, increased asymptotically near channel walls, when a constant temperature boundary condition was enforced. Considering the simulation conditions of the present study, for lower Pr's (i.e., $Pr = 0.1$, 0.7), the molecular diffusion effects are large compared to convective effects. So, the heat markers travel larger distances in the vertical direction, as was seen from previous results for forwards dispersion in Chapter 4, and the number of markers that cross the center of the bins, which can be viewed in this case as a temperature fluctuation, is higher. For larger Pr's (≥ 3), convective and diffusive effects are comparable to one other, so fewer markers move from bin to bin near the channel wall than for lower Pr, which translates to smaller temperature fluctuations in this case.

A comparison of the results for turbulent Pr using the two methods discussed here, with available data for turbulent Pr from earlier DNS works of Kasagi's group [133, 174, 180], Kawamura et al. [172, 181] and Schwertfirm and Manhart [132] is

presented in Figures 8.6(a) and (b). The results show good agreement with the previous data available for Pr_t. A comparison of the $Pr_{t\infty}$ calculated using the current method with the results from various analytical expressions discussed in the literature review in Chapter 2, as a function of *Pr,* is presented in Figure 8.7. There is qualitative agreement between the present results and these expressions. A further comparison with analytical results, not only for $Pr_{t\infty}$ but for the Pr_t as a function of y^+, is shown in Figure 8.8. The results were obtained with a consistent methodology for Prandtl numbers ranging from low to high values. So, this methodology, using Churchill's theory provides an alternative and consistent approach to determining the Pr_t in turbulent channel flows.

8.3 Conclusions

Two methods were utilized to calculate the Pr_t. Both the methods involved Churchill's model for scaling of shear stress and heat flux in estimating the turbulent Prandtl number. The first methodology used Lagrangian data to reconstruct the Eulerian mean temperature profiles and, on the basis of Eulerian equations of the Churchill model, yielded the local fraction of the shear stress and of the heat flux density that was attributed to turbulent effects. The second methodology involved determining the local rates of transfer utilizing a Lagrangian interpretation of Churchill's theoretical framework.

The Eulerian method gave a good estimate of the turbulent Prandtl number, and for both channel and Couette flow cases the Pr_t was seen to be nearly constant at large distances from channel walls. The Pr_t obtained from this method did not show definitive variations with *Pr*. However, near channel walls, the Pr_t increased with

increasing *Pr*, for Poiseuille channel flow, while for Couette flow there was no observable near-wall behavior.

The Lagrangian method provided a consistent approach to modeling and calculating the Pr_t, and it provided a physical interpretation of turbulent transport. The local fraction of normal heat flux, obtained by translating Churchill's theory into scalar marker motions, was found to be in good agreement with Eulerian results. It must be emphasized that the Lagrangian material scales play a vital role in estimating the time interval that needs to be considered for the simulation at different distances from the channel walls. The fraction of turbulent normal heat flux was higher for plane Couette flow compared to Poiseuille channel flow, indicating the importance of turbulence in a constant stress region, like the logarithmic layer. The local turbulent fraction of shear stresses obtained using an analogous application of Churchill's theory also matched previous Eulerian results. For both Poiseuille and Couette flow, similar to previous results in the literature, there was an increase of Pr_t near the walls with increasing *Pr*. For channel flow, at large distances from channel walls, the Pr_t decreased with increasing *Pr* till a $Pr = 6$, while for $Pr = 6, 10, 100$, the values were very close together, considering the error bars. The same trend was observed for plane Couette flow, as for $Pr \leq 3$ there was a decrease in Pr_t with increase in *Pr*, while $Pr = 6$, 10 and 200 were difficult to differentiate. This shows that *Pr* is important for Pr_t calculations for lower *Pr*, while for higher *Pr*, the differences are hardly felt. Even though present DNS is at a relatively low *Re*, future advances in computer power will allow the conduction of DNS at much higher *Re*'s. The methodology outlined in this paper would be expected to produce more accurate results as the *Re* increases, since Churchill's

model was developed utilizing the theoretical correlations and coefficients obtained from higher Re flow studies.

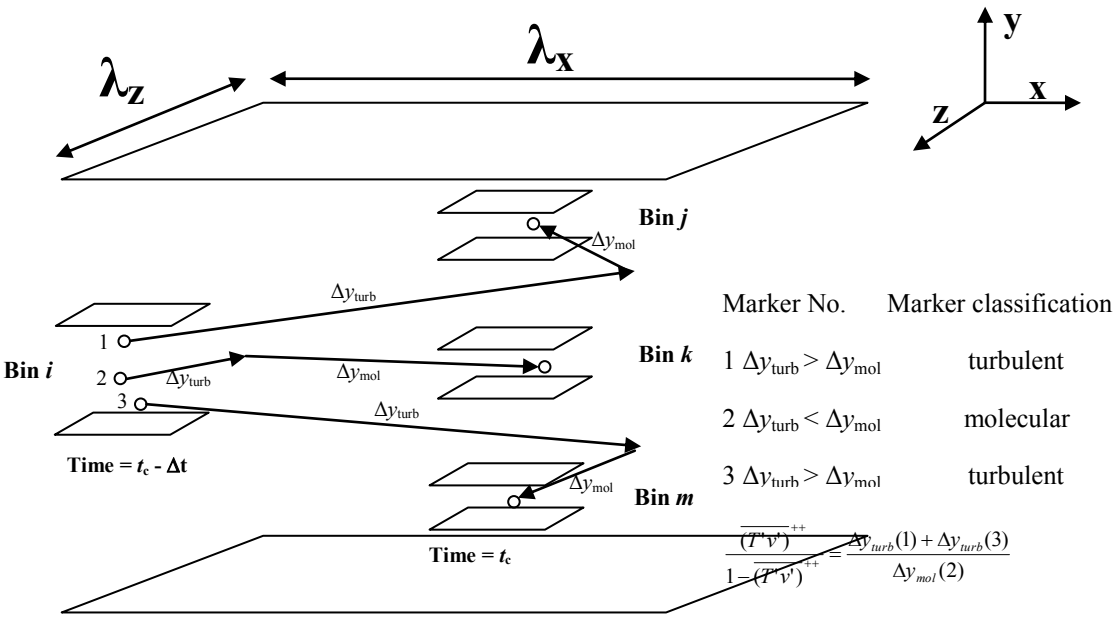

Figure 8.1: Schematic showing the simulation box and an example of classifying three markers that leave bin *i* and arrive at three other bins after a time interval Δt^+. Markers 1 and 3 in the example travel longer because of turbulence, so they would be classified as arriving to bins *j* and *m* due to turbulent motion, contributing thus to the turbulent heat flux. Marker 2, on the other hand, travels a longer distance due to molecular diffusion towards bin *k*, and would be classified as arriving to bin *k* due to molecular motion (*x* is the direction of the mean flow).

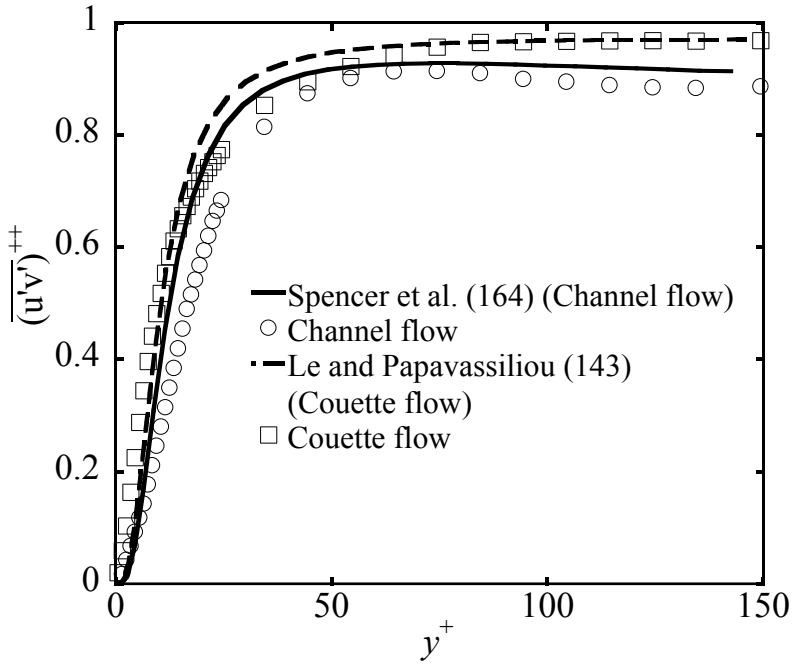

Figure 8.2: Local fraction of shear stress due to turbulence in Poiseuille channel and Couette flow plotted as a function of normal distance from the wall.

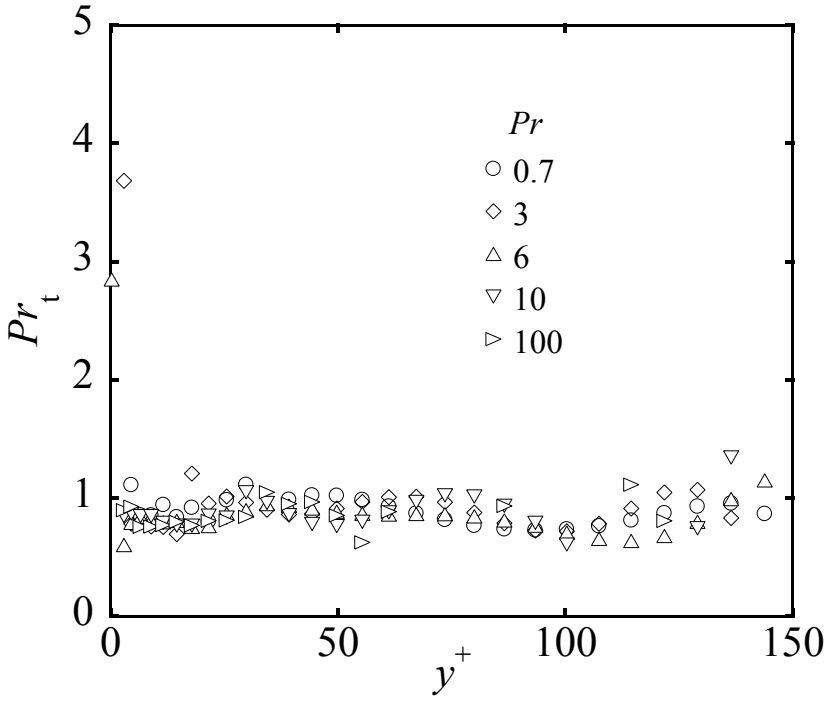

(a)

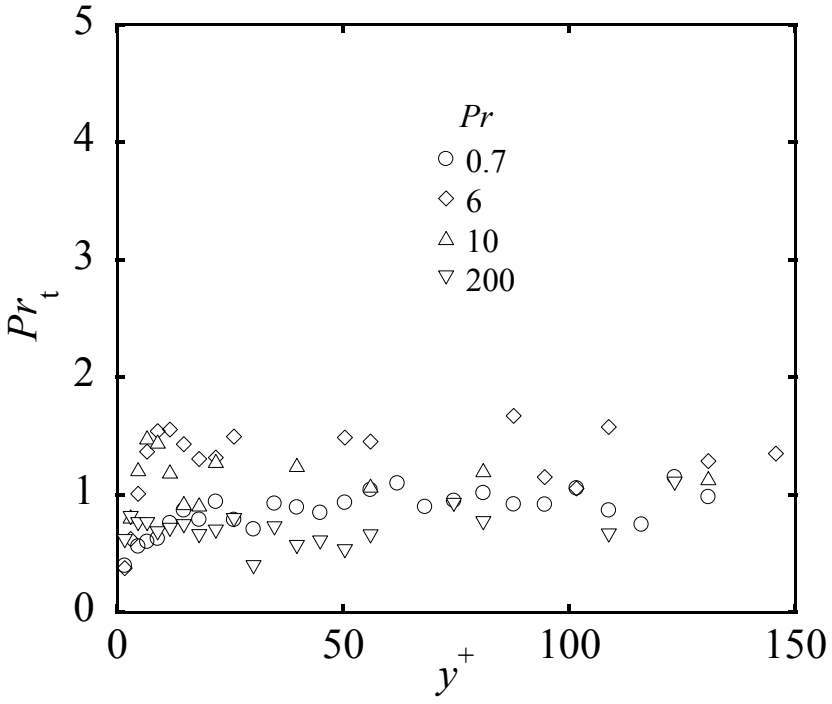

(b)

Figure 8.3: Turbulent Prandtl number calculated using Equation (2.37) plotted as a function of distance from the channel wall, for the case of different molecular Prandtl numbers for (a) Poiseuille channel flow, (b) plane Couette flow.

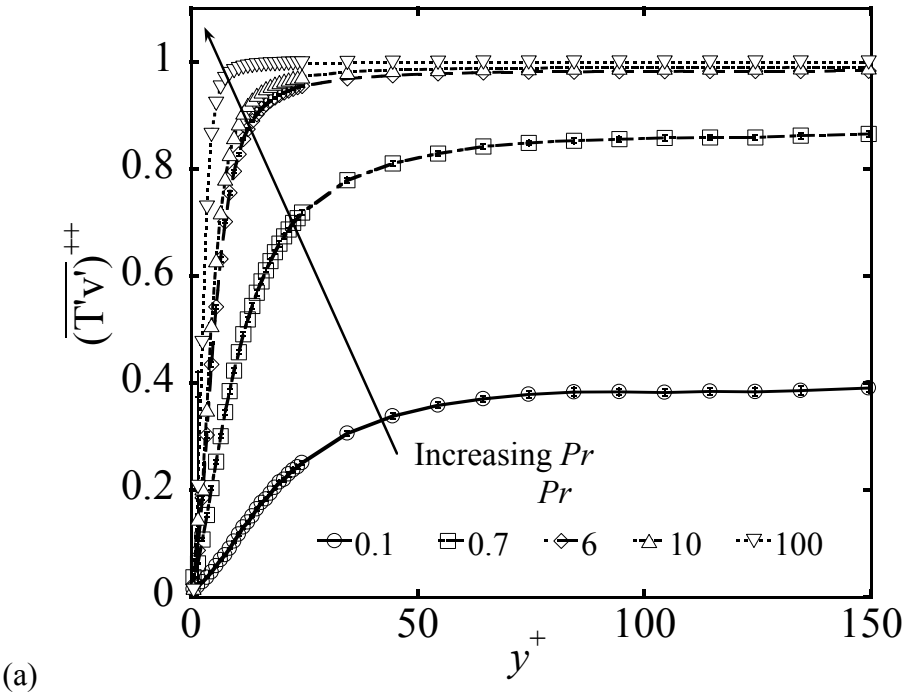

(a)

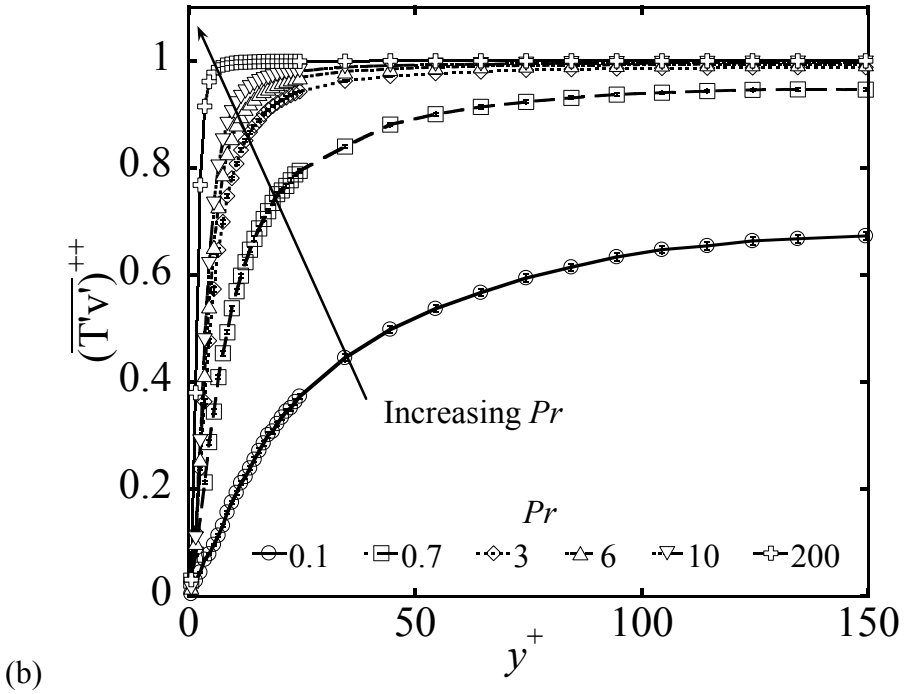

(b)

Figure 8.4: Local fraction of radial heat flux density due to turbulence calculated using DNS/LST and utilizing Churchill's concept plotted as a function of normal distance from the channel wall, for the case of different molecular Prandtl numbers for (a) Poiseuille channel flow and (b) plane Couette flow.

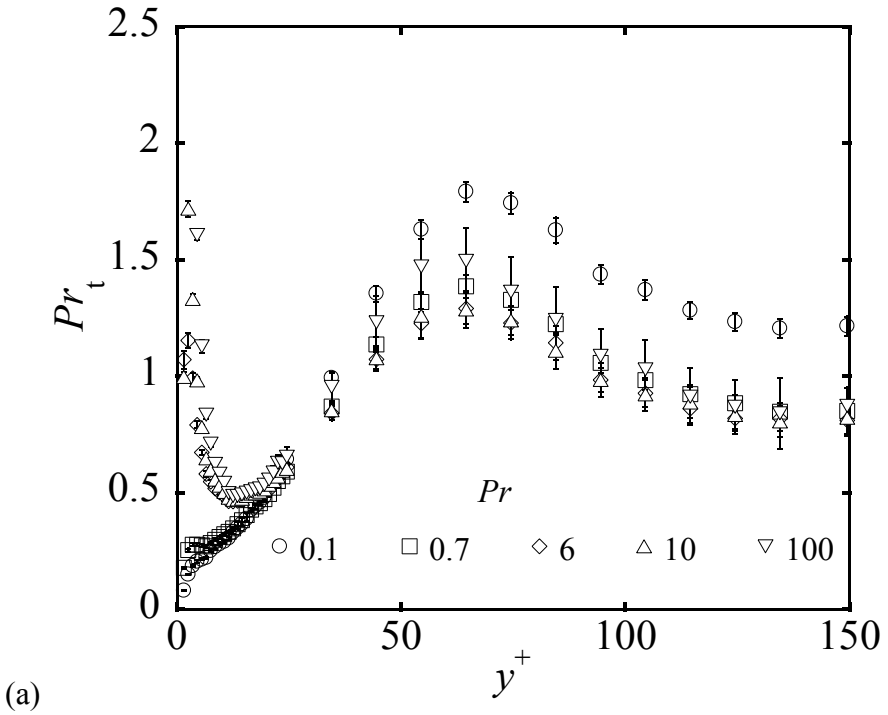

(a)

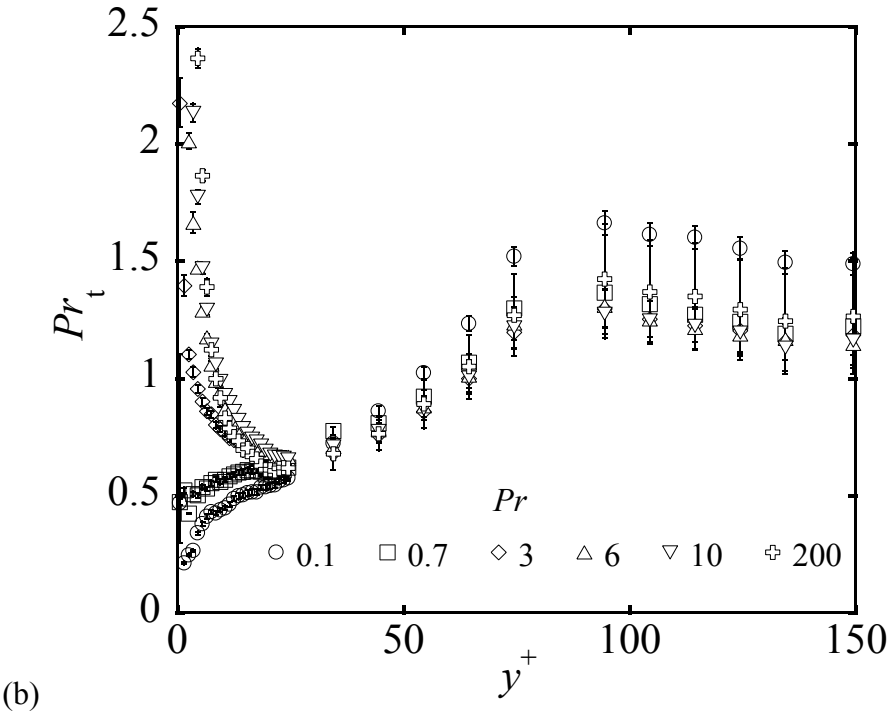

(b)

Figure 8.5: Turbulent Prandtl number calculated using Equation (2.37) with data of local shear stress and radial heat flux obtained from DNS/LST and Churchill's concept plotted as a function of normal distance from the channel wall for different molecular Prandtl numbers for (a) Poiseuille channel flow and (b) plane Couette flow.

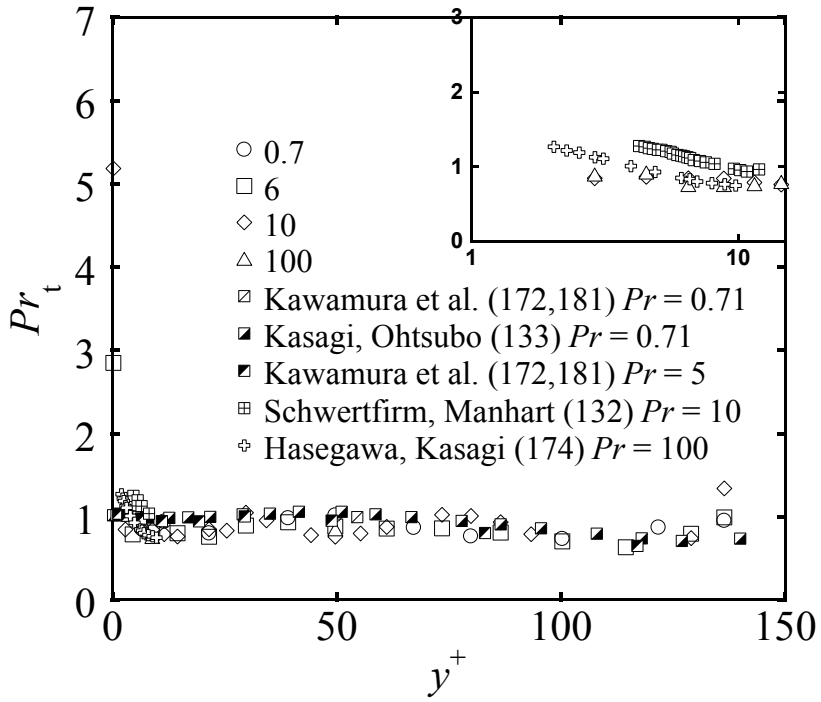

(a)

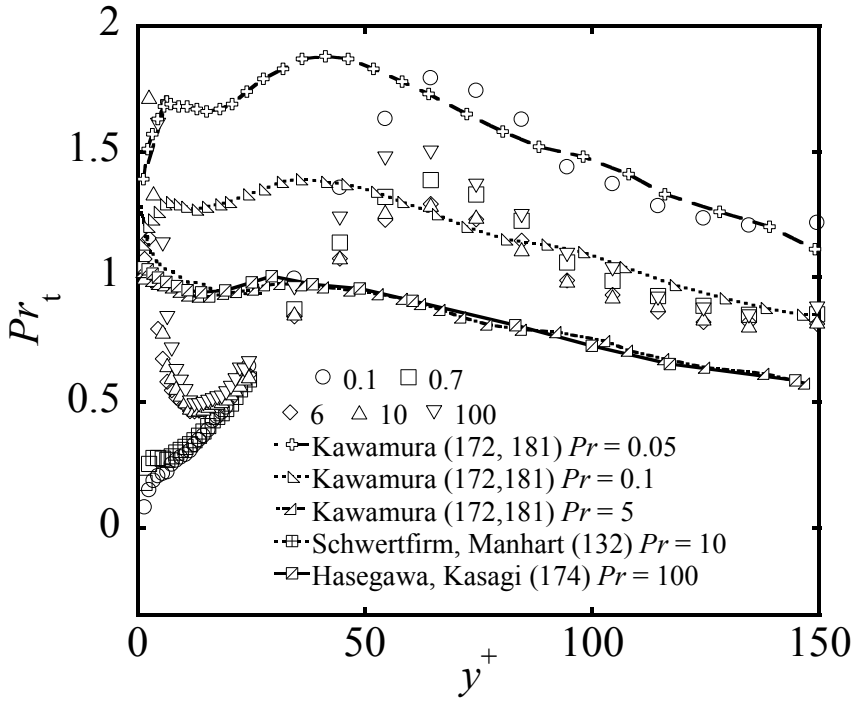

(b)

Figure 8.6: Turbulent Prandtl number for flow in a Poiseuille channel obtained herein compared with available data for turbulent Prandtl number and plotted as a function of normal distance from the wall for different molecular Prandtl number. (a) Present data obtained with Equation (2.37), (b) present data obtained with the process described in Section 8.1.

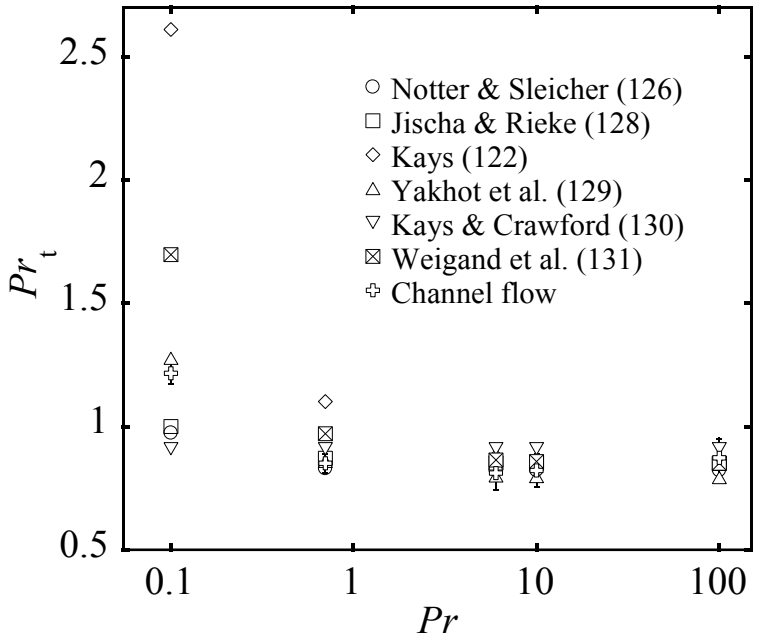

Figure 8.7: Value of turbulent Prandtl number far away from the wall obtained using the Lagrangian interpretation of Churchill's model (Section 8.1) as a function of the molecular Prandtl number, along with results obtained by using previous correlations.

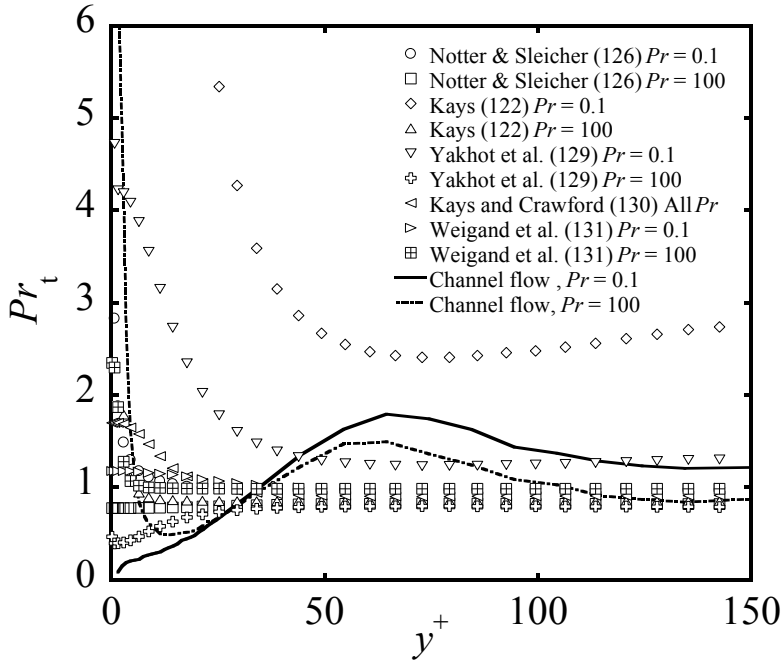

Figure 8.8: Turbulent Prandtl number plotted as a function of the normal distance from the wall, for a low (0.1) and high (100) molecular Prandtl number, for the present study and results obtained using correlations predicted in other previous studies.

Chapter 9: CONCLUSIONS

9.1 Direct numerical simulation and Lagrangian scalar tracking

In this dissertation the direct numerical simulation technique is used in conjunction with the Lagrangian scalar tracking method. This combined approach provides a Lagrangian perspective to heat transport in turbulent flow. Its inherent advantages are revealed by the success of the models that have been implemented in these studies to calculate backwards dispersion, turbulent Prandtl number and mean temperature statistics. This approach provides a framework to analyze different regions of the channel and the behavior of scalar transport in case of different types of fluids in the system, or different types of flow such as Poiseuille and Couette flow. Some of the notable results from are summarized below.

9.1.1 Forwards/backwards dispersion

a) In Poiseuille channel flow, the Lagrangian material scales for single particle dispersion increase with increase in Pr but achieve a plateau value at $Pr = 6$.

b) In Poiseuille channel for both single particle and relative particle dispersion, for all Pr, the forwards dispersion proceeds at faster rates in the viscous sub-layer, transition region and logarithmic regions. At the center of the channel, the backwards dispersion is faster than forwards dispersion

- Increased differences between forwards and backwards dispersion are observed with increase in Pr, for small Pr, while there is a plateau achieved for $Pr \geq 6$.
- With an increase in Re of turbulent flow

1. The trends become even more consistent.
2. The rates of both forwards and backwards dispersion are accelerated; hence the differences are increased too.

c) The different behavior of forwards and backwards single particle dispersion can be interpreted by the combination of:
   - Asymmetry of the pdf of the vertical velocity fluctuations that the dispersing particles experience, as it is expressed by the skewness of the pdf.
   - The coherent structures that transport these dispersing particles.

d) In addition to the above two properties, the differing behavior of forwards and backwards relative dispersion also depends on the distribution of marker pair relative velocity differences.

e) For plane Couette flow, for turbulent relative dispersion, the forwards relative dispersion is faster in the logarithmic region and the center of the channel. In the viscous sub-layer and transition region, the backwards relative dispersion is faster.
   - The same behavior is observed for all *Pr*.
   - The coherent structures – namely the large scale structures extending through these channels, found in the works of Papavassiliou and Hanratty [150] and others help in explaining these differences.

f) Different primary directions of turbulent heat transport are found for forwards and backwards dispersion.
   - Backwards dispersion shows more consistent and sustained directions of heat transport compared to forwards dispersion

- Backwards dispersion also shows increased intensity of heat transport in these directions compared to forwards dispersion
    1. This is true for all the regions of the turbulent Poiseuille and plane Couette flow.
    2. There is an increase in intensity with slight changes to the angle of primary directions of heat transport with an increase in the Pr of the fluid.
- Results show that backward dispersion is carried out by a set of relatively long-lived, stably oriented flow structures, while forwards dispersion is influenced by short-lived, constantly tumbling eddies.

g) "Turbulent Dispersive Ratio", a concept analogous to the "dispersive index" term in optics, is established as an important parameter in identifying the different primary directions of heat transport for forwards and backwards dispersion in a turbulent channel flow, for a particular type of fluid.

h) Analysis of the Lagrangian spectrum shows the existence of a universal -1 regime for both forwards and backwards dispersion.
    - This spectrum is observed in all regions of the channel, for both channel and Couette flow, for all *Pr*.

9.1.2 Scaling of heat/mass transport

a) The location and the values of the maximum normal turbulent heat flux (MNTHF) are chosen as the two main parameters for scaling of heat transport quantities
    - $\frac{y^+_{Tv\max}}{St^{\frac{1}{4}}\,\mathrm{Pr}^{\frac{1}{4}}}$ is used as the length scale while $T^+_\infty Tv^+_{\max}$ is used as the temperature scale

- This scaling shows collapse of mean temperature profiles, root mean square (rms) temperature fluctuation profiles and normal heat flux profiles for both *Re* and all *Pr* examined in the inner region.
- The above mentioned profiles all collapse for different *Re* and *Pr* for both single wall heating and both wall heating scenarios.

b) The sensitivity of the scaling to the scaling parameters shows that accurate values of location of MNTHF are vital to the better capture of the different quantities. However, a relatively rough estimate of the value of the MNTHF is adequate to obtain scaled results of various profiles.

c) Power law fits for location and values of MNTHF are calculated for easier scaling calculations for variety of *Re* and *Pr*

- $y^+_{T\overline{v'}^+_{\max}} = 140 Pe_\tau^{-0.24}$ - case of one wall heating
- $y^+_{T\overline{v'}^+_{\max}} = 107 Pe_\tau^{-0.23}$ - case of both wall heated
- $(\overline{T'v'})^+_{\max} = (1+\gamma)\left(1 - \frac{140 Pe_\tau^{-0.24}}{2h^+}\right) - \frac{1}{56 \Pr Pe_\tau^{-0.24}}$ - for one wall heating
- $(\overline{T'v'})^+_{\max} = (1+\gamma)\left(1 - \frac{107 Pe_\tau^{-0.23}}{h^+}\right) - \frac{1}{43.87 \Pr Pe_\tau^{-0.23}}$ - for two wall heating

9.1.3 Turbulent Prandtl number

a) Churchill's innovative idea is translated using an innovative particle tracking model.

b) Lagrangian material scales help in estimating the time interval of tracking of particles.

c) Individual contributions of molecular motion and turbulence to the local fraction of normal shear stress and local fraction of normal heat flux, are calculated from the model

- The local fraction of normal shear stress due to turbulence increases with increasing wall normal distance
- The local fraction of normal heat flux due to turbulence also increases with increasing wall normal distance. This quantity also increases with increase in Pr.

d) The turbulent Prandtl number (Pr_t) is observed to depend on the wall normal distance and the molecular Pr.

- There is an increase in Pr_t with molecular Pr near channel walls, for both Poiseuille channel and plane Couette flow
- For Poiseuille flow, the Pr_t at large wall normal distances decreases with increase in Pr, for small Pr, and achieves a plateau for $Pr \geq 6$.
- For plane Couette flow, the same trend is observed with plateau value achieved at $Pr \geq 3$.

9.2 Future Work

9.2.1 Variance of temperature fluctuations

There is a need to predict concentration and temperature variances with accuracy. In air pollution, for example, the variance of the concentration of the pollutant at a point in the atmosphere is of importance rather than the mean concentration, similarly, the prediction of 'temperature noise' downwind of heat sources in turbulent flows. Durbin [182] proposed a stochastic model based on two-particle dispersion and delineated a procedure to calculate the various concentration statistics including the concentration variance. The central idea of the calculations, however, was based on the concept of reversed dispersion. The procedure to obtain the concentration variance involves obtaining the two particle statistics at a particular point and given time from an ensemble of markers arriving at the particular location. The statistical equation used to calculate this has been delineated clearly by Durbin. In future, we aim to extend the ideas of backwards dispersion developed so far through the studies of Durbin to calculating the temperature and the concentration variances.

9.2.2 Scalar mixing characteristics

The phenomenon of mixing of scalars (e.g., heat, mass, etc.) within turbulent flows has a wide variety of potential applications across areas, including meteorology, oceanic science, heat transfer, combustion, and environmental pollutant dispersion. A common assumption in prior studies of scalar transport in turbulence is that the advected substance is considered to be passive and does not have a back effect on the flow field. Reviews in the literature by Shraiman and Siggia [10], Warhaft [5],

Dimotakis [11], and Sreenivasan [183] have compiled some of the important fundamental characteristics of turbulent mixing. Depending on the type of the source, whether it is a point or line source, or if it is a discrete source (puff) or continuous source (plume), the scalar field downstream gets modified. Many studies tried to understand the behavior of thermal fields downstream of scalar sources [58, 184-191] . However, the majority of this literature is with respect to the case of homogenous, isotropic turbulence or grid turbulence. Work in our laboratory, analyzing anisotropic turbulent flows, inside turbulent channels has focused on the scalar characteristics downstream of a single puff or plume source [148, 153, 157, 192-194]. Recent works of Mydlarski et al.[195] have reported statistics of scalar quantities for line source release in a high-aspect channel flow. These studies provided the first real idea of mixing of scalars inside turbulent channel flows for different wall normal source locations and at different downstream locations. An idea for future work in this direction is to use the DNS/LST approach to complement this study of Mydlarski et al. The study will focus on identifying downstream mixing characteristics of two different scalar sources released at different wall-normal locations from the channel wall. The combined DNS/LST approach will be advantageous in studying scalar mixing of sources with different *Pr* and in flows at different *Re*.

9.2.3 Batchelor and Richardson-Obukhov scaling in relative dispersion

The concept of turbulent relative dispersion was introduced by Richardson [61]. As the name suggests, it arises from understanding the motion of a particle in relation to another in the flow field. Sawford [54], Salazar and Collins [66], presented

comprehensive reviews of the theory, various models proposed, experimental and numerical findings for different statistics in the dissipative and the inertial subrange. However, it is apt to note here that the flows of interest in these reviews are isotropic in nature. The most famous theories of turbulent relative dispersion are the scaling of the mean square distance with time. Richardson [61] and Obukhov [64] separately predicted a scaling with the third power of time. However, Batchelor [62] later on predicted that within a certain timescale, the initial particle separation is quite important and the mean square distance for these times will depend on the two-thirds power of initial distance of separation. Over the last decade, these theories have been put to test for a wide variety of flows and the results obtained have indicated these scaling in a number of different cases [74, 196-201]. The idea proposed here for future research is to analyze our case of channel flow to obtain mean square dispersion statistics and validate whether the Batchelor, Richardson-Obukhov scaling are a feature even in cases of anisotropic flows. The study will also help in calculating the Richardson-Obukhov constants [73, 74, 202], reported values of which seem to vary a lot in the existing literature. The proposed research will also aim to incorporate the idea of backwards relative dispersion to characterize scaling in this type of dispersion.

Bibliography

1. Abbrecht, P.H. and S.W. Churchill, *The thermal entrance region in fully developed turbulent flow.* AIChE Journal, 1960. **6**(2): p. 268-273.
2. Lyons, S.L., *A Direct Numerical Simulation of Fully Developed Turbulent Channel Flow With Passive Heat Transfer*, 1989, University of Illinois at Urbana-Champaign: Urbana, Illinois.
3. Kim, J., P. Moin, and R. Moser, *Turbulence statistics in fully developed channel flow at low Reynolds number.* Journal of Fluid Mechanics, 1987. **177**: p. 133-166.
4. Papavassiliou, D.V., *Structure and Transport in Wall Turbulence*, 1996, Univerist of Illinois at Urbana-Champaign: Urbana, Illinois.
5. Warhaft, Z., *Passive Scalars in Turbulent Flows.* Annual Review of Fluid Mechanics, 2000. **32**(1): p. 203-240.
6. Churchill, S.W., *Critique of the Classical Algebraic Analogies between Heat, Mass, and Momentum Transfer.* Industrial & Engineering Chemistry Research, 1997. **36**(9): p. 3866-3878.
7. Churchill, S.W., *A Critique of Predictive and Correlative Models for Turbulent Flow and Convection.* Industrial & Engineering Chemistry Research, 1996. **35**(9): p. 3122-3140.
8. Mylne, K.R. and P.J. Mason, *Concentration fluctuation measurements in a dispersing plume at a range of up to 1000 m.* Quarterly Journal of the Royal Meteorological Society, 1991. **117**(497): p. 177-206.
9. Pasquill, F. and F.B. Smith, *Atmospheric Diffusion*. Third Edition ed. 1983, New York: John Wiley and Sons.
10. Shraiman, B.I. and E.D. Siggia, *Scalar turbulence.* Nature, 2000. **405**(6787): p. 639-646.
11. Dimotakis, P.E., *Turbulent Mixing.* Annual Review of Fluid Mechanics, 2005. **37**(1): p. 329-356.
12. Pratsinis, S.E. and S. Vemury, *Particle formation in gases: A review.* Powder Technology, 1996. **88**(3): p. 267-273.
13. Vaillancourt, P.A. and M.K. Yau, *Review of Particle–Turbulence Interactions and Consequences for Cloud Physics.* Bulletin of the American Meteorological Society, 2000. **81**(2): p. 285-298.
14. Shaw, R.A., *Particle-Turbulence Interactions in Atmospheric Clouds.* Annual Review of Fluid Mechanics, 2003. **35**(1): p. 183-227.
15. Dibble, R.W. and J. Warnatz, *Combustion, Physical and Chemical Fundamentals, Modeling and Simulations, Experiments, Pollutant Formation*. 1996, New York: Springer.
16. Xu, J. and S.B. Pope, *PDF calculations of turbulent nonpremixed flames with local extinction.* Combustion and Flame, 2000. **123**(3): p. 281-307.
17. Zagarola, M.V., *Mean Flow in Scaling in Turbulent Pipe Flow*, 1996, Princeton University.
18. Zagarola, M.V. and A.J. Smits, *Mean-flow scaling of turbulent pipe flow.* Journal of Fluid Mechanics, 1998. **373**: p. 33-79.

19. Osterlund, J.M., *Experimental Studies of Zero Pressure-Gradient Turbulent Boundary Layer*, 1999, KTH.
20. Smits, A.J., B.J. McKeon, and I. Marusic, *High–Reynolds Number Wall Turbulence.* Annual Review of Fluid Mechanics, 2011. **43**(1): p. 353-375.
21. Hites, M.H., *Scaling of High-Reynolds Number Turbulent Boundary Layers in the National Diagnostic Facility*, 1997, Illinois Institute of Technology.
22. Nickels, T.B., et al., *Some predictions of the attached eddy model for a high Reynolds number boundary layer.* Philosophical Transactions of the Royal Society A: Mathematical, Physical and Engineering Sciences, 2007. **365**(1852): p. 807-822.
23. Klewicki, J.C., J.F. Foss, and J.M. Wallace, *Flow at Ultra-High Reynolds and Rayleigh Numbers*, ed. R.J. Donnelly and K.R. Sreenivasan. 1998, New York: Springer.
24. Marusic, I., R. Mathis, and N. Hutchins, *Predictive Model for Wall-Bounded Turbulent Flow.* Science, 2010. **329**(5988): p. 193-196.
25. Wei, T. and W.W. Willmarth, *Reynolds-number effects on the structure of a turbulent channel flow.* Journal of Fluid Mechanics, 1989. **204**: p. 57-95.
26. Shen, X. and Z. Warhaft, *The anisotropy of the small scale structure in high Reynolds number ($R_\lambda \sim 1000$) turbulent shear flow.* Physics of Fluids, 2000. **12**(11): p. 2976-2989.
27. McKeon, B.J., *Controlling Turbulence.* Science, 2010. **327**(5972): p. 1462-1463.
28. Kasagi, N., Y. Tomita, and A. Kuroda, *Direct Numerical Simulation of Passive Scalar Field in a Turbulent Channel Flow.* Journal of Heat Transfer, 1992. **114**(3): p. 598-606.
29. Lyons, S.L., T.J. Hanratty, and J.B. McLaughlin, *Large-scale computer simulation of fully developed turbulent channel flow with heat transfer.* International Journal for Numerical Methods in Fluids, 1991. **13**(8): p. 999-1028.
30. Moser, R.D., J. Kim, and N.N. Mansour, *Direct numerical simulation of turbulent channel flow up to $Re_\tau = 590$.* Physics of Fluids, 1999. **11**(4): p. 943-945.
31. Abe, H., H. Kawamura, and H. Choi, *Very Large-Scale Structures and Their Effects on the Wall Shear-Stress Fluctuations in a Turbulent Channel Flow up to $Re_\tau = 640$.* Journal of Fluids Engineering, 2004. **126**(5): p. 835-843.
32. Hu, Z., C.L. Morfey, and N.D. Sandham, *Wall Pressure and Shear Stress Spectra from Direct Simulations of Channel Flow.* AIAA Journal, 2006. **44**(7): p. 1541-1549.
33. Hoyas, S. and J. Jimenez, *Scaling of the velocity fluctuations in turbulent channels up to $Re_\tau = 2003$.* Physics of Fluids, 2006. **18**(1): p. 011702-4.
34. Abe, H., H. Kawamura, and Y. Matsuo, *Surface heat-flux fluctuations in a turbulent channel flow up to Re_τ=1020 with Pr=0.025 and 0.71.* International Journal of Heat and Fluid Flow, 2004. **25**(3): p. 404-419.
35. Gad-el-Hak, M. and P.R. Bandyopadhyay, *Reynolds Number Effects in Wall-Bounded Turbulent Flows.* Applied Mechanics Reviews, 1994. **47**(8): p. 307-365.

36. George, W.K. and L. Castillo, *Zero-Pressure-Gradient Turbulent Boundary Layer.* Applied Mechanics Reviews, 1997. **50**(12): p. 689-729.
37. De Graaff, D.B. and J.K. Eaton, *Reynolds-number scaling of the flat-plate turbulent boundary layer.* Journal of Fluid Mechanics, 2000. **422**: p. 319-346.
38. Wei, T., et al., *Properties of the mean momentum balance in turbulent boundary layer, pipe and channel flows.* Journal of Fluid Mechanics, 2005. **522**: p. 303-327.
39. Monkewitz, P.A., K.A. Chauhan, and H.M. Nagib, *Self-consistent high-Reynolds-number asymptotics for zero-pressure-gradient turbulent boundary layers.* Physics of Fluids, 2007. **19**(11): p. 115101.
40. Barenblatt, G.I., *Scaling laws for fully developed turbulent shear flows. Part 1. Basic hypotheses and analysis.* Journal of Fluid Mechanics, 1993. **248**: p. 513-520.
41. Barenblatt, G.I., *The 1999 James Lighthill Memorial Paper: Scaling laws for turbulent wall-bounded shear flows at very large Reynolds numbers.* Journal of Engineering Mathematics, 1999. **36**(4): p. 361-384.
42. Afzal, N., *Power law and log law velocity profiles in turbulent boundary-layer flow: equivalent relations at large Reynolds numbers.* Acta Mechanica, 2001. **151**(3): p. 195-216.
43. Afzal, N., *Analysis of Instantaneous Turbulent Velocity Vector and Temperature Profiles in Transitional Rough Channel Flow.* Journal of Heat Transfer, 2009. **131**(6): p. 064503.
44. Barenblatt, G.I. and A.J. Chorin, *A mathematical model for the scaling of turbulence.* Proceedings of the National Academy of Sciences of the United States of America, 2004. **101**(42): p. 15023-15026.
45. Barenblatt, G.I., A.J. Chorin, and V.M. Prostokishin, *A note on the intermediate region in turbulent boundary layers.* Physics of Fluids, 2000. **12**(9): p. 2159-2161.
46. Marusic, I., et al., *Wall-bounded turbulent flows at high Reynolds numbers: Recent advances and key issues.* Physics of Fluids, 2010. **22**(6): p. 065103-24.
47. Kader, B.A., *Temperature and concentration profiles in fully turbulent boundary layers.* International Journal of Heat and Mass Transfer, 1981. **24**(9): p. 1541-1544.
48. Churchill, S.W., *Progress in the thermal sciences: AIChE Institute Lecture.* AIChE Journal, 2000. **46**(9): p. 1704-1722.
49. Einstein, A., *The motion of elements suspended in static liquids as claimed in the molecular kinetic theory of heat.* Annalen der Physik, 1905. **17**(8): p. 549-560.
50. Taylor, G.I., *Diffusion by Continuous Movements.* Proceedings of the London Mathematical Society, 1922. **s2-20**(1): p. 196-212.
51. Batchelor, G.K. and A.A. Townsend, *Turbulent Diffusion*, in *Surveys in Mechanics*, G.K. Batchelor, Editor. 1956, Cambridge University Press: Cambridge, United Kingdom.
52. Monin, A.S. and A.M. Yaglom, *Statistical Fluid Mechanics: Mechanics of Turbulence*. Vol. 1. 1971, Cambridge: MIT Press.

53. Hinze, J.O., *Transport Processes in Turbulent Flows*. 1987, New York: McGraw Hill.
54. Sawford, B., *Turbulent Relative Dispersion.* Annual Review of Fluid Mechanics, 2001. **33**(1): p. 289-317.
55. Corrsin, S. *Remarks on turbulent heat transfer. An account of some features of the phenomenon in fully turbulent region*. in *Proceedings of the First Iowa Symposium on Thermodynamics*. 1953. State University of Iowa, Iowa City.
56. Corrsin, S., *Progress Report on Some Turbulent Diffusion Research*, in *Advances in Geophysics*, H.E. Landsberg and J.V. Mieghem, Editors. 1959, Elsevier. p. 161-164.
57. Saffman, P.G., *On the effect of the molecular diffusivity in turbulent diffusion.* Journal of Fluid Mechanics, 1960. **8**(02): p. 273-283.
58. Shlien, D.J. and S. Corrsin, *Dispersion measurements in a turbulent boundary layer.* International Journal of Heat and Mass Transfer, 1976. **19**(3): p. 285-295.
59. Fackrell, J.E. and A.G. Robins, *Concentration fluctuations and fluxes in plumes from point sources in a turbulent boundary layer.* Journal of Fluid Mechanics, 1982. **117**: p. 1-26.
60. Hanratty, T.J., *Heat transfer through a homogeneous isotropic turbulent field.* AIChE Journal, 1956. **2**(1): p. 42-45.
61. Richardson, L.F., *Atmospheric Diffusion Shown on a Distance-Neighbour Graph.* Proceedings of the Royal Society of London. Series A, 1926. **110**(756): p. 709-737.
62. Batchelor, G.K., *The application of the similarity theory of turbulence to atmospheric diffusion.* Quarterly Journal of the Royal Meteorological Society, 1950. **76**(328): p. 133-146.
63. Ogura, Y., Y. Sekiguchi, and K. Miyakoda, *Classification of Turbulent Diffusions in the Atmosphere.* Journal of the Meteorological Society of Japan. Ser. II, 1953. **31**(8): p. 271-285.
64. Obukhov, A.M., *On the Distribution of Energy in the Spectrum of Turbulent Flow.* Izv. Akad. Nauk SSSR Ser. Geogr. Geofiz., 1941. **5**: p. 453-466.
65. Monin, A.S. and A.M. Yaglom, *Statistical Fluid Mechanics: Mechanisms of Turbulence*, ed. J.L. Lumley. Vol. 2. 1975, Cambridge: MIT Press.
66. Salazar, J.P.L.C. and L.R. Collins, *Two-Particle Dispersion in Isotropic Turbulent Flows.* Annual Review of Fluid Mechanics, 2008. **41**(1): p. 405-432.
67. Batchelor, G., *Diffusion in a Field of Homogeneous Turbulence. I. Eulerian Analysis.* Australian Journal of Chemistry, 1949. **2**(4): p. 437-450.
68. Batchelor, G.K., *Diffusion in a field of homogeneous turbulence.* Mathematical Proceedings of the Cambridge Philosophical Society, 1952. **48**(02): p. 345-362.
69. Egbert, G.D. and M.B. Baker, *Comments on paper 'the effect of gaussian particle-pair distribution functions in the statistical theory of concentration fluctuations in homogeneous turbulence' by B. L. Sawford (Q.J. April 1983, 109, 339–353).* Quarterly Journal of the Royal Meteorological Society, 1984. **110**(466): p. 1195-1200.
70. Lundgren, T.S., *Turbulent pair dispersion and scalar diffusion.* Journal of Fluid Mechanics, 1981. **111**: p. 27-57.

71. Borgas, M.S., et al., *High Schmidt number scalars in turbulence: Structure functions and Lagrangian theory.* Physics of Fluids, 2004. **16**(11): p. 3888-3899.
72. Bernard, P.S. and A.L. Rovelstad, *On the physical accuracy of scalar transport modeling in inhomogeneous turbulence.* Physics of Fluids, 1994. **6**(9): p. 3093-3108.
73. Sawford, B.L., P.K. Yeung, and M.S. Borgas, *Comparison of backwards and forwards relative dispersion in turbulence.* Physics of Fluids, 2005. **17**(9): p. 095109-9.
74. Berg, J., et al., *Backwards and forwards relative dispersion in turbulent flow: An experimental investigation.* Physical Review E, 2006. **74**(1): p. 016304.
75. Biferale, L., et al., *Multifractal Statistics of Lagrangian Velocity and Acceleration in Turbulence.* Physical Review Letters, 2004. **93**(6): p. 064502.
76. Biferale, L., et al., *Multiparticle dispersion in fully developed turbulence.* Physics of Fluids, 2005. **17**(11): p. 111701-4.
77. Theodorsen, T. *Mechnism of Turbulence*. in *Second Midwestern Conference on Fluid Mechanics*. 1952. The Ohio State University, Columbus, Ohio.
78. Townsend, A.A., *The Structure of Turbulent Shear Flow*. 1956, Cambridge, London: Cambridge University Press.
79. Robinson, S.K., *Coherent Motions in the Turbulent Boundary Layer.* Annual Review of Fluid Mechanics, 1991. **23**(1): p. 601-639.
80. Jeong, J., et al., *Coherent structures near the wall in a turbulent channel flow.* Journal of Fluid Mechanics, 1997. **332**: p. 185-214.
81. Smith, C.R. and J.D.A. Walker, *Turbulent Wall-Layer Vortices*, in *Fluid Vortices*, S. Green, Editor. 1995, Kluwer Academic: Dordrecht.
82. Adrian, R.J., C.D. Meinhart, and C.D. Tomkins, *Vortex organization in the outer region of the turbulent boundary layer.* Journal of Fluid Mechanics, 2000. **422**: p. 1-54.
83. Kaftori, D., G. Hetsroni, and S. Banerjee, *Funnel-shaped vortical structures in wall turbulence.* Physics of Fluids, 1994. **6**(9): p. 3035-3050.
84. Schoppa, W. and F. Hussain, *Coherent structure dynamics in near-wall turbulence.* Fluid Dynamics Research, 2000. **26**(2): p. 119-139.
85. Hanratty, T.J. and D.V. Papavassiliou, *The Role of Wall Vortices in Producing Turbulence*, in *Self-Sustaining Mechanisms of Wall Turbulence*, R.L. Panton, Editor. 1997, Computational Mechanics: Southampton, United Kingdom.
86. Na, Y., T. Hanratty, and Z.-C. Liu, *The Use of DNS to Define Stress Producing Events for Turbulent Flow over a Smooth Wall.* Flow, Turbulence and Combustion, 2001. **66**(4): p. 495-512.
87. Hutchins, N., B. Ganapathisubramani, and I. Marusic. *Spanwise Periodicity and the Existence of Very Large Scale Coherence in Turbulent Boundary Layers*. in *Fourth International Symposium on Turbulence and Shear Flow Phenomena*. 2005. Williamsburg, Virginia.
88. Head, M.R. and P. Bandyopadhyay, *New aspects of turbulent boundary-layer structure.* Journal of Fluid Mechanics, 1981. **107**: p. 297-338.
89. Ganapathisubramani, B., E.K. Longmire, and I. Marusic, *Experimental investigation of vortex properties in a turbulent boundary layer.* Physics of Fluids, 2006. **18**(5): p. 055105-14.

90. Moin, P. and J. Kim, *The structure of the vorticity field in turbulent channel flow. Part 1. Analysis of instantaneous fields and statistical correlations.* Journal of Fluid Mechanics, 1985. **155**: p. 441-464.
91. Kim, J. and P. Moin, *The structure of the vorticity field in turbulent channel flow. Part 2. Study of ensemble-averaged fields.* Journal of Fluid Mechanics, 1986. **162**: p. 339-363.
92. Nagano, Y. and M. Tagawa, *Coherent motions and heat transfer in a wall turbulent shear flow.* Journal of Fluid Mechanics, 1995. **305**: p. 127-157.
93. Le, P.M. and D.V. Papavassiliou, *A physical picture of the mechanism of turbulent heat transfer from the wall.* International Journal of Heat and Mass Transfer, 2009. **52**(21–22): p. 4873-4882.
94. Lumley, J.L., *The Structure of Inhomogenous Turbulent Flows*, in *Atmospheric Turbulence and Radio Wave Propagation*, A.M. Yaglom and V.I. Tatarski, Editors. 1967: Nauka, Moscow.
95. Loeve, M.M., *Probability Theory*. 1955, Princeton, New Jersey: Van Nostrand.
96. Papoulis, A., *Probability, Random Variables and Stochastic Processes*. 1965, New York: McGraw-Hill.
97. Bakewell, J.H.P. and J.L. Lumley, *Viscous Sublayer and Adjacent Wall Region in Turbulent Pipe Flow.* Physics of Fluids, 1967. **10**(9): p. 1880-1889.
98. Moin, P., *Probing Turbulence via Large Eddy Simulation*, in *Aerospace Sciences Meeting*1984: Reno, Nevada.
99. Glauser, M.N., S.J. Leib, and W.K. George, *Coherent Structures in the Axisymmetric Turbulent Jet Mixing Layer*, in *Turbulent Shear Flows 5*, F. Durst, et al., Editors. 1987, Springer-Verlag: New York. p. 134-145.
100. Herzog, S., *The Large-Scale Structure in Near Wall Region of Turbulent Pipe Flow*, 1986, Cornell University.
101. Moin, P. and R.D. Moser, *Characteristic-eddy decomposition of turbulence in a channel.* Journal of Fluid Mechanics, 1989. **200**: p. 471-509.
102. Kerr, R.M., *Higher-order derivative correlations and the alignment of small-scale structures in isotropic numerical turbulence.* Journal of Fluid Mechanics, 1985. **153**: p. 31-58.
103. Ashurst, W.T., et al., *Alignment of vorticity and scalar gradient with strain rate in simulated Navier--Stokes turbulence.* Physics of Fluids, 1987. **30**(8): p. 2343-2353.
104. Vedula, P., P.K. Yeung, and R.O. Fox, *Dynamics of scalar dissipation in isotropic turbulence: a numerical and modelling study.* Journal of Fluid Mechanics, 2001. **433**: p. 29-60.
105. Afzal, N., *Millikan's argument at moderately large Reynolds number.* Physics of Fluids, 1976. **19**(4): p. 600-602.
106. Afzal, N., *Mesolayer theory for turbulent flows.* AIAA Journal, 1984. **22**(3): p. 437-439.
107. Afzal, N., *Periods between Bursting in Turbulent Shear Flow: An Intermediate Layer.* Current Science, 1984. **53**: p. 640-642.
108. Panton, R.L., *Composite asymptotic expansions and scaling wall turbulence.* Philosophical Transactions of the Royal Society A: Mathematical, Physical and Engineering Sciences, 2007. **365**(1852): p. 733-754.

109. Klewicki, J., et al., *A physical model of the turbulent boundary layer consonant with mean momentum balance structure.* Philosophical Transactions of the Royal Society A: Mathematical, Physical and Engineering Sciences, 2007. **365**(1852): p. 823-840.
110. Wei, T., et al., *Scaling heat transfer in fully developed turbulent channel flow.* International Journal of Heat and Mass Transfer, 2005. **48**(25–26): p. 5284-5296.
111. Kawamura, H., H. Abe, and K. Shingai. *DNS of Turbulence and Heat Transport in a Channel Flow with Different Reynolds and Prandtl Numbers and Boundary Conditions*. in *3rd International Syposium on Turbulence, Heat and Mass Transfer*. 2000. Aichi Shuppan, Japan.
112. Klewicki, J.C., et al., *Overview of a Methodology for Scaling the Indeterminate Equations of Wall Turbulence.* AIAA Journal, 2006. **44**(11): p. 2475-2481.
113. Le, P.M. and D.V. Papavassiliou, *On the scaling of heat transfer using thermal flux gradients for fully developed turbulent channel and Couette flows.* International Communications in Heat and Mass Transfer, 2008. **35**(4): p. 404-412.
114. George, W.K., M. Wosnik, and L. Castillo. *Similarity Analysis for Forced Convection Turbulent Boundary Layer*. in *10th International Symposium on Transport Phenomena in Thermal Sciences and Process Engineering*. 1997. Kyoto, Japan.
115. Wang, X. and L. Castillo *, *Asymptotic solutions in forced convection turbulent boundary layers.* Journal of Turbulence, 2003: p. N6.
116. Blackwell, B.F., W.M. Kays, and R.J. Moffat, *The Turbulent Boundary Layer on a Porous Plate: An Experimental Study of Heat Transfer Behavior with Adverse Pressure Gradients*, 1972, Stanford University.
117. Blom, J., *An Experimental Determination of the Turbulent Prandtl Number in a Developing Temperature Boundary Layer*, 1970, Technishe Hogeschool: Eindhoven.
118. Orlando, A.F., W.M. Kays, and R.J. Moffat, *Turbulent Transport of Heat and Momentum in a Boundary Layer Subject to Deceleration, Suction and Variable Wall Temperature*, 1974, Stanford University.
119. Thielbahr, W.H., W.M. Kays, and R.J. Moffat, *The Turbulent Boundary Layer: Experimental Heat Transfer with Strong Favorable Pressure Gradients and Blowing*, 1969, Stanford University.
120. Wang, X., L. Castillo, and G. Araya, *Temperature Scalings and Profiles in Forced Convection Turbulent Boundary Layers.* Journal of Heat Transfer, 2008. **130**(2): p. 021701-17.
121. Reynolds, A.J., *The prediction of turbulent Prandtl and Schmidt numbers.* International Journal of Heat and Mass Transfer, 1975. **18**(9): p. 1055-1069.
122. Kays, W.M., *Turbulent Prandtl Number---Where Are We?* Journal of Heat Transfer, 1994. **116**(2): p. 284-295.
123. Reynolds, O., *On the Extent and Action of the Heating Surface on Steam Boilers*, in *Papers on Mechanical and Physical Subjects* 1874, Cambridge University Press: Cambridge.

124. Churchill, S.W., *New simplified models and formulations for turbulent flow and convection.* AIChE Journal, 1997. **43**(5): p. 1125-1140.
125. *ANSYS FLUENT 6.3 User guide 12.4.5*.
126. Notter, R.H. and C.A. Sleicher, *A solution to the turbulent Graetz problem—III Fully developed and entry region heat transfer rates.* Chemical Engineering Science, 1972. **27**(11): p. 2073-2093.
127. Azer, N.Z. and B.T. Chao, *A mechanism of turbulent heat transfer in liquid metals.* International Journal of Heat and Mass Transfer, 1960. **1**(2–3): p. 121-138.
128. Jischa, M. and H.B. Rieke, *About the prediction of turbulent prandtl and schmidt numbers from modeled transport equations.* International Journal of Heat and Mass Transfer, 1979. **22**(11): p. 1547-1555.
129. Yakhot, V., S.A. Orszag, and A. Yakhot, *Heat transfer in turbulent fluids—I. Pipe flow.* International Journal of Heat and Mass Transfer, 1987. **30**(1): p. 15-22.
130. Kays, W.M. and M.E. Crawford, *Convective Heat and Mass Transfer*. 3rd Edition ed. 1993, New York: McGraw-Hill.
131. Weigand, B., J.R. Ferguson, and M.E. Crawford, *An extended Kays and Crawford turbulent Prandtl number model.* International Journal of Heat and Mass Transfer, 1997. **40**(17): p. 4191-4196.
132. Schwertfirm, F. and M. Manhart, *DNS of passive scalar transport in turbulent channel flow at high Schmidt numbers.* International Journal of Heat and Fluid Flow, 2007. **28**(6): p. 1204-1214.
133. Kasagi, N. and Y. Ohtsubo, *Direct Numerical Simulation of Low Prandtl Number Thermal Field in a Turbulent Channel Flow.* Turbulent Shear Flow, 1993. **8**: p. 97-119.
134. Hasegawa, Y. and N. Kasagi, *Effects of interfacial velocity boundary condition on turbulent mass transfer at high Schmidt numbers.* International Journal of Heat and Fluid Flow, 2007. **28**(6): p. 1192-1203.
135. Crimaldi, J.P., J.R. Koseff, and S.G. Monismith, *A mixing-length formulation for the turbulent Prandtl number in wall-bounded flows with bed roughness and elevated scalar sources.* Physics of Fluids, 2006. **18**(9): p. 095102-9.
136. Churchill, S.W. and C. Chan, *Improved Correlating Equations for the Friction Factor for Fully Turbulent Flow in Round Tubes and between Identical Parallel Plates, both Smooth and Naturally Rough.* Industrial & Engineering Chemistry Research, 1994. **33**(8): p. 2016-2019.
137. Churchill, S.W. and C. Chan, *Theoretically Based Correlating Equations for the Local Characteristics of Fully Turbulent Flow in Round Tubes and between Parallel Plates.* Industrial & Engineering Chemistry Research, 1995. **34**(4): p. 1332-1341.
138. Churchill, S.W. and C. Chan, *Turbulent flow in channels in terms of turbulent shear and normal stresses.* AIChE Journal, 1995. **41**(12): p. 2513-2521.
139. Churchill, S.W., *A Reinterpretation of the Turbulent Prandtl Number†.* Industrial & Engineering Chemistry Research, 2002. **41**(25): p. 6393-6401.

140. Yu, B., H. Ozoe, and S. W. Churchill, *The characteristics of fully developed turbulent convection in a round tube.* Chemical Engineering Science, 2001. **56**(5): p. 1781-1800.
141. Churchill, S.W., B. Yu, and Y. Kawaguchi, *The accuracy and parametric sensitivity of algebraic models for turbulent flow and convection.* International Journal of Heat and Mass Transfer, 2005. **48**(25–26): p. 5488-5503.
142. Mitrovic, B.M., P.M. Le, and D.V. Papavassiliou, *On the Prandtl or Schmidt number dependence of the turbulent heat or mass transfer coefficient.* Chemical Engineering Science, 2004. **59**(3): p. 543-555.
143. Le, P.M. and D.V. Papavassiliou, *On temperature prediction at low Re turbulent flows using the Churchill turbulent heat flux correlation.* International Journal of Heat and Mass Transfer, 2006. **49**(19–20): p. 3681-3690.
144. Danov, S.N., N. Arai, and S.W. Churchill, *Exact formulations and nearly exact numerical solutions for convection in turbulent flow between parallel plates.* International Journal of Heat and Mass Transfer, 2000. **43**(15): p. 2767-2777.
145. Moin, P. and K. Mahesh, *DIRECT NUMERICAL SIMULATION: A Tool in Turbulence Research.* Annual Review of Fluid Mechanics, 1998. **30**(1): p. 539-578.
146. Kasagi, N. and N. Shikazono, *Contribution of Direct Numerical Simulation to Understanding and Modelling Turbulent Transport.* Proceedings: Mathematical and Physical Sciences, 1995. **451**(1941): p. 257-292.
147. Günther, A., et al., *Turbulent flow in a channel at a low Reynolds number.* Experiments in Fluids, 1998. **25**(5): p. 503-511.
148. Le, P.M. and D.V. Papavassiliou, *Turbulent dispersion from elevated line sources in channel and couette flow.* AIChE Journal, 2005. **51**(9): p. 2402-2414.
149. Le, P.M. and D.V. Papavassiliou, *Turbulent Heat Transfer in Plane Couette Flow.* Journal of Heat Transfer, 2006. **128**(1): p. 53-62.
150. Papavassiliou, D.V. and T.J. Hanratty, *Interpretation of large-scale structures observed in a turbulent plane Couette flow.* International Journal of Heat and Fluid Flow, 1997. **18**(1): p. 55-69.
151. Papavassiliou, D.V. and T.J. Hanratty, *The Use of Lagrangian Methods To Describe Turbulent Transport of Heat from a Wall.* Industrial & Engineering Chemistry Research, 1995. **34**(10): p. 3359-3367.
152. Ponoth, S.S. and J.B. McLaughlin, *Numerical simulation of mass transfer for bubbles in water.* Chemical Engineering Science, 2000. **55**(7): p. 1237-1255.
153. Papavassiliou, D.V., *Turbulent transport from continuous sources at the wall of a channel.* International Journal of Heat and Mass Transfer, 2002. **45**(17): p. 3571-3583.
154. Mito, Y. and T.J. Hanratty, *Lagrangian stochastic simulation of turbulent dispersion of heat markers in a channel flow.* International Journal of Heat and Mass Transfer, 2003. **46**(6): p. 1063-1073.
155. Mitrovic, B.M. and D.V. Papavassiliou, *Transport properties for turbulent dispersion from wall sources.* AIChE Journal, 2003. **49**(5): p. 1095-1108.
156. Papavassiliou, D.V. and T.J. Hanratty, *Transport of a passive scalar in a turbulent channel flow.* International Journal of Heat and Mass Transfer, 1997. **40**(6): p. 1303-1311.

157. Papavassiliou, D.V., *Scalar dispersion from an instantaneous line source at the wall of a turbulent channel for medium and high Prandtl number fluids.* International Journal of Heat and Fluid Flow, 2002. **23**(2): p. 161-172.
158. Kontomaris, K. and T.J. Hanratty, *Effect of molecular diffusivity on point source diffusion in the center of a numerically simulated turbulent channel flow.* International Journal of Heat and Mass Transfer, 1994. **37**(13): p. 1817-1828.
159. Kontomaris, K., T.J. Hanratty, and J.B. McLaughlin, *An algorithm for tracking fluid particles in a spectral simulation of turbulent channel flow.* Journal of Computational Physics, 1992. **103**(2): p. 231-242.
160. Hasegawa, Y. and N. Kasagi, *The Role of Splatting Effect in High Schmidt Number Turbulent Mass Transfer Across an Air-Water Interface*, in *Turbulence, Heat and Mass Transfer*, K. Hanjalic, Y. Nagano, and M. Tummers, Editors. 2003, Begell House: New York.
161. Mitrovic, B.M., *Investigation of Turbulent Transport in a Channel with Lagrangian Numerical Methods*, 2002, University of Oklahoma: Norman.
162. Nguyen, K.T. and D.V. Papavassiliou, *Flow effects on the kinetics of a second-order reaction.* Chemical Engineering Journal, 2008. **140**(1–3): p. 370-380.
163. Lombardi, P., V. De Angelis, and S. Banerjee, *Direct numerical simulation of near-interface turbulence in coupled gas-liquid flow.* Physics of Fluids, 1996. **8**(6): p. 1643-1665.
164. Spencer, N.B., et al., *Turbulence structure for plane Poiseuille–Couette flow and implications for drag reduction over surfaces with slip.* The Canadian Journal of Chemical Engineering, 2009. **87**(1): p. 38-46.
165. Corrsin, S., *Heat Transfer in Isotropic Turbulence.* Journal of Applied Physics, 1952. **23**(1): p. 113-118.
166. Komminaho, J., A. Lundbladh, and A.V. Johansson, *Very large structures in plane turbulent Couette flow.* Journal of Fluid Mechanics, 1996. **320**: p. 259-285.
167. Lu, S.S. and W.W. Willmarth, *Measurements of the structure of the Reynolds stress in a turbulent boundary layer.* Journal of Fluid Mechanics, 1973. **60**(03): p. 481-511.
168. Mito, Y., et al., *Flow Visualization of Superbursts and of the Log-Layer in a DNS at $Re_\tau = 950$.* Flow, Turbulence and Combustion, 2007. **79**(2): p. 175-189.
169. Lyons, S.L., T.J. Hanratty, and J.B. McLaughlin, *Turbulence-producing eddies in the viscous wall region.* AIChE Journal, 1989. **35**(12): p. 1962-1974.
170. Finnicum, D.S. and T.J. Hanratty, *Effect of favorable pressure gradients on turbulent boundary layers.* AIChE Journal, 1988. **34**(4): p. 529-540.
171. Kim, J. and P. Moin, *Transport of Passive Scalars in a Turbulent Channel Flow*. Turbulent Shear Flows VI, ed. J.-C. Andre, et al. 1989, Berlin: Springer-Verlag. 85-96.
172. Kawamura, H., H. Abe, and Y. Matsuo, *DNS of turbulent heat transfer in channel flow with respect to Reynolds and Prandtl number effects.* International Journal of Heat and Fluid Flow, 1999. **20**(3): p. 196-207.
173. Shaw, D.A. and T.J. Hanratty, *Influence of Schmidt number on the fluctuations of turbulent mass transfer to a wall.* AIChE Journal, 1977. **23**(2): p. 160-169.

174. Hasegawa, Y. and N. Kasagi, *Low-pass filtering effects of viscous sublayer on high Schmidt number mass transfer close to a solid wall.* International Journal of Heat and Fluid Flow, 2009. **30**(3): p. 525-533.
175. Na, Y. and T.J. Hanratty, *Limiting behavior of turbulent scalar transport close to a wall.* International Journal of Heat and Mass Transfer, 2000. **43**(10): p. 1749-1758.
176. Teitel, M. and R.A. Antonia, *Heat transfer in fully developed turbulent channel flow: comparison between experiment and direct numerical simulations.* International Journal of Heat and Mass Transfer, 1993. **36**(6): p. 1701-1706.
177. Dong, Y.-H., X.-Y. Lu, and L.-X. Zhuang, *Large eddy simulation of turbulent channel flow with mass transfer at high-Schmidt numbers.* International Journal of Heat and Mass Transfer, 2003. **46**(9): p. 1529-1539.
178. Wang, L., Y.H. Dong, and X.Y. Lu, *Large eddy simulation of turbulent open channel flow with heat transfer at high Prandtl numbers.* Acta Mechanica, 2004. **170**(3-4): p. 227-246.
179. Bergant, R. and I. Tiselj, *Near-wall passive scalar transport at high Prandtl numbers.* Physics of Fluids, 2007. **19**(6): p. 065105-18.
180. Kasagi, N. and Y. Ohtsubo. 1992; Available from: http://www.thtlab.t.u-tokyo.ac.jp/.
181. Kawamura, H., et al., *DNS of turbulent heat transfer in channel flow with low to medium-high Prandtl number fluid.* International Journal of Heat and Fluid Flow, 1998. **19**(5): p. 482-491.
182. Durbin, P.A., *A stochastic model of two-particle dispersion and concentration fluctuations in homogeneous turbulence.* Journal of Fluid Mechanics, 1980. **100**(02): p. 279-302.
183. Sreenivasan, K.R., *On Local Isotropy of Passive Scalars in Turbulent Shear Flows.* Proceedings: Mathematical and Physical Sciences, 1991. **434**(1890): p. 165-182.
184. Poreh, M. and J.E. Cermak, *Study of diffusion from a line source in a turbulent boundary layer.* International Journal of Heat and Mass Transfer, 1964. **7**(10): p. 1083-1095.
185. Raupach, M.R. and B.J. Legg, *Turbulent dispersion from an elevated line source: measurements of wind-concentration moments and budgets.* Journal of Fluid Mechanics, 1983. **136**: p. 111-137.
186. Incropera, F.P., et al., *Convection heat transfer from discrete heat sources in a rectangular channel.* International Journal of Heat and Mass Transfer, 1986. **29**(7): p. 1051-1058.
187. Karnik, U. and S. Tavoularis, *Measurements of heat diffusion from a continuous line source in a uniformly sheared turbulent flow.* Journal of Fluid Mechanics, 1989. **202**: p. 233-261.
188. Stapountzis, H. and R.E. Britter. *Turbulent Diffusion behind a Heated Line Source in a Nearly Homogenous Turbulent Shear Flow*. in *Symposium on Turbulent Shear Flows*. 1987. Toulouse: Springer.
189. Chung, M.K. and N.H. Kyong, *Measurement of turbulent dispersion behind a fine cylindrical heat source in a weakly sheared flow.* Journal of Fluid Mechanics, 1989. **205**: p. 171-193.

190. Wilson, J.D., T.K. Flesch, and G.E. Swaters, *Dispersion in sheared Gaussian homogeneous turbulence.* Boundary-Layer Meteorology, 1993. **62**(1): p. 281-290.
191. Cho, M.S. and M.K. Chung, *Application of a Reynolds Stress/Heat Flux Model to the Turbulent Thermal Dispersion behind a Line Heat Source in a Uniformly Sheared Flow.* Numerical Heat Transfer, Part A: Applications, 1997. **32**(7): p. 715-732.
192. Srinivasan, C. and D.V. Papavassiliou, *Backwards and forwards dispersion of a scalar in turbulent wall flows.* International Journal of Heat and Mass Transfer, 2010. **53**(5–6): p. 1023-1035.
193. Srinivasan, C. and D.V. Papavassiliou, *Direction of scalar transport in turbulent channel flow.* Physics of Fluids, 2011. **23**(11): p. 115105-21.
194. Srinivasan, C. and D.V. Papavassiliou, *Comparison of backwards and forwards scalar relative dispersion in turbulent shear flow.* International Journal of Heat and Mass Transfer, 2012. **55**(21–22): p. 5650-5664.
195. Lavertu, A. and L. Mydlarski, *Scalar mixing from a concentrated source in turbulent channel flow.* Journal of Fluid Mechanics, 2005. **528**: p. 135-172.
196. Ott, S. and J. Mann, *An experimental investigation of the relative diffusion of particle pairs in three-dimensional turbulent flow.* Journal of Fluid Mechanics, 2000. **422**: p. 207-223.
197. Biferale, L., et al., *Lagrangian statistics of particle pairs in homogeneous isotropic turbulence.* Physics of Fluids, 2005. **17**(11): p. 115101-9.
198. Sawford, B.L., P.K. Yeung, and J.F. Hackl, *Reynolds number dependence of relative dispersion statistics in isotropic turbulence.* Physics of Fluids, 2008. **20**(6): p. 065111-13.
199. Bourgoin, M., et al., *The Role of Pair Dispersion in Turbulent Flow.* Science, 2006. **311**(5762): p. 835-838.
200. Ishihara, T. and Y. Kaneda, *Relative diffusion of a pair of fluid particles in the inertial subrange of turbulence.* Physics of Fluids, 2002. **14**(11): p. L69-L72.
201. Luthi, B., et al., *Self-similar two-particle separation model.* Physics of Fluids, 2007. **19**(4): p. 045110-14.
202. Schumacher, J., *Lagrangian studies in convective turbulence.* Physical Review E, 2009. **79**(5): p. 056301.

Appendix A - Nomenclature

A	empirical constant value 0.3 prescribing the spatial variation of Pr_t vs Pe_t appearing in equation (2.26)
b	empirical constant with value 0.4 appearing in equation (7.16)
c_p	heat capacity at constant pressure
C_f	coefficient of friction loss
d	empirical constant appearing in equation (2.28)
D	molecular diffusivity
D_t	eddy diffusivity of mass
E	Lagrangian scalar spectrum
g	Richardson-Obukhov constant appearing in equation (2.8)
$\vec{U}$	Eigenvector obtained from the decomposition of the full material correlation coefficient tensor matrix
h	half channel height
j	heat flux density in the y direction
k	thermal conductivity
L_M	mixing length scales of momentum transfer
L_T	mixing length scales of heat transfer
P_1	probability density function for a marker to be at a certain at a location (x,y) at time t, given that it was released at a known time at a known location at the wall
Pe	Peclet Number
Pe_t	turbulent Peclet number $(Pe_t = \Pr \nu_t / \nu)$

Pr	Prandtl number $(\mathrm{Pr} = \nu / \alpha)$
Pr_{eff}	quantity appearing in equation (2.22) defined in equation (2.23)
Pr_{t}	turbulent Prandtl number ($Pr_{\mathrm{t}} = \nu_{\mathrm{t}}/\alpha_{\mathrm{t}}$)
$Pr_{\mathrm{t}\infty}$	turbulent Prandtl number far away from the wall
Q	represents the Quadrants of the velocity components
q	heat flux
r	variable appearing in equation (2.11), given by $r(\eta) = U(\eta) / U_B$
R	material correlation coefficient
R_{HF}	quantity representing ratio of molecular diffusion flux to turbulent transport flux defined in equation (2.12)
Re	Reynolds number based on mean centerline velocity
Re_{t}	Turbulent Reynolds number
R_{uu}, R_{vv}, R_{ww}	Lagrangian material correlation coefficient in the *x, y, z* directions
R_{uv}, R_{vu}	Lagrangian material cross correlation coefficients in the *x, y* directions
R_{vw}, R_{wv}	Lagrangian material cross correlation coefficients in the *y, z* directions
R_{uw}, R_{wu}	Lagrangian material cross correlation coefficients in the *z, x* directions
$\underline{\underline{R}}$	Complete material auto- and cross-correlation tensor matrix in all three x, y, z directions
s	similarity analysis parameter
S_u, S_v, S_w	skewness of the velocity fluctuations in the *x, y, z* directions
Sc	Schmidt number $\left(Sc = \nu / D\right)$
Sc_{t}	turbulent Schmidt number $\left(Sc = \nu_t / D_t\right)$

t	time
T	temperature
$(\overline{T'v'})$	turbulent heat flux in the normal direction
$\overline{(T'v')}^{++}$	local fraction of radial heat flux density due to turbulence
t	time
t_0, t_f	initial and final time of tracking of markers
t_c	time of capture of markers
U_B	bulk velocity calculated as $U_B = \frac{1}{h^+}\int_0^{h^+} U^+(y^+)dy^+$
$\vec{U}$	Eulerian velocity vector
u^*	friction velocity, $u^* = (\tau_w / \rho)^{1/2}$
u, v, w	fluctuating velocity components in the *x, y, z* directions
$\overline{u'v'}$	Reynolds stress
$\overline{(u'v')}^{++}$	local fraction of shear stress due to turbulence
V_k	Von Karman constant appearing in equation (7.8)
$\vec{V}$	Lagrangian velocity vector
x, y, z	streamwise, normal and spanwise coordinates
X	displacement of a marker from the source in the *x* direction
$\vec{X}$	position vector of a marker
$\vec{x_0}$	initial position vector of a marker
$\overline{Y}$	Average normal position of the markers

Greek symbols

α	thermal diffusivity of heat
α_t	eddy diffusivity of heat
β	variable appearing in equation (1.1) given by equation (1.3)
γ	Churchill's correction term appearing in equation (7.6)
Γ	shear stress
δ	Kronecker delta
Δt	time step
Δy	difference in the y direction
ε	rate of dissipation of turbulent kinetic energy
ζ_T	thermal boundary layer thickness
ζ_T^D	thermal displacement thickness given by $\zeta_T^D = \int_0^\infty \frac{T - T_\infty}{T_w - T_\infty} dy$
η	variable appearing in equation (2.11) $\eta = y^+ / h^+$
θ	angle the eigenvector makes with different planes
κ	turbulent kinetic energy
λ	eigenvalues obtained from the correlation coefficient tensor
ν	kinematic viscosity
ν_t	eddy viscosity
ξ	variable appearing in equation (1.1) given by equation (1.4)
π	trigonometric pi $(\pi = 3.14159...)$
ρ	fluid density
σ	standard deviation of a probability density function

τ	material timescale
τ^L	Lagrangian timescale
τ_v	Lagrangian timescale in *y*-direction
Φ	scaling variable defined by equation (2.10)
χ	periodicity lengths in the turbulent channel

Superscripts and Subscripts

$\overline{(\ )}$	ensemble average
$(\ )^L$	Lagrangian variable
$(\ )^+$	value made dimensionless with the wall parameters
$(\ )^{++}$	local fraction of a quantity due to turbulence
$(\ )_b$	value for backwards dispersion
$(\ )_f$	value for forwards dispersion
$(\ )_{\max}$	maximum value of the variable
$(\ )_{si}$	inner similarity scales
$(\ )_{so}$	outer similarity scales
$(\ )_t$	turbulent dimensionless number
$(\ )_0$	value at the instant of marker release
$(\ )_w$	value at the wall of the channel
$(\ )_\infty$	value at the center of the channel or at the outer regions of boundary layers

Appendix B - Primary directions of heat transport

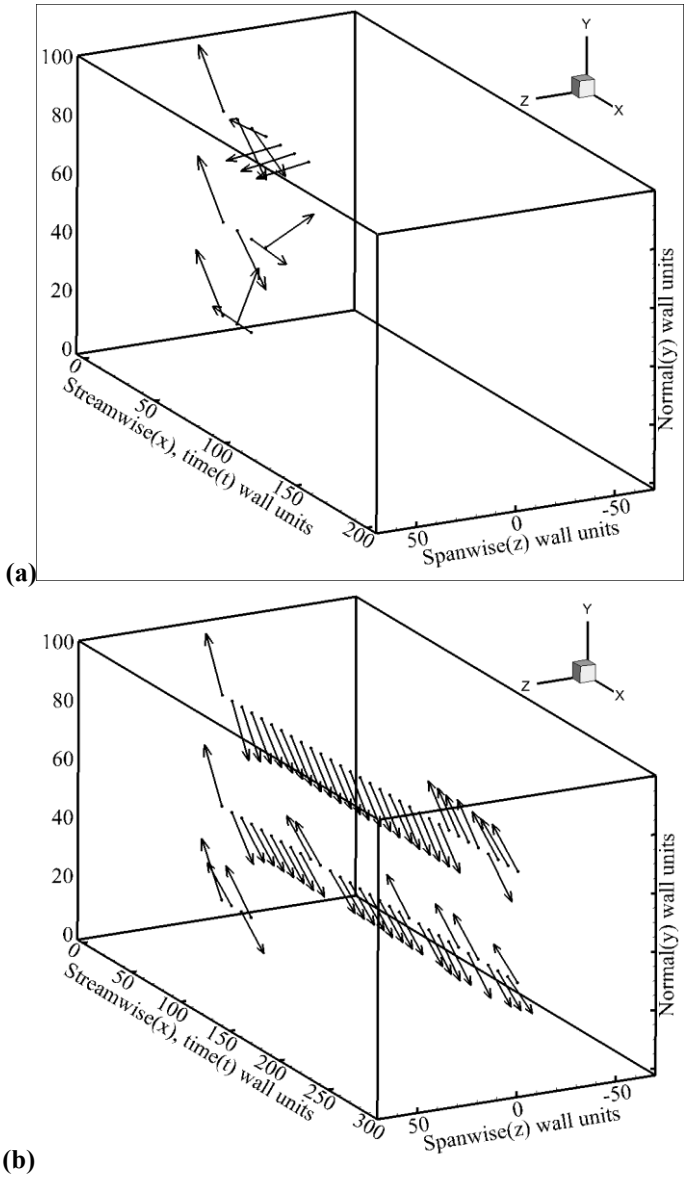

Figure B-1: Orientation of the eigenvectors corresponding to the highest eigenvalues, plotted in three dimensions in a domain comparable to the computational box, not to exact scale, as a function of time, for a $Pr = 0.7$ in all three regions of Poiseuille channel, namely, the viscous sub-layer, the transition region and the logarithmic region: (a) forwards dispersion; (b) backwards dispersion. Since for this case, at the center of channel the eigenvectors corresponding to the highest eigenvalues have random orientations, it is excluded from the figure.

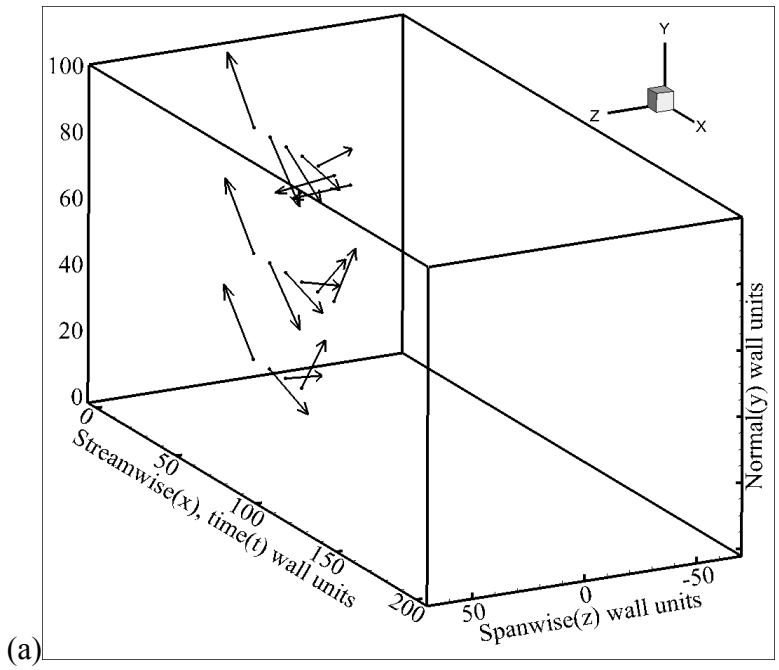

(a)

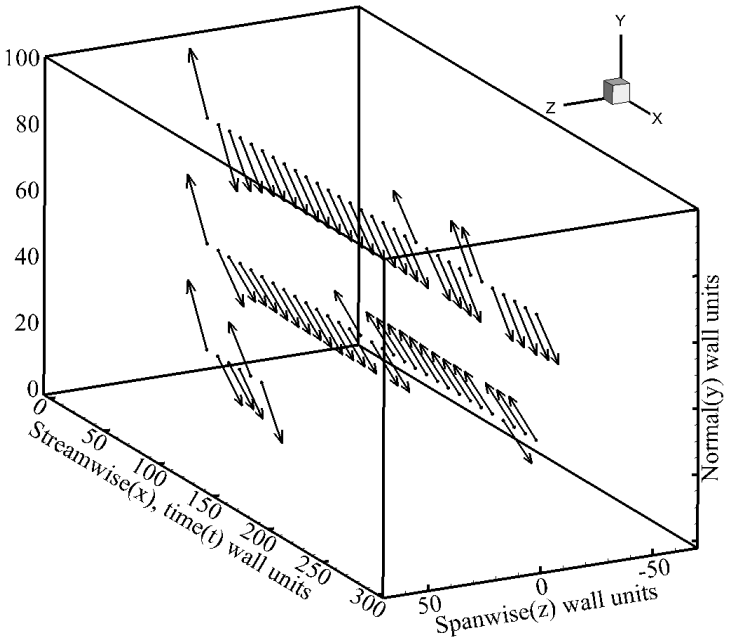

(b)

Figure B-2: Orientation of the eigenvectors corresponding to the highest eigenvalues, plotted in three dimensions in a domain comparable to the computational box, not to exact scale, as a function of time, for a $Pr = 6$ in all three regions of Poiseuille channel, namely, the viscous sub-layer, the transition region and the logarithmic region: (a) forwards dispersion; (b) backwards dispersion. Since for this case, at the center of channel the eigenvectors corresponding to the highest eigenvalues have random orientation, it is excluded from the figure.

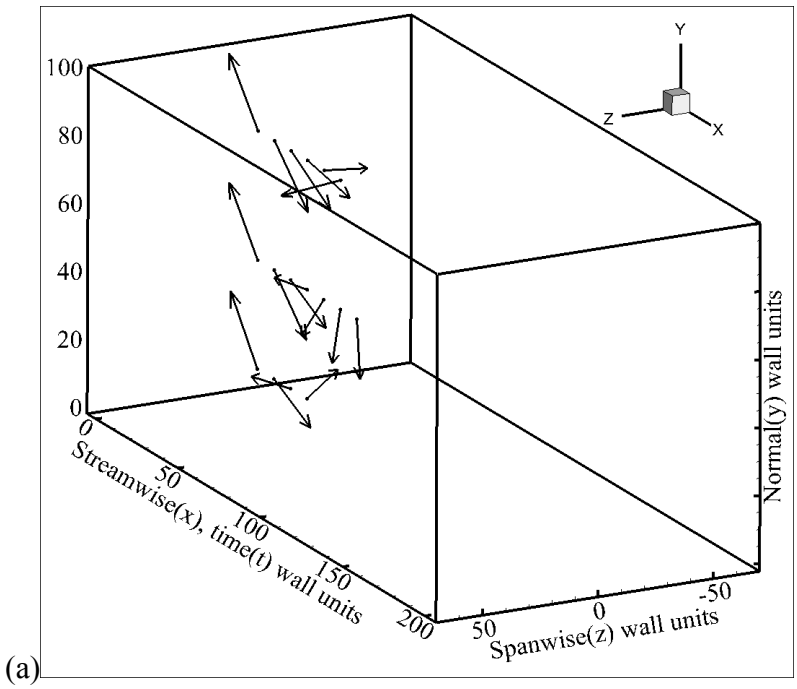

(a)

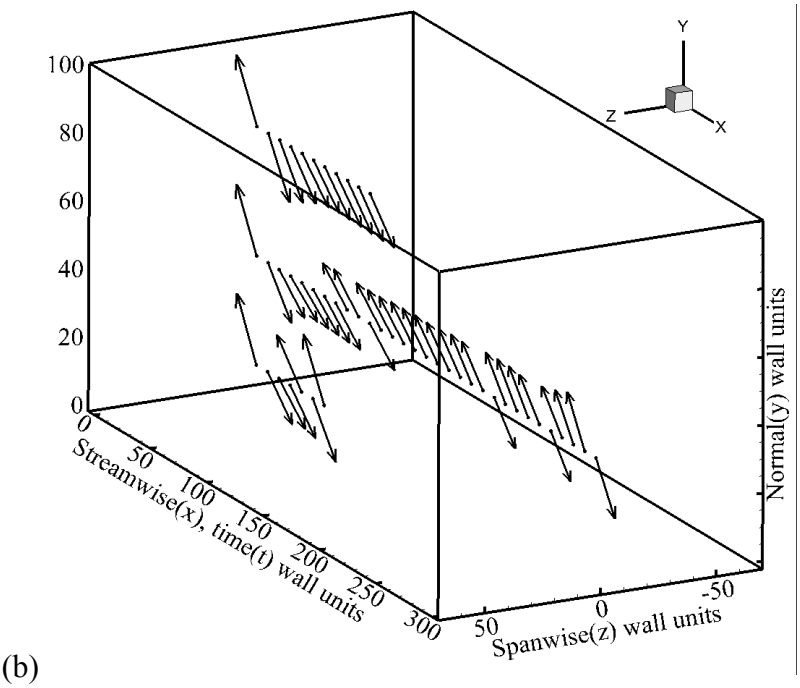

(b)

Figure B-3: Orientation of the eigenvectors corresponding to the highest eigenvalues, plotted in three dimensions in a domain comparable to the computational box, not to exact scale, as a function of time, for a Pr = 1000 in all three regions of Poiseuille channel, namely, the viscous sub-layer, the transition region and the logarithmic region: (a) forwards dispersion; (b) backwards dispersion. Since for this case, at the center of channel the eigenvectors corresponding to the highest eigenvalues have random orientation, it is excluded from the figure.

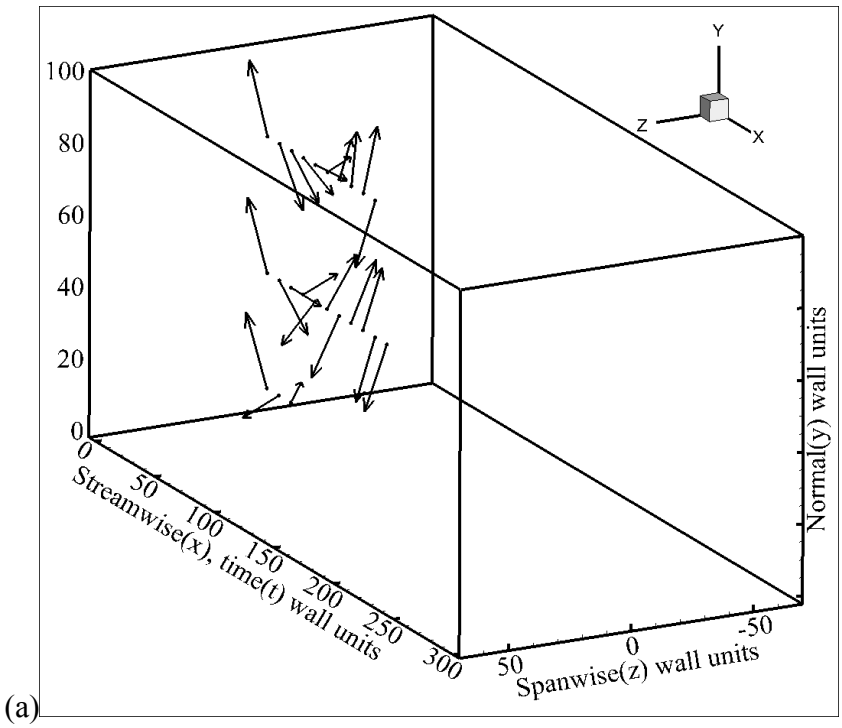

(a)

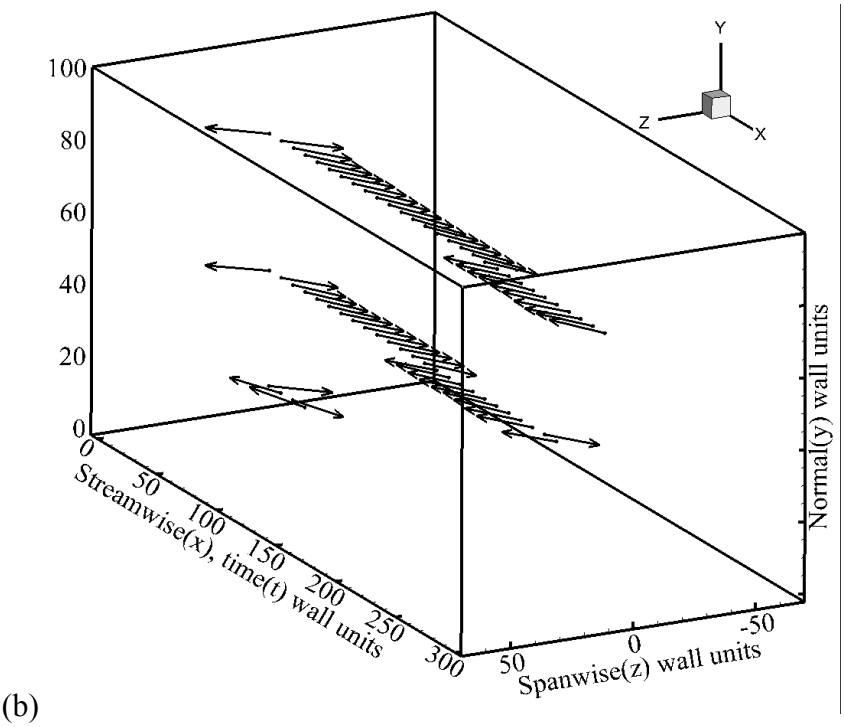

(b)

Figure B-4: Orientation of the eigenvectors corresponding to the highest eigenvalues, plotted in three dimensions in a domain comparable to the computational box, not to exact scale, as a function of time, for a $Pr = 0.7$ in all three regions of plane Couette flow: (a) forwards dispersion; (b) backwards dispersion.

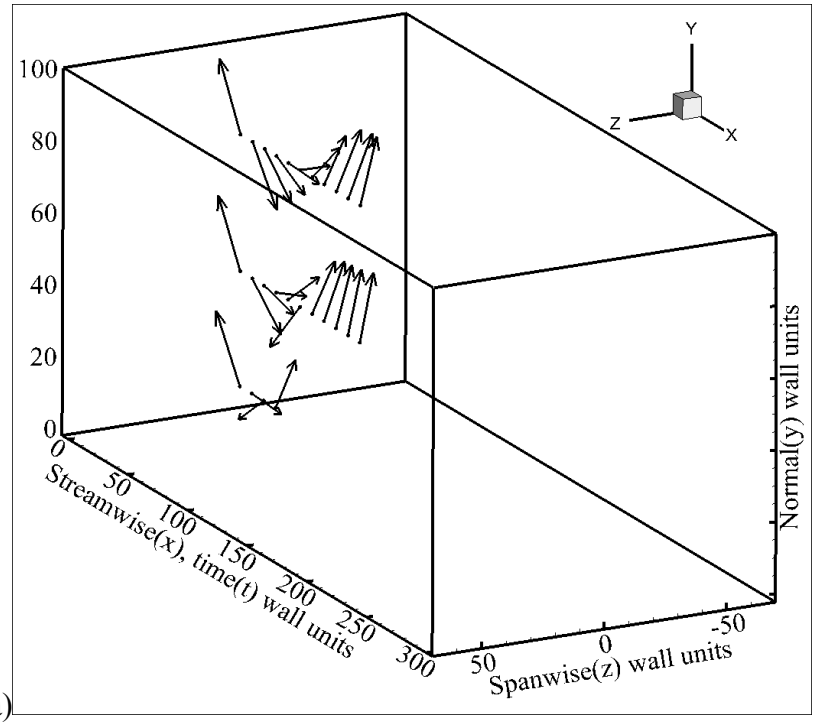

(a)

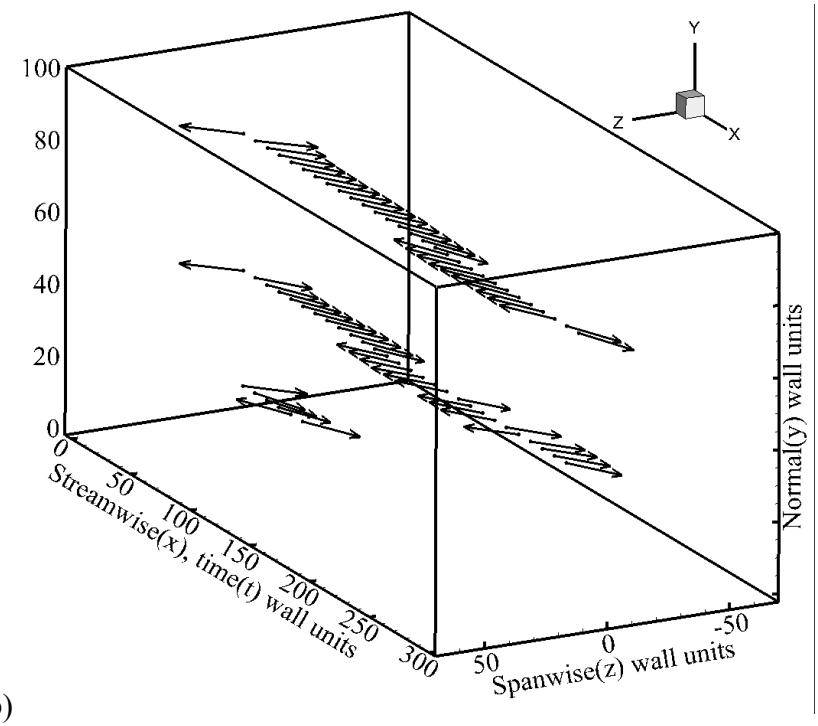

(b)

Figure B-5: Orientation of the eigenvectors corresponding to the highest eigenvalues, plotted in three dimensions in a domain comparable to the computational box, not to exact scale, as a function of time, for a $Pr = 6$ in all three regions of plane Couette flow: (a) forwards dispersion; (b) backwards dispersion.

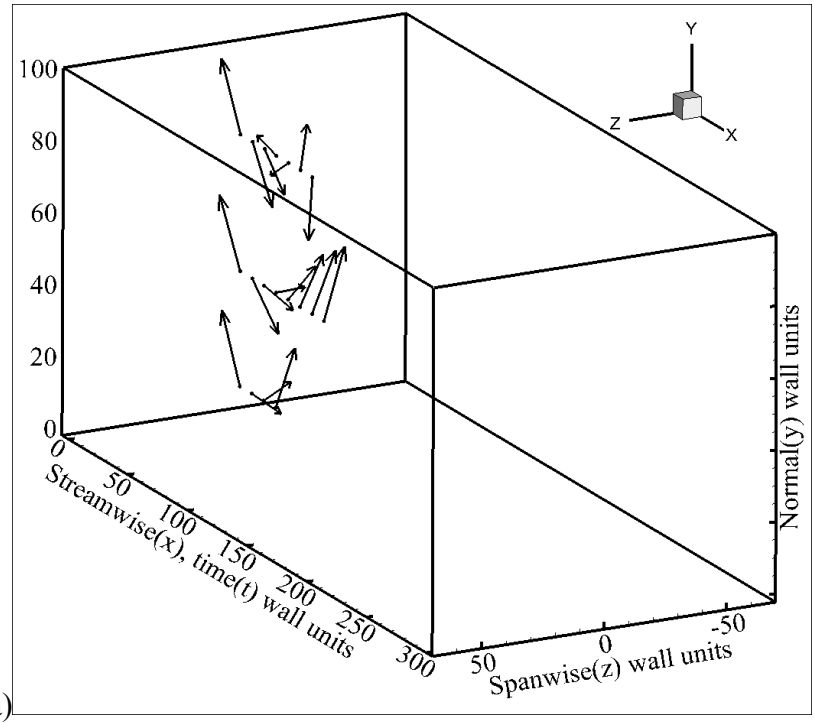

(a)

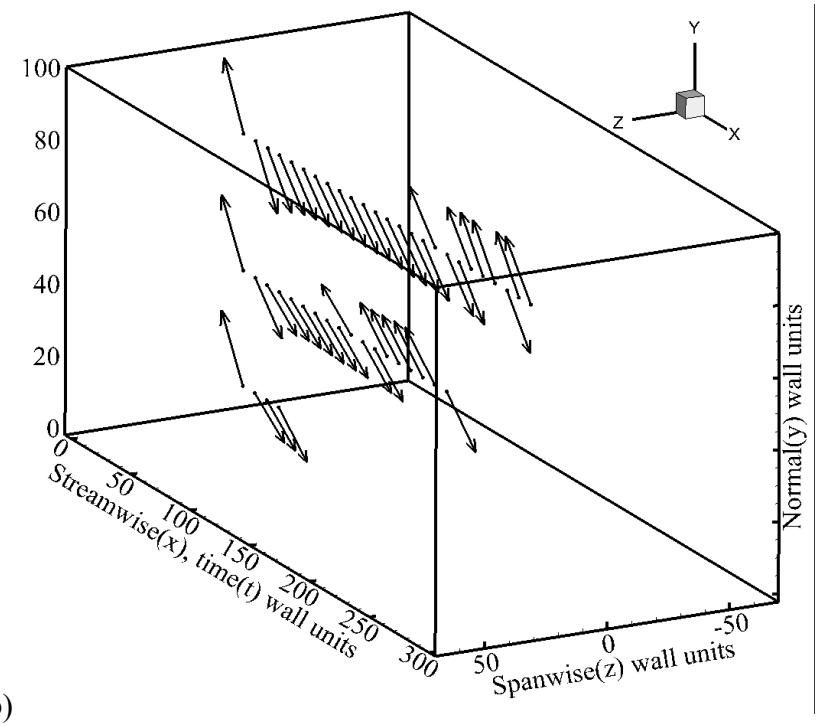

(b)

Figure B-6: Orientation of the eigenvectors corresponding to the highest eigenvalues, plotted in three dimensions in a domain comparable to the computational box, not to exact scale, as a function of time, for a $Pr = 500$ in all three regions of plane Couette flow: (a) forwards dispersion; (b) backwards dispersion.

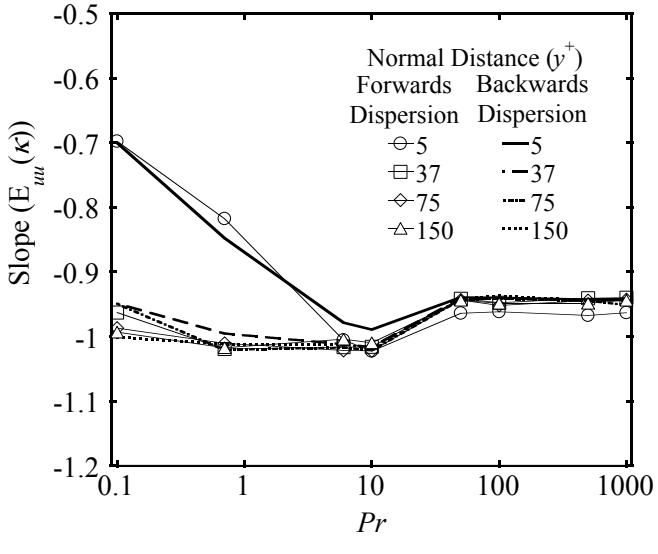
Slope ($E_{uu}(\kappa)$)
Normal Distance (y^+)
Forwards Dispersion
Backwards Dispersion
5
37
75
150
-0.5
-0.6
-0.7
-0.8
-0.9
-1
-1.1
-1.2
0.1
1
10
100
1000
Pr

(a)

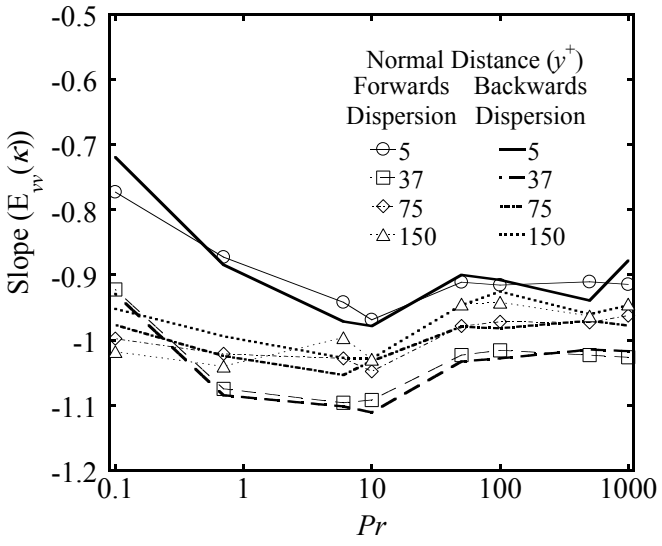
Slope ($E_{vv}(\kappa)$)
Normal Distance (y^+)
Forwards Dispersion
Backwards Dispersion
5
37
75
150
-0.5
-0.6
-0.7
-0.8
-0.9
-1
-1.1
-1.2
0.1
1
10
100
1000
Pr

(b)

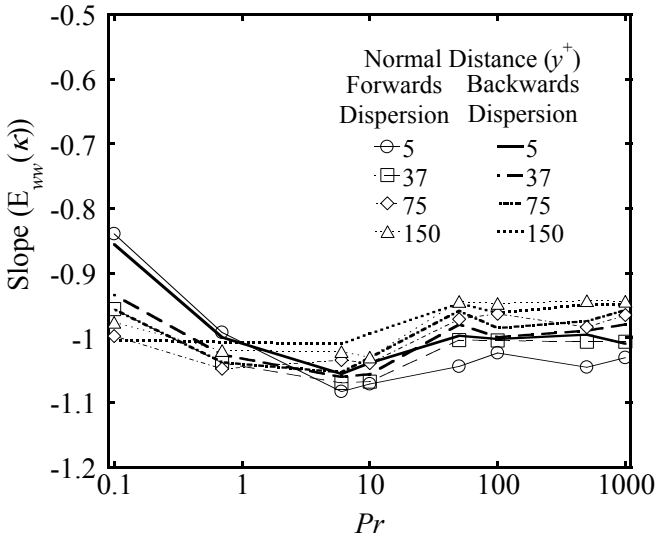
Slope ($E_{ww}(\kappa)$)
Normal Distance (y^+)
Forwards Dispersion
Backwards Dispersion
5
37
75
150
-0.5
-0.6
-0.7
-0.8
-0.9
-1
-1.1
-1.2
0.1
1
10
100
1000
Pr

(c)

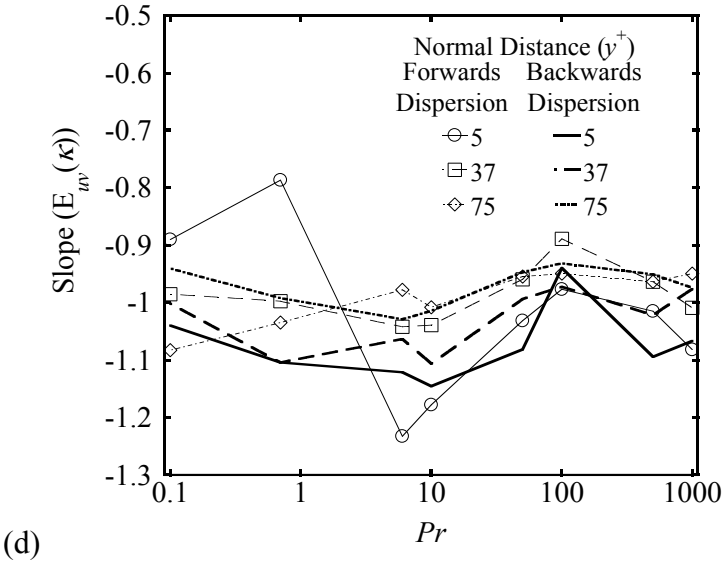

(d)

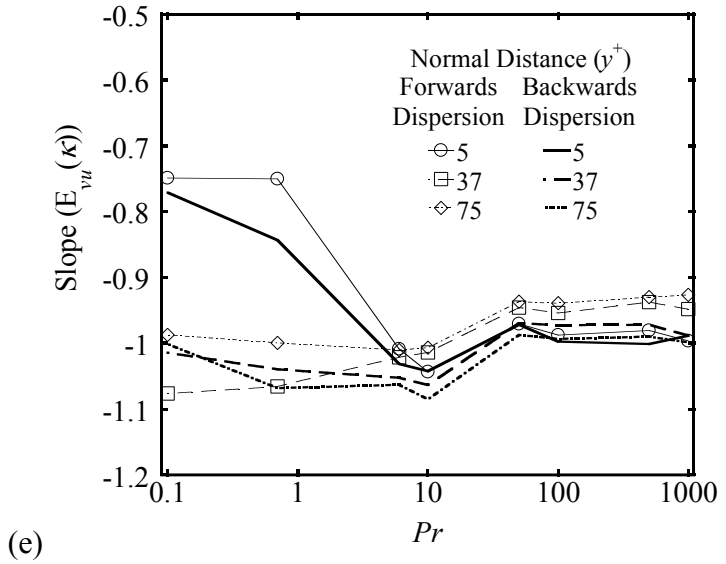

(e)

Figure B-7: Slopes of the spectrum obtained from different correlation coefficient as a function of *Pr* for different regions of Poiseuille channel flow: (a) streamwise autocorrelation; (b) normal autocorrelation; (c) spanwise autocorrelation; (d) streamwise-normal cross correlation; (e) normal-streamwise cross correlation. In figures (d) and (e), the center of channel is excluded as the slopes are close to zero.

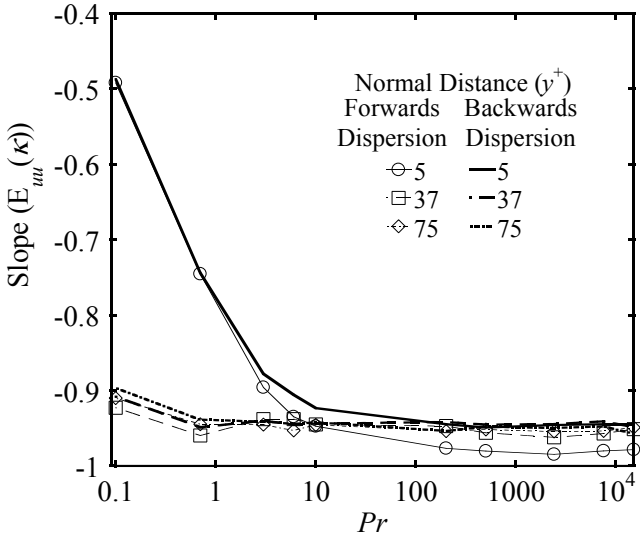
Slope (E_{uu} (κ))
-0.4
-0.5
-0.6
-0.7
-0.8
-0.9
-1
0.1
1
10
100
1000
10^4
Pr
Normal Distance (y^+)
Forwards Dispersion
Backwards Dispersion
5
37
75
5
37
75

(a)

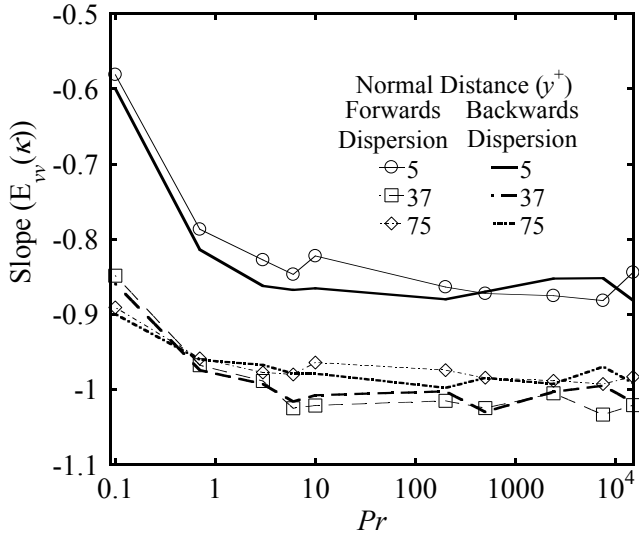
Slope (E_{vv} (κ))
-0.5
-0.6
-0.7
-0.8
-0.9
-1
-1.1
0.1
1
10
100
1000
10^4
Pr
Normal Distance (y^+)
Forwards Dispersion
Backwards Dispersion
5
37
75
5
37
75

(b)

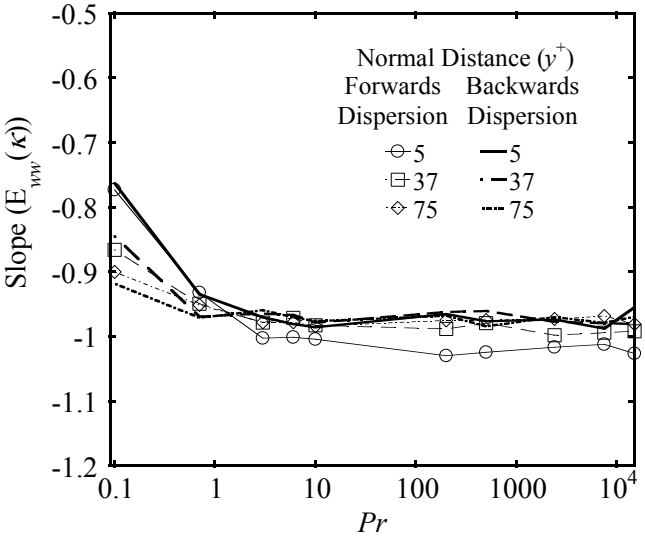
Slope (E_{ww} (κ))
-0.5
-0.6
-0.7
-0.8
-0.9
-1
-1.1
-1.2
0.1
1
10
100
1000
10^4
Pr
Normal Distance (y^+)
Forwards Dispersion
Backwards Dispersion
5
37
75
5
37
75

(c)

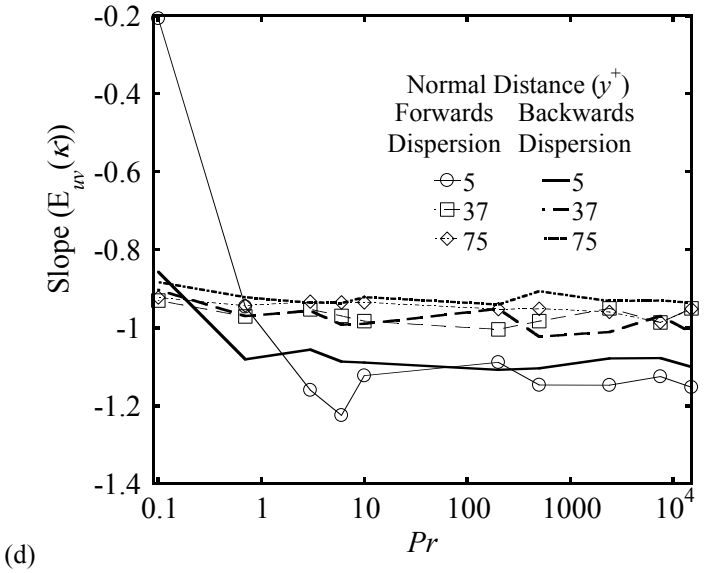

(d)

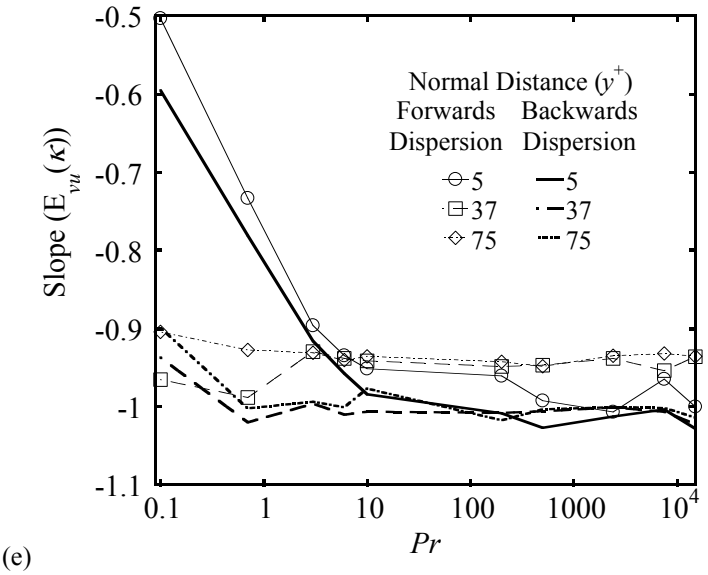

(e)

Figure B-8: Slopes of the spectrum obtained from different correlation coefficient as a function of Pr for different regions of plane Couette flow: (a) streamwise autocorrelation; (b) normal autocorrelation; (c) spanwise autocorrelation; (d) streamwise-normal cross correlation; (e) normal-streamwise cross correlation.